Eulerian modelling and computational fluid dynamics simulation of mono and polydisperse fluidized suspensions

Luca Mazzei

Department of Chemical Engineering

University College London

A thesis submitted for the degree of

Doctor of Philosophy of University College London

October 2008

I, Luca Mazzei, confirm that the work presented in this thesis is my own. Where information has been derived from other sources, I confirm that this has been indicated in the thesis.

To Evelyne

The scientist does not study Nature because it is useful; he studies it because he delights in it, and he delights in it because it is beautiful. If Nature were not beautiful, it would not be worth knowing, and if Nature were not worth knowing, life would not be worth living.

Henri Poincaré (1854 - 1912)

Abstract

This research project is concerned with the Eulerian-Eulerian mathematical modelling of fluidized suspensions. We first derive new averaged equations of motion for particulate systems made up of a finite number of monodisperse particle classes; this clarifies the mathematical origin and physical meaning of the terms featuring in the equations and allows to attain a well-posed multiphase model. We then tackle the closure problem of the fluid-particle interaction force in monodisperse fluidized suspensions, laying emphasis on the buoyancy, drag and elastic forces. We analyze critically several constitutive relations used to express these forces, we identify their shortcomings and we advance new, and more accurate, closure equations. To validate them we study, analytically and computationally, the expansion and collapse of homogeneous fluidized beds and their transition to the bubbling regime, comparing the result with experimental data.

We then address the mathematical modelling of polydisperse fluidized suspensions, which are characterized by a continuous distribution of the particle properties, such as size or velocity. Here we adopt a more powerful modelling approach based on the *generalized population balance equation* (GPBE). Whereas the classical transport equations of continuum mechanics are three-dimensional, the GPBE is usually higher-dimensional and incompatible with customary computational schemes. To solve it, we use the *method of moments* (MOM), which resorts to a limited number of GPBE moments to derive three-dimensional transport equations that can be handled by normal CFD codes. The limited set of equations, which replaces the single multidimensional GPBE, keeps the problem tractable when applied to complicated multiphase flows; the main obstacle to the method is that the moment transport equations are mathematically unclosed.

To overcome the problem, we present two very efficient methods, the *direct quadrature method of moments* (DQMOM) and the *quadrature method of moments* (QMOM). Both approximate the volume density function (VDF) featuring in the GPBE by using a quadrature formula. The methods are very flexible: the number of nodes in the quadrature corresponds to the number of disperse phases simulated. The more the nodes, the better the quadrature approximation; more nodes, however, entail also more complexity and more computational effort. For monovariate systems, *i.e.*, systems with only one internal coordinate in the generalized sense, the methods are entirely equivalent from a theoretical standpoint; computationally, however, they differ substantially.

To conclude the work, we use DQMOM to simulate the dynamics of two polydisperse powders initially arranged as two superposed, perfectly-segregated packed systems. As fluidization occurs, the simulation tracks the evolution in time and physical space of the quadrature nodes and weights and predicts the mixing attained by the system. To validate the method, we compare computational predictions with experimental results.

Acknowledgements

I would like to thank Dr. Paola Lettieri for her immense support throughout this PhD project: her constant encouragement to think freely and pursue my ideas has boosted my confidence more than she might know. I feel profoundly grateful to her for what she has taught me and for all the opportunities that she has offered me literally from day one.

I also feel greatly indebted to Dr. Daniele Marchisio for his teachings and the many intellectually stimulating discussions. I am especially thankful for the opportunity he has offered me to collaborate with him and for his warm hospitality during my secondment at the Dipartimento di Scienza dei Materiali e Ingegneria Chimica, Politecnico di Torino, Italy.

I would like to express my gratitude to Dr. Derek Colman for constantly supporting my research interests and providing constructive technical suggestions.

I also would like to thank Dr. Tim Elson for having me offered the opportunity to teach the course *Physics for Chemical Engineering* and the tutorials for the course of *Transport Processes*. Thank you for your trust, support and suggestions.

A special thanks to my former teachers at the Dipartimento di Ingegneria Chimica, Università degli Studi di Napoli Federico II, Italy: their teaching has given me the strongest scientific grounding I could hope for and has allowed me to pursue my studies effectively and fruitfully. In particular, I would like to sincerely thank Prof. Piero Salatino for his support, constant encouragement and great enthusiasm. By recommending me to Dr. Paola Lettieri, he offered me the possibility to undertake this PhD project in the first place.

My warmest and heartfelt thanks to Dr. Olumuyiwa Owoyemi for his friendship, the stimulating exchanges of ideas and for introducing me to the beautiful world of LaTeX 2_ε. The writing of this thesis would have been an insurmountable and frustrating task had he not convinced me to switch from commercial typesetting programs to this incredible documentation preparation system.

I would also like to acknowledge the support and the immense patience and kindness of Mr. Martin Town of the mechanical workshop of the Chemical Engineering Department at UCL.

Many thanks also to my fellow PhD colleagues and Erasmus students: Giovanna, Chandni, Sarah, Lilli, Liban, Alessandro, Nnamso, Panos, Igino and Andrea.

Finally, I would like to thank my entire family: not only have they always given me love and support, but they have been a constant source of encouragement throughout my entire life. I would especially like to thank my dearest wife, Evelyne, whose love is truly unique and is my greatest source of happiness and hope for the future.

I would like to acknowledge financial support from BP Chemicals, Hull (UK) and the Engineering Physical Science Research Council (EPSRC).

Table of Contents

Chapter 1

General introduction

In this chapter, we introduce fluidization, we describe the various regimes in which fluidized beds can operate, we summarize the main goals of this work and we present a brief outline of the thesis.

1.1 A brief introduction to fluidization

Stationary solid particles placed in a vertical vessel and supported by a horizontal plate spanning the whole vessel base form a *fixed bed*, also called *packed bed*. If the plate is porous and we force a fluid through it from below, the particles remain packed until we reach a certain flow rate Q_{mf}. As we raise the flow rate from zero to Q_{mf}, the force exerted by the porous plate on the particles progressively drops, while the force exerted by the fluid on the particles increases. When the flow rate becomes equal to Q_{mf}, the fluid drag force entirely counterbalances the effective weight of the particles (real weight minus buoyancy force), and these no longer rest on the plate. When this happens, we say that the particles are *fluidized*. Accordingly, we call Q_{mf} *minimum fluidization flow rate*. This quantity is not intensive, since it is proportional to the cross-sectional area A of the vessel, and therefore does not represent a property of the fluid-particle system. To obtain the latter, we must divide Q_{mf} by A; this ratio, which we call *minimum fluidization velocity* and denote by u_{mf}, represents the minimum fluidization flow rate per unit cross-sectional area of the vessel.

In liquid-solid systems, if we further increase the flow rate of fluid, the bed expands smoothly and remains statistically homogeneous. Thus, we call these systems *homogeneous* or *uniform*, while the corresponding fluidization regime *homogeneous* or *particulate*. In gas-solid systems, we observe this behaviour only under special operating conditions and for very small and light particles. In most gas-solid systems, however, if we increase the fluid flux beyond u_{mf}, the excess fluid forms regions almost devoid of particles that we call *bubbles*. We call these systems *bubbling*, and the corresponding fluidization regime *bubbling* or *aggregative*. The fluid flux u_{mb} at which the first bubbles form is also a property of the fluid-particle system, and we call it *minimum bubbling velocity*. Bubbles coalesce as they rise through the bed; so, if this is deep enough, the bubbles may eventually become as large as the cross-sectional area of the vessel. We call this fluidization regime *slugging*.

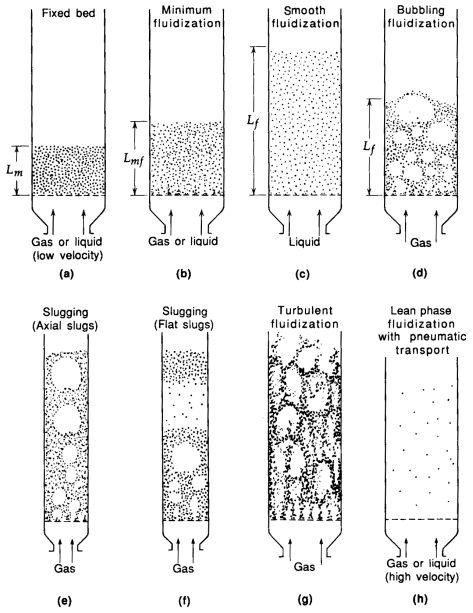

Figure 1.1: Fluidization regimes (Kunii & Levenspiel, 1989).

If the fluid flux exceeds the terminal velocity of the particles, these start moving faster and more chaotically. Streamers and clusters of particles continuously form and break, and the overall structure of the bed becomes more homogeneous. We call this new fluidization regime *turbulent*. If we further increase the fluid flux, we obtain a lean fluidized bed with *pneumatic transport*. Figure 1.1 shows the various regimes that we have described.

Physical mechanism		
gas/solid heat and/or mass transfer	solid/solid heat and/or mass transfer	bed/surface heat and/or mass transfer
• solids drying • solvent adsorption • food freezing	• granulation • solid mixing • tablet coating	• heat treatment of textile fibers, rubber and glass
Chemical mechanism		
gas/gas reaction where solids act as catalyst	gas/gas reaction where solids are transformed	
• oil cracking • oil reforming • manufacture of polyethylene, chlorinated hydrocarbons and acrylonitrile	• coal combustion • gasification • incineration of liquid and solid waste • manufacture of titanium oxide • catalyst regeneration	

Table 1.1: Industrial uses of fluidized beds (Lettieri, 2002).

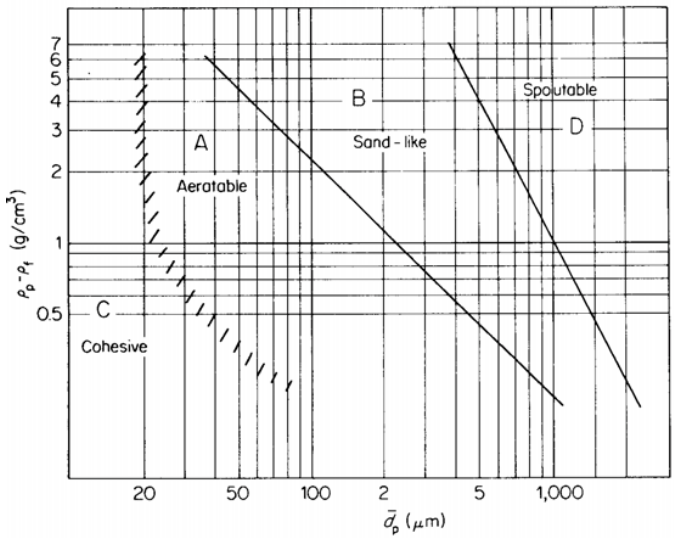

Figure 1.2: Fluid-particle system classification for air at ambient temperature (Geldart, 1973).

The interaction between fluid and particles ensures rapid heat and mass transfer, good solid mixing and fast chemical reactions. This is desirable in several industrial processes where fluid/particle and particle/particle contacting is required; for instance, processes involving gas/gas reactions catalyzed by the solid (*e.g.*, the catalytic cracking of oil) or gas/solid reactions were the solids are transformed (*e.g.*, the extraction of titanium oxide from its ore). Some industrial applications of fluidized beds are reported in Table 1.1.

The behaviour of fluid-particle systems depends on the physical properties of the materials and on the operating conditions. We have already described how by changing the fluid flow rate we can vary the fluidization quality of the powder. By carefully observing the behaviour of several fluidized suspensions, Geldart (1973) proposed a classification where fluid-particle systems are divided in four groups. Once the fluid and its temperature are assigned, a system is identified by two coordinates: the mean particle diameter of the powder and the difference between the particle and the fluid densities. Figure 1.2 reports an example for air at ambient temperature.

Group C systems are cohesive and characterized by very small particles (between 20 μm and 50 μm). In these systems, the Van der Waals attractive forces between the particles dominate over the buoyancy and drag forces exerted by the fluid; accordingly, the particles tend to stick together and do not fluidize properly. Since the fluid cannot separate the particles, it forms channels, and instead of percolating through the powder bypasses it through these shortcuts. Mechanical stirrers and vibrators improve the fluidization quality by breaking the channels as they form.

Group A systems expand homogeneously at fluid velocities between u_{mf} and u_{mb}. For this reason, they are called *aeratable*. Both fluid dynamic and interparticle forces affect the fluidization quality of these systems, and some researchers believe that the uniform structure found at low fluid fluxes is entirely due to the interparticle forces (Massimilla et al., 1972; Mutsers & Rietema, 1977; Rietema & Piepers, 1990).

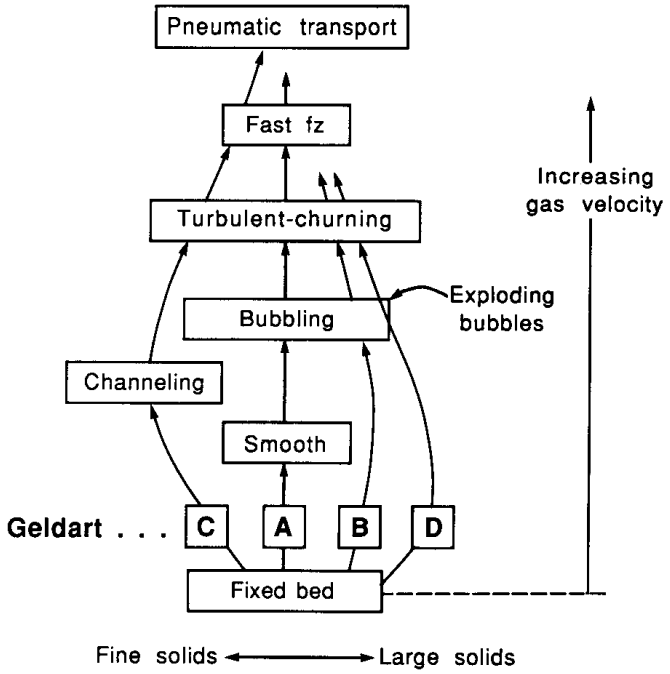

Figure 1.3: Fluidization behaviour of the Geldart fluid-particle groups (Kunii & Levenspiel, 1989).

Group B and D systems, conversely, bubble as soon as they fluidize; u_{mf} and u_{mb} thus coincide. Since the interparticle forces are negligible, these systems can be regarded as purely fluid dynamic. Whereas in Group B systems most bubbles rise through the bed more quickly than the interstitial fluid, in Group D systems the opposite occurs, the fluid flowing into the bubble bases and out of their tops. Figure 1.3 shows the fluidization behaviour of the four groups (Kunii & Levenspiel, 1989).

1.2 Computational modelling of fluidized suspensions

Fluidization has proved over the years a winning and effective technology. Designing fluidized beds, however, is quite complex because their performance is highly dependent on the *fluidization quality* of the suspension, which is strongly affected by a wide range of physical and operating variables (for instance, the particle size distribution of the powder, the density of the particles, the density, viscosity, temperature, pressure and flow rate of the fluid, and the geometry of the vessel containing the bed). Critical scale-up problems are also present and need to be thoroughly analyzed if we want to ensure that full-size commercial units will perform satisfactorily.

For many years, to design fluidized beds process engineers used only experimental correlations. This practical approach to fluidization is well reflected in the first textbooks on the subject (see, for example, Othmer, 1956; Leva, 1959; Zenz & Othmer, 1960). These correlations, nevertheless, lack general validity and can help design only standard units; they can tell us nothing about how changes in the vessel geometry, the introduction of internals (like heat exchanger tubes) or the repartition of

the feeds over more entry points can affect fluid dynamics and performance. To answer these and other similar questions and improve the design of conventional plants, we need a predictive theory for the behaviour of dense fluidized suspensions.

Since the early 1960s, researchers have endeavoured to model multiphase flows. To this end, they have used different approaches. *Eulerian-Lagrangian* models track the motion of each particle and solve the dynamics of the fluid at a length scale much smaller than the particle diameter (microscopic length scale). *Eulerian-Eulerian* models treat the fluid and solid phases as interpenetrating continua and study their dynamics by means of averaged equations of motion. Between these two approaches, the second is often preferred because it is computationally less demanding. Owing to the enormous number of particles present in industrial plants, Eulerian-Eulerian (continuum) models are not likely to be replaced by their Lagrangian-Eulerian (discrete) counterparts in the foreseeable future. Discrete modelling is nevertheless paramount. The method, to be regarded more as an effective research tool than as a practical design instrument, by providing information about the dynamics at the microscopic length scale, can significantly help develop and improve continuous macroscopic models.

The numerical solution of the Eulerian averaged transport equations is known as *computational fluid dynamics* (CFD). Since the 1980s, when engineers first realized that it was possible to base quantitative design calculations on differential equations of continuity and momentum, the use of CFD has grown increasingly in many industries. In process industries, for instance, CFD has led to reductions in the cost of product and process development activities (by reducing downtime), reduced the need for physical experimentation, shortened time to market, improved design reliability and increased conversions and yields (Davidson, 2002).

In the field of fluidization, CFD has proved a valuable research means; the main goal is succeeding in simulating and investigating directly the behaviour of full-size systems so as to avoid having to draw heavily upon uncertain results obtained from pilot plants and scale-up empirical relations. To this end, it is critical that accurate models be developed. The Eulerian equations of motion are mathematically unclosed, because the averaging process leaves behind some terms that are still related to microscopic, and not averaged, variables. To close the equations, we need to model constitutively these quantities, which coincide with the interaction forces between the phases and the fluid dynamic stress internal to each phase. To express the fluid-particle interaction force, we employ the results of classical fluid dynamics along with empirical relations about the behaviour of fluidized suspensions. Modelling the interaction forces between particles of different phases and the fluid dynamic stress internal to each phase is more difficult. Many researchers use the granular kinetic theory to translate the behaviour of many particles into one continuum (Haff, 1983; Jenkins & Savage, 1983; Lun et al., 1984; Jenkins, 1987; Lun, 1991; Gidaspow, 1994; Goldshtein & Shapiro, 1995). This approximation, however, is partially inadequate for dense suspensions (Jackson, 2000; Curtis & van Wachem, 2004). This has led researchers to borrow concepts from the field of soil mechanics and to make analogies with the continuum theory of solid elasticity to describe adequately the dense particulate phases (Savage, 1982; Johnson & Jackson, 1987; Makkawi & Ocone, 2006).

Even in the very simplest physical cases (dilute systems, purely viscous or inertial fluid dynamic regimes, etc.), determining closed governing equations for fluidized suspensions and validating them experimentally is quite difficult. This is because the behaviour of these systems is dictated by their microstructure and by the interactions between the phases at the microscopic length scale; finding constitutive equations based on averaged fluid dynamic variables that can describe these interactions accurately without needing the details of the microscopic motion is therefore exceedingly complex. It does not surprise then that these equations are still inadequate today and need to be investigated further. Their limitations is well reflected by some shortcomings of the averaged equations of motion; these, for instance, still do not predict correctly the expansion profiles of homogeneous fluidized beds, their transition to the bubbling regime, the bubble dynamics (bubble size, shape, etc.), the speed and degree of mixing and segregation, and many other physical phenomena.

Another important limitation of the averaged equations of motion is that they usually do not allow for changes in the particle properties; in particular, each Eulerian solid phase is assumed to be made up of particles with equal and constant size. Real fluidized suspensions are characterized by a polydisperse phase whose particle size distribution (PSD) changes continuously owing to chemical reactions, particle aggregation, breakage and other similar phenomena. To become a design tool for real industrial applications, a computational model must be able to predict these changes, relating them to the specific process conditions.

In this work, we focus on two problems: the closure of the fluid-particle interaction force and the mathematical modelling of polydispersity. Before addressing the first, we review how the averaged equations of motions are obtained and advance a new set of equations for fluidized suspensions made up of a finite number of monodisperse particle classes. This helps to clarify the mathematical origin and physical meaning of the unclosed terms previously described.

1.3 Computational fluid dynamics codes

Solving fluid dynamic problems by means of CFD involves three steps: pre-processing, solving and post-processing. These are briefly introduced below.

1) Pre-processing:

   The user specifies the problem by assigning all the necessary information; this, for example, might include the geometry of the computational domain, the properties of the computational grid, the number of Eulerian phases, the properties of the materials, the physical and chemical phenomena involved, the transport and constitutive equations, the time step, the numerical schemes and the initial and boundary conditions.

2) Solving:

   The numerical scheme that most commercial CFD codes adopt is the finite volume method. The code integrates the differential transport equations over each computational cell, and applying

the Gauss and Leibnitz theorems yields a set of integral equations that express conservation laws on a control-volume basis. The code then converts these equations into algebraic equations by using discretization techniques that approximate some terms of the equations (for instance, the accumulation terms) or the values of some variables (for instance, cell-face values of variables used in convective fluxes) with finite differences. Finally, the code solves iteratively the set of algebraic equations and finds the cell-centre values of the flow variables.

3) Post-processing:

The user analyzes the simulation results, generates diagrams and creates snapshots and animations by using data management and graphics tools.

If the modeler uses a commercial CFD code and does not wish to alter it or customize it, then the three steps described above are sufficient. In this work, however, we develop new equations of closure for the fluid-particle interaction force and need to implement them within the code. Moreover, when modelling polydisperse systems, we derive transport equations (for the quadrature nodes and weights and for the moments of the volume density function, refer to Chapter 5) that are not customary and also need to be implemented. Commercial CFD codes can be modified within reason. We can solve transport equations for any kind of scalar (vectors and tensors are regarded as ordered sets of scalars); to do so, we need to specify the velocity with which the scalar is advected, its coefficient of diffusion and its rate of generation. We can define these by using so-called *user defined functions*, routines that the modeler can write and implement within the code in predefined areas. The programming language required depends on the code; in this work, we use CFX and Fluent: the first requires Fortran, whereas the second C++. The closures for the fluid-particle interaction force can also be customized through user defined functions. An additional difficulty is that these routines must exchange information with the code; for instance, to compute the drag force the routine needs to import the velocity fields of the two phases involved and must return the value of the drag coefficient to the code. Thus, to allow this exchange of information, the modeler also needs to know the programming language of the code; this, of course, depends on the commercial code adopted.

In this work, the commercial CFD codes are significantly modified since many of the equations and closures that we wish to solve are new and therefore not available in the code.

1.4 Research objectives

Sponsored by BP Chemicals, Hull (UK) and the Engineering Physical Science Research Council (EPSRC), this research project is concerned with the Eulerian-Eulerian mathematical modelling of fluidized suspensions. Its main goals are:

1) deriving, using a rigourous mathematical averaging process, the Eulerian equations of motion for dense fluidized suspensions of n particle phases.

2) elucidating the origin and meaning of the interaction forces between the phases and of the fluid dynamic stress internal to each phase.
3) presenting clearly the problem of closure that characterizes the averaged equations of motion and the complexity of finding theoretical expressions for the unclosed terms.
4) finding a more accurate constitutive equation for the drag force exerted by the fluid on the particles of monodisperse fluidized suspensions; comparing the new closure with well-known closures used by the majority of the commercial CFD codes; validating these closures by using reliable experimental data reported in the literature.
5) deriving a better predictive closure for the elastic force in monodisperse fluidized suspensions that has general validity and can be implemented in CFD codes; comparing the new expression with others available in the literature; validating these closures by studying analytically the stability of homogeneous fluidized suspensions using linear stability analysis.
6) solving the averaged equations of motion numerically to investigate the dynamics and stability of homogeneous fluidized suspensions; deriving the computational expansion profiles of uniform liquid-fluidized suspensions using the new drag force closure and also the other closures examined in point 4; validating the results against experimental data; simulating the collapse and expansion of liquid-fluidized uniform suspensions; analyzing the stability of uniform gas-fluidized beds and their transition from the particulate to the aggregative regime.
7) developing a powerful and flexible mathematical model for polydisperse fluidized suspensions that can track the evolution of the particle size distribution of the powder, allowing for changes in particle size, particle aggregation, breakage and nucleation, chemical reactions and any other continuous or discontinuous process that can alter the internal state of the particles.
8) using the new model to simulate the mixing and segregation of polydisperse fluidized suspensions; performing experiments to validate the numerical results.

1.5 Thesis outline

In Chapter 2, we derive the Eulerian averaged equations of motion for dense fluidized suspensions of n particle phases, and we discuss the origin of the interaction forces between the phases and of the fluid dynamic stress. In Chapter 3, we develop new equations of closure for the drag and elastic forces, and we validate the new drag force closure. In Chapter 4, we study the stability and dynamics of uniform homogeneous beds, both analytically and computationally, and we validate the new drag and elastic force closures. In Chapter 5, we present a mathematical model for polydisperse fluidized suspensions that, among other things, allows tracking the evolution of the particle size distribution of a granular system. In Chapter 6, we use the model to simulate the mixing and segregation of polydisperse fluidized suspensions, and we present the results of the experiments that we performed to validate the numerical results.

Chapter 2

The mathematical modelling of fluidized suspensions

In this chapter, we discuss the principal mathematical strategies that can be employed to describe the dynamics of multiphase systems.

1) We present a brief overview of the approaches most widely adopted for modelling multiphase flows and, more specifically, fluidization dynamics.
2) We touch upon the main mathematical techniques used in averaging theory to derive averaged equations of motion. In particular, we discuss how Eulerian-Eulerian locally averaged equations of change can be obtained for assemblies of particles embedded in continuous media.
3) We derive new Eulerian-Eulerian locally averaged equations of motion for bidisperse fluidized suspensions. The method used is quite flexible, and can be easily generalized to cater for granular systems with any number of discontinuous phases.

The novelty of the averaging scheme herein adopted is that we derive the dynamical equations for the disperse phases by averaging the Newtonian particle equations of motion directly, rather than the microscopic equations for the particle materials. As we shall see, this means using particle averages, as opposed to the more common solid averages. This approach is much more flexible than the usual one, and leads to a clearer and more fundamental description of the particle phases.

Parts of this chapter have been published:

Owoyemi, O., Mazzei, L. & Lettieri, P. (2007). CFD modelling of binary-fluidized suspensions and investigation of the role of particle-particle drag on mixing and segregation. AIChE J. 53, 1924.

2.1 Introduction

Since 1926, when it first appeared in commercial use (Geldart, 1973), fluidization has attracted more and more the attention of the industrial world, which did not fail to recognize and appreciate the potential offered by this innovative technology. This interest, considerably boosted during the Second

World War by wartime pressure and a desperate need for aviation gasoline, explains why the new technique achieved very soon widespread use in several industrial applications, particularly in the fields of catalytic cracking and coal gasification. Since then, fluidization has always lived up to the expectations, turning into a well-established technology employed nowadays in many other areas such as, to cite just a few, coal combustion, sulphide ores roasting, food processing, biomass gasification, waste disposal and even oyster nursery (Ver & Wang, 1995).

Albeit used extensively in commercial operations, fluidization has always posed a major challenge to process engineers when they had to design new industrial plants. The performance of these systems depends strongly on the suspension fluid dynamics. This can change significantly and is affected by several variables: the properties of the powder (mainly its size distribution and the particles mean diameter and density), those of the fluid (mainly its density and viscosity), various process variables such as fluid temperature, pressure and flow rate, and geometrical properties of the vessel containing the bed. Thus, each fluidized system can be described by a *fluidization quality map* that comprises several fluid dynamic regimes wherein the system can perform. By choosing appropriately the values of the variables previously mentioned, we can have the fluidized bed work in any region of the map, attaining the fluid dynamics that best suits the application in hand.

This is the major challenge that process engineers have to undertake. On the one hand, predicting the behaviour of industrial fluidized beds is, to quote Geldart (1973), 'tougher than assessing the arrival time of a space probe travelling to Saturn.' On the other hand, as their construction and commissioning are extremely expensive, design uncertainties must be avoided or at least minimized.

For many years, and partly still today, process engineers have used pilot plants and scaling-up relationships to design fluidized beds. This practice, nonetheless, is quite risky. Whereas laboratory bench-scale experiments might well be used to test the feasibility of basic processes, they do not help much to design industrial plants, since the fluidization quality observed in the small-scale prototypes does not indicate what this will be in the corresponding commercial units (Geldart, 1973). This is all the more true if the bed is to contain internals, such as heat exchanger tubes, bound to modify the fluid dynamics of the suspension.

When fluidization was first employed in the 1920s - 1940s, engineers did not appreciate this problem, most probably because at the time the required plants performance was either not critical (as in FCC plants) or easily achievable (as in roasting and drying). Nevertheless, when later on the problem revealed itself in other, and more demanding, applications, with some plants falling far short of the expected conversions previously achieved in pilot units, it became clear that this matter had to be addressed more thoroughly. Accordingly, researchers endeavoured to find more reliable methods to predict the dynamics of fluidized beds.

In the late 1950s and early 1960s, chemical engineers made major breakthroughs. Using the *laws of conservation of mass, linear momentum and energy* to analyze nearly any physical and chemical problem, they made significant theoretical headway. This new approach, most probably also fostered

by the release of the first edition of the influential textbook *Transport Phenomena* (Bird et al., 1960), bolstered the hope to explain theoretically the behaviour of fluidized beds, and prompted the first trials to develop fluid dynamic models based on conservation equations.

Anderson & Jackson (1967) were among the first to model fluidized suspensions. Starting from the Navier-Stokes equations of continuum mechanics and the Newtonian equations for rigid-body motion, they derived averaged equations of conservation for both fluid and solid phases by applying a formal mathematical process of volume averaging. Afterwards, several others researchers did the same, see for instance Whitaker (1969), Drew (1971) and Drew & Segel (1971). Initially, they used these models to better understand the complex behaviour of multiphase systems, never considering them as a viable alternative to design real systems. But successively, when faster computer processors and advanced numerical methods to integrate coupled partial differential equations became available, they realized that a mathematical theory of multiphase flows might provide a useful design tool for applications of practical interest.

With the further development of new and more rigourous formulations of multiphase equations of motion (Buyevich, 1971; Hinch, 1977; Nigmatulin, 1979; Drew, 1983; Jenkins & Savage, 1983), the late 1970s and early 1980s witnessed the earliest endeavours to describe qualitatively, by direct numerical simulation, granular systems in flow (Pritchett et al., 1978; Gidaspow & Ettehadieh, 1983; Gidaspow et al., 1986). The promising results of these pioneering studies fuelled an increasing interest in computational fluid dynamics (CFD) and multiphase flows, which rapidly started to turn into research areas in their own right.

Nowadays, CFD has become an almost indispensable tool to solve many complex problems of academic and industrial interest. In the field of fluidization, in particular, CFD has helped understand fluid-solid interactions and has enabled to predict various macroscopic phenomena encountered in particulate systems. Similarly, multiphase flows and, more specifically, fluidization dynamics have become topics of considerable interest not only for the scientific community but also for the industrial world. Over the years, many researchers have developed mathematical models to predict the dynamics of dense fluidized suspensions. Several approaches and mathematical schemes have been employed; in the following section, we provide a succinct overview of these strategies, trying to highlight their respective advantages and limitations.

2.2 An overview on multiphase flows modelling

Multiphase flows can be modelled at different levels of detail. At the most fundamental level, the solid particles are treated individually, their motion being governed by the classical equations of rigid-body Newtonian mechanics. The discrete structure of the granular material is hence entirely retained. The interstitial fluid, on the other hand, is modelled as a continuum whose dynamics is described by the equations of conservation of mass and linear momentum to be satisfied at each point of the fluid itself.

The fluid flow field is therefore resolved at a length scale much smaller than the particle diameter; this is usually referred to as *microscopic length scale*. Each equation of the set is coupled to the others by no-slip boundary conditions assigned on the surface of each particle. Furthermore, the equations of change of the fluid phase are required to meet additional boundary conditions assigned on the remaining boundaries of the computational domain.

The main advantage of this approach, referred to as *Eulerian-Lagrangian*, lies in the simplicity of the equations. These do not contain any indeterminate terms that need closure – with the exception of the fluid stress tensor, for which the classical Newtonian constitutive equation holds, and of the coefficients of restitution that account for the inelastic collisions between pairs of particles. Even so, owing to the severe computational effort that it requires, the pure Eulerian-Lagrangian approach, in the sense previously specified, is seldom applied; it should not surprise, therefore, that the literature reports few investigations of this kind. An almost unique article, which certainly deserves mention, is that of Pan et al. (2002). Their work presents the very first Eulerian-Lagrangian simulations of a fluidized suspension at the finite Reynolds numbers encountered in practical applications. Numerical bed expansion profiles are processed to give straight lines in log-log plots leading to power laws as in the well-known experimental correlation of Richardson & Zaki (1954); furthermore, for the first time ever, the method allows to calculate directly the slip velocity and other averaged quantities used in multifluid continuum models.

Despite its simplicity, the Eulerian-Lagrangian strategy is by no means the most effective. In the first place, the computational cost is way too demanding. Indeed, simulations at this level of detail have been performed only for much diluted systems containing a truly small number of particles (1204 in the work of Pan et al., 2002); extending these calculations to dense suspensions like those characterizing industrial fluidized beds is presently clearly inconceivable. Furthermore, even if this were feasible, the amount of information provided by the solution would be far too detailed, and in any case a method of filtering or averaging would be required to elicit useful results.

These observations suggest that it might be advantageous to endeavour to formulate transport equations governing the evolution, in time and physical space, of these averages *directly*. In this alternative approach, rather than aiming at the detailed solution described above, we are satisfied with a much reduced description of the flow. Albeit there is no guarantee that these simplified equations can be really found – in closed form, that is – several studies have been conducted in this pursuit (Anderson & Jackson, 1967; Whitaker, 1969; Drew, 1971, 1983; Drew & Segel, 1971; Drew & Lahey, 1993; Gidaspow, 1994; Zhang & Prosperetti, 1994; Enwald et al., 1996; Jackson, 1997, 1998, 2000). Owing to the complexity of the problem, it is not expected, at least for the time being, that the exact averaged equations of motion that govern multiphase flows should be derived. The intent is instead far more practical and aspires to formulate relations that should be good enough to describe satisfactorily phenomena of interest for industrial applications.

Different mathematical techniques can be employed to elicit such equations, and several claims have been advanced as to the superiority of each form of averaging versus the others. Regardless of

the specific mathematical scheme adopted, however, the resulting transport equations are very similar and present many common features. Two are the most significant. First, they are all written in terms of averaged variables defined over the whole physical domain; thus, the resulting averaged equations resemble those that one would write for n imaginary fluids capable of interpenetrating each other while occupying simultaneously the same volume. The model, referred to as *Eulerian-Eulerian* or also as *multifluid*, takes therefore the form of coupled partial differential equations subjected to initial and/or boundary conditions assigned only on the system boundaries. Second, the process of averaging leaves behind a number of *indeterminate terms* not directly related to the averaged variables but still associated with details of the motion at the microscopic length scale. These terms are represented by the fluid and solid stress tensors, and by the interaction force exchanged by the phases. A *closure problem* therefore arises, which usually cannot be solved analytically and has to be overcome by means of empirical expressions. This is indeed the main shortcoming of the method.

In addition to the modelling approaches just described, there is a third that can be regarded as a hybrid between them. Averaged equations of motion are derived for the fluid phase, but classical Newtonian equations for rigid-body motion are solved for each particle of the system. These do not interact with the fluid via its microscopic velocity field, but with the averaged value of the latter. For instance, the overall force exerted by the fluid on each particle is not computed by integrating over the particle surface the local traction that arises from the fluid velocity gradients. The force is instead evaluated in terms of slip velocity between the averaged fluid velocity and the velocity of the particle centre of mass and by resorting to semiempirical correlations. The procedure, referred to as *discrete particle modelling*, is considerably less demanding computationally than the pure Eulerian-Lagrangian and has met with quite resounding success (Tsuji et al., 1993; Hoomans et al., 1996; Ouyang & Li, 1999; Kafui et al., 2002; Lu et al., 2005).

Between the three modelling approaches herein discussed, the second is often preferred to the others for its valuable feature of being computationally much less demanding. Because of the number of particles involved in industrial plants, Eulerian-Eulerian (continuum) modelling is not likely to be replaced by its Lagrangian-Eulerian (discrete) counterparts in the foreseeable future. The role of discrete modelling is yet paramount. The method, to be considered more as an effective research tool than as a practical design instrument, by providing information about the dynamics of multiphase systems at the microscopic length scale, can significantly help to develop and improve continuous average-based macroscopic models. For this very reason the article of Pan et al. (2002) previously mentioned is so important. In this view, Eulerian-Lagrangian modelling is to multiphase flows what direct numerical simulations (DNS) are to turbulent flows.

2.3 An overview on averaging theory

There are essentially three techniques that can be used to derive averages of local instantaneous point variables: volume, ensemble and time averaging (Enwald et al., 1996; Drew & Passman, 1998); the first two, in particular, are often adopted in multiphase flows theory.

Volume averages are computed over spatial domains large enough to contain several particles but small compared to the scale of point-to-point macroscopic variations within the system. An averaging volume $V(\boldsymbol{x})$ bounded by a surface $S(\boldsymbol{x})$ is attached to each spatial point $\boldsymbol{x}$; within such volume, the property of interest is averaged out by using the mean value theorem of integral calculus. When this specific volume averaging scheme is adopted, all the values of the property within $V(\boldsymbol{x})$ are accounted for and given the same weight in the average; conversely, the values outside the boundary $S(\boldsymbol{x})$ are not considered in the computation, that is, are given zero weight. This type of averages are usually referred to as *hard volume averages* to distinguish them from *soft volume averages*. These are based on an alternative technique, more elegant and convenient from a mathematical standpoint, that makes use of a radial weighting function: a continuous, monotone, decreasing function of the radial distance from the point wherein the average is to be evaluated. This mathematical device is used to ascribe a weight to the property values within the whole physical domain. The average, accordingly, is no longer computed by considering only the values attached to a well-defined averaging volume; on the contrary, all are taken in consideration, each one suitably weighted. For a formal and more detailed discussion concerning soft volume averages, we refer to § 2.4 where the volume averaged equations of motion for dense fluidized suspensions are rigorously derived.

Volume averaged variables thus defined appear to depend on the specific form chosen for the weighting function and, in particular, on its radius (that is, the size of the region over which the averaging effectively takes place; for a formal definition of weighting function radius refer to § 2.4). Nonetheless, the larger the ratio between the smallest macroscopic length scale and the particle size, the more this dependence dwindles provided that the weighting function radius is properly chosen. If this radius is denoted by r_a, the particle radius by r_p and the aforementioned macroscopic length scale by r_m, the local average is expected to be insensitive to the particular form of the weighting function provided that $r_p \ll r_a \ll r_m$. Such a choice of r_a is, of course, possible only if r_m is far greater than r_p; in such a case, there is said to be *separation of scales* between the macroscopic fluid dynamic problem and the detailed motion on the scale of a single particle. Only in this instance the locally averaged variables do possess an unambiguous physical meaning and can be employed in the development of averaged equations of motion. As expressed by Nigmatulin (1979), separation of scales requires the possibility of defining an 'elementary macrovolume ... the characteristic linear dimensions of which are many times greater than the non-uniformities ..., but at the same time much less than the characteristic macrodimension of a problem.'

Ensemble averages are based on a completely different idea that has to do with a fundamental characteristic of particulate systems: it is impossible to know the precise locations and properties (*e.g.*, linear and angular velocities) of each individual constituent of the particle population at any given time. In fact, this sort of details are not only impractical to measure, but, most importantly, are usually entirely inconsequential. Often, more gross features of the motion are of interest. Let us consider, for instance, two particulate systems subjected to the same boundary and initial conditions, with the exception of a few undefined properties *at the particle level* such as the exact position initially

occupied by each discrete element. Albeit the evolution of the two systems will be different from a microscopic standpoint – reflecting the fact that the two flows originate from dissimilar conditions at the microscopic level – they are macroscopically equivalent, since the evolution of all the macroscopic variables characterizing the systems is identical. Note that if this were not the case, repeatability of physical experiments would be impossible, for it is clearly impossible to set up intentionally the same microscopic initial conditions twice.

The set of infinite systems sharing the same boundary and initial conditions, in the sense specified above, is said to constitute an *ensemble*, with each individual system representing a *realization* of the latter. Each realization is unique, insomuch as it differs microscopically from all the others; all realizations, however, are macroscopically equivalent, since they feature identical evolutions of all the macroscopic measurable variables. Such ensembles are reasonable sets over which to perform averages because variations in the details of the flows are assured in all situations, while at the same time variations in the gross features of the flows cannot occur.

At any given time, the ensemble average of a generic property at a specified spatial location $\boldsymbol{x}$ can be defined as the arithmetic mean of the instantaneous point property of the material located at $\boldsymbol{x}$ at the time in question for each of the infinite number of realizations of the ensemble. Thus, following Kleinstreuer (2003), for a given field $\boldsymbol{\xi}(\boldsymbol{x}, t)$, it is:

$$\langle \boldsymbol{\xi} \rangle_e (\boldsymbol{x}, t) \equiv \lim_{N \to +\infty} \frac{1}{N} \sum_{n=1}^{N} \boldsymbol{\xi}_n (\boldsymbol{x}, t) \tag{2.1}$$

where $\langle \boldsymbol{\xi} \rangle_e (\boldsymbol{x}, t)$ is the ensemble average, N is the number of times the value of $\boldsymbol{\xi}(\boldsymbol{x}, t)$ is sampled and $\boldsymbol{\xi}_n(\boldsymbol{x}, t)$ is the functional form of the field at the n-th realization of the flow. An alternative technique for representing the ensemble average of $\boldsymbol{\xi}(\boldsymbol{x}, t)$ is:

$$\langle \boldsymbol{\xi} \rangle_e (\boldsymbol{x}, t) \equiv \int_{\mathcal{E}} \boldsymbol{\xi}(\boldsymbol{x}, t; \mu) dm(\mu) \tag{2.2}$$

where μ denotes a generic realization of the ensemble, $\mathcal{E}$ represents the ensemble of all possible realizations, $\boldsymbol{\xi}(\boldsymbol{x}, t; \mu)$ expresses the functional dependence of the field on the realization and $m(\mu)$ quantifies, loosely speaking, the probability of occurrence of each realization (Zhang & Prosperetti, 1994; Enwald et al., 1996; Drew & Passman, 1998; Kleinstreuer, 2003; Crowe, 2005).

To explain time averaging, we consider again the field $\boldsymbol{\xi}(\boldsymbol{x}, t)$; for any spatial fixed position $\boldsymbol{x}^*$, $\boldsymbol{\xi}(\boldsymbol{x}^*, t)$ is a pure function of time that fluctuates irregularly. The time scale τ_t that represents these fluctuations is usually referred to as *turbulent time scale*. At each given location, we can obtain a mean value of $\boldsymbol{\xi}(\boldsymbol{x}, t)$ by performing a time average over a large number of fluctuations, considering a time interval τ_a much longer than the turbulent time scale. Again, we evaluate the average by simply resorting to the mean value theorem; thus, it is:

$$\langle \boldsymbol{\xi} \rangle_t (\boldsymbol{x}, t) \equiv \frac{1}{\tau_a} \int_{t - \tau_a/2}^{t + \tau_a/2} \boldsymbol{\xi}(\boldsymbol{x}, \tau) d\tau \tag{2.3}$$

where $\langle \boldsymbol{\xi} \rangle_t(\boldsymbol{x}, t)$ is the time average and τ is a dummy integration variable. Provided the averaging time scale is sufficiently long, the turbulent fluctuations are entirely smoothed out.

Also now, it might be objected that the time average thus defined depends on the averaging time interval τ_a. This is indeed true; however, similarly to what has been previously said about volume averages, the mean value is expected to be almost entirely insensitive to the averaging time scale provided that $\tau_t \ll \tau_a \ll \tau_m$, where τ_m represents the time scale of the mean flow fluctuations (Delhaye & Achard, 1977, 1978). Separation of scales is therefore again required.

2.4 Derivation of the Eulerian-Eulerian locally averaged equations of motion for multiphase dense fluidized suspensions

Using the volume averaging scheme shown in § 2.3, we now derive the Eulerian-Eulerian averaged equations of motion for multiphase dense fluidized suspensions. Even if volume averages are more complicated to manipulate mathematically than ensemble averages, we favour them because they yield quantities more closely related to those measured experimentally. One example is enlightening. Let us consider a bubbling fluidized bed, and let us focus our attention of one specific mean variable: the bulk density. This property, if obtained by volume averaging, represents the mass to volume ratio for a blob of mixture enclosed in an averaging volume sufficiently big to contain several particles but small compared with the macroscopic length scale characterizing the flow. Accordingly, the property is sometimes representative of the mean density of the dense suspension and some other times of the mean density of a bubble, depending on which of the two, at the time in question, occupies the spatial point wherein the average is computed. Conversely, if obtained by ensemble averaging, the property results to be equal at all times to a value intermediate between the bulk densities of a bubble and of the dense suspension. This ensues directly from the definition of ensemble average given in §2.3. The two averages are obviously quite different, and the one more appropriate to investigate the dynamics of fluidized systems is clearly the former.

Several authors have advanced volume averaged equations of motion for monodisperse fluidized suspensions – that is, suspensions of equal particles. The work of Anderson & Jackson (1967), who were among the first to derive formally these equations, inspired the majority of these researchers. We now extend the equations originally proposed by Anderson & Jackson (1967), and successively revised by Jackson (1997, 1998), to the case of granular systems of n classes of particles, each of different size. We consider two solid classes, since further generalization is immediate; accordingly, the mathematical derivation is concerned with bidisperse suspensions. We also assume that the fluid is incompressible; this does not limit the analysis much, since in the majority of fluidized systems the process conditions ensure that the fluid density is fairly constant. Generalization, however, also in this case is straightforward.

In this analysis, recently put forward by Owoyemi et al. (2007), we also elucidate the origin of the fluid dynamic stress and of the fluid-particle and particle-particle interaction forces. This, along

with the analytical expressions that we will find for such terms, will make us understand much better the physical meaning of each contribution, and will help appreciate more fully the reasons behind the problem of closure, which is a prime characteristic of the multifluid modelling.

2.4.1 Weighting functions

We can define locally averaged variables using *weighting functions*. These are characterized by the following mathematical properties:

1) The weighting function is a scalar function of r defined for $r > 0$, where r denotes the distance of a generic point $\boldsymbol{y}$ from a generic point $\boldsymbol{x}$ in a three-dimensional Euclidean space:

$$\psi = \psi(r) \quad ; \quad r \equiv \|\boldsymbol{x} - \boldsymbol{y}\| \tag{2.4}$$

2) $\psi(r)$ is positive for any value of r, decreases monotonically with r and possesses continuous derivatives of any order.

3) $\psi(r)$ is normalized so that, denoting by Ω the volume of the whole system of interest (assumed to stretch out to infinity), the following property holds:

$$\int_{\Omega} \psi(\|\boldsymbol{x} - \boldsymbol{y}\|) dV_y = 4\pi \int_0^{+\infty} r^2 \psi(r) dr = 1 \tag{2.5}$$

where dV_y indicates that the spatial variable of integration is $\boldsymbol{y}$ and not $\boldsymbol{x}$ – the latter representing the spatial position wherein the average is computed.

2.4.2 Overall locally averaged variables

Given a generic point variable $\xi(\boldsymbol{x}, t)$ function of spatial position $\boldsymbol{x}$ and time t, we define its overall local average calculated in $\boldsymbol{x}$ at time t as:

$$\langle \xi \rangle(\boldsymbol{x}, t) \equiv \int_{\Omega} \xi(\boldsymbol{y}, t) \psi(\|\boldsymbol{x} - \boldsymbol{y}\|) dV_y \tag{2.6}$$

To explain the physical meaning of this definition, we resort to two examples. Consider the function $\psi(r) = 1/\Omega$. Clearly, this expression is not acceptable, for $\psi(r)$ does not decrease monotonically with r as required; all the same, we just use it temporarily to render the physical meaning of equation (2.6) more apparent. Using this weighting function, we rewrite equation (2.6) as:

$$\langle \xi \rangle(t) = \frac{1}{\Omega} \int_{\Omega} \xi(\boldsymbol{y}, t) dV_y \tag{2.7}$$

This equation merely expresses the mean value theorem of integral calculus. The problem with $\psi(r)$ is that it averages over the *entire system* without differentiating between points that are near $\boldsymbol{x}$ and

points that are far; thus, the averaged value of $\xi(\boldsymbol{x},t)$ computed in $\boldsymbol{x}$ does not depend on $\boldsymbol{x}$! In a proper definition of *local average*, points near $\boldsymbol{x}$ should count more. To obtain a more meaningful average, we set $\psi(r) = 1/\Omega_a$ for $r \leqslant r_a$ and $\psi(r) = 0$ for $r > r_a$, where Ω_a is the volume of a sphere of radius r_a. With this expression for $\psi(r)$, equation (2.6) yields:

$$\langle\xi\rangle(\boldsymbol{x},t) = \frac{1}{\Omega_a}\int_{\Omega_a}\xi(\boldsymbol{y},t)\,dV_y \tag{2.8}$$

This new definition of $\psi(r)$ ensures that only points within the spherical neighbourhood of $\boldsymbol{x}$ of radius r_a are considered in the average; the remaining ones are neglected, so that the average is local. This weighting function is said to define *hard spatial averages*, since the function is not continuous but undergoes a sharp change in correspondence of its radius. *Soft spatial averages*, based on continuous weighting functions that meet the requirements 1) to 3), are more convenient, for they allow us to use all the theorems of analytical calculus. For continuous weighting functions, the averaging radius is defined as the scalar r_a that fulfills the relation:

$$4\pi\int_0^{r_a} r^2\psi(r)\,dr = 4\pi\int_{r_a}^{+\infty} r^2\psi(r)\,dr = \frac{1}{2} \tag{2.9}$$

Thus, r_a is a measure of the linear size of the spherical neighbourhood of $\boldsymbol{x}$ wherein the spatial points have appreciable weight in the averaging process. As already mentioned, we must choose $\psi(r)$ so that the value of r_a yielded by equation (2.9) fulfills the condition $r_p \ll r_a \ll r_m$, where r_p is the particle radius and r_m is the smallest macroscopic length scale of interest.

2.4.3 Fluid phase locally averaged variables

We start by defining the void fraction, or fraction of space occupied by the interstitial fluid, calculated in the neighbourhood of $\boldsymbol{x}$ at time t:

$$\varepsilon(\boldsymbol{x},t) \equiv \int_{\Omega_f}\psi(\|\boldsymbol{x}-\boldsymbol{y}\|)\,dV_y \tag{2.10}$$

Then, we define the fluid phase local average of $\xi(\boldsymbol{x},t)$ calculated in $\boldsymbol{x}$ at time t to be:

$$\langle\xi\rangle_f(\boldsymbol{x},t) \equiv \frac{1}{\varepsilon(\boldsymbol{x},t)}\int_{\Omega_f}\xi(\boldsymbol{y},t)\psi(\|\boldsymbol{x}-\boldsymbol{y}\|)\,dV_y \tag{2.11}$$

In equations (2.10) and (2.11), Ω_f represents the volume occupied by the fluid phase at time t (we have left out the explicit dependence on t to simplify the notation). Note that, since both the fluid and the solid particles are incompressible, strictly speaking the volume they occupy – intended as physical volume – is constant in time and does not depend on t. Nevertheless, Ω_f is not a physical volume, but represents a *domain of integration*; thus, its shape and position are also important and need to be taken into account. Since both fluid and solid particles are not stationary but move continuously, the

shape and position of the volumes they occupy change in time. These variations affect the integrals above, especially their time derivatives. To distinguish between particle volume – intended as physical volume – and domain of integration, we will denote the former by v_i and the latter by Ω_p. Thus, v_i is a property of the particles of phase $\mathscr{F}_i$ and is time-independent; conversely, Ω_p is a time-dependent domain of integration bounded by the surface $\partial\Omega_p$ and coinciding with the volume occupied by a generic particle at the time of interest.

We can calculate the fluid phase local average of spatial derivatives of point variables using the relation (for proof, refer to § A.2 of Appendix A):

$$\varepsilon(\boldsymbol{x},t)\left\langle\frac{\partial\xi}{\partial x_k}\right\rangle_f(\boldsymbol{x},t)$$

$$=\frac{\partial}{\partial x_k}\Big[\varepsilon(\boldsymbol{x},t)\langle\xi\rangle_f(\boldsymbol{x},t)\Big]-\sum_{i=1}^{2}\sum_{\mathscr{F}_i}\int_{\partial\Omega_p}\xi(\boldsymbol{y},t)n_k(\boldsymbol{y},t)\psi(\|\boldsymbol{x}-\boldsymbol{y}\|)dS_y \tag{2.12}$$

Equation (2.12) modifies the expression of Anderson & Jackson (1967) for monodisperse particle systems by considering in the last contribution on the right-hand side two different particle classes, $\mathscr{F}_1$ and $\mathscr{F}_2$. Generalizing this expression to any number of particle classes is quite simple; we just need to extend the first summation to all the particle classes of the system by replacing the summation limit 2 with the overall number of classes n.

Similarly, for bidisperse suspensions, we can prove (refer to § A.3 of Appendix A) that the fluid phase local average of time derivatives of point variables is given by:

$$\varepsilon(\boldsymbol{x},t)\left\langle\frac{\partial\xi}{\partial t}\right\rangle_f(\boldsymbol{x},t)$$

$$=\frac{\partial}{\partial t}\Big[\varepsilon(\boldsymbol{x},t)\langle\xi\rangle_f(\boldsymbol{x},t)\Big]+\sum_{i=1}^{2}\sum_{\mathscr{F}_i}\int_{\partial\Omega_p}\xi(\boldsymbol{y},t)\boldsymbol{u}(\boldsymbol{y},t)\cdot\boldsymbol{n}(\boldsymbol{y},t)\psi(\|\boldsymbol{x}-\boldsymbol{y}\|)dS_y \tag{2.13}$$

In the last two equations, the integrals are taken over the particle surfaces $\partial\Omega_p$, the vectors $\boldsymbol{n}(\boldsymbol{x},t)$ and $\boldsymbol{u}(\boldsymbol{x},t)$ are the outward unit normal to $\partial\Omega_p$ and the fluid velocity, respectively, and $n_k(\boldsymbol{x},t)$ is the k-th component of $\boldsymbol{n}(\boldsymbol{x},t)$ with respect to a generic orthonormal vector basis.

2.4.4 Solid phase locally averaged variables

In the present analysis, we assume that the granular material is composed of two classes of particles, $\mathscr{F}_1$ and $\mathscr{F}_2$. Each class is made up of identical spherical rigid particles of a specific constant size. We define the volume fraction of the generic particle species $\mathscr{F}_i$ calculated in $\boldsymbol{x}$ at time t as:

$$\phi_i(\boldsymbol{x},t)\equiv\sum_{\mathscr{F}_i}\int_{\Omega_p}\psi(\|\boldsymbol{x}-\boldsymbol{y}\|)dV_y \tag{2.14}$$

where the summation is intended over all the particles of phase $\mathscr{F}_i$ and where the integral is taken over the volume Ω_p occupied at time t by a generic particle of the set.

We can also define solid phase averages of point variables for each solid phase $\mathscr{F}_i$ of the system; these are analogous to the fluid phase averages, and take the form:

$$\langle \xi \rangle_s^i(\boldsymbol{x}, t) \equiv \frac{1}{\phi_i(\boldsymbol{x}, t)} \sum_{\mathscr{F}_i} \int_{\Omega_p} \xi(\boldsymbol{y}, t) \psi(\|\boldsymbol{x} - \boldsymbol{y}\|) dV_y \tag{2.15}$$

However, to derive the averaged transport equations for the solid phases, we do not use these averages, but favour particle phase averages based on properties $\xi^p(t)$ of the particles *as a whole*, as opposed to the point properties $\xi(\boldsymbol{x}, t)$ varying *within the particles* used in equation (2.15).

2.4.5 Particle phase locally averaged variables

Since the particles are rigid, their motion is determined by the translation of their centres of mass and by the rotation of their bodies about instantaneous axes of rotation (only six degrees of freedom are present). As a consequence, the resultant forces and the resultant torques acting on the particles suffice to establish their motion. We can then introduce a different kind of local average that depends only on the properties of the particles *as a whole*. Examples of such properties are the velocities of their centres of mass, their angular velocities, the resultant forces and torques previously mentioned and similar overall quantities. We define the number density $n_i(\boldsymbol{x}, t)$, that is, the number of particles of class $\mathscr{F}_i$ per unit volume of physical space calculated in $\boldsymbol{x}$ at time t, as:

$$n_i(\boldsymbol{x}, t) \equiv \sum_{\mathscr{F}_i} \psi(\|\boldsymbol{x} - \boldsymbol{x}^p\|) \tag{2.16}$$

where $\boldsymbol{x}^p(t)$ denotes the position occupied at time t by the centre of mass of a generic particle of the phase under consideration. The volume fraction $\phi_i(\boldsymbol{x}, t)$ is related to the number density $n_i(\boldsymbol{x}, t)$ by the following approximate relationship:

$$\phi_i(\boldsymbol{x}, t) \approx n_i(\boldsymbol{x}, t) v_i \tag{2.17}$$

To derive this result, we expand the function $\phi_i(\boldsymbol{x}, t)$ in a Taylor series about $\boldsymbol{x}^p(t)$ and retain only the constant term of the series. Complete proof is given in § A.1 of Appendix A.

Generalizing the averaging scheme advanced by Jackson (1997), we define the particle phase average for the phase $\mathscr{F}_i$ of a particle property $\xi^p(t)$ calculated in $\boldsymbol{x}$ at time t as:

$$\langle \xi \rangle_p^i(\boldsymbol{x}, t) \equiv \frac{1}{n_i(\boldsymbol{x}, t)} \sum_{\mathscr{F}_i} \left[\xi^p(t) \psi(\|\boldsymbol{x} - \boldsymbol{x}^p\|) \right] \tag{2.18}$$

It can be shown (for mathematical proof, refer to § A.4 of Appendix A) that the particle phase local averages of particle properties time derivatives is given by:

$$n_i(\boldsymbol{x},t)\left\langle \frac{d\xi}{dt}\right\rangle_p^i(\boldsymbol{x},t) = \frac{\partial}{\partial t}\Big[n_i(\boldsymbol{x},t)\langle\xi\rangle_p^i(\boldsymbol{x},t)\Big] + \frac{\partial}{\partial x_k}\sum_{\mathscr{F}_i}\Big[n_i(\boldsymbol{x},t)\langle\xi\, v_k\rangle_p^i(\boldsymbol{x},t)\Big] \tag{2.19}$$

where $\langle\xi\, v_k\rangle_p^i(\boldsymbol{x},t)$ is the average of the product of the particle property $\xi^p(t)$ and the k-th component $v_k^p(t)$ of the velocity of the centre of a generic particle of the phase under consideration. Since particle properties are pure functions of time, no analogous expression to equations (2.12) and (2.14) can be derived for this kind of averages.

Here and in what follows, we adopt the convention that repeated *lower* indices are summed over the values one to three, with the exception of i, used as phase index, and of f and p, used to specify the type of average; upper indices are *not* to be regarded as dummy indices implying summation. Hitherto, we have stated explicitly the dependence on time t and position $\boldsymbol{x}$; from now onwards, however, to simplify the notation, we shall often leave it out.

2.4.6 Averaged equations of motion for the fluid phase

We now apply the definitions and mathematical relationships just presented to derive the macroscopic locally averaged transport equations for the continuous phase.

Continuity equation

The equation is obtained by setting $\xi = u_k$ and $\xi = 1$ in equations (2.12) and (2.13), respectively, and then by adding the results. As the fluid is incompressible, doing so yields:

$$\frac{\partial\varepsilon}{\partial t} + \frac{\partial}{\partial x_k}\Big(\varepsilon\langle u_k\rangle_f\Big) = 0 \tag{2.20}$$

Dynamical equation

At the microscopic level, the fluid satisfies the point Navier-Stokes differential equation:

$$\rho_f\left[\frac{\partial u_j}{\partial t} + \frac{\partial}{\partial x_k}(u_j u_k)\right] = \frac{\partial T_{jk}}{\partial x_k} + \rho_f g_j \tag{2.21}$$

where ρ_f is the fluid density, $T_{jk}(\boldsymbol{x},t)$ is the jk-th component of the point fluid stress tensor and g_j is the j-th component of the gravitational field. To average this equation, we multiply both sides by $\psi(\|\boldsymbol{x}-\boldsymbol{y}\|)$ and integrate over Ω_f with respect to $\boldsymbol{y}$. To treat the left-hand side of equation (2.21), we use equations (2.12) and (2.13) with $\xi = u_j u_k$ and $\xi = u_j$, respectively; to treat the right-hand side, we use equation (2.10) and equation (2.12) with $\xi = T_{jk}$. The result is:

$$\rho_f\left[\frac{\partial}{\partial t}\Big(\varepsilon\langle u_j\rangle_f\Big) + \frac{\partial}{\partial x_k}\Big(\varepsilon\langle u_j u_k\rangle_f\Big)\right] = \frac{\partial}{\partial x_k}\Big(\varepsilon\langle T_{jk}\rangle_f\Big) + \varepsilon\rho_f g_j$$

$$-\sum_{i=1}^{2}\sum_{\mathscr{F}_i}\int_{\partial\Omega_p} T_{jk}(\boldsymbol{y})n_k(\boldsymbol{y})\psi(\|\boldsymbol{x}-\boldsymbol{y}\|)dS_y \tag{2.22}$$

The last term on the right-hand side is the sum over the two particle classes of the mean resultant traction force exerted by the fluid on the particles of each class. The traction force:

$$\sum_{\mathscr{F}_i} \int_{\partial\Omega_p} T_{jk}(\boldsymbol{y}) n_k(\boldsymbol{y}) \psi(\|\boldsymbol{x}-\boldsymbol{y}\|) dS_y \tag{2.23}$$

is the summation of the mean resultant forces exerted by the fluid on the particles of the i-th phase. To compute this force for each particle, we first weight the differential traction forces acting on each infinitesimal part of the particle surface using $\psi(\|\boldsymbol{x}-\boldsymbol{y}\|)$ at the locations under consideration, and we then sum all the contributions. The *fluid-solid interaction force*, defined by equation (2.23), couples the dynamical equation of the fluid to those of each particle class of the mixture.

It is useful to transform equation (2.23) from a situation where the differential traction forces exerted on every infinitesimal element of the fluid-solid interface are first weighted using the values of the weighting function at the location of the surface elements and then summed, to one where the overall force acting on the entire surface of each particle is first calculated and then weighted by using the value of the weighting function at the particle centre. This second average interprets better the fluid-particle interaction force and *fulfills the principle of action and reaction*. To transform the force, we expand $\psi(\|\boldsymbol{x}-\boldsymbol{y}\|)$ in a Taylor series about the centre $\boldsymbol{x}^p(t)$ of a generic particle of the phase under consideration. For the particles of phase $\mathscr{F}_i$, we have (refer to § A.1 of Appendix A):

$$\psi(\|\boldsymbol{x}-\boldsymbol{y}\|) = \psi(\|\boldsymbol{x}-\boldsymbol{x}^p\|) - \frac{\partial\psi}{\partial x_m}(\|\boldsymbol{x}-\boldsymbol{x}^p\|)(y_m - x_m^p)$$

$$+ \frac{1}{2}\frac{\partial^2\psi}{\partial x_m \partial x_r}(\|\boldsymbol{x}-\boldsymbol{x}^p\|)(y_m - x_m^p)(y_r - x_r^p) - \cdots \tag{2.24}$$

At any spatial location within each particle, we can truncate the Taylor series at the second order term with acceptably small error (Jackson, 1997). Since it is:

$$\forall\, \boldsymbol{y} \in \partial\Omega_p : \boldsymbol{y} - \boldsymbol{x}^p = r_i\, \boldsymbol{n}(\boldsymbol{y}, t) \tag{2.25}$$

where $\partial\Omega_p$ is the surface bounding each particle, $\boldsymbol{n}(\boldsymbol{y}, t)$ is the outward unit normal to $\partial\Omega_p$ and r_i is the radius of the particles of species $\mathscr{F}_i$, we can write:

$$\forall\, \boldsymbol{y} \in \partial\Omega_p : \psi(\|\boldsymbol{x}-\boldsymbol{y}\|) \approx \psi(\|\boldsymbol{x}-\boldsymbol{x}^p\|) - r_i\,\frac{\partial\psi}{\partial x_m}(\|\boldsymbol{x}-\boldsymbol{x}^p\|) n_m(\boldsymbol{y})$$

$$+ \frac{1}{2}\, r_i^2\, \frac{\partial^2\psi}{\partial x_m \partial x_r}(\|\boldsymbol{x}-\boldsymbol{x}^p\|) n_m(\boldsymbol{y}) n_r(\boldsymbol{y}) \tag{2.26}$$

Using this relation, we approximate equation (2.23) as:

$$\sum_{\mathscr{F}_i} \left[\psi(\|\boldsymbol{x}-\boldsymbol{x}^p\|) \int_{\partial\Omega_p} T_{jk}(\boldsymbol{y}) n_k(\boldsymbol{y}) dS_y \right]$$

$$- r_i \frac{\partial}{\partial x_m} \sum_{\mathscr{F}_i} \left[\psi(\|\boldsymbol{x} - \boldsymbol{x}^p\|) \int_{\partial\Omega_p} T_{jk}(\boldsymbol{y}) n_k(\boldsymbol{y}) n_m(\boldsymbol{y}) dS_y \right]$$

$$+ \frac{1}{2} r_i^2 \frac{\partial^2}{\partial x_m \partial x_r} \sum_{\mathscr{F}_i} \left[\psi(\|\boldsymbol{x} - \boldsymbol{x}^p\|) \int_{\partial\Omega_p} T_{jk}(\boldsymbol{y}) n_k(\boldsymbol{y}) n_m(\boldsymbol{y}) n_r(\boldsymbol{y}) dS_y \right] \tag{2.27}$$

If we then define the quantities:

$$n_i \langle f_j \rangle_p^i(\boldsymbol{x}, t) \equiv \sum_{\mathscr{F}_i} \left[\psi(\|\boldsymbol{x} - \boldsymbol{x}^p\|) \int_{\partial\Omega_p} T_{jk}(\boldsymbol{y}) n_k(\boldsymbol{y}) dS_y \right] \tag{2.28}$$

$$n_i \langle A_{jm} \rangle_p^i(\boldsymbol{x}, t) \equiv r_i \sum_{\mathscr{F}_i} \left[\psi(\|\boldsymbol{x} - \boldsymbol{x}^p\|) \int_{\partial\Omega_p} T_{jk}(\boldsymbol{y}) n_k(\boldsymbol{y}) n_m(\boldsymbol{y}) dS_y \right] \tag{2.29}$$

$$n_i \langle B_{jmr} \rangle_p^i(\boldsymbol{x}, t) \equiv r_i^2 \sum_{\mathscr{F}_i} \left[\psi(\|\boldsymbol{x} - \boldsymbol{x}^p\|) \int_{\partial\Omega_p} T_{jk}(\boldsymbol{y}) n_k(\boldsymbol{y}) n_m(\boldsymbol{y}) n_r(\boldsymbol{y}) dS_y \right] \tag{2.30}$$

we can express the traction term in equation (2.23) as:

$$n_i \langle f_j \rangle_p^i - \frac{\partial}{\partial x_m} \Big(n_i \langle A_{jm} \rangle_p^i \Big) + \frac{1}{2} \frac{\partial^2}{\partial x_m \partial x_r} \Big(n_i \langle B_{jmr} \rangle_p^i \Big) \tag{2.31}$$

Using the Reynolds decomposition for the average of the dyadic product featuring on the left-hand side of equation (2.22), we can express the nonlinear term as:

$$\langle u_j u_k \rangle_f = \langle u_j \rangle_f \langle u_k \rangle_f + \langle \hat{u}_j \hat{u}_k \rangle_f \tag{2.32}$$

where $\hat{u}_j(\boldsymbol{x}, t)$ and $\hat{u}_k(\boldsymbol{x}, t)$ are the deviations of the velocity components $u_j(\boldsymbol{x}, t)$ and $u_k(\boldsymbol{x}, t)$ from their respective means $\langle u_j \rangle_f(\boldsymbol{x}, t)$ and $\langle u_k \rangle_f(\boldsymbol{x}, t)$, respectively. If we introduce equations (2.31) and (2.32) into equation (2.22), after few manipulations, we obtain:

$$\rho_f \left[\frac{\partial}{\partial t} \Big(\varepsilon \langle u_j \rangle_f \Big) + \frac{\partial}{\partial x_k} \Big(\varepsilon \langle u_j \rangle_f \langle u_k \rangle_f \Big) \right] = \frac{\partial \langle S_{jk} \rangle_f}{\partial x_k} - \sum_{i=1}^{2} \Big(n_i \langle f_j \rangle_p^i \Big) + \varepsilon \rho_f g_j \tag{2.33}$$

where, by definition, it is:

$$\langle S_{jk} \rangle_f(\boldsymbol{x}, t) \equiv \varepsilon \langle T_{jk} \rangle_f + \sum_{i=1}^{2} \left[n_i \langle A_{jk} \rangle_p^i - \frac{1}{2} \frac{\partial}{\partial x_r} \Big(n_i \langle B_{jkr} \rangle_p^i \Big) \right] - \varepsilon \rho_f \langle \hat{u}_j \hat{u}_k \rangle_f \tag{2.34}$$

This term constitutes the fluid phase *effective stress tensor*. The quantity $\langle \hat{u}_j \hat{u}_k \rangle_f(\boldsymbol{x}, t)$ is analogous to the Reynolds stresses of turbulent flows and represents the fluctuations of the fluid velocity about its mean value. Finding an analytical closure for the effective fluid stress tensor is extremely complex;

however, a closure has been derived by Jackson (1997) on theoretical grounds in the limiting case of diluted, Stokesian monodisperse mixtures fluidized by Newtonian fluids. Appropriate closures for the terms on the right-hand side of equation (2.33) are described later on in Chapter 3.

2.4.7 Averaged equations of motion for the particle phases

We now apply similar principles to derive the averaged transport equations for each particle species in the system. To do so, we refer to the generic particle phase $\mathscr{F}_i$.

Continuity equation

We derive the equation by simply setting $\xi^p = 1$ in equation (2.19); doing so yields:

$$\frac{\partial n_i}{\partial t} + \frac{\partial}{\partial x_k}\Big(n_i \langle v_k \rangle_p^i\Big) = 0 \tag{2.35}$$

Dynamical equation

To derive this equation, we start from the linear momentum balance equation written for a generic particle of species $\mathscr{F}_i$. The forces at play are the traction force exerted by the fluid on the particle, the forces that result from the collisions between the particle in question and particles of the same and of different species at their mutual points of contact and the effect of gravity. Thus, we write:

$$\rho_i v_i \dot{v}_j^p = \int_{\partial\Omega_p} T_{jk}(\boldsymbol{y}) n_k(\boldsymbol{y}) dS_y + \sum_{k=1}^{2} \sum_{\mathscr{F}_k} f_j^{pq} + \rho_i v_i g_j \tag{2.36}$$

where ρ_i is the density of the particles of phase $\mathscr{F}_i$, $\dot{v}_j^p(t)$ is the j-th component of the acceleration of the particle centre of mass and $f_j^{pq}(t)$ is the j-th component of the force exerted by the generic particle q of phase $\mathscr{F}_k$ on the particle p under consideration when a collision takes place. Note that $f_j^{pq}(t) \neq 0$ only for the particles that are in *direct contact* with the particle p.

To average equation (2.36), we multiply both sides by $\psi(\|\boldsymbol{x} - \boldsymbol{x}^p\|)$ and sum over all the particles that belong to the phase under consideration. Doing so gives:

$$\rho_i v_i \sum_{\mathscr{F}_i} \Big[\psi(\|\boldsymbol{x} - \boldsymbol{x}^p\|) \dot{v}_j^p\Big] = \sum_{\mathscr{F}_i} \left[\psi(\|\boldsymbol{x} - \boldsymbol{x}^p\|) \int_{\partial\Omega_p} T_{jk}(\boldsymbol{y}) n_k(\boldsymbol{y}) dS_y\right]$$

$$+ \sum_{\mathscr{F}_i} \left[\psi(\|\boldsymbol{x} - \boldsymbol{x}^p\|) \sum_{k=1}^{2} \sum_{\mathscr{F}_k} f_j^{pq}\right] + \rho_i v_i g_j \sum_{\mathscr{F}_i} \psi(\|\boldsymbol{x} - \boldsymbol{x}^p\|) \tag{2.37}$$

If we now use equations (2.16), (2.18), (2.19) and (2.28), choosing in the second $\xi^p = \dot{v}_j^p$ and in the third $\xi^p = v_j^p$, and employ the relation:

$$\sum_{\mathscr{F}_i}\left[\psi(\|\boldsymbol{x}-\boldsymbol{x}^p\|)\sum_{k=1}^{2}\sum_{\mathscr{F}_k} f_j^{pq}\right]=\sum_{k=1}^{2}\sum_{\mathscr{F}_i}\left[\psi(\|\boldsymbol{x}-\boldsymbol{x}^p\|)\sum_{\mathscr{F}_k} f_j^{pq}\right] \tag{2.38}$$

we can rewrite equation (2.37) in the form:

$$\rho_i v_i\left[\frac{\partial}{\partial t}\Big(n_i\langle v_j\rangle_p^i\Big)+\frac{\partial}{\partial x_k}\Big(n_i\langle v_j v_k\rangle_p^i\Big)\right]=n_i\langle f_j\rangle_p^i+n_i\rho_i v_i g_j$$

$$+\sum_{k=1}^{2}\sum_{\mathscr{F}_i}\left[\psi(\|\boldsymbol{x}-\boldsymbol{x}^p\|)\sum_{\mathscr{F}_k} f_j^{pq}\right] \tag{2.39}$$

The first term on the right-hand side is the fluid-particle interaction force, which has its exact analogue in equation (2.33), while the last term combines the resultant forces arising from the particle-particle contacts between particles belonging to the same phase ($k=i$) and particles belonging to different phases ($k\neq i$). These contributions are conceptually different: the former is a self-interaction term that represents the *stress internal to the phase under examination*, whereas the latter is a *contact force acting between the Eulerian solid phases*. In order for the solid stress tensor associated to phase $\mathscr{F}_i$ to appear explicitly in equation (2.39), further mathematical manipulations are required. We start by considering the following double sum over the particles p of phase $\mathscr{F}_i$:

$$\sum_{\mathscr{F}_i}\sum_{\mathscr{F}_i}\Big[\psi(\|\boldsymbol{x}-\boldsymbol{x}^{pq}\|)\,f_j^{pq}\Big] \tag{2.40}$$

where $\boldsymbol{x}^{pq}(t)$ is the position vector of the point of mutual contact between the rigid particles p and q, both belonging to the same phase $\mathscr{F}_i$. The double sum clearly vanishes since $\boldsymbol{x}^{pq}(t)=\boldsymbol{x}^{qp}(t)$ and, for the principle of action and reaction, $f_j^{pq}(t)=-f_j^{qp}(t)$. By expanding the function $\psi(\|\boldsymbol{x}-\boldsymbol{x}^{pq}\|)$ in a Taylor series about the centre $\boldsymbol{x}^p(t)$ of the particles, we obtain:

$$\sum_{\mathscr{F}_i}\left[\psi(\|\boldsymbol{x}-\boldsymbol{x}^p\|)\sum_{\mathscr{F}_i} f_j^{pq}\right]-\,r_i\,\frac{\partial}{\partial x_m}\sum_{\mathscr{F}_i}\left[\psi(\|\boldsymbol{x}-\boldsymbol{x}^p\|)\sum_{\mathscr{F}_i}\Big(f_j^{pq}n_m^{pq}\Big)\right]$$

$$+\frac{1}{2}\,r_i^2\,\frac{\partial^2}{\partial x_m\partial x_r}\sum_{\mathscr{F}_i}\left[\psi(\|\boldsymbol{x}-\boldsymbol{x}^p\|)\sum_{\mathscr{F}_i}\Big(f_j^{pq}n_m^{pq}n_r^{pq}\Big)\right]-\cdots=0 \tag{2.41}$$

where $\boldsymbol{n}^{pq}(t)$ is the unit vector of $\boldsymbol{x}^{pq}(t)-\boldsymbol{x}^p(t)$. If we now introduce the functions:

$$n_i\langle M_{jm}\rangle_p^i(\boldsymbol{x},t)\equiv r_i\sum_{\mathscr{F}_i}\left[\psi(\|\boldsymbol{x}-\boldsymbol{x}^p\|)\sum_{\mathscr{F}_i}\Big(f_j^{pq}n_m^{pq}\Big)\right] \tag{2.42}$$

$$n_i\langle N_{jmr}\rangle_p^i(\boldsymbol{x},t)\equiv r_i^2\sum_{\mathscr{F}_i}\left[\psi(\|\boldsymbol{x}-\boldsymbol{x}^p\|)\sum_{\mathscr{F}_i}\Big(f_j^{pq}n_m^{pq}n_r^{pq}\Big)\right] \tag{2.43}$$

we can approximate equation (2.41) by writing:

$$\sum_{\mathscr{F}_i}\left[\psi(\|\boldsymbol{x}-\boldsymbol{x}^p\|)\sum_{\mathscr{F}_i} f_j^{pq}\right] \approx \frac{\partial}{\partial x_m}\left[n_i\langle M_{jm}\rangle_p^i - \frac{1}{2}\frac{\partial}{\partial x_r}\Big(n_i\langle N_{jmr}\rangle_p^i\Big)\right] \tag{2.44}$$

Let us now tackle the second contribution to the overall particle-particle contact force that appears on the right-hand side of equation (2.39). We express this term, which represents the contact forces acting between the particles p of the phase $\mathscr{F}_i$ under examination and the particles q of the other phase $\mathscr{F}_k$ of the granular material, as:

$$\sum_{\mathscr{F}_i}\left[\psi(\|\boldsymbol{x}-\boldsymbol{x}^p\|)\sum_{\mathscr{F}_k} f_j^{pq}\right] \tag{2.45}$$

where $k \neq i$, $p \in \mathscr{F}_i$ and $q \in \mathscr{F}_k$. Given its definition, this force should fulfill the principle of action and reaction; that is, it should be:

$$\sum_{\mathscr{F}_i}\left[\psi(\|\boldsymbol{x}-\boldsymbol{x}^p\|)\sum_{\mathscr{F}_k} f_j^{pq}\right] = -\sum_{\mathscr{F}_k}\left[\psi(\|\boldsymbol{x}-\boldsymbol{x}^q\|)\sum_{\mathscr{F}_i} f_j^{qp}\right] \tag{2.46}$$

where $\boldsymbol{x}^p(t)$ and $\boldsymbol{x}^q(t)$ are the positions of the centres of the particles p and q, respectively. Clearly, this condition is not met, for even if Newton's third law of mechanics tells us that $f_j^{pq}(t) = -f_j^{qp}(t)$, it is $\psi(\|\boldsymbol{x}-\boldsymbol{x}^p\|) \neq \psi(\|\boldsymbol{x}-\boldsymbol{x}^q\|)$. To overcome this conceptual paradox, we expand $\psi(\|\boldsymbol{x}-\boldsymbol{x}^p\|)$ in a Taylor series about the point $\boldsymbol{x}^{pq}(t)$ of mutual contact between the particles. If we retain only the first three terms of the series, we obtain:

$$\sum_{\mathscr{F}_i}\left[\psi(\|\boldsymbol{x}-\boldsymbol{x}^p\|)\sum_{\mathscr{F}_k} f_j^{pq}\right] \approx n_i\langle f_j\rangle_p^{ik} - \frac{\partial}{\partial x_m}\left[n_i\langle M_{jm}\rangle_p^{ik} + \frac{1}{2}\frac{\partial}{\partial x_r}\Big(n_i\langle N_{jmr}\rangle_p^{ik}\Big)\right] \tag{2.47}$$

where, by definition, it is:

$$n_i\langle f_j\rangle_p^{ik}(\boldsymbol{x},t) \equiv \sum_{\mathscr{F}_i}\left[\psi(\|\boldsymbol{x}-\boldsymbol{x}^{pq}\|)\sum_{\mathscr{F}_k} f_j^{pq}\right] \tag{2.48}$$

$$n_i\langle M_{jm}\rangle_p^{ik}(\boldsymbol{x},t) \equiv r_i\sum_{\mathscr{F}_i}\left[\psi(\|\boldsymbol{x}-\boldsymbol{x}^{pq}\|)\sum_{\mathscr{F}_k}\Big(f_j^{pq}n_m^{pq}\Big)\right] \tag{2.49}$$

$$n_i\langle N_{jmr}\rangle_p^{ik}(\boldsymbol{x},t) \equiv r_i^2\sum_{\mathscr{F}_i}\left[\psi(\|\boldsymbol{x}-\boldsymbol{x}^{pq}\|)\sum_{\mathscr{F}_k}\Big(f_j^{pq}n_m^{pq}n_r^{pq}\Big)\right] \tag{2.50}$$

If we now introduce equations (2.44) and (2.47) into equation (2.39), and we apply the Reynolds decomposition to the advection term, we obtain:

$$\rho_i v_i\left[\frac{\partial}{\partial t}\Big(n_i\langle v_j\rangle_p^i\Big) + \frac{\partial}{\partial x_m}\Big(n_i\langle v_j\rangle_p^i\langle v_m\rangle_p^i\Big)\right] = \frac{\partial\langle S_{jm}\rangle_p^i}{\partial x_m}$$

$$+ n_i\langle f_j\rangle_p^i + n_i\langle f_j\rangle_p^{ik} + n_i\rho_i v_i g_j \tag{2.51}$$

where, by definition, it is:

$$\langle S_{jm}\rangle_p^i(\boldsymbol{x},t) \equiv n_i\langle M_{jm}\rangle_p^i - n_i\langle M_{jm}\rangle_p^{ik}$$

$$-\frac{1}{2}\frac{\partial}{\partial x_r}\Big(n_i\langle N_{jmr}\rangle_p^i - n_i\langle N_{jmr}\rangle_p^{ik}\Big) - n_i\rho_i v_i\langle\hat{v}_j\hat{v}_m\rangle_p^i \tag{2.52}$$

Here $\hat{v}_j(\boldsymbol{x},t)$ and $\hat{v}_m(\boldsymbol{x},t)$ are the deviations of the velocity components $v_j^p(\boldsymbol{x},t)$ and $v_m^p(\boldsymbol{x},t)$ from their respective means $\langle v_j\rangle_p^i(\boldsymbol{x},t)$ and $\langle v_m\rangle_p^i(\boldsymbol{x},t)$, respectively.

The term $n_i\langle f_j\rangle_p^{ik}(\boldsymbol{x},t)$ fulfills the principle of action and reaction and therefore can be regarded as the *effective interaction force* between the granular phases. The other terms of the Taylor series on the right-hand side of equations (2.44) and (2.47) are instead lumped in the *effective solid stress tensor*, defined by equation (2.52), and constitute the so-called *collisional stress*. The part of the stress tensor related to the velocity fluctuations instead represents the so-called *kinetic stress*.

Table 2.1 reports, in absolute notation, the Eulerian-Eulerian locally averaged equations of motion for suspensions of n particle classes; these are an immediate generalization of the equations that we have just derived for bidisperse suspensions. To write them, we have resorted to equation (2.17). Note that in the dynamical equation for the i-th solid phase, the index k, which appears in the summation on the right-hand side of the equation, must be different from the index i. This is because the force $n_i\langle\boldsymbol{f}\rangle_p^{ik}(\boldsymbol{x},t)$ models the interaction between different particle classes.

As previously pointed out, the process of averaging generates a number of indeterminate terms not directly related to the averaged variables but still associated with details of the motion at the microscopic length scale. A clear example is given by the fluid-particle interaction force:

Continuity Equation - Fluid Phase $\dfrac{\partial\varepsilon}{\partial t} + \boldsymbol{\nabla}\cdot\Big(\varepsilon\langle\boldsymbol{u}\rangle_f\Big) = 0$
Continuity Equation - Particle Phase i $\dfrac{\partial\phi_i}{\partial t} + \boldsymbol{\nabla}\cdot\Big(\phi_i\langle\boldsymbol{v}\rangle_p^i\Big) = 0$
Dynamical Equation - Fluid Phase $\rho_f\left[\dfrac{\partial}{\partial t}\Big(\varepsilon\langle\boldsymbol{u}\rangle_f\Big) + \boldsymbol{\nabla}\cdot\Big(\varepsilon\langle\boldsymbol{u}\rangle_f\langle\boldsymbol{u}\rangle_f\Big)\right] = \boldsymbol{\nabla}\cdot\langle\boldsymbol{S}\rangle_f - \displaystyle\sum_{i=1}^{n}\Big(n_i\langle\boldsymbol{f}\rangle_p^i\Big) + \varepsilon\rho_f\boldsymbol{g}$
Dynamical Equation - Particle Phase i $\rho_i\left[\dfrac{\partial}{\partial t}\Big(\phi_i\langle\boldsymbol{v}\rangle_p^i\Big) + \boldsymbol{\nabla}\cdot\Big(\phi_i\langle\boldsymbol{v}\rangle_p^i\langle\boldsymbol{v}\rangle_p^i\Big)\right] = \boldsymbol{\nabla}\cdot\langle\boldsymbol{S}\rangle_p^i + n_i\langle\boldsymbol{f}\rangle_p^i + \displaystyle\sum_{k=1}^{n}\Big(n_i\langle\boldsymbol{f}\rangle_p^{ik}\Big) + \phi_i\rho_i\boldsymbol{g}$

Table 2.1: Eulerian-Eulerian locally averaged equations of motion for a system of n particle classes. In the particle dynamical equation, the index k must be different from the index i.

$$n_i \langle \boldsymbol{f} \rangle_p^i \equiv \sum_{\mathscr{F}_i} \left[\psi(\|\boldsymbol{x} - \boldsymbol{x}^p\|) \int_{\partial\Omega_p} \boldsymbol{T} \cdot \boldsymbol{n} dS_y \right] \tag{2.53}$$

To evaluate this force, we need to know the point fluid stress tensor $\boldsymbol{T}(\boldsymbol{x}, t)$, which is related to the microscopic fluid velocity field $\boldsymbol{u}(\boldsymbol{x}, t)$ and not its averaged value $\langle \boldsymbol{u} \rangle_f(\boldsymbol{x}, t)$. The problem of closure that arises is extremely difficult to tackle on purely theoretical grounds and has to be overcome by means of semitheoretical expressions. We will address this subject in the following chapter, where we will analyze in detail the fluid-particle interaction force, and we will develop new constitutive expressions for the drag and the elastic forces.

Chapter 3

The problem of closure

This chapter is concerned with the problem of closure of Eulerian-Eulerian locally averaged equations of motion for monodisperse fluidized suspensions.

1) We introduce the problem, and we discuss a few basic principles of general validity that should be considered in the development of proper closure relationships.
2) We present some strategies to close the self-interaction terms of the dynamical equations, which characterize the stress of each Eulerian phase.
3) We study in detail the fluid-particle interaction force, and we overview critically some constitutive equations used to model the buoyancy and drag forces in multiphase flows.
4) We develop a new drag force equation of closure for uniform fluidized suspensions of identical spherical solid particles.
5) We introduce an additional force, related to the drag, due to the presence of void fraction gradients within the suspensions, and we advance a constitutive equation for this contribution.

Parts of this chapter have been published:

Mazzei, L., Lettieri, P., Elson, T. & Colman, D. (2006). A revised monodimensional particle bed model for fluidized beds. Chem. Eng. Sci. 61, 1958.

Mazzei, L. & Lettieri, P. (2007). A drag force closure for uniformly dispersed fluidized suspensions. Chem. Eng. Sci. 62, 6129.

3.1 Introduction

Most of the theoretical studies concerned with the dynamics of populations of discrete elements aim to derive field equations that might represent them as continua. Classical continuum mechanics has succeeded quite remarkably in describing single-phase systems; multiphase systems, conversely, have proved much more complex to treat. In both instances, field equations based on suitably averaged

variables are derived; however, as shown in Chapter 2, these equations are underdetermined and appropriate closures must be supplied. Whereas in the area of classical fluid dynamics constitutive equations of broad validity and remarkable accuracy have been found, in multiphase flows theory the problem of closure still requires much investigation.

Some important basic principles that provide valuable guidance in the development of acceptable closure laws should be fulfilled. We mention here the *principles of frame indifference*, *well-posedness* and *fulfillment of the entropy inequality*. The first asserts that constitutive equations must be objective, and must not depend on any specific physical observer (Astarita & Marrucci, 1974; Truesdell, 1977; Lai et al., 1993; Massaudi, 2002; Gurtin, 2003). The second requires that the fluid dynamics should be described by a set of equations with unique solution and dependent continuously on their initial and boundary conditions (Drew & Passman, 1998). Finally, the third demands the fulfillment of the second law of thermodynamics: entropy generation must never be negative (Sandler, 1989).

For monodisperse suspensions, the problem of closure consists in finding constitutive expressions for the stress tensors of the fluid and particle phases and for the fluid-particle interaction force between the phases. As already pointed out, finding analytical closures based on purely theoretical arguments is prohibitively difficult; in fact, there is no guarantee that such equations even exist. The goal here is less ambitious and merely aims at finding equations that consent to analyze the systems of interest with the desired degree of accuracy. In this spirit, the problem can be reformulated as that of finding closures that are as simple as possible, whilst still being capable of capturing enough physics to attain a satisfactory description of the flow. This is exactly the opposite of the *principle of equipresence*, which states that in functional dependencies any possible variable should be included, unless it can be shown that a particular dependence cannot occur (Enwald et al., 1996; Drew & Passman, 1998). This principle essentially requires that constitutive equations should contain every sort of contribution that does not violate certain general principles of continuum mechanics. Even if in theory the idea is correct, the weakness of the method lies in the multitude of parameters present in these *equipresent equations* and in the impossibility of discriminating between them by means of any conceivable set of experimental measurements (Jackson, 2000). Thus, especially in the framework of multiphase flows, this principle is seldom observed (Drew & Passman, 1998; Jackson, 2000).

In what follows, we first describe some strategies for modelling the Eulerian stress tensors; we then perform a detailed analysis of the fluid-particle interaction force, laying particular emphasis on the buoyancy and drag forces. This will lead us to develop a new equation of closure for the drag force and to introduce an additional contribution, the *elastic force*, related to the drag and arising from the lack of homogeneity in solid compaction.

3.2 Stress tensors

Equations (2.34) and (2.52), presented in Chapter 2, reveal quite clearly the complexity of the Eulerian stress; this arises from the several contributions that make up the effective stress tensors yielded by

the averaging process. Finding closure laws for these quantities is further complicated by the absence of experimental measurements having a direct bearing on them. Numerous attempts to investigate the viscous behaviour of particulate mixtures are found in the literature. In most of these studies, the suspensions are treated as Newtonian pseudofluids, and quantitative measurements of their effective viscosities are provided (Rutgers, 1962; Prudhoe & Whitmore, 1964; Grace, 1970; King et al., 1981; Reiling, 1992; Poletto & Joseph, 1995). This problem has also been the subject of various theoretical (Einstein, 1906, 1911; Vand, 1948; Brinkman, 1952; Frankel & Acrivos, 1967; Batchelor & Green, 1972; Graham, 1981) and semitheoretical (Mooney, 1951; Thomas, 1965; Barnea & Mizrahi, 1973; Metzner, 1985) investigations. However, as mentioned earlier, all these analyses are concerned with, and provide insight into, the rheology of the mixtures and not of their Eulerian constituent phases. Relating the two is difficult and much research is still needed (Enwald et al., 1996).

A common assumption is to consider a Newtonian behaviour for each continuum, albeit there are clear indications that such a view is oversimplistic (Jackson, 1997, 1998, 2000). Thus, the effective stress tensors take the form:

$$\langle \boldsymbol{S} \rangle_f = -\langle p \rangle_f \boldsymbol{I} + 2\mu_f \langle \boldsymbol{D} \rangle_f + \left(\kappa_f - \frac{2}{3}\mu_f \right) \mathrm{tr}\langle \boldsymbol{D} \rangle_f \boldsymbol{I} \tag{3.1}$$

$$\langle \boldsymbol{S} \rangle_p = -\langle p \rangle_p \boldsymbol{I} + 2\mu_p \langle \boldsymbol{D} \rangle_p + \left(\kappa_p - \frac{2}{3}\mu_p \right) \mathrm{tr}\langle \boldsymbol{D} \rangle_p \boldsymbol{I} \tag{3.2}$$

where $\langle p \rangle_f(\boldsymbol{x}, t)$ and $\langle p \rangle_p(\boldsymbol{x}, t)$, μ_f and μ_p, and κ_f and κ_p are the averaged pressures, shear viscosities and dilatational viscosities of the fluid and particle phases, respectively. Moreover, $\boldsymbol{I}$ is the identity tensor, while $\langle \boldsymbol{D} \rangle_f(\boldsymbol{x}, t)$ and $\langle \boldsymbol{D} \rangle_p(\boldsymbol{x}, t)$ are the rate of deformation tensors:

$$\langle \boldsymbol{D} \rangle_f \equiv \frac{1}{2}\Big(\boldsymbol{\nabla} \langle \boldsymbol{u} \rangle_f + \boldsymbol{\nabla} \langle \boldsymbol{u} \rangle_f^T \Big) \quad ; \quad \langle \boldsymbol{D} \rangle_p \equiv \frac{1}{2}\Big(\boldsymbol{\nabla} \langle \boldsymbol{v} \rangle_p + \boldsymbol{\nabla} \langle \boldsymbol{v} \rangle_p^T \Big) \tag{3.3}$$

The problem of closure thus reduces to finding appropriate constitutive expressions for the pressure, the shear viscosity and the dilatational viscosity of each phase. The fluid phase is usually considered incompressible; hence, its pressure does not need to be specified constitutively. Furthermore, often μ_f is assumed to be constant, and κ_f is entirely neglected. For the solid phase, conversely, more elaborate constitutive expressions have been developed.

We can adopt various strategies to model the flow parameters of equation (3.2). One is resorting to empirical relations based on the particle properties and on the local void fraction. These are easily implemented in numerical codes and relatively inexpensive computationally. For a detailed review, refer to Massaudi et al. (1992) and Enwald et al. (1996). Another strategy is using the kinetic theory approach, derived from the mathematical theory of dense non-uniform gases (Chapman & Cowling, 1970). These models are much more complex and numerically quite demanding; however, they are more promising and suitable for a wider class of applications. Since our focus is not on the problem of closure of the solid stress, we refer for further details to the abundant literature available on the subject (see, for instance, Gidaspow, 1994, Drew & Passman, 1998 and Jackson, 2000).

3.3 Fluid-particle interaction force

It is generally agreed that there are five main contributors to the fluid-particle interaction force. The first is the *buoyancy force*, whose definition in the context of multiphase flows is not unique and needs to be discussed. The second acts in the direction of the fluid-particle slip velocity – that is, the velocity of the fluid relative to an observer moving with the same local mean velocity as the particles. The third is normal to the slip velocity, the fourth is parallel to the relative acceleration between the phases and the fifth is proportional to the local mean acceleration of the fluid. The last four terms are commonly referred to as *drag force*, *lift force*, *virtual mass force* and *local fluid acceleration force*, respectively. As we shall see, the local fluid acceleration force is not always present, but features only when one specific definition of buoyancy force is employed – in particular, the *classical definition* presented later on. Among these five terms, in most cases of practical interest the buoyancy and drag forces are dominant; consequently, particular effort has been put into finding reliable equations of closure for such contributions.

3.3.1 Buoyancy force

The definition of buoyancy force, normally considered fairly obvious for single objects in pure fluids, is in our setting quite ambiguous and has been the subject of heated debates for several years. A comprehensive treatment of the topic can be found in Jackson (2000). For fluidized suspensions, at least three alternative definitions have been put forward. The first regards the force as equal to the weight of the fluid displaced by the solid, as suggested for instance by Richardson & Zaki (1954), Wen & Yu (1966), Epstein (1984), Clift et al. (1987) and Jean & Fan (1992). Accordingly, if we refer the force to the unit volume of suspension, this takes the form:

$$n\langle \boldsymbol{f}_s \rangle_p = -\phi \rho_f \boldsymbol{g} \tag{3.4}$$

Since we are dealing with monodisperse systems, to simplify the notation we have dropped the phase suffix i used in Chapter 2 to denote particle phase averages. This definition coincides with the original formulation of the Archimedes's principle; therefore, we refer to it as *classical definition*.

The second definition relates the force to the fluid stress tensor, as reported by Jackson (2000). Again per unit volume of suspension, it is:

$$n\langle \boldsymbol{f}_s \rangle_p^* = \phi \boldsymbol{\nabla} \cdot \langle \boldsymbol{S} \rangle_f \tag{3.5}$$

The last definition, endorsed by Foscolo et al. (1983), Gibb (1991), Astarita (1993), Di Felice (1994) and Gibilaro (2001), to mention just a few, deems the force proportional to the fluid pressure gradient. The constant of proportionality is once again the volume fraction of solid:

$$n\langle \boldsymbol{f}_s \rangle_p^\circ = -\phi \boldsymbol{\nabla} \langle p \rangle_f \tag{3.6}$$

For homogeneous dispersions, the second and third definitions coincide, since $\langle \boldsymbol{D} \rangle_f(\boldsymbol{x}, t)$ vanishes. In uniform mixtures, the solid particles are motionless and equally distributed in space; moreover, whereas the point fluid velocity is a non-homogeneous field due to the fluid flow around the particles occurring at the microscopic length scale, the locally averaged velocity field is uniform (in the bulk of the suspension, sufficiently far from the system boundaries). Thus, the rate of deformation tensors vanish and the stress tensors of both phases are isotropic. Furthermore, since no collisions are present between the particles, the solid pressure is zero and, from equation (3.2), no stress arises in the solid phase. Equation (3.1), taken in conjunction with the definitions (3.5) and (3.6), instead gives:

$$\langle \boldsymbol{S} \rangle_f = -\langle p \rangle_f \boldsymbol{I} \quad \Rightarrow \quad n\langle \boldsymbol{f}_s \rangle_p^* = n\langle \boldsymbol{f}_s \rangle_p^\circ \equiv n\langle \boldsymbol{f}_s \rangle_p^\bullet \tag{3.7}$$

A useful, and quite revealing, expression for $n\langle \boldsymbol{f}_s \rangle_p^\bullet(\boldsymbol{x}, t)$ can be derived from the locally averaged dynamical equations reported in Table 2.1 of Chapter 2; in light of the previous considerations, the two transport equations reduce to:

$$n\langle \boldsymbol{f} \rangle_p = -\boldsymbol{\nabla}\langle p \rangle_f + \varepsilon \rho_f \boldsymbol{g} \quad ; \quad n\langle \boldsymbol{f} \rangle_p = -\phi \rho_p \boldsymbol{g} \tag{3.8}$$

where ρ_p denotes the particle density. The equation on the right merely states that the particle weight must be counterbalanced by the fluid-particle interaction force. By subtracting the two equations, we obtain an explicit expression for the pressure gradient valid for homogeneous suspensions:

$$\boldsymbol{\nabla}\langle p \rangle_f = (\varepsilon \rho_f + \phi \rho_p)\boldsymbol{g} \tag{3.9}$$

whence, from equations (3.6) and (3.7), we obtain:

$$n\langle \boldsymbol{f}_s \rangle_p^\bullet = -\phi(\varepsilon \rho_f + \phi \rho_p)\boldsymbol{g} \tag{3.10}$$

We then conclude that for homogeneous fluidized suspensions the difference between the first and the other two definitions of buoyancy force reduces to the mere choice of which density to employ in the expression of the force: in the first instance the *fluid density* is required, whereas in the second the *suspension bulk density*. As we shall see in § 3.4.2, the buoyancy force definition is important in the development, or simply the choice, of drag force closures.

In the present work, the classical definition of buoyancy force, equation (3.4), is employed. This, in the author's opinion, should be favoured since it is the only definition that preserves the distinctive feature of such a force: being *constant* and altogether *unrelated* to the specific characteristics of the flow (Bird et al., 2007). It should be emphasized that in the present setting relating the buoyancy force to the suspension bulk density, as the other two definitions implicitly do, is physically incorrect. In a fluidized suspension of monodisperse solid particles, or more generally of particles whose dimensions do not differ by orders of magnitude, each single particle moves *through the fluid* and displaces its own volume of fluid as it flows, not of suspension. If it were not for the collisions that inevitably

take place among the particles, these would not feel the presence of the surrounding others. This is particularly evident in diluted systems. In light of these considerations, the definition of buoyancy force that most naturally suggests itself is the one that relates the force to the fluid density. This conclusion, as already pointed out, holds true *as long as all the particles have similar dimensions*. For large objects in suspensions of small particles the situation is quite different: here the motion of such bodies takes place *through the suspension* and the volume displaced comprises both fluid and particles. It makes therefore physical sense to relate the buoyancy force to the suspension bulk density. In this regard, we mention the work of Poletto & Joseph (1995), where the motion of single test spheres in monodisperse mixtures was investigated. The dispersion was modelled as a pseudofluid with effective density and viscosity. The study aimed to determine the values of these properties that allowed predicting the settling velocity of test spheres in sedimenting and fluidized suspensions using appropriate modifications of the equation of Francis (1933) for the settling of single spheres in pure Newtonian fluids. The article, in particular, proposed to establish the limits of applicability of the notion that the effective density of a mixture, on which the expression of the buoyancy force is based, should be the suspension bulk density. Experimental evidence showed that this approach is applicable as long as the test spheres are rather larger than the suspended particles and provided that the solid concentration in the suspension is sufficiently high (more quantitative data can be found in the paper). For dilute suspensions and test particles of similar or smaller size than the suspended particles the model failed. This corroborates the idea that the suspension bulk density should be used only when large objects move through suspensions of much smaller particles.

3.3.2 Local fluid acceleration force

If the classical definition of buoyancy force is adopted, equation (3.4), the interaction force between fluid and particles must include an additional term known as *local fluid acceleration force*. This is true not only for solid suspensions but also for single bodies. The origin of this force is clearly presented by Maxey & Riley (1983) in the study of the motion of small rigid spheres in non-uniform flows. Per unit volume of suspension, the force is taken to be:

$$n\langle \boldsymbol{f}_a \rangle_p = \phi \rho_f \frac{D_f \langle \boldsymbol{u} \rangle_f}{Dt} \tag{3.11}$$

Here the derivative on the right-hand side is a *material derivative* relative to a Lagrangian observer moving with the locally averaged velocity of the fluid. An analogous material derivative can also be introduced for the particle phase; the two are formally defined as:

$$\frac{D_f \langle \boldsymbol{u} \rangle_f}{Dt} \equiv \frac{\partial \langle \boldsymbol{u} \rangle_f}{\partial t} + \langle \boldsymbol{u} \rangle_f \cdot \boldsymbol{\nabla} \langle \boldsymbol{u} \rangle_f \quad ; \quad \frac{D_p \langle \boldsymbol{v} \rangle_p}{Dt} \equiv \frac{\partial \langle \boldsymbol{v} \rangle_p}{\partial t} + \langle \boldsymbol{v} \rangle_p \cdot \boldsymbol{\nabla} \langle \boldsymbol{v} \rangle_p \tag{3.12}$$

Often the acceleration of the fluid is far less than the gravitational acceleration; if so, the local fluid acceleration force is negligible compared with the buoyancy force. Notwithstanding, this term plays

an important conceptual role; to prove this point, we resort to a simple thought experiment. A uniform set of solid particles is at rest in a body of fluid. The fluid is also at rest in a vertical container placed on a horizontal plane. The whole system resides in a uniform gravitational field. At a specified time, the plane that supports the container and the constraints that keep the particles at rest are removed. The whole system falls freely with an acceleration equal to the gravitational field. Since the mean velocity fields of both phases are uniform and no pressure gradients are present, the effective stress tensors $\langle \boldsymbol{S} \rangle_f(\boldsymbol{x}, t)$ and $\langle \boldsymbol{S} \rangle_p(\boldsymbol{x}, t)$ vanish; accordingly, the averaged dynamical equations of motion reported in Table 2.1 of Chapter 2 reduce to:

$$\varepsilon \rho_f \frac{D_f \langle \boldsymbol{u} \rangle_f}{Dt} = -\, n \langle \boldsymbol{f} \rangle_p + \varepsilon \rho_f \boldsymbol{g} \quad ; \quad \phi \rho_p \frac{D_p \langle \boldsymbol{v} \rangle_p}{Dt} = n \langle \boldsymbol{f} \rangle_p + \phi \rho_p \boldsymbol{g} \tag{3.13}$$

For convenience, we have used the non-conservative formulation of the equations; these are obtained by combining the linear momentum equations of conservation and the equations of continuity (refer, for instance, to Bird et al., 2007). Both material derivatives are equal to the gravitational acceleration; hence, the two equations of motion lead to the same result: the fluid-particle interaction force must vanish. Clearly, this condition can be met only if the contribution due to the local fluid acceleration force is accounted for. In fact, as the two phases undergo the same motion, no slip velocity is present between them; consequently, the drag, the virtual mass and the lift forces are all zero. The buoyancy force, conversely, is constant; therefore, the overall interaction force can go to zero only if the local fluid acceleration force is considered. Indeed it is:

$$n \langle \boldsymbol{f} \rangle_p = n \langle \boldsymbol{f}_s \rangle_p + n \langle \boldsymbol{f}_a \rangle_p = -\, \phi \rho_f \boldsymbol{g} + \phi \rho_f \boldsymbol{g} = \boldsymbol{0} \tag{3.14}$$

Since the averaged fluid acceleration is often far less than the local gravitational field, this ideal experiment does not reflect the normal conditions wherein fluidized systems are usually operated.

3.3.3 Virtual mass and lift forces

If a body immersed in a fluid accelerates, some of the surrounding medium must accelerate as well; this results in a force named *virtual mass force*. For a quite insightful analysis on this topic we refer to Birkhoff (1950). If an object moves in a fluid that is in shearing flow, it experiences a force transverse to the direction of relative motion. This force is called *lift force*.

Exact expressions for these forces have been derived analytically by some authors for the case of single particles, usually of spherical or nearly spherical shape, in non-uniform flows (Maxey & Riley, 1983; Nadim & Stone, 1991). Closures of this kind, nevertheless, lack general validity and apply to very specific fluid dynamic conditions (*e.g.*, vanishing or very low Reynolds numbers). More recently, these results have been used to develop analytical closures for monodisperse fluidized suspensions; we mention, for instance, the work of Zhang & Prosperetti (1994, 1997) and Jackson (1997, 1998). The equations so obtained, however, are valid for low particle concentrations and apply under very

restricting assumptions, such as vanishing viscosity (Zhang & Prosperetti, 1994) or small Stokes and Reynolds numbers (Jackson, 1997, 1998; Zhang & Prosperetti, 1997). Their generalization to other fluid dynamic conditions is by no means straightforward and often raises conceptual issues (related, for example, to frame indifference and objectivity). It is interesting to report, for example, that the lift force on an isolated spherical particle takes quite different functional forms in the inviscid and low Reynolds number cases (Saffman, 1965; Auton et al., 1988; Jackson, 2000); finding an expression of general validity for this term still appears, for the time being, to be a daunting task.

A quite well established expression for the virtual mass force is:

$$n\langle \boldsymbol{f}_v \rangle_p = C_v(\phi)\phi\rho_f \left(\frac{D_f \langle \boldsymbol{u} \rangle_f}{Dt} - \frac{D_p \langle \boldsymbol{v} \rangle_p}{Dt} \right) \tag{3.15}$$

Theoretical, and even empirical, expressions for the coefficient $C_v(\phi)$ are still to be found. For dilute mixtures of spherical particles, $C_v(\phi)$ is taken to be $1/2$, since this is the calculated value for a single sphere in an infinite fluid (Maxey & Riley, 1983; Nadim & Stone, 1991). A similar result was also found analytically by Zhang & Prosperetti (1994), who derived an exact expression of the force for inviscid fluids at low particle concentrations.

The lift force is usually taken to be:

$$n\langle \boldsymbol{f}_l \rangle_p = -\, C_l(\phi)\phi\rho_f \left(\boldsymbol{\nabla} \times \langle \boldsymbol{u} \rangle_f \right) \times \left(\langle \boldsymbol{u} \rangle_f - \langle \boldsymbol{v} \rangle_p \right) \tag{3.16}$$

Equations (3.15) and (3.16) are not frame independent, if taken separately, yet their sum fulfills the principle of material objectivity provided that $C_v(\phi)$ and $C_l(\phi)$ are equal (Drew & Passman, 1998). For this reason, in dilute flows of spherical particles, also $C_l(\phi)$ is taken to be $1/2$.

3.3.4 Drag and elastic forces

The drag force is the most important contribution to the fluid-particle interaction force. We conduct a detailed analysis concerning this term in §3.4, where we present an overview of the most commonly used constitutive equations, and we develop a new equation of closure.

In this work, the elastic force represents the component of the drag arising from gradients in the suspension void fraction. In uniform dispersions this force vanishes, but is important in the study of the stability of the homogeneous fluidization state. We present the force in §3.5, where we also derive a closure relationship.

3.3.5 Other forces

Various other contributions could, at least in principle, be considered. However, very little is known about most of them, and since the majority does not play a dominant role, they are usually neglected

in multiphase flows models. A comprehensive overview can be found in Drew & Passman (1998). Here we cite only the *Faxen force* and a history-dependent term analogous to the *Basset force* for the motion of isolated particles (Basset, 1888). For the latter, it seems reasonable to believe that for dense fluidized suspensions, the space-averaging of history-dependent forces should result into a vanishing contribution: the averaging procedure would most probably erase any historical effect of the motion of the particles on the fluid in their immediate neighbourhood (Jackson, 2000). The Faxen force, on the other hand, arises from viscous effects in the fluid phase and is taken to be (Brenner, 1964):

$$n\langle \boldsymbol{f}_f \rangle_p = C_f(\phi)\phi\mu_f \boldsymbol{\nabla}^2 \langle \boldsymbol{u} \rangle_f \tag{3.17}$$

Single-sphere calculations indicate a value of $3/4$ for $C_f(\phi)$; accordingly, this value is expected to be valid in the limit of vanishing small particle concentrations (see Jackson, 1997, 1998).

3.4 Drag force analysis

In this section, we analyze some well-known drag force constitutive equations, and we advance a new closure of general validity. The following refers to homogeneous fluidized suspensions; the effect of non-uniformities in solid compaction will be addressed in §3.5.

3.4.1 The problem of closure for the drag force

We are concerned here with uniform monodisperse suspensions of spherical solid particles fluidized by incompressible, isothermal Newtonian fluids. For these systems, the incompressibility assumption does not restrict the analysis to liquid fluidization, since the overall pressure drop across beds fluidized by gases is usually small enough to render variations in the density of the fluid utterly negligible. The suspension consists of motionless spheres not interacting with one another in any way. Effects due to particle collisions and/or interparticle forces are not accounted for; each particle interacts solely with the fluid and finds itself in equilibrium. In these hypotheses, we propose to find a constitutive equation for the drag force exerted by the fluid on the particles. Since this force is *by definition* parallel to the fluid-particle slip velocity, its general expression can reasonably be:

$$n\langle \boldsymbol{f}_d \rangle_p = \beta(\varepsilon, \|\langle \boldsymbol{u} \rangle_f - \langle \boldsymbol{v} \rangle_p\|)(\langle \boldsymbol{u} \rangle_f - \langle \boldsymbol{v} \rangle_p) \tag{3.18}$$

The form of the scalar function $\beta(\varepsilon, \|\langle \boldsymbol{u} \rangle_f - \langle \boldsymbol{v} \rangle_p\|)$ is to be determined and will presumably depend on the physical properties of the fluid (density and viscosity) and on the particle diameter, in addition to the arguments explicitly shown in equation (3.18). For the time being, that such a dependence really exists is just a sensible assumption; later on we shall have to prove that this is the case. The problem of closure reduces therefore to finding an expression for $\beta(\varepsilon, \|\langle \boldsymbol{u} \rangle_f - \langle \boldsymbol{v} \rangle_p\|)$. Before addressing it, we first examine the relationship between the buoyancy and drag forces.

3.4.2 Relationship between buoyancy force and drag force

The definition of buoyancy force is important, insomuch as it directly affects the closure for the drag. If we denote by $n\langle \boldsymbol{f}_d \rangle_p$ and $n\langle \boldsymbol{f}_d \rangle_p^\bullet$ the drag forces per unit volume of suspension consistent with the buoyancy force definitions (3.4) and (3.10), respectively, it is:

$$n\langle \boldsymbol{f}_d \rangle_p^\bullet = \varepsilon\, n\langle \boldsymbol{f}_d \rangle_p \tag{3.19}$$

For the systems under scrutiny, the local fluid acceleration force (if present) and the virtual mass and lift forces vanish; thus, from equation (3.8), we have:

$$n\langle \boldsymbol{f} \rangle_p = n\langle \boldsymbol{f}_s \rangle_p + n\langle \boldsymbol{f}_d \rangle_p = n\langle \boldsymbol{f}_s \rangle_p^\bullet + n\langle \boldsymbol{f}_d \rangle_p^\bullet = -\,\phi \rho_p \boldsymbol{g} \tag{3.20}$$

Then, equations (3.4) and (3.10) give:

$$n\langle \boldsymbol{f}_d \rangle_p = -\,\phi(\rho_p - \rho_f)\boldsymbol{g} \quad ; \quad n\langle \boldsymbol{f}_d \rangle_p^\bullet = -\,\varepsilon\phi(\rho_p - \rho_f)\boldsymbol{g} \tag{3.21}$$

whence equation (3.19) immediately ensues. This relation is necessary to render drag force closures based on different buoyancy force definitions consistent with one another.

3.4.3 Relationship between the steady-state expansion of homogeneous beds and drag force constitutive equations

The experimental information with most direct bearing on the drag force is the relation between the sedimentation velocity u_s of an assembly of particles in a generic fluid of interest and the void fraction ε of the dispersion. This problem was investigated extensively by Richardson & Zaki (1954), who advanced the following empirical correlation:

$$u_s = u_t \varepsilon^{n_e} \tag{3.22}$$

where u_t is the unhindered terminal settling velocity of the particles and n_e is an empirical parameter dependent on the free fall particle Reynolds number:

$$Re_t \equiv \frac{\rho_f}{\mu_f} u_t d_p \tag{3.23}$$

Here d_p is the particle diameter. Several correlations have been proposed to estimate n_e, their main difference consisting in the limiting values ascribed to the parameter. In some equations, in the limits of viscous and inertial regimes, n_e is equal to 4.65 and 2.39 (Richardson & Zaki, 1954), in others takes the values of 4.70 and 2.35 (Rowe, 1987), whereas in still others tends to 4.80 and 2.40 (Khan & Richardson, 1989; Gibilaro, 2001), respectively. Here, we use the correlation:

$$n_e(Re_t) = \frac{4.8 + 2.4 \cdot 0.175 Re_t^{3/4}}{1 + 0.175 Re_t^{3/4}} \tag{3.24}$$

This is a modification of the empirical expression of Rowe (1987), where the limits for n_e suggested by Khan & Richardson and Gibilaro are used.

Equations (3.22) and (3.24) were initially found to hold for liquid-fluidized suspensions, where they proved to be highly accurate, giving an excellent description of the expansion profiles of such systems. Once the physical properties of the fluid (density and viscosity) and the particles (density and diameter) have been assigned, the voidage of a liquid-fluidized suspension, and in turn its expansion, turns out to be a simple function of the superficial fluid flux:

$$\varepsilon = \varepsilon(u_s) \tag{3.25}$$

Subsequently, the question was raised as to the validity of these empirical findings also for systems fluidized by gases. This issue was first addressed by Godard & Richardson (1968), who conducted several expansion experiments on various powders fluidized by air and characterized by very narrow size distributions. They found that the relationship between u_s and ε could still be expressed in the form of equation (3.22). However, the values of n_e for many of the powders tested appeared to be higher than those predicted by equation (3.24). Similar results have also been obtained by many other researchers, we refer for instance to Geldart & Wong (1984, 1985) and Lettieri et al. (2000, 2002). The experimental evidence collected in these and several other studies allows drawing the following conclusion: the simple relation expressed by equation (3.24) applies only to the case of *non-cohesive* systems where potential interparticle forces are virtually absent or play a negligible role compared with that ascribable to their hydrodynamic counterparts. Equation (3.22), *along with equation* (3.24), is purely hydrodynamical and provides an accurate description of the expansion characteristics for fluidized emulsions only if these are subjected solely to the buoyancy and drag forces without being affected by any other contributions of different nature. For cohesive systems, conversely, n_e combines the effects of both hydrodynamic and interparticle forces; its value, therefore, cannot be assessed by means of simple hydrodynamical correlations, such as equation (3.24). In this framework, since our analysis has to do with a fluid dynamic force, we can – and indeed must – base the mathematical development on the assumption of perfect non-cohesiveness. This allows employing equations (3.22) and (3.24). If we assume therefore their full validity, such correlations provide a simple and effective way of testing the correctness of drag force closure relationships. For a generic non-cohesive fluidized suspension, uniformly-dispersed and in fluid dynamic equilibrium, a drag force expression is accurate only if it yields a similar expansion profile to the one predicted by equations (3.22) and (3.24) for any fluid dynamic regime and void fraction. This concept can be formalized as follows. For the systems under scrutiny, equation (3.21) holds; thus, equation (3.18) yields:

$$\beta(\varepsilon, \|\langle \boldsymbol{u} \rangle_f - \langle \boldsymbol{v} \rangle_p\|)(\langle \boldsymbol{u} \rangle_f - \langle \boldsymbol{v} \rangle_p) = -\phi(\rho_p - \rho_f)\boldsymbol{g} \tag{3.26}$$

For a homogeneous suspension and an observer at rest relatively to the particles, it is:

$$\langle \boldsymbol{u} \rangle_f = \frac{\boldsymbol{u}_s}{\varepsilon} \quad ; \quad \langle \boldsymbol{v} \rangle_p = \boldsymbol{0} \quad ; \quad \|\langle \boldsymbol{u} \rangle_f - \langle \boldsymbol{v} \rangle_p\| = \frac{u_s}{\varepsilon} \tag{3.27}$$

where $\boldsymbol{u}_s$ is the superficial fluid velocity. As $\boldsymbol{u}_s$ and $\boldsymbol{g}$ are parallel and opposite, introducing equation (3.27) into equation (3.26) and replacing ϕ with $1-\varepsilon$ gives:

$$\hat{\beta}(\varepsilon, u_s) = \frac{\varepsilon}{u_s}(1-\varepsilon)(\rho_p - \rho_f)g \tag{3.28}$$

Similar to equation (3.22), equation (3.28) is also a functional relationship between u_s and ε. This equation is directly related to the closure used for $\beta(\varepsilon, \|\langle \boldsymbol{u} \rangle_f - \langle \boldsymbol{v} \rangle_p\|)$. Thus, a most convenient way of testing the validity of the latter is to ascertain that the predictions based on equation (3.28) are fully consistent with those obtained from its counterpart, equations (3.22) and (3.24), over the whole range of fluid dynamic regimes and for any value of the fluid volume fraction.

This requirement, as we shall presently see, is not met by the equations of closure reported in the literature and employed in most commercial CFD codes. Some are in good agreement with equations (3.22) and (3.24) in the extremes of purely viscous and/or purely inertial regimes; in the intermediate region, however, no accord is usually found. Few researchers have addressed this issue; to the author's knowledge only Di Felice (1994) and, more recently, Yang & Renken (2003). They both derived empirical correlations to dwindle the discrepancy between their closures and equations (3.22) and (3.24). Notwithstanding, no constitutive relation is entirely consistent with the Richardson & Zaki equation. Our closure overcomes this limitation, and does not need, in addition to equations (3.22) and (3.24), any other empirical correlation.

For briefness, from now on we will refer only to equation (3.22), assuming that such equation is always used in conjunction with equation (3.24).

3.4.4 Limitations of some existing drag force closures

We report here some of the most well-known expressions used to model the drag force in fluidized systems of uniformly-dispersed particles. We then compare their predictions in terms of homogeneous bed expansion to those based on equation (3.22). All the closures hereunder are consistent with the classical definition of buoyancy force, or are rendered so by resorting to equation (3.19).

3.4.4.1 Ergun drag force closure

The Ergun (1952) empirical correlation was originally developed to assess the unrecoverable pressure drop through *packed beds*. If we extend its range of validity to homogeneous fluidized suspensions, we can express the pressure gradient for such systems as:

$$\boldsymbol{\nabla}\langle p \rangle_f = \rho_f \boldsymbol{g} - \left[150 \frac{\mu_f (1-\varepsilon)^2}{d_p^2 \varepsilon^3} + 1.75 \frac{\rho_f u_s (1-\varepsilon)}{d_p \varepsilon^3} \right] \boldsymbol{u}_s \tag{3.29}$$

This relation, if taken in conjunction with the averaged linear momentum equation for the fluid phase, can be used to derive a constitutive expression for the drag. For homogeneous suspensions in fluid

dynamic equilibrium, the equation of conservation just mentioned reduces to:

$$n\langle \boldsymbol{f}_s \rangle_p + n\langle \boldsymbol{f}_d \rangle_p = -\boldsymbol{\nabla}\langle p \rangle_f + \varepsilon \rho_f \boldsymbol{g} \tag{3.30}$$

If we replace equations (3.4), (3.27) and (3.29) into equation (3.30), we obtain:

$$n\langle \boldsymbol{f}_d \rangle_p = \left[150 \frac{\mu_f (1-\varepsilon)^2}{d_p^2 \varepsilon^2} + 1.75 \frac{\rho_f \| \langle \boldsymbol{u} \rangle_f - \langle \boldsymbol{v} \rangle_p \| (1-\varepsilon)}{d_p \varepsilon} \right] (\langle \boldsymbol{u} \rangle_f - \langle \boldsymbol{v} \rangle_p) \tag{3.31}$$

whence, from equation (3.18), it is:

$$\beta(\varepsilon, \| \langle \boldsymbol{u} \rangle_f - \langle \boldsymbol{v} \rangle_p \|) = 150 \frac{\mu_f (1-\varepsilon)^2}{d_p^2 \varepsilon^2} + 1.75 \frac{\rho_f \| \langle \boldsymbol{u} \rangle_f - \langle \boldsymbol{v} \rangle_p \| (1-\varepsilon)}{d_p \varepsilon} \tag{3.32}$$

Equation (3.32) does not bear any link with the Richardson & Zaki equation; thus, predictions of bed expansion profiles based on the Ergun closure are likely not to agree with those yielded by equation (3.22). To make a comparison between them, we operate as follows. For a generic Geldart Group A powder (Geldart, 1973) fluidized by liquid or gas, we assign the superficial velocity of the fluid, and we calculate the corresponding value of the suspension void fraction $\varepsilon_{R\&Z}$ yielded by equation (3.22). Then, for the same value of u_s, we solve equation (3.28) using the closure for $\beta(\varepsilon, \| \langle \boldsymbol{u} \rangle_f - \langle \boldsymbol{v} \rangle_p \|)$ given by equation (3.32), and we evaluate the corresponding value of the voidage, denoted by ε_E. Finally, we compute the ratio between the two results and quantify its deviation from unity. Naturally, the more the deviation, the less the agreement between the two relations.

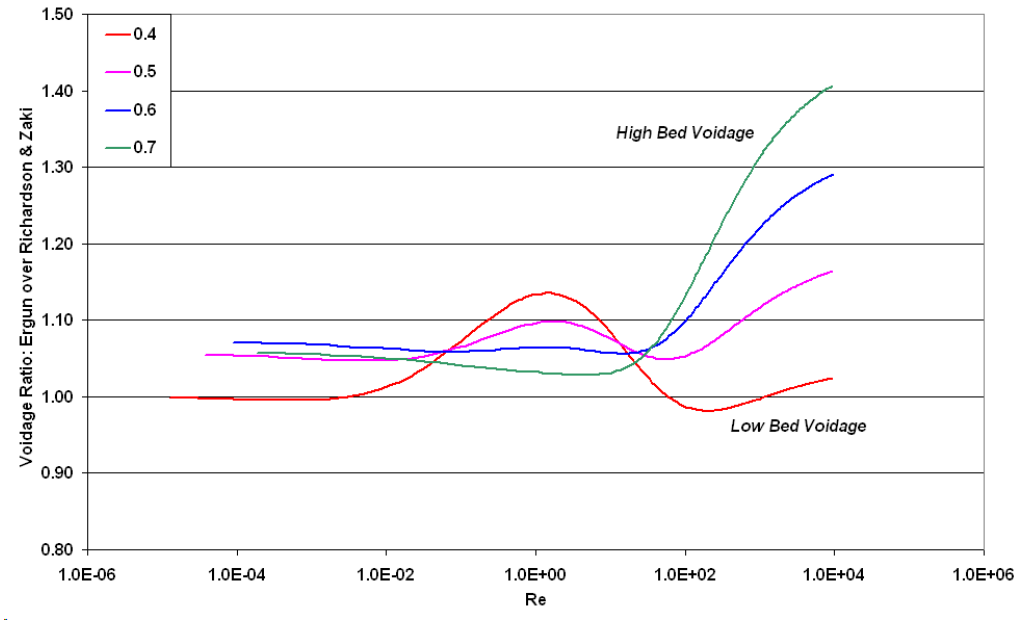

Figure 3.1: Ratio between ε_E and $\varepsilon_{R\&Z}$. The curves are parametric in $\varepsilon_{R\&Z}$.

Figure 3.1 reports the voidage ratio between ε_E and $\varepsilon_{R\&Z}$ as a function of the particle Reynolds number usually employed in multiphase flows theory:

$$Re \equiv \frac{\rho_f}{\mu_f}\,\varepsilon\|\langle\boldsymbol{u}\rangle_f - \langle\boldsymbol{v}\rangle_p\|\,d_p \tag{3.33}$$

The function is parametric in $\varepsilon_{R\&Z}$. As we can clearly see, no curve is constantly equal to one. Good agreement between ε_E and $\varepsilon_{R\&Z}$ is found for a value of the void fraction equal to 0.40 – indeed, the one employed in the original Ergun equation developed for fixed beds – and in the limits of viscous and inertial regimes. Conversely, in the intermediate region a significant deviation of ε_E from $\varepsilon_{R\&Z}$ is observed. This discrepancy is also encountered in all the other curves shown in the chart, which refer to lower values of the powder compaction. This is particularly evident in the inertial regime where, as a general trend, the greater the void fraction of the suspension, the greater the voidage ratio. Such an outcome had to be expected and is explained by the limited range of validity of equation (3.32), which applies only to dense suspensions near their minimum fluidization voidage. In this regard, it is worth pointing out that the Ergun correlation was developed only for *packed beds* and was never meant to account for large variations in powder compaction as those experienced by fluidized emulsions.

In spite of this limitation, equation (3.32) is often used over a wide range of bed void fractions. In the multiphase flow model proposed by Gidaspow (1994), for instance, which is adopted as default in the majority of the commercial CFD codes used nowadays, this correlation is employed for values of the fluid volume fraction up to 0.80.

3.4.4.2 Lewis, Wen & Yu and Kmiec drag force closures

Some other popular constitutive equations are those of Lewis et al. (1949), Wen & Yu (1966) and Kmiec (1982). In particular, the first is the default correlation in most commercial CFD codes when the void fraction of the suspension exceeds the threshold value of 0.80 (limit suggested by Gidaspow, 1994). All three relationships can be put in the form:

$$\beta(\varepsilon, \|\langle\boldsymbol{u}\rangle_f - \langle\boldsymbol{v}\rangle_p\|) = \frac{3}{4}C_D(Re)\frac{\rho_f\|\langle\boldsymbol{u}\rangle_f - \langle\boldsymbol{v}\rangle_p\|(1-\varepsilon)}{d_p}\varepsilon^{-\alpha} \tag{3.34}$$

where $\alpha = 2.65$ for Lewis et al., $\alpha = 2.70$ for Wen & Yu and $\alpha = 2.78$ for Kmiec. Here the particle Reynolds number is defined as per equation (3.33) and the drag coefficient $C_D(Re)$ is calculated using the expression suggested by Schiller & Naumann (1935):

$$C_D(Re) = \begin{cases} \dfrac{24}{Re}\left(1 + 0.15\,Re^{0.687}\right) & \text{for} \quad Re < 1000 \\ 0.44 & \text{for} \quad Re \geqslant 1000 \end{cases} \tag{3.35}$$

Even if these closures are empirical, they are related to the Richardson & Zaki equation, as opposed to equation (3.32). For purely viscous and inertial regimes, equations (3.34) and (3.22) are almost in

perfect agreement. For vanishingly small Reynolds numbers, from equation (3.35), $C_D(Re)$ tends to $24/Re$. Hence, from equations (3.33) and (3.34), it is:

$$\hat{\beta}(\varepsilon, u_s) = \frac{18\mu_f(1-\varepsilon)}{d_p^2\varepsilon^{\alpha+1}} \tag{3.36}$$

In the limit of creeping flow, the Stoke's law applies (Bird et al., 2007):

$$u_t = \frac{(\rho_p - \rho_f)gd_p^2}{18\mu_f} \tag{3.37}$$

and equation (3.36) becomes:

$$\hat{\beta}(\varepsilon, u_s) = \frac{(1-\varepsilon)(\rho_p - \rho_f)g}{u_t\varepsilon^{\alpha+1}} \tag{3.38}$$

By substituting this result into equation (3.28) and solving with respect to u_s, we obtain:

$$u_s = u_t\varepsilon^{\alpha+2} \tag{3.39}$$

This expression coincides with equation (3.22) for α equal to 2.65, 2.70 or 2.80, depending on which limiting value we consider for n_e (4.65, 4.70 and 4.80, respectively). In the first case we obtain the value of α advanced by Lewis et al., in the second that proposed by Wen & Yu and in the third a similar value to the one used by Kmiec. In the inertial limit, $C_D(Re)$ tends to 0.44; thus, from equations (3.33) and (3.34), it is:

$$\hat{\beta}(\varepsilon, u_s) = \frac{\rho_f\|\langle\boldsymbol{u}\rangle_f - \langle\boldsymbol{v}\rangle_p\|(1-\varepsilon)}{3.03d_p\varepsilon^{\alpha}} \tag{3.40}$$

Since, in this instance, the particle terminal velocity is given by (Gibilaro, 2001):

$$u_t = \sqrt{3.03gd_p\frac{\rho_p - \rho_f}{\rho_f}} \tag{3.41}$$

from equation (3.27), it is:

$$\hat{\beta}(\varepsilon, u_s) = \frac{(1-\varepsilon)(\rho_p - \rho_f)gu_s}{u_t^2\varepsilon^{\alpha+1}} \tag{3.42}$$

This relation, replaced into equation (3.28), yields:

$$u_s = u_t\varepsilon^{0.5\alpha+1} \tag{3.43}$$

This coincides with equation (3.22) for α equal to 2.70, 2.78 or 2.80, depending on the limiting value used for n_e (2.35, 2.39 and 2.40, respectively). Again these results are in good agreement

with the values used in equation (3.34) by the three groups of researchers. This confirms the strong link between their closures and the correlation of Richardson & Zaki *in the two limiting regimes hitherto investigated.* These findings might easily lead to the erroneous conclusion that α must be fairly constant also in the other fluid dynamic regimes with a value between 2.65 and 2.80. This is not true. Far from being constant, or even variable in a narrow range, in the intermediate regime α drops significantly, reaching values as low as 1.90 (this is shown in § 3.4.5; in particular, refer to Figures 3.4 and 3.6). Consequently, albeit equation (3.34) is correct in the viscous and inertial limits, it needs to be revised in the intermediate region, where its predictions differ substantially from those of equation (3.22). This discrepancy is clearly shown in Figure 3.2, where, choosing as an example the equation of closure of Wen & Yu, we have reported the voidage ratio as a function of Re parametric in $\varepsilon_{R\&Z}$. As expected, the ratio tends to one only in the limits of very high and very low Reynolds numbers; here the predictions of the constitutive equation are almost in perfect agreement with those of equation (3.22). Conversely, between these two extremes, a considerable discrepancy is observed, with equation (3.34) yielding a far greater bed expansion than that predicted by the Richardson & Zaki correlation. This is particularly true for low values in the bed voidage, a fact that should make us restrict, as suggested by Gidaspow (1994), the employability of these closures only to situations involving diluted systems with void fractions higher than 0.80.

To extend the range of validity of equation (3.34) to any fluid dynamic regime and any possible value of the suspension void fraction, we need to replace the constant exponent α with a variable exponent whose arguments and functional expression are still to be determined. This is what we intend to do in the remaining part of this study.

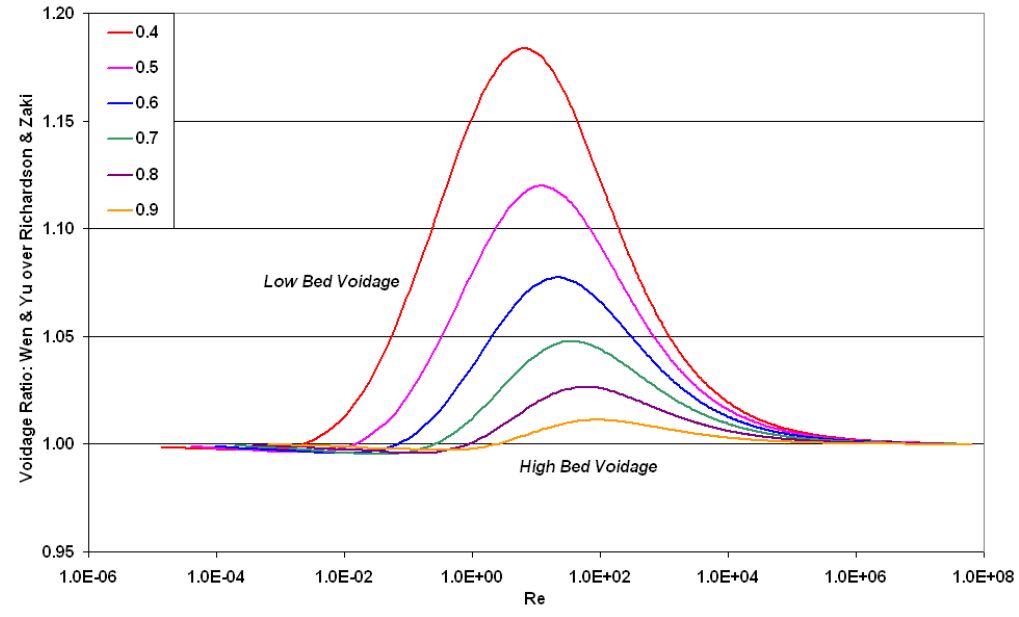

Figure 3.2: Ratio between $\varepsilon_{W\&Y}$ and $\varepsilon_{R\&Z}$. The curves are parametric in $\varepsilon_{R\&Z}$.

3.4.4.3 Di Felice drag force closure

Recognizing the variability of α, Di Felice (1994) proposed the empirical relation:

$$\hat{\alpha}_d(Re) = 3.7 - 0.65 \exp\left[-\frac{1}{2}(1.5 - \log_{10} Re)^2\right] \tag{3.44}$$

Since his closure is in terms of superficial fluid velocity, and not of fluid-particle slip velocity, $\hat{\alpha}_d(Re)$ cannot be directly compared with α. To show how this velocity choice affects the exponent value, we combine equations (3.18) and (3.34) by writing:

$$n\langle \boldsymbol{f}_d \rangle_p = \left[\frac{3}{4} C_D(Re) \frac{\rho_f \|\langle \boldsymbol{u} \rangle_f - \langle \boldsymbol{v} \rangle_p\| (1-\varepsilon)}{d_p} \varepsilon^{-\alpha}\right] (\langle \boldsymbol{u} \rangle_f - \langle \boldsymbol{v} \rangle_p) \tag{3.45}$$

Then, using equation (3.27), we replace the fluid-particle slip velocity with the superficial velocity of the fluid. Doing so yields:

$$n\langle \boldsymbol{f}_d \rangle_p = \left[\frac{3}{4} C_D(Re) \frac{\rho_f u_s (1-\varepsilon)}{d_p} \varepsilon^{-(\alpha+2)}\right] \boldsymbol{u}_s \tag{3.46}$$

Therefore, the value of α that refers to u_s is obtained by adding two to the exponent that refers to $\|\langle \boldsymbol{u} \rangle_f - \langle \boldsymbol{v} \rangle_p\|$. Consequently, to render $\hat{\alpha}_d(Re)$ comparable to α, we must replace the constant 3.7 in equation (3.44) with 1.7. The revised expression is:

$$\tilde{\alpha}_d(Re) = 1.7 - 0.65 \exp\left[-\frac{1}{2}(1.5 - \log_{10} Re)^2\right] \tag{3.47}$$

This exponent still cannot be used in equation (3.34), because Di Felice adopts a different definition of buoyancy force, equation (3.6). To obtain an expression for α consistent with our definition of buoyancy force, we must use equation (3.19). The final result is:

$$\alpha_d(Re) = 2.7 - 0.65 \exp\left[-\frac{1}{2}(1.5 - \log_{10} Re)^2\right] \tag{3.48}$$

For very low and very high values of Re, the exponent tends to 2.7, coinciding with the value of α used by Wen & Yu. Even so, in the intermediate regime $\alpha_d(Re)$ drops significantly, reaching a minimum value of about 2.1 in correspondence of a value of Re of roughly 28.

Figure 3.3 shows how the introduction of the variable exponent $\alpha_d(Re)$ affects the predictions of equation (3.34). The deviation of the voidage ratio from unity is substantially reduced compared with the values reported in Figure 3.2. The correction in particular works most effectively for the lowest values of the voidage, for which the original equations proposed by Lewis et al., Wen & Yu and Kmiec proved particularly approximate. Albeit dampened, however, the deviation does not vanish; for $\varepsilon = 0.40$, for instance, it is reduced more or less to the same values previously found in Figure 3.1, where the Ergun equation of closure was used.

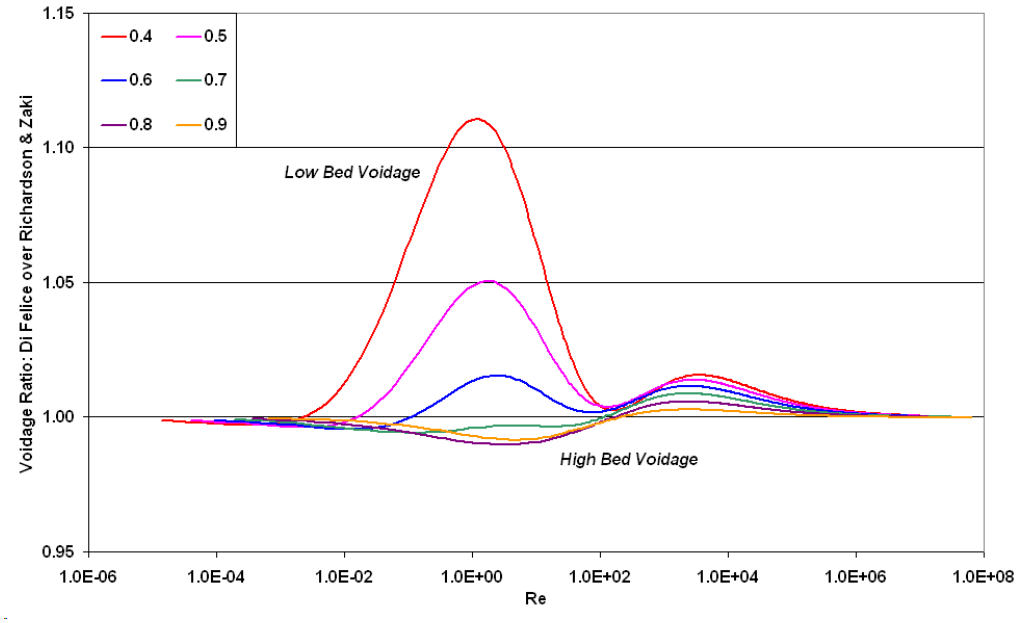

Figure 3.3: Ratio between ε_D and $\varepsilon_{R\&Z}$. The curves are parametric in $\varepsilon_{R\&Z}$.

This analysis has shown that all the closures hitherto examined are not fully consistent with the correlation of Richardson & Zaki. Some are accurate only in specific fluid dynamic regimes (most of the time, that purely viscous or that purely inertial), others only for some values of the suspension void fraction (usually for very compact or very diluted emulsions). In the next section, we develop a closure of general validity, entirely based on equations (3.22) and (3.24) and therefore consistent with them for any fluid dynamic regime and void fraction. Such correlation does not require, in addition to the equations just mentioned, any other empirical information.

3.4.5 A new equation of closure for the drag force

Let us consider the steady-state upward flow of an incompressible, isothermal Newtonian fluid around a single motionless particle. Since the particle is in equilibrium, a simple force balance yields:

$$\boldsymbol{f}_d = -\frac{\pi}{6} d_p^3 (\rho_p - \rho_f) \boldsymbol{g} \tag{3.49}$$

where $\boldsymbol{f}_d$ is the drag force exerted by the fluid on the particle. Consider now the same particle as part of a homogeneous assembly of identical particles in equilibrium within the same upflowing stream. Also in this case, the drag force must counterbalance the effective weight of the body. So, if we show that this last force is not affected by the presence of the surrounding solid – that is, it does not change in magnitude when passing from the former situation to the one currently examined – we will also have proved that the same is true for the drag force. The effective weight is the difference between the real weight of the body and the buoyancy force acting on it. The former, of course, is not influenced

by the presence of the other particles; the latter is constant *by definition* and also remains unvaried. We have therefore proved our point. This result is very welcome, as it allows us to use the empirical correlations for single unhindered bodies in pure fluids.

The starting point in the derivation of our constitutive equation is the definition of particle terminal drag coefficient (Bird et al., 2007):

$$C_D^t \equiv \|\boldsymbol{f}_d\| \left[\left(\frac{\pi}{4} d_p^2 \right) \left(\frac{1}{2} \rho_f u_t^2 \right) \right]^{-1} \tag{3.50}$$

The coefficient is a function of the free fall particle Reynolds number formerly defined in equation (3.23). This dependence is well described by several empirical correlations; here, we opt for that of Dallavalle (1948), which we favour for its continuous form:

$$C_D^t(Re_t) = \left(0.63 + 4.8 Re_t^{-1/2} \right)^2 \tag{3.51}$$

Equations (3.50) and (3.51) permit to calculate the drag force magnitude, once the physical properties of the system are known. Our intent, though, is not relating the force to the particle terminal velocity, but is finding its dependence on the suspension void fraction and the fluid-particle slip velocity. To this end, we use the correlation of Richardson & Zaki. Introducing equations (3.22), (3.23) and (3.27) into equations (3.50) and (3.51) yields:

$$\|\boldsymbol{f}_d\| = \left(\frac{\pi}{4} d_p^2 \right) \left[\frac{1}{2} \rho_f \left(\frac{\|\langle \boldsymbol{u} \rangle_f - \langle \boldsymbol{v} \rangle_p\|}{\varepsilon^{n_e - 1}} \right)^2 \right] C_D^*(Re^*) \tag{3.52}$$

where, by definition, it is:

$$Re^* \equiv \frac{\rho_f}{\mu_f} \frac{\|\langle \boldsymbol{u} \rangle_f - \langle \boldsymbol{v} \rangle_p\|}{\varepsilon^{n_e - 1}} d_p = \frac{Re}{\varepsilon^{n_e}} \tag{3.53}$$

and where $C_D^*(Re^*)$ and $n_e(Re^*)$ are given by:

$$C_D^*(Re^*) = \left(0.63 + 4.8 Re^{*\,-1/2} \right)^2 \quad ; \quad n_e(Re^*) = \frac{4.8 + 2.4 \cdot 0.175 Re^{*3/4}}{1 + 0.175 Re^{*3/4}} \tag{3.54}$$

In multiphase flows theory, it is customary to use the particle Reynolds number defined as per equation (3.33) and a drag coefficient computed accordingly; in our case, we then write:

$$C_D(Re) = \left(0.63 + 4.8 Re^{-1/2} \right)^2 \tag{3.55}$$

Conforming to such a practice, we express equation (3.52) in terms of these adimensional quantities. By multiplying and dividing the equation by $C_D(Re)$, we obtain:

$$\|\boldsymbol{f}_d\| = \left[\left(\frac{\pi}{4} d_p^2 \right) \left(\frac{1}{2} \rho_f \|\langle \boldsymbol{u} \rangle_f - \langle \boldsymbol{v} \rangle_p\|^2 \right) C_D(Re) \right] \varphi(\varepsilon, Re) \tag{3.56}$$

where, regarding C_D^* as a function of Re and ε, it is:

$$\varphi(\varepsilon, Re) \equiv \frac{\hat{C}_D^*(\varepsilon, Re)}{C_D(Re)}\,\varepsilon^{2(1-n_e)} \tag{3.57}$$

If in equation (3.56) $\varphi(\varepsilon, Re)$ were neglected, the drag force would be somewhat underestimated; this is because the averaged fluid-particle slip velocity employed in equation (3.56) is far less than the particle terminal velocity, which, as we have seen, should be used when calculating $\|\boldsymbol{f}_d\|$. Thus, $\varphi(\varepsilon, Re)$ can be interpreted as a *corrective function* that makes up for the difference between the underrated value of the drag magnitude and its actual value.

Since the drag force is by definition parallel to the fluid-particle slip velocity, equation (3.56) can be rearranged as follows:

$$\boldsymbol{f}_d = \left[\left(\frac{\pi}{4}d_p^2\right)\left(\frac{1}{2}\rho_f\|\langle\boldsymbol{u}\rangle_f - \langle\boldsymbol{v}\rangle_p\|\right)C_D(Re)\varphi(\varepsilon, Re)\right](\langle\boldsymbol{u}\rangle_f - \langle\boldsymbol{v}\rangle_p) \tag{3.58}$$

The locally averaged value of $\boldsymbol{f}_d$ can be readily computed by applying the definition of particle phase average, equation (2.18), given in Chapter 2. Since the dispersion is homogeneous, $\boldsymbol{f}_d$ does not vary from particle to particle; accordingly, it is:

$$n\langle\boldsymbol{f}_d\rangle_p = \sum_{\mathscr{F}}\left[\psi(\|\boldsymbol{x} - \boldsymbol{x}^p\|)\,\boldsymbol{f}_d\right] = \boldsymbol{f}_d\sum_{\mathscr{F}}\psi(\|\boldsymbol{x} - \boldsymbol{x}^p\|) = n\,\boldsymbol{f}_d \tag{3.59}$$

where the definition of particle number density, equation (2.16), has been employed. If we now use the approximated relationship:

$$n \approx \frac{6(1-\varepsilon)}{\pi d_p^3} \tag{3.60}$$

previously discussed in §2.4.5 of Chapter 2 and formally demonstrated in §A.1 of Appendix A, from equations (3.18), (3.58) and (3.59), we finally obtain the closure:

$$\beta(\varepsilon, \|\langle\boldsymbol{u}\rangle_f - \langle\boldsymbol{v}\rangle_p\|) = \frac{3}{4}C_D(Re)\frac{\rho_f\|\langle\boldsymbol{u}\rangle_f - \langle\boldsymbol{v}\rangle_p\|(1-\varepsilon)}{d_p}\varphi(\varepsilon, Re) \tag{3.61}$$

This result confirms the initial assumption regarding the functional dependence of the coefficient on the suspension void fraction and on the magnitude of the fluid-particle slip velocity, in addition to the physical properties of the fluid and to the particle diameter. Equation (3.61) strongly resembles the closures of Lewis et al., Wen & Yu, Kmiec and Di Felice; the only difference resides in the expression of $\varphi(\varepsilon, Re)$. The first three groups of researchers take it to be an exponential of the bed voidage whose exponent α is constant and equal to 2.65, 2.70 and 2.78, respectively.

$$\varphi(\varepsilon, Re) = \varepsilon^{-\alpha} \quad ; \quad \begin{cases} \alpha = 2.65 & \text{for} \quad \text{Lewis et al. (1949)} \\ \alpha = 2.70 & \text{for} \quad \text{Wen \& Yu (1966)} \\ \alpha = 2.78 & \text{for} \quad \text{Kmiec (1982)} \end{cases} \tag{3.62}$$

Di Felice, on the other hand, still assuming the corrective function to be an exponential of the void fraction, suggests a dependence of its exponent on the particle Reynolds number.

$$\varphi(\varepsilon, Re) = \varepsilon^{-\alpha_d(Re)} \quad ; \quad \alpha_d(Re) = 2.7 - 0.65 \exp\left[-\frac{1}{2}(1.5 - \log_{10} Re)^2\right] \tag{3.63}$$

However, as equation (3.57) shows, $\varphi(\varepsilon, Re)$ is not an exponential of ε, but a more complex function of both Re and ε.

To simplify the analysis and compare more effectively our equation of closure to the others, it is convenient to define the function:

$$\psi_e(\varepsilon, Re) \equiv -\frac{\ln \varphi(\varepsilon, Re)}{\ln \varepsilon} \tag{3.64}$$

and rewrite equation (3.61) as:

$$\beta(\varepsilon, \|\langle \boldsymbol{u} \rangle_f - \langle \boldsymbol{v} \rangle_p\|) = \frac{3}{4} C_D(Re) \frac{\rho_f \|\langle \boldsymbol{u} \rangle_f - \langle \boldsymbol{v} \rangle_p\| (1-\varepsilon)}{d_p} \varepsilon^{-\psi_e(\varepsilon, Re)} \tag{3.65}$$

For creeping flows, equations (3.54) and (3.55) give:

$$\lim_{Re \to 0} C_D(Re) = \frac{4.8^2}{Re} \quad ; \quad \lim_{Re \to 0} \hat{C}_D^*(\varepsilon, Re) = \frac{4.8^2}{Re^*(\varepsilon, Re)} \tag{3.66}$$

whence, from equations (3.53) and (3.57), we obtain:

$$\lim_{Re \to 0} \varphi(\varepsilon, Re) = \frac{Re}{Re^*(\varepsilon, Re)} \varepsilon^{2(1-n_e)} = \varepsilon^{2-n_e} \tag{3.67}$$

For vanishingly small Reynolds numbers, n_e tends to 4.80, and equation (3.67) yields:

$$\lim_{Re \to 0} \varphi(\varepsilon, Re) = \varepsilon^{-2.80} \quad \Rightarrow \quad \lim_{Re \to 0} \psi_e(\varepsilon, Re) = 2.80 \tag{3.68}$$

Similarly, for turbulent flows, it is:

$$\lim_{Re \to \infty} C_D(Re) = 0.63^2 \quad ; \quad \lim_{Re \to \infty} \hat{C}_D^*(\varepsilon, Re) = 0.63^2 \tag{3.69}$$

Thus, equation (3.57) reduces to:

$$\lim_{Re \to \infty} \varphi(\varepsilon, Re) = \varepsilon^{2(1-n_e)} \tag{3.70}$$

Since in this regime n_e tends to 2.40, equation (3.70) gives:

$$\lim_{Re \to \infty} \varphi(\varepsilon, Re) = \varepsilon^{-2.80} \quad \Rightarrow \quad \lim_{Re \to \infty} \psi_e(\varepsilon, Re) = 2.80 \tag{3.71}$$

We conclude that in these limits $\psi_e(\varepsilon, Re)$ tends to the same value. This value is very similar to that

assumed by $\alpha_d(Re)$ in the same limits and to those used in equation (3.34) by Lewis et al., Wen & Yu and Kmiec. *In the two extremes hitherto considered* all the equations of closure examined are therefore essentially equivalent. As we shall presently see, we cannot extend this property to the intermediate fluid dynamic region; here the differences are no longer negligible.

It is now convenient to report the diagram of $\psi_e(\varepsilon, Re)$ as a function of Re parametric in ε. This is done in Figure 3.4, where some experimental values of the exponent are also presented; their discussion is for now postponed. Albeit in the extremes of purely viscous and purely inertial regimes $\psi_e(\varepsilon, Re)$ is constant, in the intermediate region it drops significantly reaching values as low as 1.90. Furthermore, the exponent does not depend solely on the particle Reynolds number, since a strong dependence is also found on the suspension void fraction. Thus, the minimum value of $\psi_e(\varepsilon, Re)$ is not uniquely defined (as it was in the correlation advanced by Di Felice) but results to be an increasing function of ε varying roughly between 1.90 and 2.30.

Also in this case we compare the bed expansion predictions obtained from the drag force closure with those yielded by the Richardson & Zaki correlation. To do so, we calculate the voidage ratio between the equilibrium void fraction $\varepsilon_{M\&L}$, obtained by solving equation (3.28) in conjunction with equation (3.65), and that predicted by equations (3.22) and (3.24). This, as usual, is reported as a function of Re parametric in $\varepsilon_{R\&Z}$. In Figure 3.5, the ratio is constantly equal to one over the whole range of fluid dynamic regimes and for any value of the bed void fraction. This had to be expected, since equation (3.65) is entirely based on the Richardson & Zaki correlation.

In order to test the validity of equation (3.65), its predictions are compared with experimental results obtained for homogeneous suspensions of monodisperse spherical particles available in the

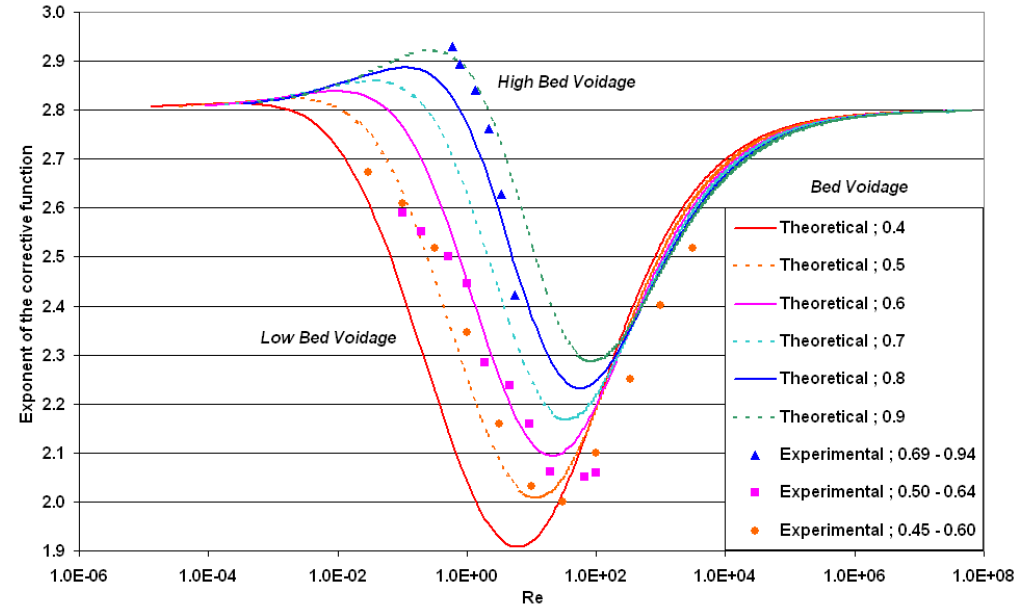

Figure 3.4: Comparison between theoretical and experimental values of the exponent $\psi_e(\varepsilon, Re)$. The empirical data are of Happel & Epstein (1954) and Rumpf & Gupte (1971).

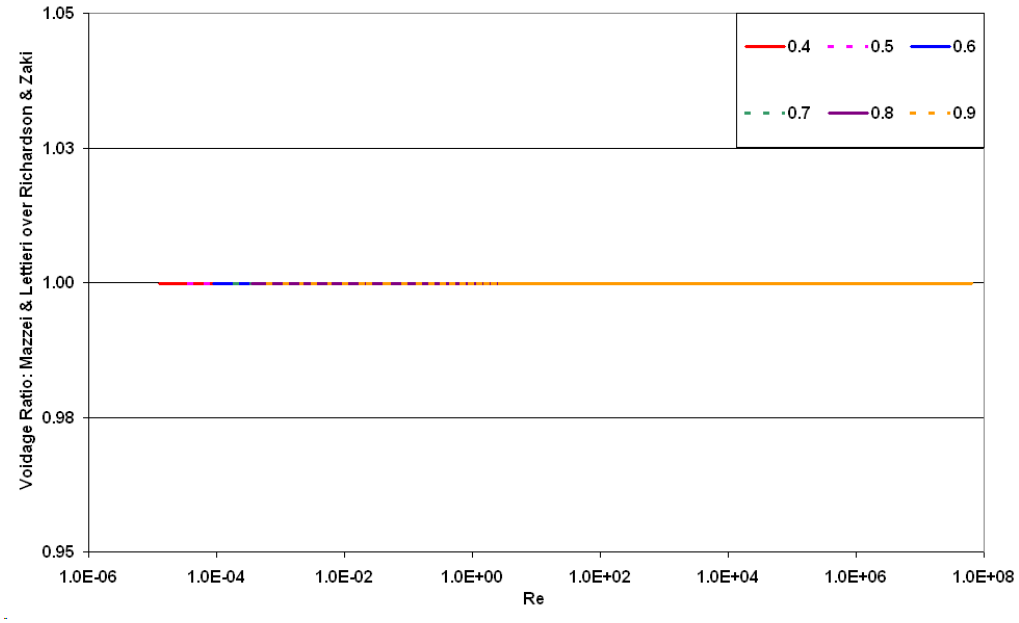

Figure 3.5: Ratio between $\varepsilon_{M\&L}$ and $\varepsilon_{R\&Z}$. The curves are parametric in $\varepsilon_{R\&Z}$.

literature and spanning a broad range of fluid dynamic conditions and bed void fractions. As these data are usually reported in terms of unrecoverable pressure drop as a function of the particle Reynolds number and of the bed voidage, to carry out a comparison we operate as follows. For a generic value of Re and ε, we use the experimental measurement of the unrecoverable pressure drop to evaluate the corresponding value of the drag force magnitude. This can be easily done by resorting to the equation of conservation of the linear momentum written for the fluid phase and referred to homogeneous suspensions in fluid dynamic equilibrium:

$$n\langle \boldsymbol{f}_d \rangle_p = -\boldsymbol{\nabla}\langle p \rangle_f + \rho_f \boldsymbol{g} = -\boldsymbol{\nabla}\langle \mathscr{P} \rangle_f \tag{3.72}$$

Here $\langle \mathscr{P} \rangle_f(\boldsymbol{x}, t)$ denotes the *modified pressure* whose gradient directly provides the unrecoverable pressure drop through the system. This is defined as follows (Batchelor, 1967):

$$\langle \mathscr{P} \rangle_f \equiv \langle p \rangle_f + \rho_f g h \tag{3.73}$$

where h is the *upward distance*, *i.e.*, the distance in the direction opposed to gravity, of the point under consideration from a horizontal reference plane arbitrarily chosen. After determining the drag force magnitude, we calculate, from equations (3.18) and (3.65), the empirical value of $\psi_e(\varepsilon, Re)$ and we compare it with the theoretical one obtained from equations (3.57) and (3.64). The results are shown in Figure 3.4. The experimental data are of Happel & Epstein (1954) and Rumpf & Gupte (1971). By adopting ingenious methods, these groups of researchers measured the unrecoverable pressure drop for uniform assemblies of spherical particles of identical size over a wide range of Reynolds numbers and for void fractions up to the value of 0.94.

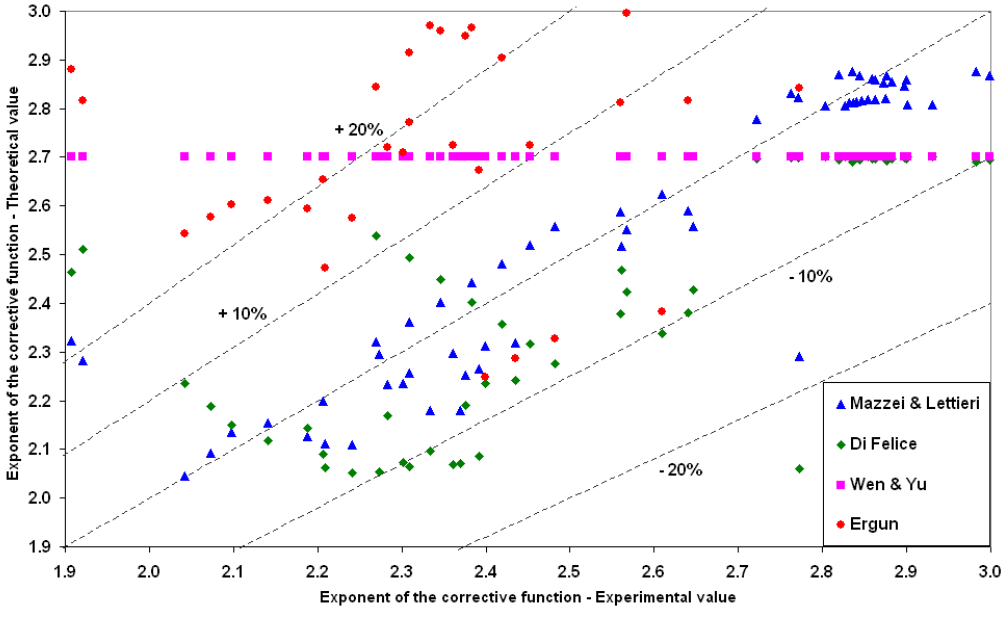

Figure 3.6: Comparison between theoretical and experimental values of the exponent $\psi_e(\varepsilon, Re)$. The empirical data are of Richardson & Zaki (1954) and Wilhelm & Kwauk (1948).

To complete the analysis, the predictions of equation (3.65) are also compared with those of the other constitutive equations previously examined. Once again, we refer to $\psi_e(\varepsilon, Re)$. For the Ergun closure, equation (3.32), an *equivalent exponent* is calculated by equating equation (3.32) to equation (3.65) and finding the value of $\psi_e(\varepsilon, Re)$ which satisfies the equality. In Figure 3.6, theoretical and experimental values of $\psi_e(\varepsilon, Re)$ are compared. The latter were derived from the empirical data of Richardson & Zaki (1954) and Wilhelm & Kwauk (1948) regarding the sedimentation and fluidization of homogeneous systems of identical particles.

In Figures 3.4 and 3.6, good agreement is found between the experimental values of $\psi_e(\varepsilon, Re)$ and those predicted by equation (3.65). In Figure 3.6, whereas equation (3.65) gives an error within $\pm 10\%$, the other closures are often less accurate, especially those of Ergun and Wen & Yu. The diagrams clearly show the variability of the exponent with the particle Reynolds number and bed voidage. This dependence, entirely or partially neglected in the other equations of closure, should be properly accounted for to ensure a good assessment of the drag force magnitude and an accurate prediction of the bed expansion of homogeneous non-cohesive powders. These requirements are now fulfilled by the equation of closure developed in this study.

3.5 Elastic force analysis

Heretofore, we have intentionally confined our attention to homogeneous fluidized suspensions. Their simple structure renders the particulate fluidization state the easiest to investigate. In general, though, the dynamics of fluidized powders is much more varied and complex. Many systems initially display

homogeneous behaviour, with the particles floating, most of the time, around nearly-fixed positions. If the fluid flow rate is increased sufficiently, however, the formation of large voids, called *bubbles*, is detected; these contain a much smaller concentration of particles than the bulk of the bed and, by rising through the latter, disrupt the uniform structure previously observed.

Homogeneous fluidization promotes intimate contact between the fluid and the particles, a most attractive feature in processes where uniform conditions are desirable. In other applications, solid mixing is to be emphasized, along with mass and heat transfer; these are induced by bubbling, which stirs the solid within the bed. Whichever the case, we are interested to know, with a reasonable degree of accuracy, in which regime a system with assigned physical properties will operate for any given set of operating conditions.

The transition from particulate to aggregative fluidization has been, for many decades, object of investigation. The phenomenon, deemed to result from fluid dynamic instabilities, is still nowadays incompletely understood. This lack of insight hampers the design of fluidized systems and compels much conservative safety margins to be employed. The majority of the theoretical studies regarding the stability of homogenous dispersions was carried out analytically, without the aid of computational tools. This is not surprising, if we think that decades ago the computing power of personal computers was much less than it is today. Some researchers ascribed the stability of uniform suspensions to the effect of interparticle forces (Massimilla et al., 1972; Mutsers & Rietema, 1977; Rietema & Piepers, 1990), whereas others sought for a purely fluid dynamical explanation (Jackson, 1963; Murray, 1965; Pigford & Baron, 1965; Verloop & Heertjes, 1970). The first approach failed to yield quantitative results; this major shortcoming might explain why the second approach has undergone much more development. The method adopted in this instance was usually that of linear stability analysis. The equations of motion were first written monodimensionally and then linearized; finally, the stability of the system, when subjected to small perturbations, was examined. The hope was to find formal stability for sufficiently low values of the fluid flux and instability for values greater than a certain, well-defined threshold limit. But this expectation was not met: the homogeneous state resulted to be intrinsically unstable, this being true even if, in addition to the buoyancy and drag forces, the other contributions previously discussed – that is, virtual mass force, lift force and the like – are taken into account in the interaction force between the phases.

Some researchers, see for instance Jackson (2000), accepted this conclusion, putting forward the following explanation: homogeneous beds do not exist *formally* – that is, in a mathematical sense; however, what really counts is the *rate of growth* of the disturbances within the bed. In liquid-fluidized systems the rate is always very contained, so that disturbances develop so slowly that the status of visible bubbles is never attained. The suspension, although formally unstable, appears to be uniform. In systems fluidized by gases, conversely, the rate of growth is such that disturbances swiftly reach detectable size, even in shallow beds.

Some scientists, here we mention Foscolo & Gibilaro (1987) but other could be cited, found this explanation quite wanting. They maintained that several fluidized systems display an indisputable

homogeneous behaviour, which equations of motion of sufficient accuracy should be able to predict. This led Foscolo & Gibilaro to the introduction of a new force, the *elastic force*, whose origin is purely hydrodynamical and based on rather simple physical considerations (further details can be found in Gibilaro, 2001). The force takes the form:

$$n\langle \boldsymbol{f}_e \rangle_p = E_f(\varepsilon)(\boldsymbol{\nabla}\varepsilon \cdot \boldsymbol{e})\boldsymbol{e} \tag{3.74}$$

where $\boldsymbol{e}$ is a unit vector parallel and opposite to the gravitational field and $E_f(\varepsilon)$ is a positive scalar, named *elastic modulus*, that is equal to:

$$E_f(\varepsilon) = 3.2 d_p (1-\varepsilon)(\rho_p - \rho_f) g \tag{3.75}$$

If this additional contribution is included in the interaction force between the fluid and the particles, the application of linear stability analysis results in a fairly straightforward analytical criterion for discriminating between stable and unstable fluidization: the particulate regime is stable as long as the stability function reported below is negative.

$$S_f(\varepsilon) = 1 - \left(\frac{3.2}{n_e^2} \cdot \frac{d_p g}{u_t^2} \cdot \frac{\rho_p - \rho_f}{\rho_p} \cdot \frac{\varepsilon^{2(1-n_e)}}{1-\varepsilon} \right)^{1/2} \tag{3.76}$$

The loss of stability was interpreted by Foscolo & Gibilaro as the onset of bubbling; in this view, the minimum bubbling voidage coincides with the zero of the stability function. To Jackson (2000) and other researchers, this conclusion seemed quite far-fetched: loss of formal stability merely indicates that small disturbances no longer dampen out; they might, however, grow so slowly as to never really turn into visible bubbles. In this case, the system would continue to *appear* perfectly stable.

We address this issue in the next chapter, where we investigate the dynamics and stability of uniform fluidized suspensions. In the final part of this chapter, we instead develop a new equation of closure for the elastic force based on our drag force constitutive equation. To do so, we use a rigourous approach, which, as opposed to the original analysis of Foscolo & Gibilaro (1987), does not resort to equilibrium-based relations; hence, the result is enhanced in accuracy and breadth of validity. We first review the Foscolo & Gibilaro (1987) elastic force closure. Then, we report the closure of Jean & Fan (1992), which modifies the original expression. Finally, we develop our own constitutive equation. The three equations are compared and validated in Chapter 4.

3.5.1 Limitations of equilibrium drag force closures

In the following, to simplify the mathematics, we restrict the treatment to one-dimensional systems. Generalization of the results to the three-dimensional case is straightforward. The independent spatial variable $\boldsymbol{x}$ is thus replaced with the scalar variable x denoting the axial coordinate in the upward vertical direction; more generally, any vector is replaced with its scalar component in the direction of the unit vector $\boldsymbol{e}$ previously defined.

The drag force constitutive equations considered in § 3.4 are valid only for uniform fluidization. This is because to derive them we have used equilibrium relations, such as the Richardson & Zaki (1954) equation. Thus, using them in unsteady-state regimes is questionable.

Before proceeding, to preserve generality, it is convenient to express these closures by means of a generic mathematical function; thus, we write:

$$\langle f_d \rangle_p^e(x,t) = F\big[u_s(t) - \langle v \rangle_p(x,t), \varepsilon(x,t)\big] \tag{3.77}$$

This function relates the *equilibrium drag force* per unit particle to the superficial velocity of the fluid relative to the particles and to the suspension void fraction. In equation (3.77), $u_s(t)$ and $\langle v \rangle_p(x,t)$ are not independent, but have to satisfy the Richardson & Zaki (1954) equation:

$$u_s - \langle v \rangle_p = u_t \varepsilon^{n_e} \tag{3.78}$$

This equation is usually written with respect to an observer at rest relative to the particles; here, however, it is convenient to adopt the more general formulation given above. In the last two equations, $u_s(t) - \langle v \rangle_p(x,t)$ could be replaced with the slip velocity between the phases, since it is:

$$u_s - \langle v \rangle_p = \varepsilon(\langle u \rangle_f - \langle v \rangle_p) \tag{3.79}$$

This relation is obtained by summing the averaged continuity equations of both Eulerian phases. These are reported in Table 2.1 of Chapter 2. For one-dimensional systems, doing so yields:

$$\frac{\partial}{\partial x}\Big[\varepsilon \langle u \rangle_f + (1-\varepsilon)\langle v \rangle_p\Big] = 0 \quad \Rightarrow \quad \varepsilon \langle u \rangle_f + (1-\varepsilon)\langle v \rangle_p = \text{constant} \tag{3.80}$$

whence equation (3.79) immediately ensues, since the total flux through the bed (*i.e.*, the integration constant) must be equal to that of the fluid entering the bed.

A simple way of overcoming the closure problem just mentioned consists in extending the validity of equation (3.77) to the case of unsteady-state regimes by simply breaking the equilibrium bond represented by equation (3.78). Thus, we would write:

$$\langle f_d \rangle_p^d(x,t) = F\big[u_s(t) - \langle v \rangle_p(x,t), \varepsilon(x,t)\big] \tag{3.81}$$

which expresses the *dynamic drag force* by means of the same constitutive function used in equation (3.77), where $u_s(t)$ and $\langle v \rangle_p(x,t)$ are now to be intended as independent variables.

Although attractive for its straightforwardness, this solution does not guarantee that all the physics necessary to fully characterize unsteady-state systems is captured: some features might be completely lost in the extended constitutive equation (3.81). A safer approach consists in determining what is distinctive of such unsteady systems and ensuring that these aspects be properly accounted for in the dynamic counterpart of equation (3.77).

3.5.2 Foscolo & Gibilaro elastic force

Foscolo & Gibilaro (1987) endeavoured to do so. Their analysis led to the *Particle Bed Model* (PBM), in which they argue that in dynamic conditions the functional dependence of both drag force and effective weight on the bed voidage has to be revised to account for the *elasticity* of the disperse phase, a feature of the system that becomes apparent only in transient conditions when axial voidage gradients are generated. Their assumption can be rendered as follows:

$$\text{steady-state conditions:} \qquad \langle\Phi\rangle_p^e(x,t) = G\big[u_s(t) - \langle v\rangle_p(x,t), \varepsilon(x,t)\big] \tag{3.82}$$

$$\text{unsteady-state conditions:} \qquad \langle\Phi\rangle_p^d(x,t) = G\big[u_s(t) - \langle v\rangle_p(x,t), \tilde{\varepsilon}(x,t)\big] \tag{3.83}$$

where $\langle\Phi\rangle_p^e(x,t)$ and $\langle\Phi\rangle_p^d(x,t)$ are the net forces – drag force plus effective weight – acting on a single particle in steady and unsteady-state conditions, respectively, $G(u_s - \langle v\rangle_p, \varepsilon)$ is a constitutive function and $\tilde{\varepsilon}(x,t)$ is an *effective bed voidage* defined as:

$$\tilde{\varepsilon}(x,t) \equiv \varepsilon(x-\theta,t) \tag{3.84}$$

with θ being a *penetration distance* proportional to the particle diameter:

$$\theta \equiv \frac{2}{3} d_p \tag{3.85}$$

The separation of scales hypothesis guarantees that θ is much smaller than the macroscopic length scale over which the averaged fluid dynamic variables vary appreciably. Thus, it is:

$$\tilde{\varepsilon}(x,t) \approx \varepsilon(x,t) - \frac{\partial\varepsilon}{\partial x}(x,t)\theta \tag{3.86}$$

Following Foscolo & Gibilaro, the difference between $\langle\Phi\rangle_p^d(x,t)$ and $\langle\Phi\rangle_p^e(x,t)$ is defined to be the *elastic force*; per unit volume of suspension, we can therefore write:

$$n\langle f_e\rangle_p \equiv n\langle\Phi\rangle_p^d - n\langle\Phi\rangle_p^e \tag{3.87}$$

The approximate relation (3.86) allows rearranging this equation in the more convenient form:

$$n\langle f_e\rangle_p(x,t) = E_f\big[u_s(t) - \langle v\rangle_p(x,t), \varepsilon(x,t)\big]\frac{\partial\varepsilon}{\partial x}(x,t) \tag{3.88}$$

where the *elastic modulus* of the dispersion is:

$$E_f \equiv -\frac{4(1-\varepsilon)}{\pi d_p^2}\left(\frac{\partial G}{\partial\varepsilon}\right)_{u_s - \langle v\rangle_p} \tag{3.89}$$

This mathematical notation emphasizes that the partial derivative must be computed while keeping the

independent variable $u_s - \langle v \rangle_p$ constant. A quantitative expression for the elastic force can be obtained if a suitable constitutive equation for $G(u_s - \langle v \rangle_p, \varepsilon)$ is supplied. Foscolo & Gibilaro adopted the following relation, based on the buoyancy force definition (3.6):

$$G = \frac{\pi d_p^3}{6}\left[-\frac{\partial \langle p \rangle_f}{\partial x} - \rho_p g + \frac{(\rho_p - \rho_f)g}{\varepsilon^{3.8}}\left(\frac{u_s - \langle v \rangle_p}{u_t}\right)^{4.8/n_e}\right] \tag{3.90}$$

Deriving this function with respect to ε is not simple, for we must know the functional dependence of the pressure gradient on the variables $u_s - \langle v \rangle_p$ and ε. To overcome the problem, Foscolo & Gibilaro approximated the gradient with its equilibrium expression, equation (3.9):

$$-\frac{\partial \langle p \rangle_f}{\partial x} \approx \left[\varepsilon \rho_f + (1-\varepsilon)\rho_p\right] g \tag{3.91}$$

thus replacing equation (3.90) with:

$$G = \frac{\pi d_p^3}{6}\frac{(\rho_p - \rho_f)g}{\varepsilon^{3.8}}\left[-\varepsilon^{4.8} + \left(\frac{u_s - \langle v \rangle_p}{u_t}\right)^{4.8/n_e}\right] \tag{3.92}$$

Furthermore, *after* deriving function (3.92), they used the Richardson & Zaki equilibrium relation, equation (3.78), making the approximation:

$$\varepsilon^{4.8} \approx \left(\frac{u_s - \langle v \rangle_p}{u_t}\right)^{4.8/n_e} \tag{3.93}$$

which led them to the expression of the elastic modulus given in equation (3.75). Note that $E_f(\varepsilon)$ is a function of the sole bed voidage: no dependence is found on $u_s - \langle v \rangle_p$. This dependence is lost, since the equilibrium equation (3.78) turns the variable into a function of the void fraction.

3.5.3 Jean & Fan elastic force

In the revised formulation of the monodimensional PBM proposed by Jean & Fan (1992), a new expression for the elastic modulus was developed. The modification merely consisted in replacing equation (3.90) with an equivalent expression consistent with the classical definition of buoyancy force, equation (3.4). The new constitutive equation becomes:

$$G = \frac{\pi d_p^3}{6}\frac{(\rho_p - \rho_f)g}{\varepsilon^{4.8}}\left[-\varepsilon^{4.8} + \left(\frac{u_s - \langle v \rangle_p}{u_t}\right)^{4.8/n_e}\right] \tag{3.94}$$

Note that this relation is not an approximation derived from the equilibrium condition (3.91): the approximation is no longer needed insomuch as the classical definition of buoyancy force is adopted. Following the same procedure outlined for the original PBM, we obtain the final result:

$$E_j(\varepsilon) = \frac{E_f(\varepsilon)}{\varepsilon} \tag{3.95}$$

Also in this instance, the dependence of the elastic modulus on the superficial fluid flux and on the averaged particle velocity is lost.

3.5.4 A new equation of closure for the elastic force

From the previous considerations, it should be clear that the elastic force has a fluid dynamic origin: it does not rise from particle-particle interactions, but finds its justification in purely fluid dynamic arguments. As a result, the force should be related only to the drag force, this usually representing the component of the fluid-particle interaction affected by the flow. Yet, as equations (3.82) and (3.83) clearly indicate, Foscolo & Gibilaro (1987) argue in terms of *net force*, bringing into their analysis the effective weight of the particles as well. This apparent inconsistency stems from their definition of buoyancy force, which relates the force to the averaged pressure field. In our model, this issue no longer presents itself, since the effective weight is constant and its derivative with respect to ε is zero. We can therefore replace equations (3.82) and (3.82) with:

$$\text{steady-state conditions:} \qquad \langle f_d \rangle_p^e(x,t) = F\big[u_s(t) - \langle v \rangle_p(x,t), \varepsilon(x,t)\big] \tag{3.96}$$

$$\text{unsteady-state conditions:} \qquad \langle f_d \rangle_p^d(x,t) = F\big[u_s(t) - \langle v \rangle_p(x,t), \tilde{\varepsilon}(x,t)\big] \tag{3.97}$$

In dynamic conditions, the bed voidage is again replaced with the effective bed voidage defined by equation (3.84). The definition of the elastic modulus changes accordingly and becomes:

$$E_r \equiv -\frac{4(1-\varepsilon)}{\pi d_p^2}\left(\frac{\partial F}{\partial \varepsilon}\right)_{u_s - \langle v \rangle_p} \tag{3.98}$$

The constitutive function $F(u_s - \langle v \rangle_p, \varepsilon)$ is expressed using our new drag force closure; starting from equation (3.52), simple rearrangement results in:

$$\hat{F}(Re^*) = \hat{F}_0 C_D^*(Re^*) Re^{*2} \quad ; \quad \hat{F}_0 \equiv \frac{\pi \mu_f^2}{8\rho_f} \tag{3.99}$$

where, for convenience, we have replaced the arguments $u_s - \langle v \rangle_p$ and ε with Re^*. Deriving $\hat{F}(Re^*)$ with respect to ε does not require any simplifying assumption. We start by writing:

$$\frac{\partial F}{\partial \varepsilon} = 2\hat{F}_0 Re^* \left(\frac{\partial Re^*}{\partial \varepsilon} C_D^* + \frac{\partial C_D^*}{\partial \varepsilon}\frac{Re^*}{2}\right) \tag{3.100}$$

where it is understood that the partial derivatives must be calculated while holding $u_s - \langle v \rangle_p$ constant. From equations (3.27) and (3.53), the first partial derivative yields:

$$\frac{\partial Re^*}{\partial \varepsilon} = \frac{\partial}{\partial \varepsilon}\left(\frac{\rho_f \|u_s - \langle v \rangle_p\| d_p}{\mu_f \varepsilon^{n_e}}\right) = -Re^*\left(\frac{n_e}{\varepsilon} + \frac{\partial n_e}{\partial \varepsilon}\ln \varepsilon\right) \tag{3.101}$$

Note that n_e is a function of Re^*, and in turn of the variables $u_s - \langle v \rangle_p$ and ε; hence, its derivative

with respect to ε does not vanish but yields:

$$\frac{\partial n_e}{\partial \varepsilon} = \frac{\partial Re^*}{\partial \varepsilon} N(Re^*) \tag{3.102}$$

where it is:

$$N(Re^*) \equiv \frac{3}{4} \cdot 0.175 \left(\frac{2.40}{Re^{*1/4}(1 + 0.175 Re^{*3/4})} - \frac{4.80 + 2.40 \cdot 0.175 Re^{*3/4}}{Re^{*1/4}(1 + 0.175 Re^{*3/4})^2} \right) \tag{3.103}$$

By introducing equation (3.102) into equation (3.101), we obtain:

$$\frac{\partial Re^*}{\partial \varepsilon} = C(\varepsilon, Re^*) \left(-\frac{n_e(Re^*) Re^*}{\varepsilon} \right) \tag{3.104}$$

where, by definition, it is:

$$C(\varepsilon, Re^*) \equiv \frac{1}{1 + Re^* N(Re^*) \ln \varepsilon} \tag{3.105}$$

Note that, if the dependence of n_e on Re^* is neglected, that is, if a constant value for the exponent is used instead of equation (3.54), the function $C(\varepsilon, Re^*)$ is equal to one; thus, $C(\varepsilon, Re^*)$ can be regarded as a correction accounting for variations in the exponent due to changes in the Reynolds number. This justifies the way equation (3.104) is written.

Once the partial derivative of the Reynolds number has been calculated, working out that for the drag coefficient is quite straightforward:

$$\frac{\partial C_D^*}{\partial \varepsilon} = \frac{\partial}{\partial \varepsilon} \left(0.63 + 4.8 Re^{*\,-1/2} \right)^2 = C(\varepsilon, Re^*) \left(\frac{n_e(Re^*) D(Re^*) C_D^*(Re^*)}{\varepsilon} \right) \tag{3.106}$$

where equations (3.54) and (3.104) have been used. Here, by definition, it is:

$$D(Re^*) \equiv \frac{4.8 Re^{*\,-1/2}}{0.63 + 4.8 Re^{*\,-1/2}} \tag{3.107}$$

Replacing equations (3.104) and (3.106) into equation (3.100) gives:

$$\frac{\partial F}{\partial \varepsilon} = H(\varepsilon, Re^*) \hat{F}(Re^*) \tag{3.108}$$

where the new function on the right-hand side is defined to be:

$$H(\varepsilon, Re^*) \equiv C(\varepsilon, Re^*) \left(\frac{n_e(Re^*) \left[D(Re^*) - 2 \right]}{\varepsilon} \right) \tag{3.109}$$

From equation (3.98), we then obtain:

$$E_r(\varepsilon, Re^*) = -\frac{4(1 - \varepsilon)}{\pi d_p^2} H(\varepsilon, Re^*) \hat{F}(Re^*) \tag{3.110}$$

This new expression of the elastic modulus retains the dependence on the fluid dynamics: in addition to the void fraction, the constitutive function above features also the Reynolds number as argument. Equation (3.110) is more general than equations (3.75) and (3.95), the last being a simplified version of the first of limited validity. In this regard, we note that in equilibrium conditions, since drag and effective weight are equal, equation (3.110) becomes:

$$E_r^e(\varepsilon, Re^*) = -\frac{2}{3} d_p (1-\varepsilon)(\rho_p - \rho_f) g H(\varepsilon, Re^*) \tag{3.111}$$

In the limits of viscous and inertial flows, it is:

$$\lim_{Re^* \to 0} E_r^e(\varepsilon, Re^*) = \lim_{Re^* \to \infty} E_r^e(\varepsilon, Re^*) = E_j(\varepsilon) \tag{3.112}$$

Equation (3.112) coincides with equation (3.95). This result suggests the proper range of applicability of equations (3.75) and (3.95): they are appropriate only in equilibrium conditions and in the limits of viscous and inertial flow regimes.

The elastic force per unit volume of suspension is:

$$n \langle f_e \rangle_p = E_r(\varepsilon, Re^*) \frac{\partial \varepsilon}{\partial x} = -\frac{4(1-\varepsilon)}{\pi d_p^2} H(\varepsilon, Re^*) \hat{F}(Re^*) \frac{\partial \varepsilon}{\partial x} \tag{3.113}$$

Since it is:

$$\hat{F}(Re^*) = \frac{\pi d_p^3}{6(1-\varepsilon)} n \langle f_d \rangle_p \tag{3.114}$$

we can rewrite equation (3.113) as:

$$n \langle f_e \rangle_p = -\left(\frac{2}{3} d_p H(\varepsilon, Re^*) \frac{\partial \varepsilon}{\partial x} \right) n \langle f_d \rangle_p \tag{3.115}$$

This equation offers a clear interpretation of the elastic force: it is a component of the drag force related to gradients in void fraction. Drag force and elastic force are parallel, and the void fraction gradient is computed in the direction of these vectors. Thus, in absolute notation, it is:

$$n \langle \boldsymbol{f}_e \rangle_p = -\left(\frac{2}{3} d_p H(\varepsilon, Re^*) \boldsymbol{\nabla} \varepsilon \cdot \boldsymbol{n}_d \right) n \langle \boldsymbol{f}_d \rangle_p \tag{3.116}$$

where $\boldsymbol{n}_d(\boldsymbol{x}, t)$ is the drag force unit vector. Note that equation (3.74), even if written in absolute notation, is valid only for one-dimensional systems, for only in this case $\boldsymbol{e}$ coincides with $\boldsymbol{n}_d$.

3.6 Conclusions

Finding analytical closures for the undefined terms of the averaged equations of motion that describe particulate systems in flow is exceedingly difficult. The problem is usually overcome by resorting to

Drag Force Closure

$$n\langle \boldsymbol{f}_d\rangle_p = \beta\Big(\langle \boldsymbol{u}\rangle_f - \langle \boldsymbol{v}\rangle_p\Big) \;\;;\;\; \beta = \frac{3}{4}C_D\frac{\rho_f\|\langle \boldsymbol{u}\rangle_f - \langle \boldsymbol{v}\rangle_p\|(1-\varepsilon)}{d_p}\varepsilon^{-\psi_e} \;\;;\;\; \psi_e = -\frac{\ln\varphi}{\ln\varepsilon}$$

$$\varphi = \frac{C_D^*}{C_D}\,\varepsilon^{2(1-n_e)} \;\;;\;\; C_D^* = \Big(0.63 + 4.8Re^{*\,-1/2}\Big)^2 \;\;;\;\; C_D = \Big(0.63 + 4.8Re^{-1/2}\Big)^2$$

$$n_e = \frac{4.8 + 2.4\cdot 0.175Re^{*3/4}}{1 + 0.175Re^{*3/4}} \;\;;\;\; Re^* = \frac{Re}{\varepsilon^{n_e}} \;\;;\;\; Re = \frac{\rho_f}{\mu_f}\,\varepsilon\|\langle \boldsymbol{u}\rangle_f - \langle \boldsymbol{v}\rangle_p\|d_p$$

Elastic Force Closure

$$n\langle \boldsymbol{f}_e\rangle_p = -\frac{2}{3}d_pH(\boldsymbol{\nabla}\varepsilon\cdot\boldsymbol{n}_d)n\langle \boldsymbol{f}_d\rangle_p \;\;;\;\; H = \frac{n_e\big(D-2\big)C}{\varepsilon}$$

$$D = \frac{4.8Re^{*\,-1/2}}{0.63 + 4.8Re^{*\,-1/2}} \;\;;\;\; C = \frac{1}{1 + Re^*N\ln\varepsilon}$$

$$N = \frac{3}{4}\cdot 0.175\left(\frac{2.40}{Re^{*1/4}(1+0.175Re^{*3/4})} - \frac{4.80 + 2.40\cdot 0.175Re^{*3/4}}{Re^{*1/4}(1+0.175Re^{*3/4})^2}\right)$$

Table 3.1: New closures for the drag and elastic forces developed in this work.

semitheoretical constitutive equations. Those for the drag force present a serious shortcoming: they are inconsistent with the empirical correlation of Richardson & Zaki (1954). Even if this correlation is not exact, it provides the most accurate predictions of the uniform expansion of non-cohesive fluidized suspensions. Theoretical expansion profiles, obtained by using appropriate drag force closures, should therefore be in good agreement with these predictions. This is seldom the case. The new equation of closure developed in this chapter is entirely based on the Richardson & Zaki correlation; accordingly, it should be more accurate than the other equations available in the literature. Another unclosed term, which plays an important role in the stability of homogeneous fluidized suspensions, is the elastic force. The closure advanced by Foscolo & Gibilaro (1987), who were the first to give a formal definition of this force, lacks general validity and is, in some respects, not rigourous – refer for instance to equations (3.91) and (3.93). The equation of closure that we have derived, based on our new drag force constitutive equation, overcomes these limitations. Obtained by a rigourous approach, the closure holds in a much more general framework and reduces to the original expression of Foscolo & Gibilaro (1987) only in some limiting cases. Table 3.1 reports the new drag and elastic closures.

Chapter 4

The dynamics and stability of uniform suspensions

In this chapter, we analyze the dynamics and stability of homogeneous fluidized suspensions.

1) Using different constitutive equations for the drag force, we evaluate the steady-state expansion profiles of liquid-fluidized suspensions by integrating the averaged equations of motion.
2) We investigate the behaviour of uniform fluidized systems subjected to sudden changes in fluid flux, comparing the numerical results with the predictions of the mechanistic monodimensional model of Gibilaro et al. (1984).
3) We study the stability of homogeneous gas-fluidized suspensions analytically, by carrying out a linear stability analysis of the equilibrium solutions of the averaged transport equations.
4) We simulate the transition from the particulate to the aggregative fluidization state, and debate the meaning of fluid dynamic stability.

With the exception of the second point, we validate the numerical predictions by using experimental data reported in the literature; all the results are therefore tested.

Parts of this chapter have been published:

Mazzei, L., Lettieri, P., Elson, T. & Colman, D. (2006). A revised monodimensional particle bed model for fluidized beds. Chem. Eng. Sci. 61, 1958.

Mazzei, L. & Lettieri, P. (2008). CFD investigation into the dynamics and stability of homogeneous fluidized suspensions. Chem. Eng. Sci. In press.

4.1 Introduction

Among all the fluidization regimes, the homogeneous is certainly the simplest to study: the dynamics are not chaotic, no bubbles are present, and the mixing is contained. Presenting a direct link between bed expansion and drag force magnitude, uniform non-cohesive systems consent to validate closures for the drag by simply comparing theoretical and experimental expansion profiles. We perform this

analysis in the first part of this chapter, where we test the new closure derived in § 3.4.5 and other well-known expressions that model this force.

Successively, we study the dynamic response of contracting and expanding homogeneous beds to sudden variations in fluid flux. During a bed collapse, albeit these variations disrupt the equilibrium of the system, the suspension retains almost entirely a uniform structure; thus, simple monodimensional models, like the one of Gibilaro et al. (1984), can describe its dynamics. A more complex behaviour, conversely, characterizes expanding suspensions, where internal mixing, promoted by gravitational instabilities, completely erases their homogeneity. In this case, only the numerical integration of the averaged equations of motion can provide an adequate description of the flow. To gain insight into this problem and fully understand the limitations of simplified analyses, we simulate these systems computationally and discuss their transient behaviour.

The chapter terminates with the study of the stability of the particulate fluidization state. We first consider the monodimensional averaged equations of motion and conduct a linear stability analysis of their equilibrium solutions. This method, as discussed in Chapter 3, tells us whether or not small perturbations about equilibrium states die away. If so, the bed is stable. The instability threshold, however, does not necessarily coincide with the onset of bubbling, since nothing is known about the ultimate fate of the perturbations. As we shall see, only the solution of the non-linear equations of motion can provide this information.

4.2 Multiphase fluid dynamic model

Table 4.1 reports the equations of motion. The effective stress tensors are closed using the Newtonian constitutive equations (3.1) and (3.2). The fluid is incompressible, with constant shear viscosity and negligible dilatational viscosity; the kinetic theory of granular gases (Gidaspow, 1994) is used to model the flow properties of the solid. The fluid-particle interaction force comprises buoyancy, drag and elastic forces. The classical definition of buoyancy force, equation (3.4), is adopted; the drag and elastic forces are expressed using the new constitutive equations derived in Chapter 3. The local fluid acceleration force should be accounted for; however, following Gidaspow (1994), we ignore this contribution because, in the problems that we shall treat, is negligible.

4.3 Computational set-up

4.3.1 Numerical schemes and techniques

The simulations are carried out using the commercial CFD code CFX 4.4 (Ansys Inc., formerly AEA Technology). Governing and constitutive equations are implemented in the *Multi Fluid Model* of the package, based on a Eulerian-Eulerian description of the flow.

Continuity Equation - Fluid Phase
$$\frac{\partial \varepsilon}{\partial t} + \boldsymbol{\nabla} \cdot \left(\varepsilon \langle \boldsymbol{u} \rangle_f \right) = 0$$
Continuity Equation - Solid Phase
$$\frac{\partial \phi}{\partial t} + \boldsymbol{\nabla} \cdot \left(\phi \langle \boldsymbol{v} \rangle_p \right) = 0$$
Dynamical Equation - Fluid Phase
$$\rho_f \left[\frac{\partial}{\partial t} \left(\varepsilon \langle \boldsymbol{u} \rangle_f \right) + \boldsymbol{\nabla} \cdot \left(\varepsilon \langle \boldsymbol{u} \rangle_f \langle \boldsymbol{u} \rangle_f \right) \right] = \boldsymbol{\nabla} \cdot \langle \boldsymbol{S} \rangle_f - n \langle \boldsymbol{f} \rangle_p + \varepsilon \rho_f \boldsymbol{g}$$
Dynamical Equation - Solid Phase
$$\rho_p \left[\frac{\partial}{\partial t} \left(\phi \langle \boldsymbol{v} \rangle_p \right) + \boldsymbol{\nabla} \cdot \left(\phi \langle \boldsymbol{v} \rangle_p \langle \boldsymbol{v} \rangle_p \right) \right] = \boldsymbol{\nabla} \cdot \langle \boldsymbol{S} \rangle_p + n \langle \boldsymbol{f} \rangle_p + \phi \rho_p \boldsymbol{g}$$

Table 4.1: Eulerian-Eulerian locally averaged equations of motion for monodisperse systems.

A finite-volume scheme is used. The Rhie-Chow interpolation procedure prevents chequerboard oscillations of the pressure. To reduce nodal continuity errors, pressure gradients are second-order accurate; a quadratic extrapolation of the pressure is performed to ensure a second-order accurate one-sided gradient at the domain boundaries. The method of discretization chosen for the advection terms of all the transport equations is the hybrid differencing scheme.

The coupled transport equations are solved by the algorithm IPSAC (Inter-Phase Slip Algorithm Consistent), a modified version of IPSA (Inter-Phase Slip Algorithm) developed by Spalding (1976). IPSAC, albeit computationally more expensive than its original formulation, is preferred because, especially for drag-dominated flows, it displays better convergence characteristics. Furthermore, it is required by the code if, in the linear momentum equations of conservation, the fluid pressure is not shared between the phases, but appears only in the dynamical equation of the fluid. This happens in our model, since the buoyancy force is not related to the fluid pressure.

Convergence is accelerated by the SIMPLEC (Simultaneous Solution of Non-linearly Coupled Equations Corrected) method, a modification of the SIMPLE (Simultaneous Solution of Non-linearly Coupled Equations) algorithm proposed by Lo (1989). Its computational cost is nearly identical to the original scheme; the revised method, however, being less sensitive to the selection of under-relaxation factors, is usually favoured.

At each time step, a minimum of 10 iterations and a maximum of 50 is used to compute the flow variables. With the tolerance set to 10^{-8}, full numerical convergence is always achieved in less than 50 iterations. Convergence attainment is established by analyzing only the mass flow residuals. Under-relaxation factors equal to 0.30 are adopted for all the variables with the exception of volume fractions and fluid pressure. For the former a factor equal to 0.65 is used; the pressure, conversely, is not under-relaxed, as required by the SIMPLEC algorithm.

4.3.2 Boundary and initial conditions

The computational grid (uniform, with square cells of 5.0 mm side) is two-dimensional. Front and back wall effects are neglected, while no-slip velocity boundary conditions for both phases model the left and right walls of the domain. At the bottom of the bed, Dirichlet boundary conditions specify a uniform gas inlet velocity and absence of solid (*i.e.*, the solid volume fraction is set to zero). The boundary condition assigned at the upper boundary of the computational domain sets the pressure to the reference value of $1.015 \cdot 10^5$ Pa.

The initial conditions, except for the contraction and expansion of perturbed homogeneous beds, reflect the following situation: the powder, contained in a vertical two-dimensional rectangular vessel (height 120 cm, width 35 cm, depth 1 cm) initially forms a fixed bed (height 30 cm, voidage 0.4). At time $t = 0$, a constant flow rate of fluid, sufficient to fluidize the system and bring it to homogeneous or bubbling operating conditions, is fed (*i.e.*, the superficial velocity is increased stepwise from zero to the final operating value).

4.3.3 Time step

Some considerations are necessary to explain the time step choice. This work, among other things, tests the constitutive equations for drag and elastic forces used in the multiphase model. For the drag, this can be done by computing numerically the expansion profiles of uniform systems and verifying their agreement with experimental data. For a proper analysis, several simulations are required, and in each the steady state must necessarily be attained. We can estimate the time required by a suspension, initially not fluidized, to reach this state by using the relationship:

$$h(t) = h_2 - (h_2 - h_1) \exp\left(-\frac{u_2 - u_1}{h_2 - h_1}\, t\right) \tag{4.1}$$

This expresses the time variation of the height h of a homogeneous system evolving from an initial equilibrium state (u_1, h_1) to a final equilibrium state (u_2, h_2), with $u_2 > u_1$, in the assumption that at time $t = 0$ the superficial velocity of the fluid is changed stepwise from u_1 to u_2. In §4.5.2 we shall derive this expression. With $u_1 = u_{mf}$ (minimum fluidization velocity) and $h_1 = h_{mf}$ (minimum fluidization height), the time t_e required to reach an equilibrium state (u, h) starting from minimum fluidization (which is reached almost instantaneously from packed-bed conditions, if the superficial velocity is changed from zero to u stepwise) can be estimated using the formula:

$$t_e \approx 3\tau \quad ; \quad \tau \equiv \frac{h - h_{mf}}{u - u_{mf}} \tag{4.2}$$

t_e is the characteristic response time of the exponential in equation (4.1): it indicates how long $h(t)$ takes to increase by 95% of its total variation. τ instead is the time that the system would require to reach equilibrium conditions if $h(t)$ were linear instead of exponential. Since h_{mf} is roughly equal

to the initial bed height h_0, if u_{mf} is far lower than u, it is:

$$\tau \approx \frac{h - h_0}{u} \tag{4.3}$$

This value can be substantial. Consider, for instance, particles of density $2620\ \mathrm{kg/m^3}$ and diameter $230\ \mu$m and a liquid of density $2170\ \mathrm{kg/m^3}$ and viscosity $1.61 \cdot 10^{-3}$ Pa s (this system was investigated by Richardson & Zaki, 1954). The minimum fluidization velocity is $1.30 \cdot 10^{-4}$ m/s. If we choose an initial bed height of 0.30 m and a superficial fluid velocity of $4.70 \cdot 10^{-4}$ m/s, the equilibrium bed height is nearly 0.39 m. Thus, from equation (4.2), it is:

$$t_e \approx \frac{3\,(0.39 - 0.30)}{4.70 \cdot 10^{-4} - 1.30 \cdot 10^{-4}} \approx 800\,\mathrm{s} \tag{4.4}$$

The system should reach the steady state in about 13 minutes! This surprising conclusion was verified computationally. Figure 4.1 reports the bed height as a function of time; clearly, the profile takes roughly 800 s to flatten out.

Thus, in this kind of simulations, we really must find an optimal time step to ensure accuracy and minimize the computational cost. To this end, we perform a sensitivity analysis to quantify the loss in accuracy caused by a time step increase. Using time steps of 10^{-2}, 10^{-3} and 10^{-4} s, we simulate the expansion of a gas-fluidized bed ($\rho_f = 1.18\ \mathrm{kg/m^3}$, $\mu_f = 1.81 \cdot 10^{-5}$ Pa s, $\rho_p = 1210\ \mathrm{kg/m^3}$, $d_p = 137\ \mu$m) initially packed. To reach the stationary state in a reasonably short time, we choose a system with a small characteristic response time. Minimum fluidization velocity, initial bed height

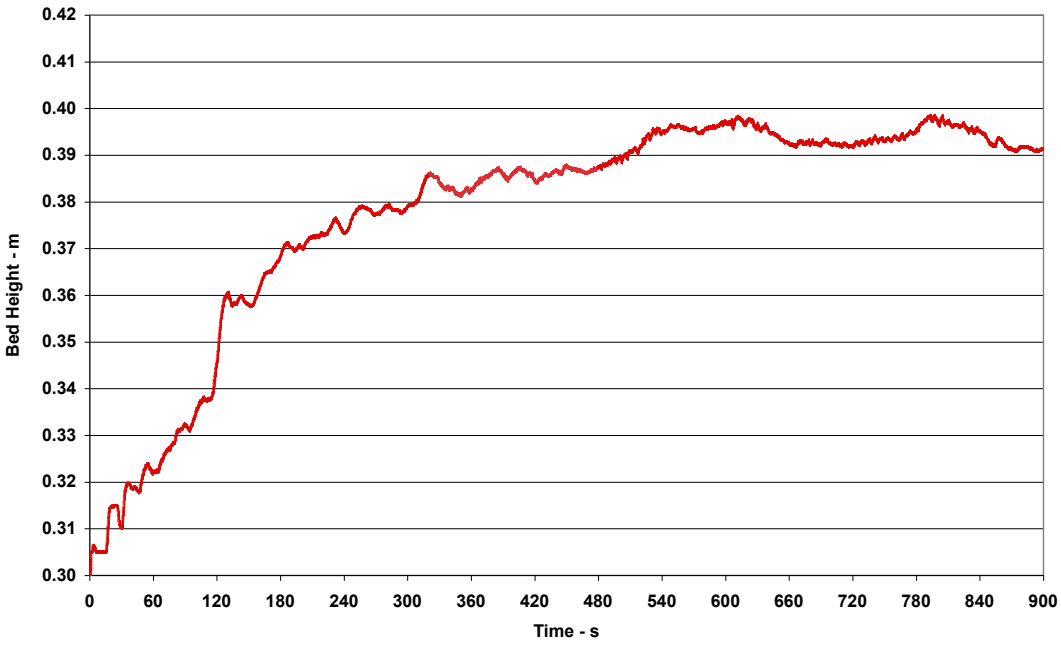

Figure 4.1: Height variation of a particulate system that, starting from packed-bed conditions, attains a state of homogeneous fluidization.

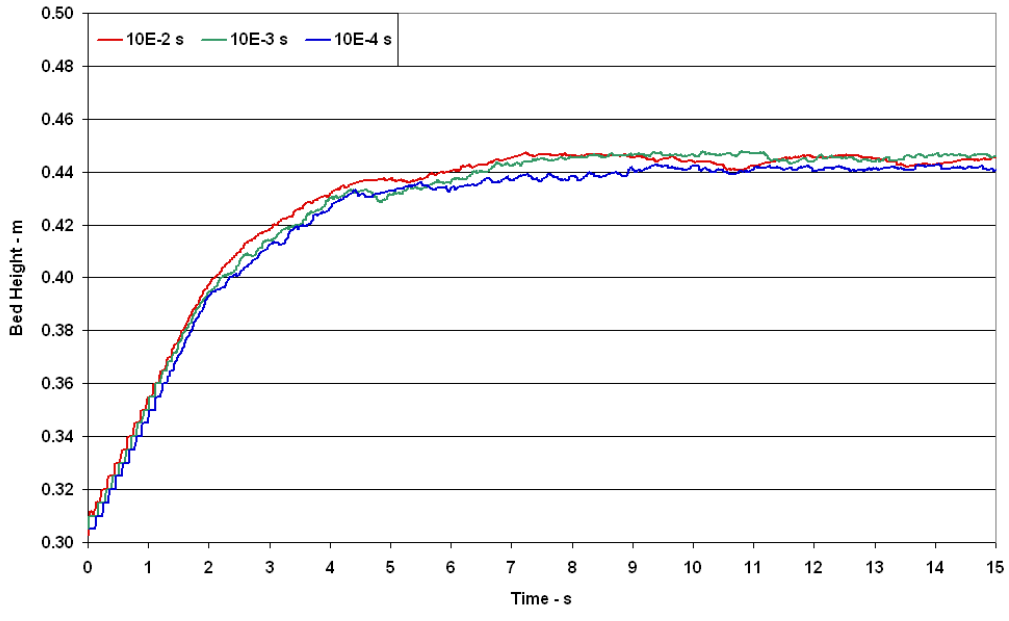

Figure 4.2: Height variation of a particulate system that, starting from packed-bed conditions, attains a state of homogeneous fluidization. Different time steps are considered.

and superficial fluid velocity are equal to $8.73 \cdot 10^{-3}$ m/s, 0.30 m and $5.77 \cdot 10^{-2}$ m/s, respectively. With this choice, the equilibrium bed height is 0.45 m, and we have:

$$t_e \approx \frac{3(0.45 - 0.30)}{5.77 \cdot 10^{-2} - 8.73 \cdot 10^{-3}} \approx 9\,\mathrm{s} \tag{4.5}$$

Figure 4.2 reports the bed height profiles. The system is simulated for 15 s; stationary conditions are nevertheless attained after about 9 s, in agreement with our estimate. Each curve refers to a different time step. The differences between them are minimal, and the steady-state value of the bed height is virtually unaffected by the time step choice. Hence, a time step of 10^{-2} s is selected to run all the numerical simulations.

4.4 Expansion profiles of liquid-fluidized uniform beds: experimental validation of the new drag force closure

Drag force closures can be tested by comparing computational and experimental expansion profiles of homogeneous fluidized suspensions. Here we examine the closures reported in Table 4.2; this choice reflects the widespread use of the Ergun (1952) and Wen & Yu (1966) constitutive equations in CFD numerical codes. To evaluate the expansion profiles, we do not operate analytically, considering an idealized uniform one-dimensional bed and requesting that the effective weight of the powder be counterbalanced by the drag, but we implement the closures in the CFD code and solve the transport equations without simplifications.

Ergun (1952) − Equation (3.32) $\beta = 150\dfrac{\mu_f(1-\varepsilon)^2}{d_p^2\varepsilon^2} + 1.75\dfrac{\rho_f\|\langle\boldsymbol{u}\rangle_f - \langle\boldsymbol{v}\rangle_p\|(1-\varepsilon)}{d_p\varepsilon}$
Wen & Yu (1966) − Equation (3.34) $\beta = \dfrac{3}{4}C_D(Re)\dfrac{\rho_f\|\langle\boldsymbol{u}\rangle_f - \langle\boldsymbol{v}\rangle_p\|(1-\varepsilon)}{d_p}\varepsilon^{-\alpha}$
New closure − Equation (3.65) $\beta = \dfrac{3}{4}C_D(Re)\dfrac{\rho_f\|\langle\boldsymbol{u}\rangle_f - \langle\boldsymbol{v}\rangle_p\|(1-\varepsilon)}{d_p}\varepsilon^{-\psi_e(\varepsilon,Re)}$

Table 4.2: Drag force closures tested.

The multiphase model described in § 4.2 is hydrodynamical: interparticle forces, electrostatic or otherwise, are neglected. This approximation holds for non-cohesive systems; here equilibrium bed expansion and drag force are directly related, since no other contributions come into play, with the exception, of course, of the buoyancy and weight forces (local fluid acceleration, elastic, virtual mass and lift forces vanish when stationary conditions are attained). For cohesive systems, conversely, interparticle forces are significant, and hydrodynamic models are bound to be inaccurate. To test our new drag force closure, we favour therefore liquid-fluidized systems, since their dynamics are virtually unaffected by the presence of this additional class of forces. Three are considered: the first (system 1) was investigated experimentally by Richardson & Zaki (1954), the other two (systems 2 and 3) by Wilhelm & Kwauk (1948); their experimental findings are used to validate the computational results. The physical properties of each system are shown in Table 4.3.

To perform the analysis, we compute numerically the equilibrium bed height and void fraction for different superficial fluid velocities: we assign u, we run the simulation until the steady state is attained, and we finally evaluate h and ε. For each system and each superficial velocity, we run several numerical simulations, each time using a different drag force closure. The computational expansion profiles are then compared with experimental data and predictions from the Richardson & Zaki (1954) correlation. Percent errors are calculated to render the comparison quantitative.

42 simulations are run. Table 4.4 reports the computational and experimental results, showing the system response times (an estimate of the time needed to reach the steady state) and equilibrium

Property	System 1	System 2	System 3	Units
ρ_f	998	1005	1005	$\mathrm{kg/m^3}$
μ_f	$1.00 \cdot 10^{-3}$	$1.00 \cdot 10^{-3}$	$1.00 \cdot 10^{-3}$	Pa s
ρ_p	2780	2639	2351	$\mathrm{kg/m^3}$
d_p	253	373	521	μm

Table 4.3: Physical properties of the experimental systems used.

$u\,(\mathrm{m/s})$	$t_e\,(\mathrm{s})$	$\varepsilon_{M\&L}$	$\varepsilon_{W\&Y}$	ε_E	$\varepsilon_{R\&Z}$	ε_{exp}
System 1 – Experimental data by Richardson & Zaki (1954)						
$2.72 \cdot 10^{-3}$	93	0.498	0.525	0.551	0.504	0.500
$5.28 \cdot 10^{-3}$	100	0.599	0.617	0.628	0.604	0.600
$9.25 \cdot 10^{-3}$	106	0.699	0.706	0.712	0.703	0.700
$1.50 \cdot 10^{-2}$	127	0.797	0.802	0.790	0.802	0.800
System 2 – Experimental data by Wilhelm & Kwauk (1948)						
$9.05 \cdot 10^{-3}$	52	0.589	0.610	0.629	0.591	0.581
$1.12 \cdot 10^{-2}$	53	0.629	0.644	0.663	0.630	0.617
$1.53 \cdot 10^{-2}$	57	0.690	0.698	0.713	0.692	0.679
$2.47 \cdot 10^{-2}$	71	0.796	0.793	0.799	0.799	0.787
$2.85 \cdot 10^{-2}$	82	0.832	0.825	0.828	0.835	0.826
System 3 – Experimental data by Wilhelm & Kwauk (1948)						
$7.71 \cdot 10^{-2}$	3	0.502	0.504	0.550	0.504	0.520
$8.38 \cdot 10^{-2}$	4	0.520	0.518	0.579	0.521	0.552
$1.11 \cdot 10^{-1}$	5	0.583	0.571	0.691	0.584	0.614
$1.62 \cdot 10^{-1}$	7	0.679	0.651	0.878	0.682	0.722
$1.84 \cdot 10^{-1}$	8	0.717	0.682	0.956	0.720	0.762

Table 4.4: Expansion profiles of uniform fluidized beds. Computational and experimental results.

bed voidages. ε_E, $\varepsilon_{W\&Y}$ and $\varepsilon_{M\&L}$ are determined computationally. The first two refer to the drag force closures of Ergun (1952) and Wen & Yu (1966), equations (3.32) and (3.34), respectively; the last is based on our new closure, equation (3.65). Finally, $\varepsilon_{R\&Z}$ derives from the Richardson & Zaki correlation, whereas ε_{exp} denotes the experimental data.

Figures 4.3 - 4.8 present more effectively the results and help visualize the trends. For each superficial fluid velocity in Table 4.4, Figures 4.3, 4.5 and 4.7 report ε_E, $\varepsilon_{W\&Y}$ and $\varepsilon_{M\&L}$ against ε_{exp}. Therefore, different values of ε_{exp} correspond to different fluid fluxes. The figures refer to the systems 1, 2 and 3, respectively; the first uses the experimental data of Richardson & Zaki (1954), the others of Wilhelm & Kwauk (1948). Of course, the closer the points are to the bisecting line of the diagram, the better the match between theoretical and experimental results. The values of $\varepsilon_{R\&Z}$ are also included to quantify the accuracy of the Richardson & Zaki correlation.

Figures 4.4, 4.6 and 4.8 report the percent error of the theoretical voidage predictions against the experimental voidage. Taking $\varepsilon_{M\&L}$ as an example, the error is given by:

$$e_{M\&L}(\varepsilon_{exp}) = \left| \frac{\varepsilon_{M\&L} - \varepsilon_{exp}}{\varepsilon_{exp}} \right| \cdot 100 \tag{4.6}$$

Also these figures refer to the three systems investigated in the order formerly specified, and different values of ε_{exp} reflect different superficial fluid velocities.

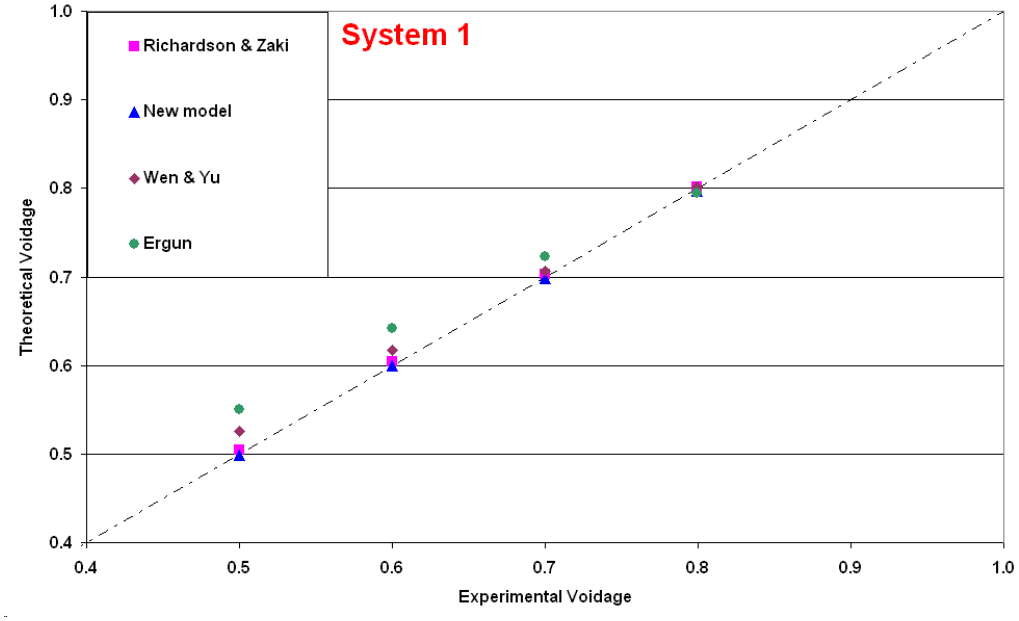

Figure 4.3: Comparison between theoretical and experimental results. This figure plots ε_E, $\varepsilon_{W\&Y}$, $\varepsilon_{M\&L}$ and $\varepsilon_{R\&Z}$ against ε_{exp} for system 1.

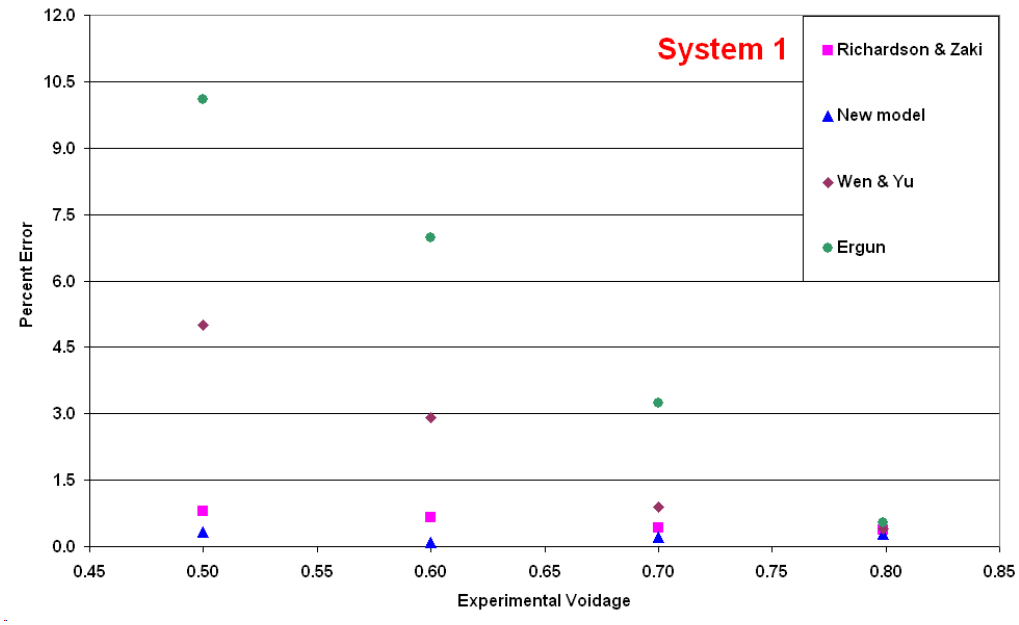

Figure 4.4: Comparison between theoretical and experimental results. This figure plots the percent error of the theoretical predictions for ε_E, $\varepsilon_{W\&Y}$, $\varepsilon_{M\&L}$ and $\varepsilon_{R\&Z}$ against ε_{exp} for system 1.

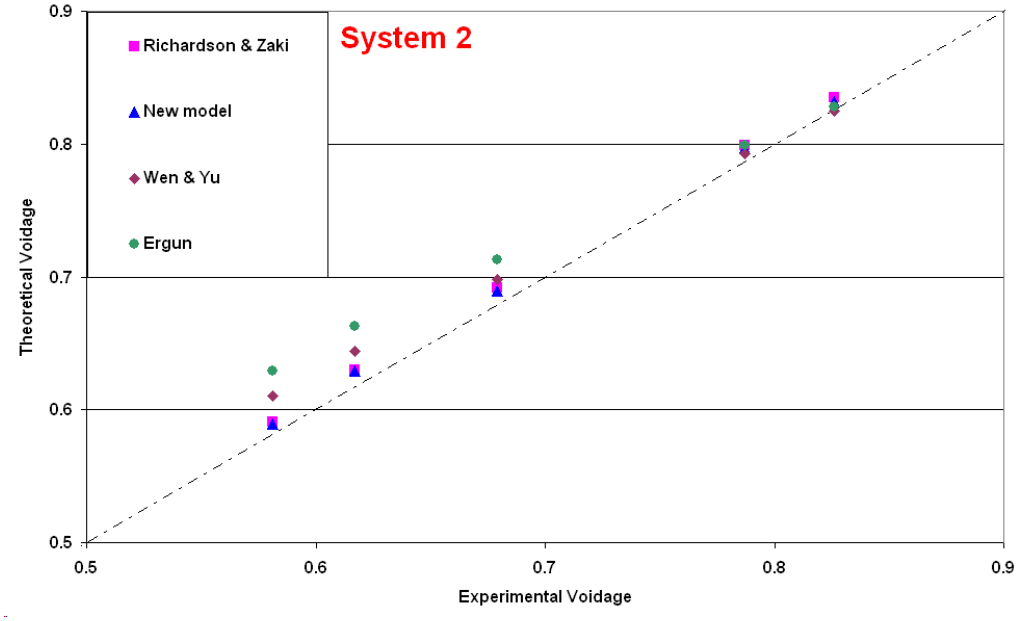

Figure 4.5: Comparison between theoretical and experimental results. This figure plots ε_E, $\varepsilon_{W\&Y}$, $\varepsilon_{M\&L}$ and $\varepsilon_{R\&Z}$ against ε_{exp} for system 2.

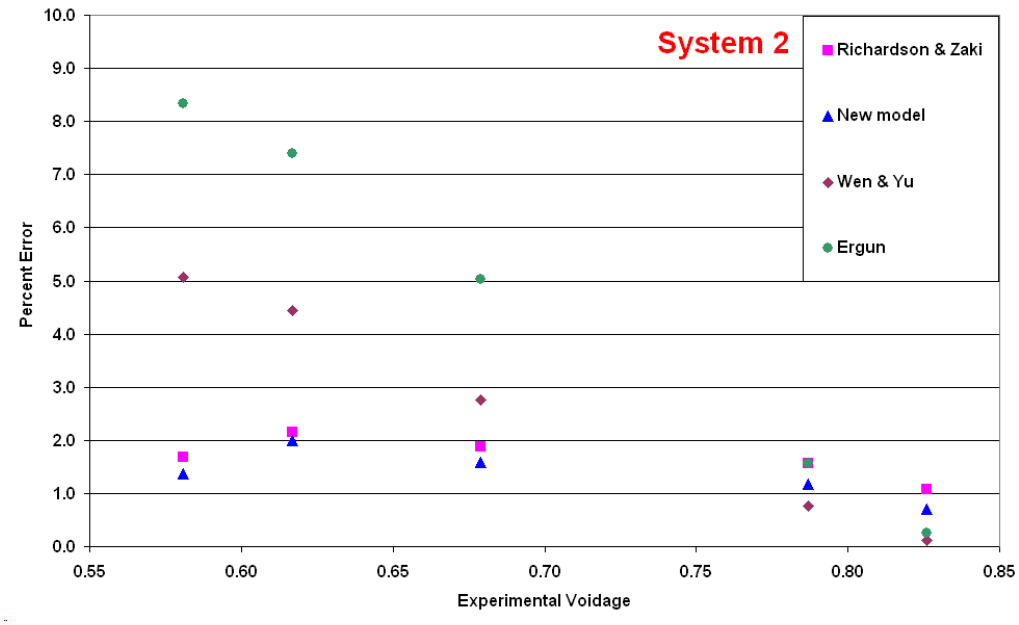

Figure 4.6: Comparison between theoretical and experimental results. This figure plots the percent error of the theoretical predictions for ε_E, $\varepsilon_{W\&Y}$, $\varepsilon_{M\&L}$ and $\varepsilon_{R\&Z}$ against ε_{exp} for system 2.

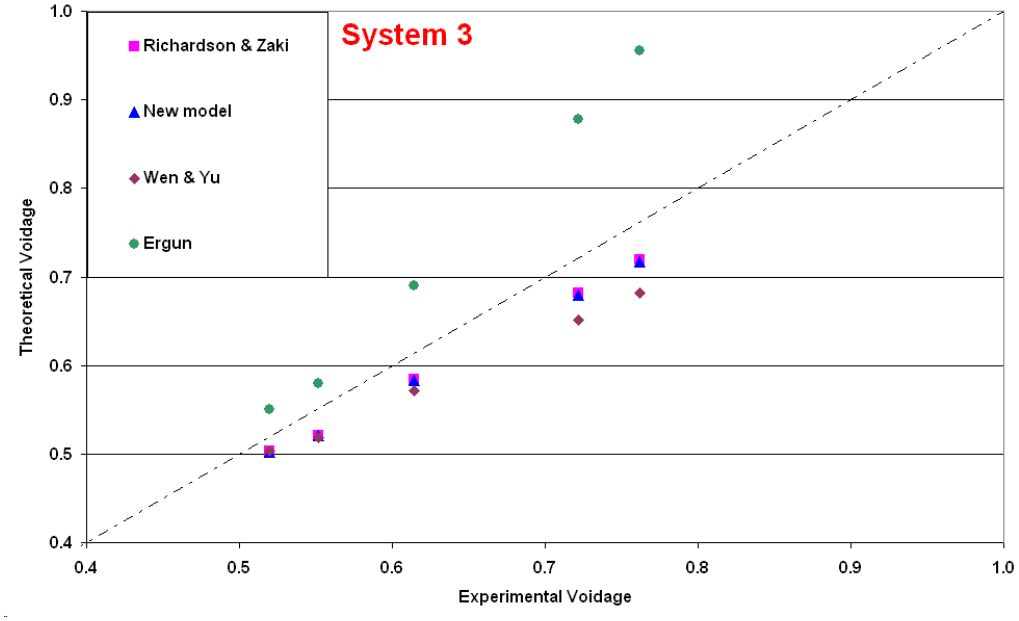

Figure 4.7: Comparison between theoretical and experimental results. This figure plots ε_E, $\varepsilon_{W\&Y}$, $\varepsilon_{M\&L}$ and $\varepsilon_{R\&Z}$ against ε_{exp} for system 3.

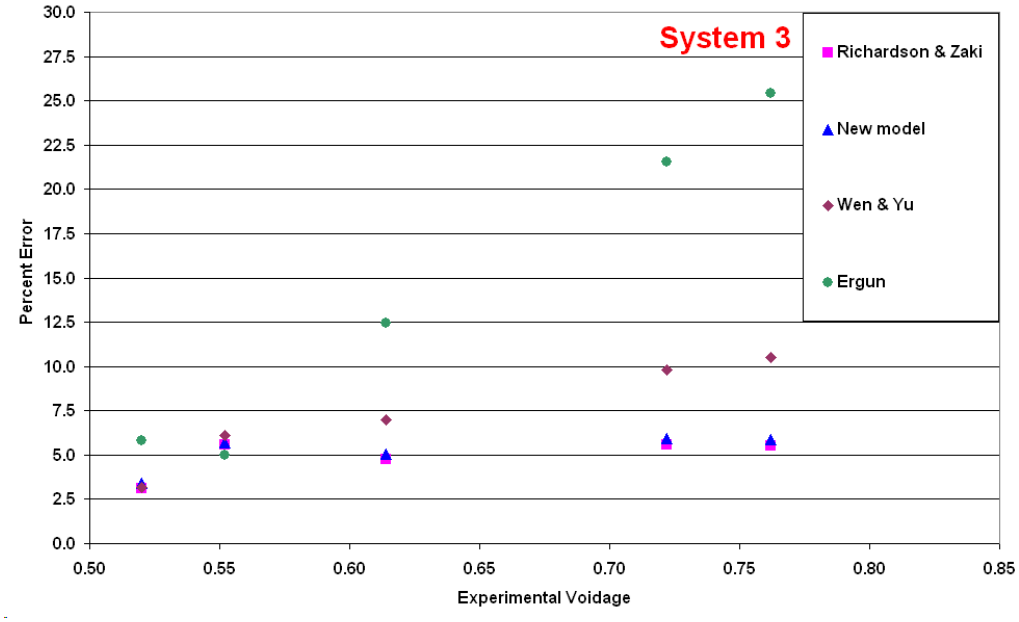

Figure 4.8: Comparison between theoretical and experimental results. This figure plots the percent error of the theoretical predictions for ε_E, $\varepsilon_{W\&Y}$, $\varepsilon_{M\&L}$ and $\varepsilon_{R\&Z}$ against ε_{exp} for system 3.

As expected, the Richardson & Zaki correlation and equation (3.65) agree perfectly. The latter is always more accurate than equations (3.32) and (3.34), with the exception of just one case involving system 2 where at very high dilutions the other closures are slightly more precise. The disparity, though, is not substantial, as Figure 4.6 shows. The agreement between the closures varies with the void fraction: for systems 1 and 2 it improves as the voidage rises, while for system 3 an opposite behaviour is observed. Furthermore, whereas the accuracy of equations (3.32) and (3.34) is strongly dependent on the voidage, that of equation (3.65) is not.

Note that, in almost all the simulations, a commercial CFD code would use the Ergun equation, since the voidage is often less than 0.80 (refer to §3.4.4.1). This is unfortunate, because the Wen & Yu closure is clearly more accurate and should be used in its place. These conclusions, however, cannot be generalized to any system. Sometimes, equation (3.32) does yield better predictions. The question, therefore, is when the CFD code should switch from one equation to the other. The threshold of 0.80 is not always the best choice. Also in this respect, the new closure offers an improvement: holding for any fluid dynamic regime and void fraction, no switching is required.

Figures 4.4 and 4.6 reveal that, for systems 1 and 2, the accuracy of equation (3.32) improves as the suspensions become more diluted. This surprises because the Ergun correlation was derived for fixed beds and was not meant to account for large variations in powder compaction. Note also that the best predictions are found for void fractions equal to or greater than 0.80, beyond the threshold where the closure is usually no longer used because deemed too inaccurate. To explain this apparent inconsistency we resort to Figure 3.1, previously discussed in §3.4.4.1, reporting in it the equilibrium

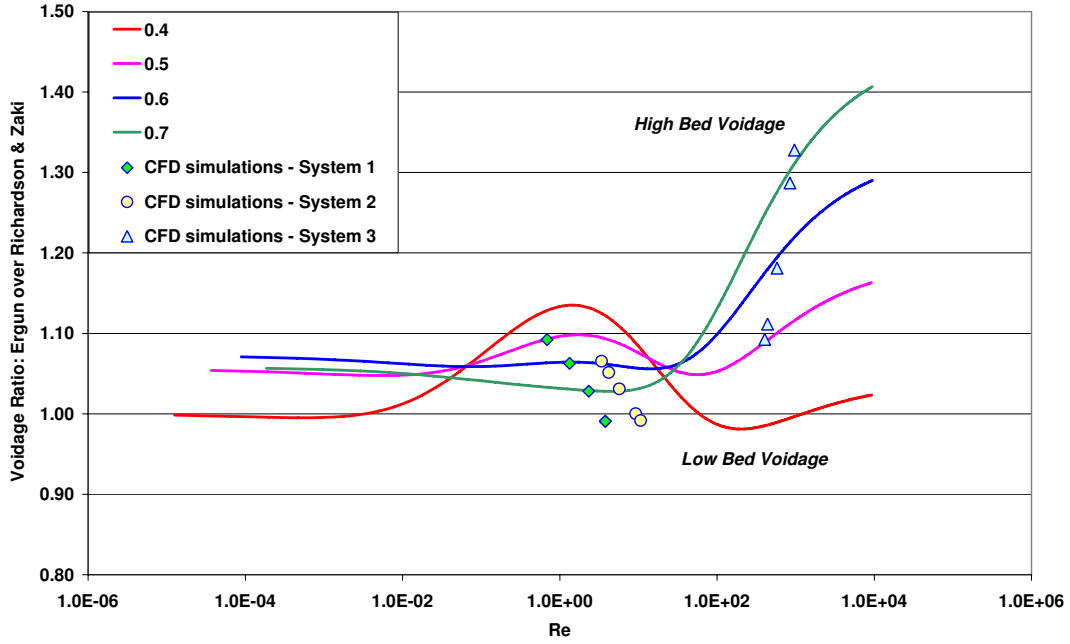

Figure 4.9: Equilibrium states of the systems when full expansion is attained.

states in which the systems reside when full expansion is reached. Let us clarify how we represent these states on the diagram. For a given superficial fluid velocity, Table 4.4 provides the equilibrium void fractions ε_E and $\varepsilon_{R\&Z}$; from these, we can calculate the Reynolds number Re and the voidage ratio $\varepsilon_E/\varepsilon_{R\&Z}$. The equilibrium states are identified by the points with coordinates $(Re, \varepsilon_E/\varepsilon_{R\&Z})$. This is done in Figure 4.9. The points can be regarded as states in which the systems operate when the transient regime comes to an end. Systems 1 and 2 both operate in the intermediate fluid dynamic region; here the Ergun closure is more accurate at high dilution, in agreement with the trend found in Figures 4.4 and 4.6. System 3, conversely, operates in the inertial region of the chart, where the closure rapidly loses accuracy as the dilution increases. This behaviour is also in agreement with the trend found in Figure 4.8.

4.5 Contracting and expanding liquid-fluidized uniform beds

In this section, we analyze the response of uniform fluidized beds to sudden changes in fluid flux. We can formulate the problem as follows. Initially the system is in the equilibrium state (u_1, h_1). At time $t = 0$, the superficial velocity of the fluid is changed stepwise from u_1 to u_2. The system responds by contracting or expanding (depending on whether u_2 is smaller or greater than u_1, respectively) until the new equilibrium state (u_2, h_2) is reached. In general, as we know, the new state is not necessarily homogeneous (when it is not, stationary conditions are never really reached in a fluid dynamic sense); for many systems, if the fluid flux is increased sufficiently, bubbles form with ensuing disruption of the homogeneous structure. Here we restrict the analysis to liquid-fluidized beds, where this phenomenon does not occur. The investigation of the stability of gas-fluidized systems and their transition from the particulate to the aggregative state is presented later on in §4.6.3.

The response of homogeneous systems to abrupt changes in superficial fluid velocity is somewhat different for decreases in fluid flux than for increases. We shall first consider the former case, the contracting bed, which is more straightforward.

4.5.1 Dynamics of contracting liquid-fluidized uniform beds

The fluid flux is reduced stepwise from the value u_1 to a lower value u_2. The question is how the system responds to this perturbation. Before the fluid flux is varied, the suspension is in equilibrium, with the particles lying motionless within the fluid; this exerts on them a force made up of a constant term (buoyancy force) and a dynamic term (drag force). The overall force exactly counterbalances the weight of the particles; we can thus write:

$$n\langle \boldsymbol{f}_d \rangle_p = -\phi(\rho_p - \rho_f)\boldsymbol{g} \tag{4.7}$$

When the fluid flux is reduced, the slip velocity between the phases, and in turn the drag, decreases. Since the effective weight of the particles remains constant, equation (4.7) is no longer satisfied:

a net downward force accelerates the particles towards the bottom of the vessel. As these move together, preserving their equilibrium void fraction, the acceleration causes a progressive increase in the fluid-particle slip velocity and in the drag. The process continues until $n\langle \boldsymbol{f}_d \rangle_p$ attains again the equilibrium value that fulfils equation (4.7); when this happens, the suspension starts moving downwards uniformly at a constant velocity u_{de}.

Whereas in the upper region of the bed the particles surely behave as described, those located at the bottom, near the distributor, must behave differently. Not being able to move downwards, they remain motionless, soon to be joined by others arriving from above. Thus, at the bottom of the bed the solid builds up, giving rise to a growing uniform zone of stationary particles that adjust to new equilibrium conditions corresponding to voidage ε_2, zero particle velocity and fluid flux u_2.

After a very short phase characterized by the downward acceleration of the bed (which usually amounts to a very small fraction of the total transient response time), this consists of two regions, both in fluid-particle equilibrium: an upper zone with void fraction ε_1 where the particles fall at constant velocity u_{de} and a lower zone where the particles are stationary and dispersed uniformly with void fraction ε_2. Accordingly, there are two travelling interfaces: the falling surface of the bed, which moves downwards at constant velocity u_{de}, and the rising discontinuity surface, or shock wave, between the two bed regions, which travels upwards at constant velocity u_{ks}. The rearrangement terminates, and the transient state comes to an end, when the two surfaces meet. When this happens, the whole bed reaches new homogeneous equilibrium conditions with void fraction ε_2, zero particle velocity and fluid flux u_2.

Even if idealized, this description appears to be reasonable. To verify, we simulate the bed collapse of system 1, whose properties are reported in Table 4.3, choosing the initial and final values of the fluid flux equal to $1.50 \cdot 10^{-2}$ m/s and $2.72 \cdot 10^{-3}$ m/s, respectively.

Figure 4.10 shows the evolution of the bed void fraction profile. The numerical results confirm our predictions: two regions at different dilution, separated by a sharp horizontal surface, are clearly identifiable. However, whereas in the final configuration the bed is perfectly homogeneous, the initial configuration presents some regions characterized by higher voidage. These, albeit well-bounded and delimited, cannot be classified as bubbles, but do disrupt the perfect bed homogeneity. We shall return on this matter later on in § 4.4, where we analyze the stability of homogeneous systems; now we simply acknowledge the existence of these regions, realizing that the bed, albeit not bubbling, is neither perfectly homogeneous nor perfectly stable (in a formal, mathematical sense).

It is interesting to compare the numerical results of the simulations with the predictions of the theoretical model of Gibilaro et al. (1984). Based on simple kinematic considerations, this provides a mechanistic description of the response of uniform systems to sudden changes in fluid flux. Analytical expressions for the velocities u_{de} and u_{ks} are found by using one-dimensional mass conservation equations (for further details see Gibilaro, 2001); in particular, u_{de} is equal to the difference between the two fluid fluxes. Hence, to make a comparison, we must simply verify that the bed height profile found numerically is linear with a slope equal to $u_2 - u_1$.

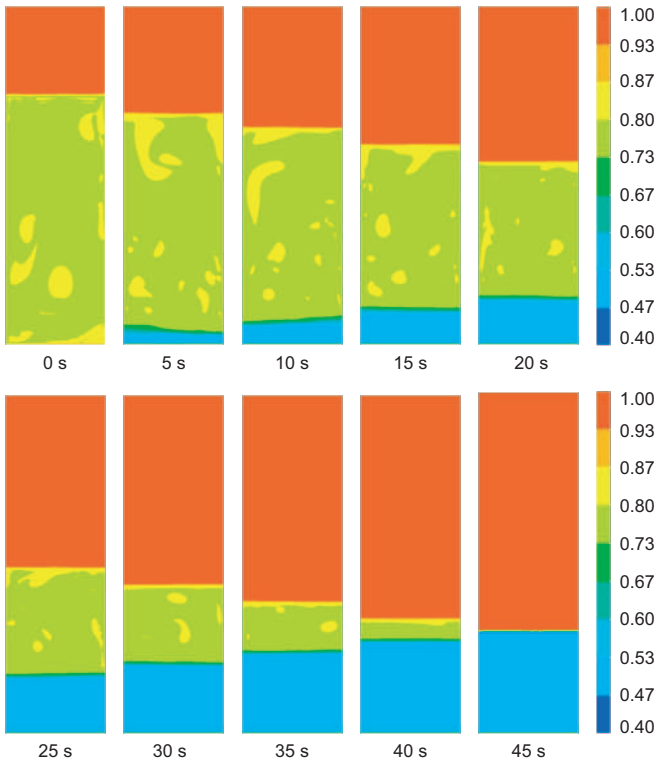

Figure 4.10: Response of a uniform fluidized bed to a sudden reduction in fluid flux. The snapshots show the void fraction profile at different times during the transient regime.

Figure 4.11 reports the bed height as a function of time. Two profiles are shown: one is numerical, obtained from the CFD simulation, while the other is theoretical, based on the model of Gibilaro et al. (1984). The latter, in particular, is the graph of the function:

$$h(t) = \begin{cases} h_1 + (u_2 - u_1)t & \text{for} \quad h < h_2 \\ \\ h_2 & \text{for} \quad h \geqslant h_2 \end{cases} \tag{4.8}$$

A perfect match is found between the two profiles; this confirms the soundness of the model, which, even if based on strikingly simple physical assumptions, yields in this case accurate predictions.

4.5.2 Dynamics of expanding liquid-fluidized uniform beds

The rise in fluid flux, from u_1 to u_2, increases the drag and accelerates the solid upwards; this motion reduces the fluid-particle slip velocity until the force regains its original value. When this occurs, the bed, still uniform, travels upwards piston-like at constant velocity u_{de}.

Fortunately, this condition is not stable, otherwise fluidized beds would not exist. Should a small disturbance cause the displacement of a particle from the top interface of the rising suspension into the clear fluid above, the fluid-particle relative velocity would drop and the resulting net downward

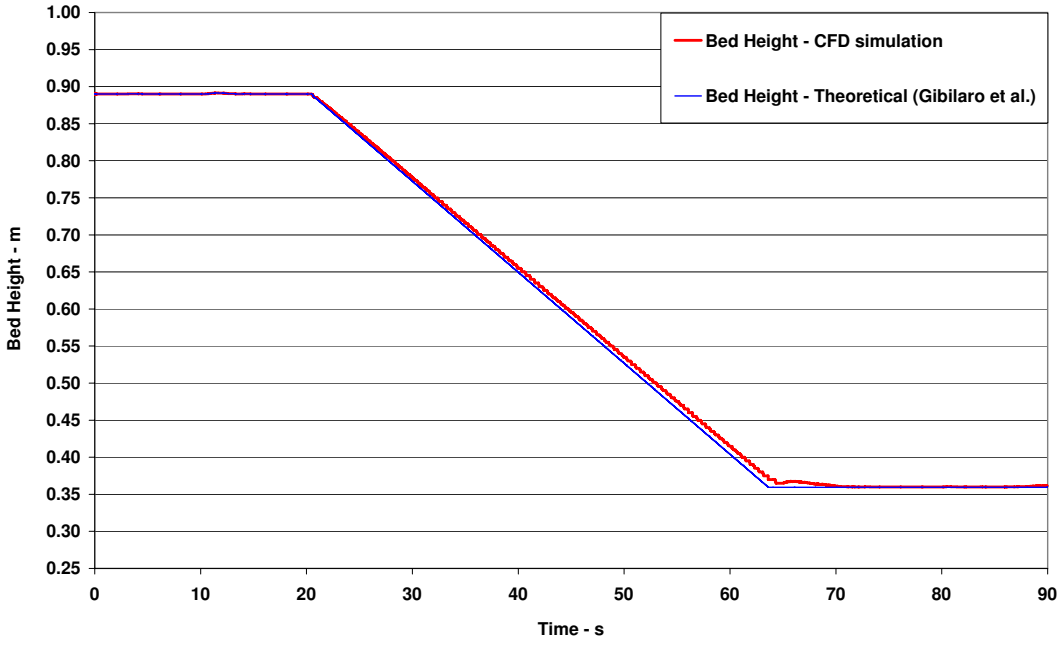

Figure 4.11: Bed height profile. Comparison between numerical results and theoretical predictions of the Gibilaro et al. (1984) model.

force on the particle would return it to its previous position. The upper interface is therefore stable. Conversely, should a particle be displaced from the bottom interface of the rising bed into the clear fluid beneath, a net downward force would push it away from the suspension. The bottom interface is therefore unstable. Particles detach from it continuously and, settling on the distributor, form a new uniform suspension. Two regions therefore coexist, both in fluid-particle equilibrium: an upper zone at void fraction ε_1 where the particles rise at constant velocity u_{de} and a lower zone at void fraction ε_2 where the particles are stationary. When the shock wave between these regions, which travels upwards at constant velocity u_{ks}, reaches the upper surface of the bed, the rearrangement terminates, the whole bed being homogeneous with void fraction ε_2 and zero particle velocity.

To verify if this really happens, we simulate the expansion of system 1, choosing this time the initial and final values of the fluid flux equal to $5.28 \cdot 10^{-3}$ m/s and $1.50 \cdot 10^{-2}$ m/s, respectively.

The evolution of the bed void fraction profile, reported in Figure 4.12, is not what is expected: the two-region structure observed in contracting beds is no longer present. Gravitational instabilities cause this dissymmetry. In an expanding bed, if the two regions were actually present, the lower one would be less dense (having higher voidage). This configuration is unstable, since the slightest disturbance would result into blobs of dilute suspension forming at the region interface and rising through the denser suspension. This mechanism, as the snapshots clearly show, sets off immediately, as soon as the particle piston starts rising; the two-region structure is thus swiftly disrupted.

Figure 4.13 reports the bed height against time. Three profiles are shown: one obtained from the mechanistic model of Gibilaro et al. (1984) and another one from a CFD simulation; the third

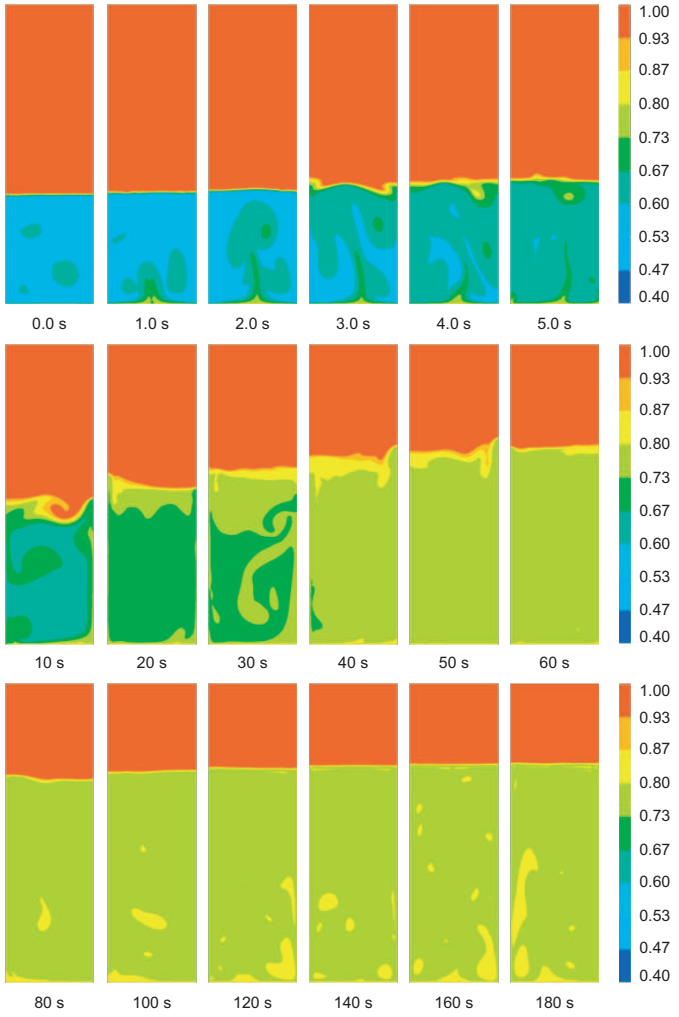

Figure 4.12: Response of a uniform fluidized bed to a sudden increase in fluid flux. The snapshots show the void fraction profile at different times during the transient regime.

will be examined later on. The computational profile indicates that the expansion is exponential, as if the driving force behind the process dwindled with time. This result is quite general; seeming to hold for any expanding particulate system (many other simulations were performed in this study; for each system examined, the time dependence always resulted to be exponential), it consents to derive a simple analytical expression for the bed height. We start by writing:

$$h(t) = a - b\exp(-ct) \tag{4.9}$$

where a, b and c are positive constants. Our aim is to express a, b and c in terms of simple parameters directly related to the fluidization process. Let us first determine the constant a. As time tends to infinite, the height of the bed tends to its steady-state value h_2; moreover, the exponential in equation (4.9) vanishes and $h(t)$ tends to a. Thus, we have:

$$a = h_2 \tag{4.10}$$

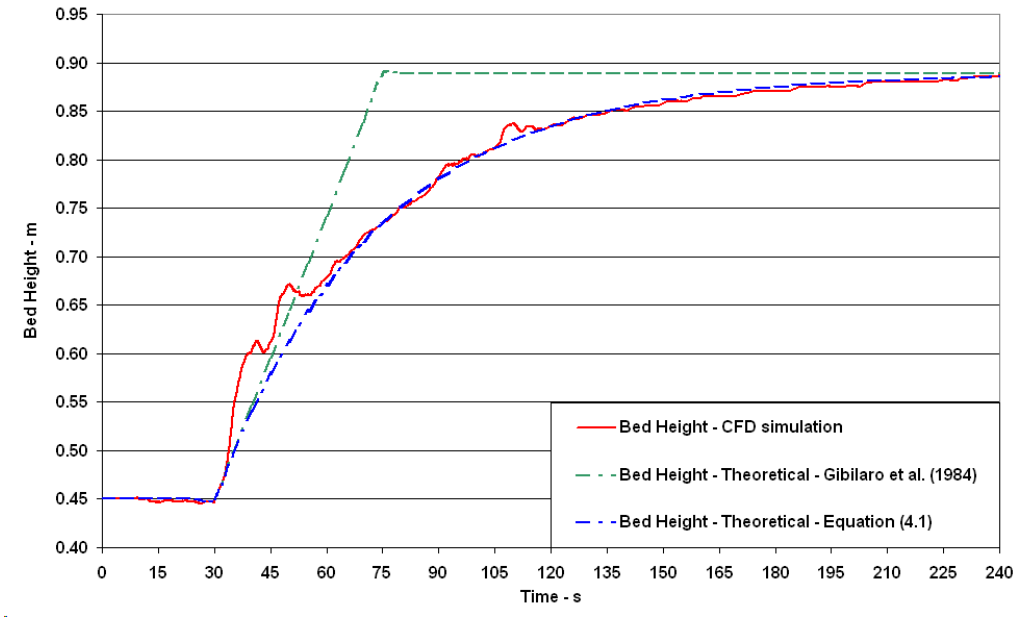

Figure 4.13: Bed height profile. Comparison between numerical results and theoretical predictions of the Gibilaro et al. (1984) model and of equation (4.1).

At time $t = 0$, the height of the bed is equal to the initial value h_1; thus, it is:

$$h(0) = h_2 - b = h_1 \quad \Rightarrow \quad b = h_2 - h_1 \tag{4.11}$$

To determine the last constant, we derive $h(t)$. The derivative is equal to:

$$\frac{dh}{dt}(t) = c(h_2 - h_1)\exp(-ct) \tag{4.12}$$

As pointed out, the rate of change of the bed height is not equal to the difference in fluid flux, since the two-region structure is disrupted by the internal mixing. This occurs as soon as the flux is changed. Accordingly, the derivative $h'(t)$ is in general different from $u_2 - u_1$. However, the equality between these two quantities can be assumed to hold at the very beginning of the process, that is in the limit of a vanishingly small time. Thus, we have:

$$\frac{dh}{dt}(0) = c(h_2 - h_1) = u_2 - u_1 \quad \Rightarrow \quad c = \frac{u_2 - u_1}{h_2 - h_1} \tag{4.13}$$

whence equation (4.1), hereunder reported for convenience, is found:

$$h(t) = h_2 - (h_2 - h_1)\exp\left(-\frac{u_2 - u_1}{h_2 - h_1}\,t\right)$$

This expression indicates the time required by an expanding homogeneous suspension to attain new equilibrium conditions, provided that these, as in liquid-fluidized beds, are hydrodynamically stable. Figure 4.13 reports also its diagram, comparing it to the profile obtained numerically. An almost perfect match is found, showing that the assumption used in equation (4.13) is correct.

The exponential behaviour just described is not found only in our simulations. Similar experimental and computational results (but not derived by using the multifluid modelling approach) are reported in the literature; we cite the experimental findings mentioned in Gibilaro (2001) and the numerical results of Pan et al. (2002) obtained by direct numerical simulation (refer to §2.2).

4.6 Stability of the uniformly fluidized state

The stability of the uniformly fluidized state is investigated first analytically using conventional linear stability analysis and then computationally integrating the averaged equations of motion.

4.6.1 Linear stability analysis

The averaged equations of motion reported in Table 4.1 consent to study analytically the stability of uniform fluidized suspensions. Following Gibilaro (2001), we write the equations in the direction of the vertical axial coordinate x, we neglect the effective stress in both phases and we consider in the fluid-particle interaction only the buoyancy, drag and elastic forces. In this one-dimensional formulation, the continuity equations are given by:

$$\frac{\partial \varepsilon}{\partial t} + \frac{\partial}{\partial x}\Big(\varepsilon \langle u \rangle_f\Big) = 0 \quad ; \quad \frac{\partial \phi}{\partial t} + \frac{\partial}{\partial x}\Big(\phi \langle v \rangle_p\Big) = 0 \tag{4.14}$$

Their sum provides the mass conservation equation for the suspension:

$$\frac{\partial}{\partial x}\Big(\varepsilon \langle u \rangle_f + \phi \langle v \rangle_p\Big) = 0 \tag{4.15}$$

The total flux of suspension is therefore constant. At the bed distributor, the fluid flux is equal to the superficial fluid velocity u_s and the solid flux is zero; thus, it is:

$$\varepsilon \langle u \rangle_f + \phi \langle v \rangle_p = u_s \quad \Leftrightarrow \quad \langle u \rangle_f - \langle v \rangle_p = \frac{u_s - \langle v \rangle_p}{\varepsilon} \tag{4.16}$$

This equation shows that the slip velocity between the phases is a function of $u_s - \langle v \rangle_p$ and ε. The linear momentum equation of conservation for the particle phase is:

$$\phi \rho_p \left(\frac{\partial \langle v \rangle_p}{\partial t} + \langle v \rangle_p \frac{\partial \langle v \rangle_p}{\partial x} \right) = n \langle \Phi \rangle_p^e + n \langle f_e \rangle_p \tag{4.17}$$

where $n \langle \Phi \rangle_p^e$ lumps together drag force and effective weight, whereas $n \langle f_e \rangle_p$ denotes the elastic force; both refer to the unit volume of suspension. In general, these forces are functions of the fluid-particle slip velocity and void fraction; however, equation (4.16) allows writing:

$$n \langle \Phi \rangle_p^e = F_1(u_s - \langle v \rangle_p, \varepsilon) \quad ; \quad n \langle f_e \rangle_p = F_2(u_s - \langle v \rangle_p, \varepsilon) \tag{4.18}$$

where F_1 and F_2 are generic constitutive functions with arguments $u_s - \langle v \rangle_p$ and ε. The variable $\langle u \rangle_f$ has therefore been eliminated. This result shows that the dynamical equations of the two phases are not coupled. Since the motion of each phase is governed by an independent set of transport equations, we can restrict the analysis to that of the solid alone.

Equations (3.99) and (3.113) provide closure for F_1 and F_2; if we adopt the classical definition of buoyancy force, equation (3.4), it is:

$$F_1 = (1-\varepsilon)\left[\frac{6\hat{F}}{\pi d_p^3} - (\rho_p - \rho_f)g\right] \quad ; \quad F_2 = E_r \frac{\partial \varepsilon}{\partial x} \tag{4.19}$$

In these expressions the drag force per unit particle $\hat{F}$ and the elastic modulus E_r must be considered functions of $u_s - \langle v \rangle_p$ and ε. In homogeneous fluidized suspensions, the particles are motionless and the solid compaction is uniform; accordingly, convection is absent and the elastic force vanishes. Since the system is stationary, equation (4.17) yields:

$$F_1(u_s - 0, \varepsilon) = 0 \tag{4.20}$$

This equation provides all the equilibrium states (u_s, ε) in which a uniform fluidized suspension can reside; for a given fluid flux, a unique value of the voidage, corresponding to the equilibrium expansion of the system, fulfills equation (4.20). Let us now consider a generic equilibrium state represented by $u_s = \bar{u}_s$, $\langle v \rangle_p = 0$ and $\varepsilon = \bar{\varepsilon}$. Keeping u_s constant, we intend to examine the stability of this solution against small perturbations in ε and $\langle v \rangle_p$ using conventional linear stability analysis. We start by linearizing the continuity equation, which we write in the form:

$$\frac{\partial \hat{\varepsilon}}{\partial t} + \langle v \rangle_p \frac{\partial \hat{\varepsilon}}{\partial x} - (1 - \bar{\varepsilon} - \hat{\varepsilon}) \frac{\partial \langle v \rangle_p}{\partial x} = 0 \tag{4.21}$$

Here $\hat{\varepsilon}$ is the deviation of the void fraction from its steady-state value $\bar{\varepsilon}$. Note that $\langle v \rangle_p$ is already a deviation about the equilibrium value of 0. We now eliminate the non-linear terms, which contain the product of two or more independent variables, obtaining:

$$\frac{\partial \hat{\varepsilon}}{\partial t} - (1 - \bar{\varepsilon}) \frac{\partial \langle v \rangle_p}{\partial x} = 0 \tag{4.22}$$

Proceeding similarly, we approximate the left-hand side of equation (4.17) by writing:

$$\phi \rho_p \left(\frac{\partial \langle v \rangle_p}{\partial t} + \langle v \rangle_p \frac{\partial \langle v \rangle_p}{\partial x} \right) \approx (1 - \bar{\varepsilon}) \rho_p \frac{\partial \langle v \rangle_p}{\partial t} \tag{4.23}$$

Since u_s is kept constant, we can regard $n \langle \Phi \rangle_p^e$ and $n \langle f_e \rangle_p$ as functions only of $\langle v \rangle_p$ and $\hat{\varepsilon}$. Truncating the Taylor expansion of $\hat{F}_1(\langle v \rangle_p, \hat{\varepsilon})$ at the first order yields:

$$\hat{F}_1(\langle v \rangle_p, \hat{\varepsilon}) \approx \hat{F}_1(0,0) + A \langle v \rangle_p + B \hat{\varepsilon} \tag{4.24}$$

where, by definition, it is:

$$A \equiv \frac{\partial \hat{F}_1}{\partial \langle v \rangle_p}(0,0) \quad ; \quad B \equiv \frac{\partial \hat{F}_1}{\partial \hat{\varepsilon}}(0,0) \tag{4.25}$$

In stationary conditions, the drag force counterbalances the effective weight; accordingly, $\hat{F}_1(0,0)$ is equal to zero. Moreover, equation (4.19) gives:

$$A = \Big[(1-\bar{\varepsilon})(\rho_p - \rho_f)g\Big]\frac{D-2}{\bar{u}_s} \quad ; \quad B = \Big[(1-\bar{\varepsilon})(\rho_p - \rho_f)g\Big]\frac{(D-2)n_e}{\bar{\varepsilon}} \tag{4.26}$$

where D is defined by equation (3.107). If we use the Richardson & Zaki (1954) correlation to link $\bar{u}_s$ and n_e, the ratio A/B can be expressed as:

$$\frac{A}{B} = \frac{1-\bar{\varepsilon}}{u_k} \quad ; \quad u_k \equiv u_t n_e (1-\bar{\varepsilon})\bar{\varepsilon}^{n_e - 1} \tag{4.27}$$

u_k is referred to as *kinematic wave velocity*. It is possible to demonstrate that this parameter is equal to the shock wave velocity u_{ks} introduced in § 4.5 in the limit of vanishingly small variations of superficial fluid flux (Gibilaro, 2001); in other words, it is:

$$u_k = \lim_{\Delta u \to 0} u_{ks} \quad ; \quad \Delta u \equiv u_2 - u_1 \tag{4.28}$$

To linearize $\hat{F}_2(\langle v \rangle_p, \hat{\varepsilon})$ we expand the elastic modulus in a Taylor series about the equilibrium state, and we neglect all the resulting non-linear terms; thus, we write:

$$\hat{F}_2(\langle v \rangle_p, \hat{\varepsilon}) \approx \left(E_r(0,0) + \frac{\partial E_r}{\partial \langle v \rangle_p}(0,0)\langle v \rangle_p + \frac{\partial E_r}{\partial \hat{\varepsilon}}(0,0)\hat{\varepsilon}\right)\frac{\partial \hat{\varepsilon}}{\partial x} \approx E_r^e \frac{\partial \hat{\varepsilon}}{\partial x} \tag{4.29}$$

$E_r^e = E_r(0,0)$ is the elastic modulus computed in equilibrium conditions; its expression, derived in Chapter 3, is given by equation (3.111). If we now introduce equations (4.23), (4.24) and (4.29) into equation (4.17), the latter can be arranged in the form:

$$(1-\bar{\varepsilon})\frac{\partial \langle v \rangle_p}{\partial t} = -K(1-\bar{\varepsilon})\langle v \rangle_p - K u_k \hat{\varepsilon} + u_d^2 \frac{\partial \hat{\varepsilon}}{\partial x} \tag{4.30}$$

Here u_d and K are defined to be:

$$u_d \equiv \sqrt{\frac{E_r^e}{\rho_p}} \quad ; \quad K \equiv -\frac{A}{(1-\bar{\varepsilon})\rho_p} \tag{4.31}$$

u_d is referred to as *dynamic wave velocity*. Dynamic waves occur when imposed perturbations in void fraction generate moving concentration gradients; u_d is the velocity of these compression waves (Gibilaro, 2001). From equation (3.111), we have:

$$u_d = \left(-\Big[(1-\bar{\varepsilon})(\rho_p - \rho_f)g\Big]\frac{2d_p H}{3\rho_p}\right)^{1/2} \tag{4.32}$$

Deriving equations (4.22) and (4.30) with respect to t and x, respectively, and subtracting the two resulting expressions yields:

$$\frac{\partial^2 \hat{\varepsilon}}{\partial t^2} - u_d^2 \frac{\partial^2 \hat{\varepsilon}}{\partial x^2} + K\left(\frac{\partial \hat{\varepsilon}}{\partial t} + u_k \frac{\partial \hat{\varepsilon}}{\partial x}\right) = 0 \tag{4.33}$$

where the linearized continuity equation has been used to eliminate the variable $\langle v \rangle_p$. We look for irreducible solutions of the form (Georgi, 1993):

$$\hat{\varepsilon}(x,t) = \hat{\varepsilon}_a \exp\Big[at + ik(x - \nu_w t)\Big] \tag{4.34}$$

This is a travelling planar wave with initial amplitude $\hat{\varepsilon}_a$, amplitude growth rate a, wave number k and wave velocity ν_w. Introducing this function into equation (4.33) gives a complex algebraic equation that allows computing a and k. The result is:

$$a = \frac{K}{2\nu_w}(u_k - \nu_w) \quad ; \quad k^2 = \frac{K^2}{4\nu_w^2}\left(\frac{u_k^2 - \nu_w^2}{\nu_w^2 - u_d^2}\right) \tag{4.35}$$

Homogeneous fluidization is stable when the amplitude of $\hat{\varepsilon}(x,t)$ decays with time: a must therefore be negative. Since K is positive (this can be readily verified), this condition requires that ν_w be greater than u_k. If this happens, $u_k^2 - \nu_w^2$ is negative, and real values of k can be obtained only if u_d is greater than ν_w. We then conclude that uniform fluidization is stable when the dynamic wave velocity is greater than the kinematic wave velocity. Equating the two allows determining the void fraction that marks the onset of instability; this coincides with the zero of the stability function:

$$S_r(\varepsilon) = 1 - \left(-\frac{2H}{3n_e^2} \cdot \frac{d_p g}{u_t^2} \cdot \frac{\rho_p - \rho_f}{\rho_p} \cdot \frac{\varepsilon^{2(1-n_e)}}{1-\varepsilon}\right)^{1/2} \tag{4.36}$$

obtained from equations (4.27) and (4.32). Uniform fluidization is stable as long as $S_r(\varepsilon)$ is negative; when it becomes positive, void fraction perturbations no longer die away. Nothing is known, however, about their behaviour; loss of stability, therefore, does not necessarily entail bubbling. For gas-fluidized systems, though, the two are usually concomitant, and the stability limit given by $S_r(\varepsilon)$ is referred to as *minimum bubbling voidage*.

Adopting a similar procedure, Foscolo & Gibilaro (1987) and Jean & Fan (1992) have derived stability functions based on the equations of closure for buoyancy, drag and elastic forces discussed in §3.5.2 and §3.5.3, respectively. These functions – in particular that of Jean & Fan, which is based on the same definition of buoyancy force – can be regarded as asymptotic expressions, valid in the viscous and inertial limits, of the more general equation (4.36). The stability function of Foscolo & Gibilaro has already been presented in §3.5; its expression, given by equation (3.76), is:

$$S_f(\varepsilon) = 1 - \left(\frac{3.2}{n_e^2} \cdot \frac{d_p g}{u_t^2} \cdot \frac{\rho_p - \rho_f}{\rho_p} \cdot \frac{\varepsilon^{2(1-n_e)}}{1-\varepsilon}\right)^{1/2}$$

Jean & Fan instead advance the function:

$$S_j(\varepsilon) = 1 - \left(\frac{3.2}{n_e^2} \cdot \frac{d_p g}{u_t^2} \cdot \frac{\rho_p - \rho_f}{\rho_p} \cdot \frac{\varepsilon^{1-2n_e}}{1-\varepsilon} \right)^{1/2} \tag{4.37}$$

The only difference between the two is the buoyancy force definition: Foscolo & Gibilaro relate it to the gradient of the averaged fluid pressure, while Jean & Fan endorse the classical definition (3.4). In all other respects, the two functions are equivalent. Since, as can be readily verified, it is:

$$\lim_{Re^* \to 0} H(\varepsilon, Re^*) = \lim_{Re^* \to \infty} H(\varepsilon, Re^*) = -\frac{4.80}{\varepsilon} \tag{4.38}$$

in the viscous and inertial limits equation (4.36) reduces to equation (4.37), confirming therefore what previously anticipated.

4.6.2 Experimental validation of the theoretical results

Linear stability analysis is used to investigate the behaviour of gas-fluidized Group A suspensions (Geldart, 1973). Results based on the stability functions (3.76), (4.36) and (4.37) are compared with experimental data by Xie & Geldart (1995), Lettieri (1999) and Lettieri et al. (2001).

Powder number	Material –	d_p μm	ρ_p kg/m^3	F_{45} %	$c.v.$ –	Geldart Group
Experimental data by Xie & Geldart (1995)						
1	FCC	137	1210	0.00	0.60	A
2	FCC	130	1220	0.00	0.60	A
3	FCC	115	1230	0.00	0.70	A
4	FCC	110	1240	0.00	0.60	A
5	FCC	94	1260	0.00	1.00	A
6	FCC	71	1300	0.01	0.70	A
7	FCC	68	1310	0.11	1.00	A
8	FCC	63	1310	0.20	1.60	A
9	FCC	47	1350	0.22	1.20	A
10	FCC	26	1420	0.84	1.20	A
Experimental data by Lettieri (1999) and Lettieri et al. (2001)						
11	Silica	109	880	4	0.39	A
12	FCC	71	1420	5	0.34	A
13	Ballotini	62	2550	2	0.26	A
14	FCC	57	1420	16	0.58	A
15	FCC	49	1420	25	0.61	A

Table 4.5: Physical properties of the powders investigated.

Powder number	Temperature ^oC	ε^{mb}_{exp} $-$	$\varepsilon^{mb}_{F\&G}$ $-$	$\varepsilon^{mb}_{J\&F}$ $-$	$\varepsilon^{mb}_{M\&L}$ $-$
Ambient temperature					
1	20	0.418	0.359	0.421	0.401
2	20	0.441	0.369	0.431	0.413
3	20	0.449	0.397	0.456	0.440
4	20	0.454	0.406	0.465	0.450
5	20	0.481	0.440	0.497	0.485
6	20	0.482	0.503	0.556	0.549
7	20	0.495	0.512	0.565	0.559
8	20	0.539	0.532	0.583	0.578
9	20	0.581	0.606	0.654	0.652
10	20	0.646	0.855	0.896	0.902
11	20	0.448	0.456	0.513	0.500
12	20	0.553	0.483	0.536	0.529
13	20	0.514	0.430	0.485	0.477
14	20	0.583	0.537	0.588	0.584
15	20	0.542	0.578	0.626	0.624
Higher temperatures					
12	100	0.579	0.512	0.563	0.559
12	200	0.593	0.543	0.592	0.590
12	300	0.595	0.568	0.616	0.615
12	400	0.607	0.588	0.635	0.635
12	500	0.608	0.609	0.655	0.656
12	600	0.611	0.629	0.674	0.675
13	100	0.509	0.452	0.505	0.500
13	200	0.507	0.480	0.532	0.529
13	300	0.563	0.503	0.553	0.551

Table 4.6: Experimental and theoretical values of the minimum bubbling voidage. $\varepsilon^{mb}_{F\&G}$, $\varepsilon^{mb}_{M\&L}$ and $\varepsilon^{mb}_{J\&F}$ are derived from the stability functions (3.76), (4.36) and (4.37), respectively.

The analysis involves two sets of powders. The first, analyzed by Xie & Geldart (1995), comprises ten FCC catalysts with similar particle densities, mean particle diameters in the range $26 - 137$ μm and a very low amount of fines (F_{45} less than 0.8% by weight). The second, studied by Lettieri (1999) and Lettieri et al. (2001), includes various kinds of FCC, Ballotini and Silica powders with different densities, mean particle diameters in the range $49-109$ μm and a higher content of fines (F_{45} between 2 and 25% by weight). Table 4.5 gives the main physical properties of these powders. The fluidizing medium is air and nitrogen for the first and second sets of materials, respectively. Table 4.6 reports the experimental and theoretical values of the minimum bubbling voidage for all the systems tested. The

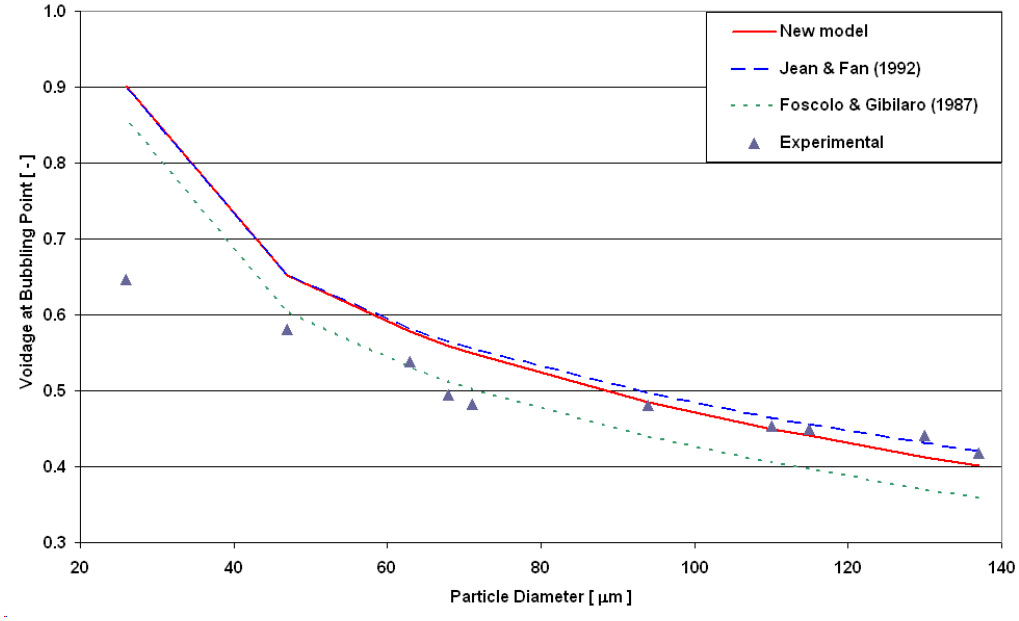

Figure 4.14: Comparison between theoretical and experimental minimum bubbling void fractions for various powders at ambient temperature. Experimental data by Xie & Geldart (1995).

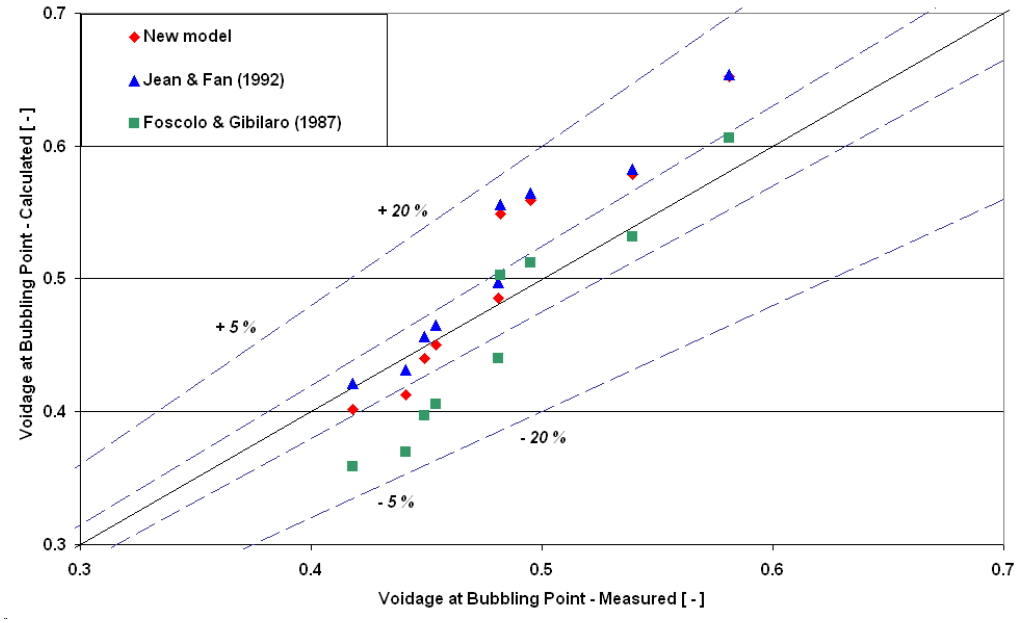

Figure 4.15: Comparison between theoretical and experimental minimum bubbling void fractions for various powders at ambient temperature. Experimental data by Xie & Geldart (1995).

predicted void fractions are denoted by $\varepsilon^{mb}_{F\&G}$, $\varepsilon^{mb}_{J\&F}$ and $\varepsilon^{mb}_{M\&L}$, the first two relating to the models of Foscolo & Gibilaro (1987) and Jean & Fan (1992), respectively, while the last one to our new model; the experimental void fractions are instead denoted by ε^{mb}_{exp}. Note that referring to these quantities as minimum *bubbling* void fractions is legitimate because experimental evidence shows quite clearly that bubbling occurs as soon as the stability is lost.

We first consider ambient operating conditions and the powders of Xie & Geldart. Figure 4.14 reports the minimum bubbling voidage against the mean particle diameter; Figure 4.15 compares the void fraction experimental and theoretical values. The predictions of our model agree well with the experimental data (error within $\pm 5\%$) for powders with mean particle diameter greater than about 90 μm; in this range, the model of Foscolo & Gibilaro underestimates ε^{mb}_{exp} (error within $\pm 20\%$), anticipating the onset of bubbling. For diameters between 70 and 40 μm, conversely, the theoretical results of Foscolo & Gibilaro are more accurate (error within $\pm 5\%$), whereas our model delays the transition between particulate and aggregative fluidization. Finally, for particle sizes smaller than about 40 μm, both models are inaccurate (error greater than $\pm 20\%$). A possible explanation for the poor quality of the predictions in this size range can be found in the role, altogether neglected in the present models, played by the interparticle forces, as discussed by Geldart & Wong (1984), Geldart & Wong (1985), Xie & Geldart (1995) and Lettieri (1999).

In the whole size range investigated, from 26 to 137 μm, good agreement is found between the results of Jean & Fan and ours. This had to be expected because a) the two models are based on the same buoyancy force definition, b) the study involves only *equilibrium states* and does not extend to non-homogenous systems, c) the majority of uniform gas-fluidized powders are operated in the *viscous regime*, or very close to it, where the drag force corrective function $\varphi(\varepsilon, Re)$ is not dominant. Our model is more general than the other two, for it is based on constitutive equations of broad validity; these allow the study of any kind of fluidization regimes, without restrictions to uniform suspensions. In this analysis, however, since we investigate the stability of homogeneous systems using linearized transport equations, the differences between the models are somewhat reduced. In this regard, refer to equations (3.111) and (3.112), which show the asymptotic behaviour of our elastic modulus when equilibrium and viscous conditions are approached.

Figure 4.16 plots theoretical against experimental values of the minimum bubbling voidage for the powders investigated by Lettieri (1999) and Lettieri et al. (2001) at ambient operating conditions. Our model yields satisfactory results, being capable of predicting the instability onset with a smaller margin of error (within $\pm 5\%$) than Foscolo & Gibilaro's model. The only exception is represented by the FCC powder 15 of Table 4.5, which has the smallest diameter of the group under examination (49 μm). Good agreement is again found between our predictions and Jean & Fan's, especially for very small particle mean diameters.

We now extend the analysis to higher operating temperatures. Figure 4.17 reports the minimum bubbling voidage, experimental and theoretical, against the temperature for the FCC powder 12 of Table 4.5; Figure 4.18 compares expected and measured void fractions for the same powder. No model predicts well the trend of $\varepsilon^{mb}_{exp}(T)$: whereas experimental evidence shows a slight increase of

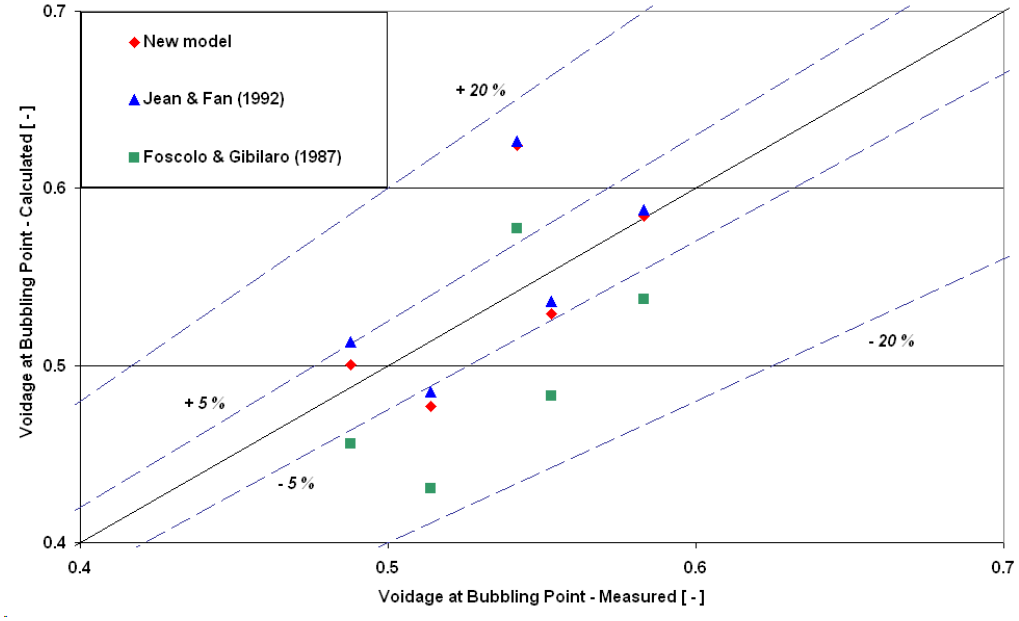

Figure 4.16: Theoretical against experimental minimum bubbling void fractions for various powders at ambient temperature. Experimental data by Lettieri (1999).

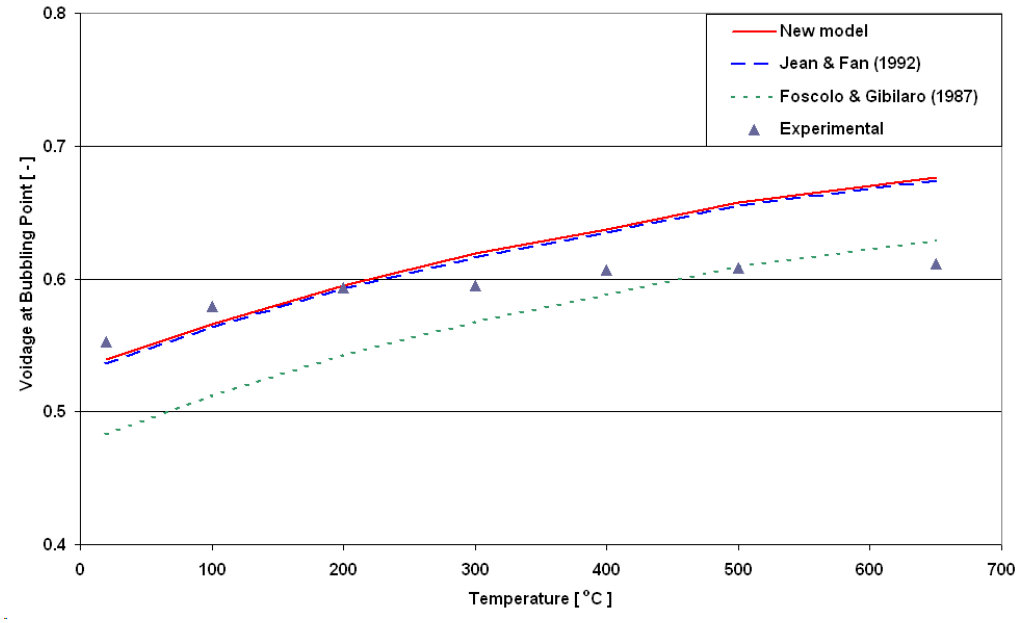

Figure 4.17: Comparison between theoretical and experimental minimum bubbling void fractions for the FCC powder 12 of Table 4.5 at different temperatures. Experimental data by Lettieri (1999).

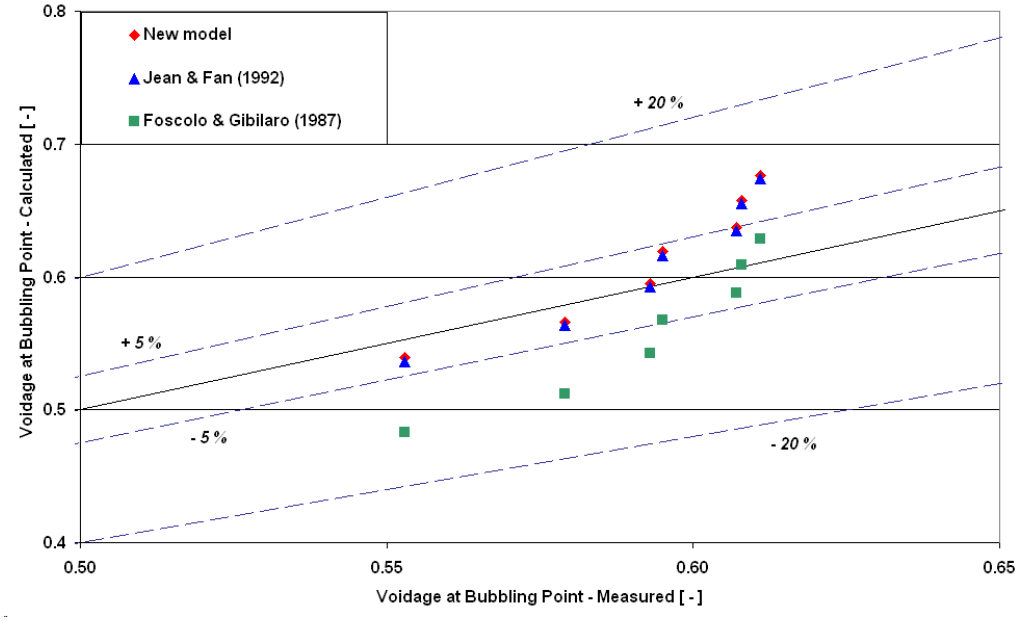

Figure 4.18: Comparison between theoretical and experimental minimum bubbling void fractions for the FCC powder 12 of Table 4.5 at different temperatures. Experimental data by Lettieri (1999).

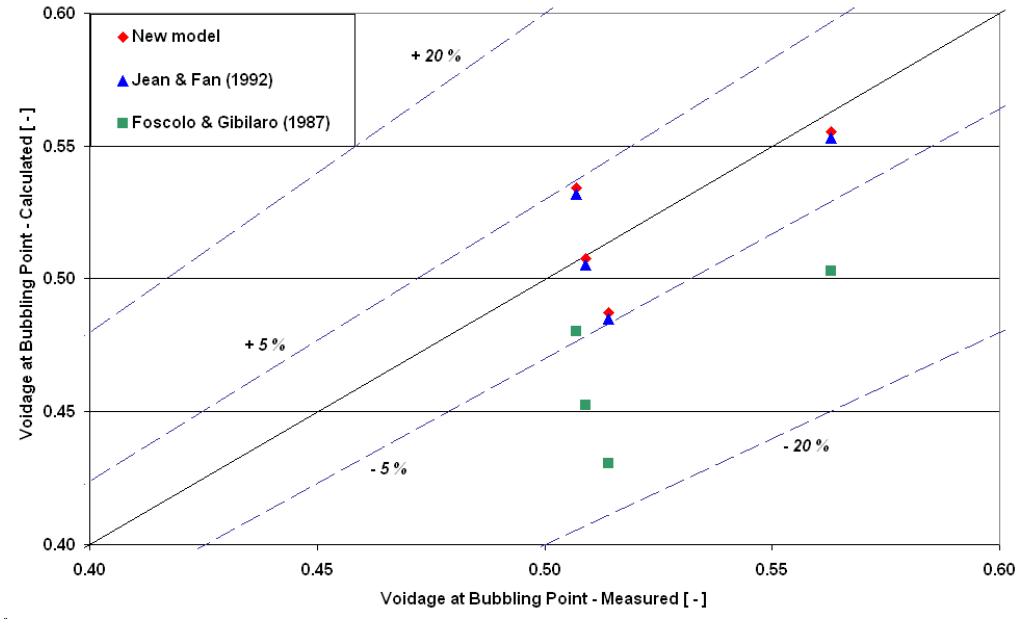

Figure 4.19: Theoretical against experimental minimum bubbling void fractions for the Ballotini powder 13 of Table 4.5 at different temperatures. Experimental data by Lettieri (1999).

the voidage with the temperature, the predicted trends are steeper. This discrepancy was extensively discussed by Lettieri et al. (2001), who modified the elastic force closure of Foscolo & Gibilaro to account for the effect of the interparticle forces when temperature is increased.

To conclude, Figure 4.19 compares theoretical and experimental minimum bubbling voidages for the Ballotini powder 13 of Table 4.5 at different temperatures. Since the interparticle forces seem to be negligible, our model and Jean & Fan's yield good predictions; the results of Foscolo & Gibilaro, conversely, anticipate the onset of bubbling.

4.6.3 Computational study of the uniformly fluidized state stability

Linear stability analysis is an effective method of studying uniformly fluidized suspensions – without the aid of powerful personal computers, the only possible method. The information that this analysis provides, however, is limited, for nothing can be said about the behaviour of the perturbations when instability is detected. To have a complete picture, we must solve the averaged equations of motion without simplifications.

The inclusion of the elastic force has a dramatic effect on the linearized one-dimensional transport equations: without it, formal stability of the uniformly fluidized state is not possible (Jackson, 1963); once the force is accounted for, however, the state is no longer intrinsically unstable, and the averaged equations yield a simple quantitative criterion to discriminate between stable and unstable particulate fluidization. Albeit the void fraction that marks the onset of instability does not necessarily coincide with the minimum bubbling voidage, experimental evidence shows that in gas-fluidized suspensions this often occurs: at low fluid fluxes these systems display an unambiguously homogeneous structure, which small particle-free voids abruptly disrupt when a critical, well-defined value of the superficial fluid velocity is reached.

We now integrate numerically the equations of motion of our model (reported in Table 4.1 and described in §4.2) to simulate the transition of a gas-fluidized Group A powder (Geldart, 1973) from the particulate to the aggregative state. The intent is to see if a) also computationally the elastic force plays an important role, b) the onset of bubbling is as abrupt as experimental evidence shows, c) the analytical (through linear stability analysis) and numerical predictions of the minimum bubbling void fraction agree.

The system investigated consists of particles of density $2500\ \mathrm{kg/m^3}$ and mean diameter $71.5\ \mu\mathrm{m}$ fluidized by air (density $1.19\ \mathrm{kg/m^3}$ and viscosity $1.82 \cdot 10^{-5}$ Pa s). This suspension initially expands homogeneously; then, when the fluid flux reaches a value of about $1.55\ \mathrm{cm/s}$, corresponding to a void fraction of about 0.470, the formation of tiny bubbles is observed.

The application of linear stability analysis yields different results depending on the fluid dynamic model employed – more specifically, on the closures adopted for the buoyancy, drag and elastic forces. The model of Foscolo & Gibilaro (1987) predicts loss of stability at a fluid flux of $0.55\ \mathrm{cm/s}$, resulting

into a void fraction of 0.403. Thus, if these values mark the onset of bubbling, no homogeneous expansion occurs, and the system behaves as a Group B powder. This conclusion is clearly at variance with experimental evidence. Our model, on the other hand, predicts loss of stability at a fluid flux of about 1.00 cm$/$s, corresponding to a void fraction of about 0.460. In the assumption that at higher fluid flow rates bubbling immediately occurs, this result agrees satisfactorily with the experimental values previously reported.

To check these findings computationally, we simulate the system at different superficial fluid velocities. Figure 4.20 reports the void fraction profiles, in pseudo stationary conditions, obtained numerically. The result is quite unexpected. At low fluid fluxes, the bed is almost entirely uniform; when the superficial fluid velocity is increased to the value of 1.00 cm$/$s, some regions more diluted than the bulk of the bed appear. They cannot be classified as bubbles, however, for their average void fraction is much lower than the threshold value of about 0.80 or 0.90 usually ascribed to real bubbles (Yates et. al, 1994). This seems to agree with Jackson's line of reasoning: loss of formal stability does not necessarily entail bubbling. Small perturbations grow, more in dimension than in dilution, but do not develop into bubbles. Their ultimate fate, unpredictable when linear stability analysis is applied, is revealed by the simulation snapshots. As shown in Figure 4.21, which refer to a fluid flux of 1.00 cm$/$s, the disturbances origin within the bed (anywhere, not necessarily at the bottom), grow in dimension whilst preserving their dilution, and eventually shrink and disappear. These results do not match the experimental evidence, since, when the homogeneous structure of the bed is lost, almost immediately vigorous bubbling ensues.

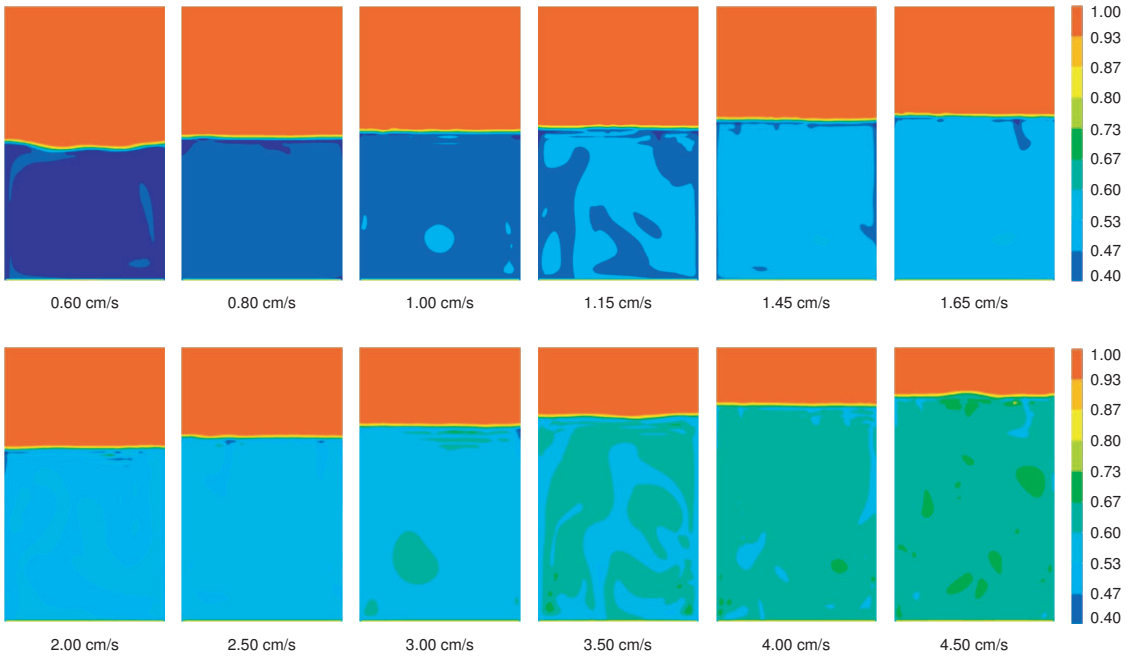

Figure 4.20: Computational stability analysis for uniform gas-fluidized beds. Void fraction profiles at different superficial fluid velocities when pseudo stationary conditions are reached.

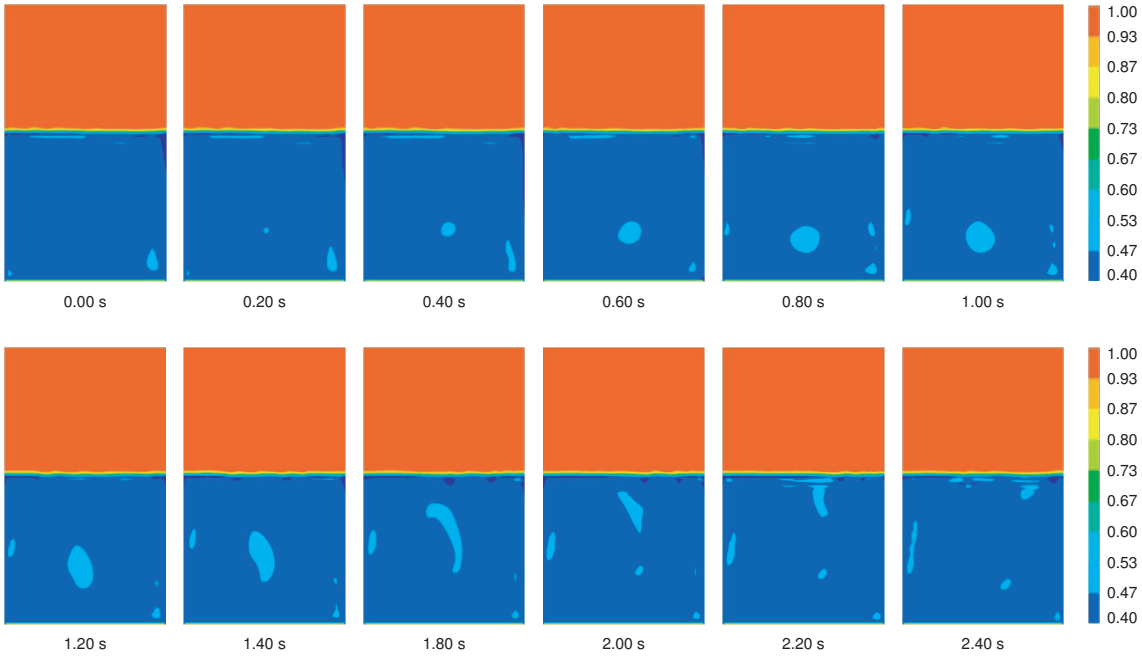

Figure 4.21: Dynamic evolution of small disturbances within homogeneous gas-fluidized systems. The disturbances origin within the bed, grow in dimension whilst preserving their dilution, and then shrink and disappear.

If the fluid flux is further increased, the regions at higher dilution become progressively more and more extended, until eventually the whole system evolves towards a new configuration that is essentially uniform and at higher voidage (observe, for example, the snapshots in Figure 4.20 where the fluid flux is set to 1.15 cm/s and 1.45 cm/s). At higher superficial fluid velocities, the dynamic response of the system does not change qualitatively: for $u_s = 2.00\,\mathrm{cm/s}$, for instance, the system displays once again an almost perfect uniformity; for $u_s = 3.00\,\mathrm{cm/s}$, well-defined discontinuities at higher void fraction appear again. This trend continues as the fluid flux is raised. The height of the bed gradually increases, along with the average void fraction of the suspension, but the structure of the system remains substantially unaltered, mainly homogeneous with regions at higher dilution which occasionally appear and then vanish. Of course, the higher the fluid flux, the more expanded the bed and the more dilute the regions; thus, eventually, when the fluid velocity is raised sufficiently, bubbles are indeed formed. This is shown in Figure 4.22A, where, at a flux of 15.00 cm/s, voids are clearly visible. The process that leads to the formation of these voids, the degree of bed expansion when proper bubbling develops and, more generally, the bed structure, are however somewhat different from those found experimentally. Experimental evidence suggests that, when the flow rate is increased sufficiently, bubbling occurs quite suddenly – not smoothly, like in the simulations; moreover, the transition to the aggregative regime is followed by a rather marked contraction of the bed, which does not preserve its former expansion.

It might be argued that the dynamics are not correctly predicted since the model does not account for the effect of the interparticle forces, whose role might be dominant in some gas-fluidized systems.

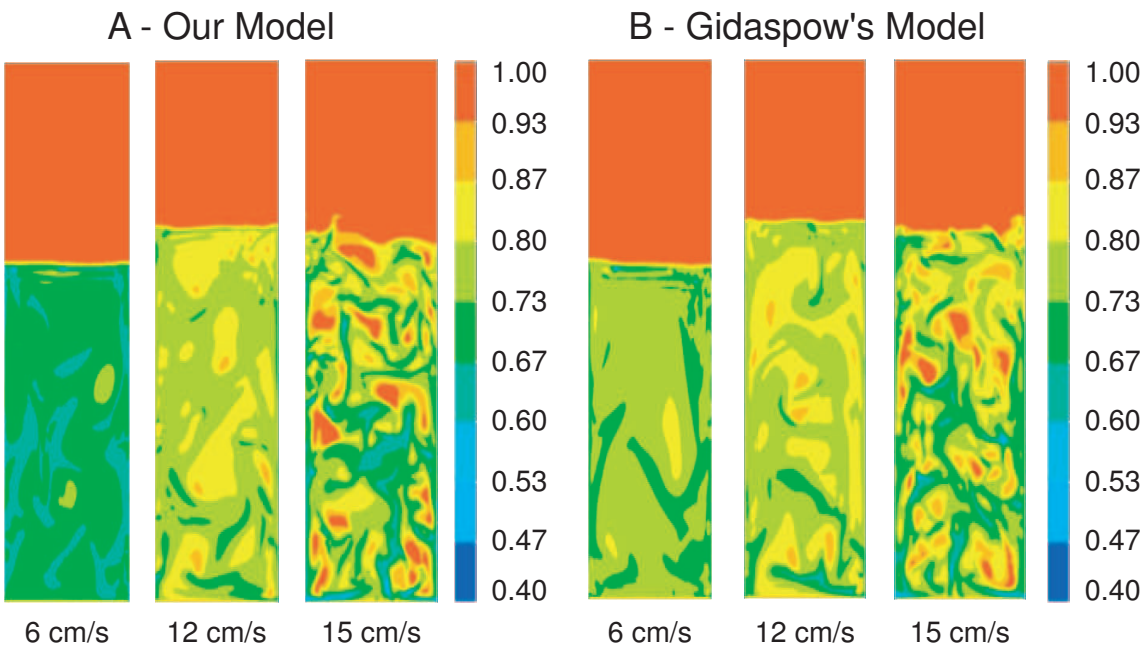

Figure 4.22: Computational stability analysis for uniform gas-fluidized beds. Void fraction profiles at different superficial fluid velocities when pseudo stationary conditions are reached. The snapshots on the left refer to our model, those on the right to the model of Gidaspow (1994).

The action of such forces, nevertheless, would result into a greater stability of the fluidized suspension and a delayed transition into the bubbling regime. In other words, neglecting this contribution should lead to premature onset of bubbling and an underestimation of the minimum bubbling void fraction. This is not what we observe in the snapshots; in fact, if anything, the bed seems to retain for too long its uniform structure. Moreover, for liquid-fluidized beds, where the interparticle forces do not affect significantly the dynamics, a similar qualitative behaviour is found: voids do not form (unless, perhaps, the fluid flux is increased to unrealistic values), but, as previously shown in Figure 4.10, regions at higher degree of dilution do appear, and their qualitative behaviour is the same as that found in gas-fluidized beds.

Exactly the same qualitative results are obtained if we use the model of Gidaspow (1994). Figure 4.22B reports the void fraction profiles in pseudo stationary conditions, for the same physical system and operating conditions considered in Figure 4.22A, derived by solving Gidaspow's equations of motion. These equations do not account for the elastic force, are based on the classical definition of buoyancy force and adopt the closures of Ergun (1952) and Wen & Yu (1966) for the drag. The snapshots are virtually indistinguishable. The inclusion of the elastic force, albeit radically changing the analytical behaviour of the one-dimensional linearized equations of motion, does not seem to alter substantially the overall fluidized bed dynamics. In both cases, the averaged transport equations do not predict correctly the transition from the particulate to the aggregative regime. The cause lies in the constitutive equations: either the fluid-particle interaction force still misses a significant contribution, or the effective stress in both phases is not properly modelled.

4.7 Conclusions

The equilibrium expansion profiles of homogeneous liquid-fluidized suspensions were derived by integrating the averaged equations of motion. For each physical system, simulations were run using the new drag force closure presented in Chapter 3 and those of Ergun (1952) and Wen & Yu (1966). By comparing numerical and experimental results, we conclude that:

- The new closure agrees almost perfectly with the Richardson & Zaki (1954) empirical equation, and is better predictive than the expressions of Ergun (1952) and Wen & Yu (1966). Whereas the accuracy of equations (3.32) and (3.34) depends quite strongly on the suspension void fraction, the precision of equation (3.65) is not affected by it.
- Most commercial CFD codes use the Ergun's closure up to a voidage of 0.80 and Wen & Yu's afterwards. At void fractions far lower than 0.80, however, the latter is often the most precise between the two; when this occurs, the threshold of 0.80 is incorrect and should be decreased. Our new equation of closure overcomes this issue: being valid, and quite accurate, for any void fraction and fluid dynamic regime, no switching to other closures is required.

The transient response of homogeneous fluidized systems to sudden variations in fluid flux was then investigated. The numerical results were compared with the predictions of the theoretical model of Gibilaro et al. (1984). The analysis indicates that:

- Contraction and expansion are not specular. The former is characterized by the presence of two well-defined uniform regions in fluid-particle equilibrium separated by a sharp horizontal shock surface. Since the lower region is denser, the configuration is dynamically stable. The system is monodimensional (its structure can be described by a single spatial coordinate), and its height decreases linearly with time. In an expansion, conversely, two uniform regions initially tend to form, but since the upper region is denser, the configuration is dynamically unstable. The density difference triggers internal mixing and disrupts the orderly structure of the system. This is no longer monodimensional (at least two spatial coordinates are needed to describe its dynamics), and its height varies exponentially with time.
- The model of Gibilaro et al. describes well bed contractions but not bed expansions. Its simple kinematic equations do not suffice to capture the complex dynamics of this process: only the multidimensional averaged transport equations can succeed in this task.

The stability of homogeneous gas-fluidized beds has been investigated analytically by linear stability analysis and computationally by simulating the transition from the particulate to the aggregative state. The main conclusions are:

- For non-cohesive powders, good agreement is found between the predictions of the linearized one-dimensional equations of our model and the experimental data reported in the literature. For very fine powders, since the interparticle forces dominate the dynamics, hydrodynamical equations are inadequate.

- The Eulerian-Eulerian transport equations fail to correctly predict the onset of bubbling. Formal stability is lost at fairly low values of the superficial fluid velocity, but the regions at higher voidage that disrupt the uniform bed structure are not bubbles, for their void fraction is too low. The formation of real voids is observed at excessively high fluid fluxes.

- Whereas the introduction of the elastic force radically changes the analytical behaviour of the linearized one-dimensional equations of motion, its influence on the fluidization dynamics, when studied computationally, is rather limited. The same qualitative results were found when using our model, which accounts for the elastic force, and that of Gidaspow (1994), where the force is neglected.

Chapter 5

A modelling approach for multiphase polydisperse flows

This chapter presents a theory for modelling polydisperse fluidized suspensions.

1) We discuss the basics of polydisperse multiphase flows modelling, and derive the generalized population balance equation, which governs the evolution of discrete systems.
2) We describe the method of moments, which is used to solve the generalized population balance equation, and present the resulting problem of closure. To solve it, we introduce the quadrature methods of moments.

This chapter presents the first attempt to use quadrature methods of moments to describe the flow of dense polydisperse granular systems. The main novelty of the approach herein advanced is that each quadrature class in which the particle population is partitioned is advected with its own velocity field. This is essential to capture many features that characterize the motion of polydisperse fluidized suspensions, for instance their tendency to segregate or mix. In other quadrature models all the classes share the same velocity field and therefore these phenomena cannot be predicted.

5.1 Introduction

In Chapter 2, we have derived the equations of motion for bidisperse fluidized suspensions. These systems consist of a continuous phase, also referred to as *environmental phase*, and two monodisperse sets of particles. We considered only two sets to simplify the mathematics, but generalizing the results to n sets is immediate. In most of today's numerical simulations, fluidization dynamics is investigated through these equations. The powders are usually assumed to be monodisperse (Kuipers et al., 1993; Pain et al., 2001; Lettieri et al., 2003, 2004; Cammarata et al., 2003), even if more recently some research groups have performed computational studies of bidisperse suspensions, trying to predict particle mixing and segregation (van Wachem et al., 2001; Gera et al., 2004; Cooper & Coronella, 2005; Owoyemi et al., 2007). The results are promising, but much research is still needed to find more reliable expressions for the unclosed terms of the equations.

The constant particle size in each discrete phase limits the flexibility of these models. Solids can mix and segregate, but variations in their diameters are not allowed for. In reality, however, particles can shrink, aggregate, break and nucleate; accordingly, their size distribution changes continuously in time and space. Predicting this evolution, which depends on the local conditions wherein the system operates, is essential for a reliable description of the suspension behavior. This can be accomplished by solving, along with the averaged transport equations already mentioned, the so-called *generalized population balance equation* (GPBE). Since the dimensionality of the latter differs in general from that of classical fluid dynamic equations, succeeding in this task is exceedingly difficult. Few attempts to implement the GPBE into multiphase CFD codes can be found in the literature. Olmos et al. (2001) have employed this method to simulate bubble columns. They considered ten different size groups to represent the bubbles, but solved only the dynamical equation for the mixture to save computational time. All the discrete phases were therefore convected with the same velocity. Other researchers have applied similar strategies to investigate gas-liquid systems (Lehr & Mewes, 2001; Buwa & Ranade, 2002; Venneker et al., 2002); dense gas-solid systems, conversely, have never been investigated, with the exception of the pioneering work of Fan et al. (2004).

In this chapter, we overview the mathematical modelling of polydisperse fluidized suspensions. We derive the generalized population balance equation, we describe a method that allows reducing its dimensionality to that of classical transport equations, we discuss the problem of closure that ensues and an effective strategy to solve it.

5.2 Basics of polydisperse multiphase flows modelling

We limit the discussion to particulate systems; however, this theory holds in a much wider context (Chapman & Cowling, 1970; Randolph & Larson, 1971; Ramkrishna, 2000). The starting point for our discussion is the introduction of suitable density functions.

5.2.1 Definitions

Let us consider a polydisperse system of solid particles embedded in a continuous medium. Discrete elements, which are said to form a *population*, constitute the disperse phase. Each element can be identified by a number of properties known as *coordinates*; these are usually classified as *external* and *internal*. The former are the spatial coordinates, whereas the latter refer to all the other properties of the elements, such as their velocities, sizes or temperatures. The external coordinates are three and coincide with the components (with respect to a generic vector basis) of the position vector $\boldsymbol{x}$ relative to a generic observer in the three-dimensional physical space. The number of internal coordinates, on the other hand, is not uniquely defined, but depends on the particular application in hand; it coincides with the least number of independent coordinates necessary to provide a complete description of the particle properties. These n scalars, with the exception of the particle velocity $\boldsymbol{v}$, are grouped in the n-dimensional vector $\boldsymbol{\xi}$, which is referred to as *internal state vector*.

To shorten the notation, we define the vectors $\boldsymbol{\zeta}$ and $\boldsymbol{\psi}$. Referred to as *generalized internal state vector* and *particle state vector*, respectively, the first lumps the vectors $\boldsymbol{\xi}$ and $\boldsymbol{v}$ in the reported order, while the second the vectors $\boldsymbol{\zeta}$ and $\boldsymbol{x}$. Although we treat them similarly, $\boldsymbol{x}$ and $\boldsymbol{v}$ are the standard vectors for position and velocity used in Newtonian mechanics, whereas $\boldsymbol{\xi}$, $\boldsymbol{\zeta}$ and $\boldsymbol{\psi}$ are generalized vectors of length n, $n+3$ and $n+6$, respectively, in the sense of linear algebra. The domain of variation of $\boldsymbol{x}$, which is the set of points in physical space where the particles can be present, is denoted by Ω_x. The domains of variation of $\boldsymbol{\xi}$ and $\boldsymbol{v}$, referred to as *internal state space* and *velocity state space*, respectively, are denoted by Ω_ξ and Ω_v. Since all these domains are disjuncted, $\Omega_\zeta \equiv \Omega_\xi \cup \Omega_v$ and $\Omega_\psi \equiv \Omega_\zeta \cup \Omega_x$, where Ω_ζ and Ω_ψ, referred to as *generalized internal state space* and *particle state space*, respectively, are the domains of variation of $\boldsymbol{\zeta}$ and $\boldsymbol{\psi}$.

5.2.2 Convection in particle state space

In any particulate process, individual members of the population continuously change their positions in particle state space. Each particle moves in physical space with velocity $\boldsymbol{v}$. Concomitantly, since $\boldsymbol{v}$ is usually not constant, the particle accelerates; this acceleration, denoted by $\dot{\boldsymbol{v}}$, can be regarded as a linear velocity in the velocity state space. Similarly, since also $\boldsymbol{\xi}$ is usually time-dependent, the elements of the population move in internal state space with a velocity $\dot{\boldsymbol{\xi}}$.

The velocities $\boldsymbol{v}$, $\dot{\boldsymbol{v}}$ and $\dot{\boldsymbol{\xi}}$ describe changes in position, in the relevant coordinate spaces, taking place gradually and continuously. Particle coordinates, however, can also undergo abrupt variations, which cannot be represented by these velocity vectors, but must be described differently. We postpone temporarily this discussion, which will be addressed more thoroughly in §5.3.

The particle velocity is an internal – and therefore independent – coordinate; particle acceleration and internal state velocity, conversely, are functions of the particle state. In other words, it is:

$$\dot{\boldsymbol{v}} = \dot{\boldsymbol{v}}(\boldsymbol{\xi}, \boldsymbol{v}, \boldsymbol{x}, t) \quad ; \quad \dot{\boldsymbol{\xi}} = \dot{\boldsymbol{\xi}}(\boldsymbol{\xi}, \boldsymbol{v}, \boldsymbol{x}, t) \tag{5.1}$$

Note that, once the state of a particle is assigned, the value of any property that is not an internal coordinate is fixed, and can be determined by mathematical relationships. Otherwise, a distribution would be present for the property in question, and the latter should be included in the set of internal coordinates, since its value would be necessary to uniquely define the particle state.

5.2.3 Number, volume and mass density functions

In a Eulerian framework, the disperse phase is generally described by a *number density function* (NDF). Denoted by $f_n(\boldsymbol{\xi}, \boldsymbol{v}, \boldsymbol{x}, t)$, the NDF specifies how the population of elements is distributed over the properties of interest. It is a function of internal coordinates, particle velocity, external coordinates and time. Henceforth, we shall include the explicit dependence on these variables only

when required for clarity. If we consider a differential volume $d\boldsymbol{x}$ around a point $\boldsymbol{x}$ in physical space, then by definition the quantity:

$$f_n(\boldsymbol{\xi}, \boldsymbol{v}, \boldsymbol{x}, t) d\boldsymbol{\xi} d\boldsymbol{v} d\boldsymbol{x} \tag{5.2}$$

indicates the expected number of particles present in $d\boldsymbol{x}$ which at the time t of interest have an internal state vector in the range $d\boldsymbol{\xi}$ (*i.e.*, with values between $\boldsymbol{\xi}$ and $\boldsymbol{\xi} + d\boldsymbol{\xi}$) around $\boldsymbol{\xi}$ and a particle velocity in the range $d\boldsymbol{v}$ (*i.e.*, with values between $\boldsymbol{v}$ and $\boldsymbol{v} + d\boldsymbol{v}$) around $\boldsymbol{v}$. Whenever we are interested in evaluating the number of elements of a population having certain assigned properties (for instance, a certain specified velocity or size), we must consider a *differential range* centered around the values of such properties. If we take the velocity as an example, the problem is correctly formulated when posed as follows: which is the number of elements with velocity in the range $d\boldsymbol{v}$ around $\boldsymbol{v}$? The number is, of course, infinitesimal (since the range $d\boldsymbol{v}$ is differential), but not null; the number of elements having velocity equal to $\boldsymbol{v}$, conversely, is statistically always zero.

In particle state space, the differential volume $d\boldsymbol{\psi}$ coincides with $d\boldsymbol{\xi} d\boldsymbol{v} d\boldsymbol{x}$; accordingly, we can rewrite equation (5.2) as $f_n(\boldsymbol{\psi}, t) d\boldsymbol{\psi}$. This indicates the expected number of particles present in the volume $d\boldsymbol{\psi}$ around $\boldsymbol{\psi}$ (or, equivalently, with particle state vector in the range $d\boldsymbol{\psi}$ around $\boldsymbol{\psi}$) at the time t of interest. This last relation provides a most transparent interpretation of the physical meaning of the NDF: it represents the expected number of particles *per unit volume of particle state space* at the time t of interest. In this space, the NDF is therefore a *number density*; of course, the same is not true if we consider the subspaces of the internal, velocity and spatial coordinates separately.

Although stochastic algorithms can be used to simulate the evolution of a population of particles represented by the NDF, the NDF is not a random quantity, rather it is the ensemble average of an infinite number of realizations of the stochastic algorithm. The number density function is an *average quantity*, which possesses all the mathematical characteristics of averaged functions: it is smooth and differentiable with respect to its arguments.

In addition to the number density function, it is convenient to introduce also a *volume density function* (VDF) and a *mass density function* (MDF); these are defined to be:

$$f_v(\boldsymbol{\xi}, \boldsymbol{v}, \boldsymbol{x}, t) \equiv f_n(\boldsymbol{\xi}, \boldsymbol{v}, \boldsymbol{x}, t) v_p \quad ; \quad f_m(\boldsymbol{\xi}, \boldsymbol{v}, \boldsymbol{x}, t) \equiv f_n(\boldsymbol{\xi}, \boldsymbol{v}, \boldsymbol{x}, t) m_p \tag{5.3}$$

where v_p and m_p denote the particle volume and mass, respectively. These functions give the expected volume and mass of particles per unit volume of particle state space at the time t of interest.

5.2.4 Number density, volume fraction and mass density

The quantity $f_n(\boldsymbol{\xi}, \boldsymbol{v}, \boldsymbol{x}, t) d\boldsymbol{\xi} d\boldsymbol{v}$ represents the number density of particles in physical space having internal coordinates in the range $d\boldsymbol{\xi}$ and velocity in the range $d\boldsymbol{v}$. Henceforth, if we do not specify explicitly to which phase space the density refers to, the physical space is implied. If we integrate

the NDF over all the possible values of $\boldsymbol{\xi}$, we obtain the total number of particles per unit volume of physical space having velocity between $\boldsymbol{v}$ and $\boldsymbol{v} + d\boldsymbol{v}$. If we then integrate this quantity over all the possible values of $\boldsymbol{v}$ we obtain the particle number density, that is, the expected total number of particles per unit volume of physical space:

$$n(\boldsymbol{x},t) \equiv \int_{\Omega_\xi}\int_{\Omega_v} f_n(\boldsymbol{\xi},\boldsymbol{v},\boldsymbol{x},t)\,d\boldsymbol{\xi}\,d\boldsymbol{v} = \int_{\Omega_\zeta} f_n(\boldsymbol{\zeta},\boldsymbol{x},t)\,d\boldsymbol{\zeta} \tag{5.4}$$

The volume fraction and mass density of the disperse phase are given by similar expressions; they are obtained by replacing in equation (5.4) the number density function with the volume density function and mass density function, respectively:

$$\phi(\boldsymbol{x},t) \equiv \int_{\Omega_\zeta} f_v\,d\boldsymbol{\zeta} \quad ; \quad \rho_d(\boldsymbol{x},t) \equiv \int_{\Omega_\zeta} f_m\,d\boldsymbol{\zeta} \tag{5.5}$$

5.2.5 Number, volume and mass averages

We can define various averaged properties for the disperse phase. Given a scalar, vectorial or tensorial function $\boldsymbol{\Phi}(\boldsymbol{\zeta})$, we define its number-averaged mean value as:

$$\langle\boldsymbol{\Phi}\rangle_n(\boldsymbol{x},t) \equiv \frac{1}{n(\boldsymbol{x},t)}\int_{\Omega_\zeta} f_n(\boldsymbol{\zeta},\boldsymbol{x},t)\,\boldsymbol{\Phi}(\boldsymbol{\zeta})\,d\boldsymbol{\zeta} \tag{5.6}$$

Similarly, its volume-averaged and mass-averaged mean values are defined to be:

$$\langle\boldsymbol{\Phi}\rangle_v(\boldsymbol{x},t) \equiv \frac{1}{\phi(\boldsymbol{x},t)}\int_{\Omega_\zeta} f_v\,\boldsymbol{\Phi}(\boldsymbol{\zeta})\,d\boldsymbol{\zeta} \quad ; \quad \langle\boldsymbol{\Phi}\rangle_m(\boldsymbol{x},t) \equiv \frac{1}{\rho_d(\boldsymbol{x},t)}\int_{\Omega_\zeta} f_m\,\boldsymbol{\Phi}(\boldsymbol{\zeta})\,d\boldsymbol{\zeta} \tag{5.7}$$

If all the particles have the same volume, it is:

$$v_p = \text{constant} \quad \rightarrow \quad \phi(\boldsymbol{x},t) = n(\boldsymbol{x},t)v_p \quad \rightarrow \quad \langle\boldsymbol{\Phi}\rangle_n(\boldsymbol{x},t) = \langle\boldsymbol{\Phi}\rangle_v(\boldsymbol{x},t) \tag{5.8}$$

If they have the same density, it is:

$$\rho_p = \text{constant} \quad \rightarrow \quad \rho_d(\boldsymbol{x},t) = \phi(\boldsymbol{x},t)\rho_p \quad \rightarrow \quad \langle\boldsymbol{\Phi}\rangle_v(\boldsymbol{x},t) = \langle\boldsymbol{\Phi}\rangle_m(\boldsymbol{x},t) \tag{5.9}$$

Finally, if they have the same mass, it is:

$$m_p = \text{constant} \quad \rightarrow \quad \rho_d(\boldsymbol{x},t) = n(\boldsymbol{x},t)m_p \quad \rightarrow \quad \langle\boldsymbol{\Phi}\rangle_m(\boldsymbol{x},t) = \langle\boldsymbol{\Phi}\rangle_n(\boldsymbol{x},t) \tag{5.10}$$

The definitions (5.6) and (5.7) consent to evaluate averages of any scalar, vectorial and tensorial quantity. Using the velocity as an example, we make few considerations to clarify the meaning of these definitions. From equation (5.6), it is:

$$\langle\boldsymbol{v}\rangle_n(\boldsymbol{x},t) \equiv \frac{1}{n(\boldsymbol{x},t)}\int_{\Omega_\zeta} f_n(\boldsymbol{\zeta},\boldsymbol{x},t)\,\boldsymbol{v}\,d\boldsymbol{\zeta} \tag{5.11}$$

What is the physical meaning of this relation? It is a simple *number average*. We consider a generic value of the velocity $\boldsymbol{v}$ and a range $d\boldsymbol{v}$ around it. The number of particles per unit volume of physical space having velocity in the range $d\boldsymbol{v}$ around $\boldsymbol{v}$ is:

$$\left(\int_{\Omega_\xi} f_n(\boldsymbol{\xi}, \boldsymbol{v}, \boldsymbol{x}, t)\, d\boldsymbol{\xi}\right) d\boldsymbol{v} \tag{5.12}$$

This expression is derived by first considering the number of particles per unit volume of physical space having velocity in the range $d\boldsymbol{v}$ around $\boldsymbol{v}$ and internal state vector in the range $d\boldsymbol{\xi}$ around $\boldsymbol{\xi}$, and then by integrating over all the possible values of the internal coordinates. All the particles under examination have approximately the same velocity $\boldsymbol{v}$. To be more precise, each particle has a velocity $\hat{\boldsymbol{v}}$ which lies in the range $d\boldsymbol{v}$ around $\boldsymbol{v}$; thus, the difference $d\hat{\boldsymbol{v}} = \hat{\boldsymbol{v}} - \boldsymbol{v}$ is infinitesimal and has the same order of magnitude as $d\boldsymbol{v}$. The overall velocity of this set of particles can be calculated by simply summing vectorially the velocity of each member of the set:

$$\left(\int_{\Omega_\xi} f_n(\boldsymbol{\xi}, \boldsymbol{v}, \boldsymbol{x}, t)\, d\boldsymbol{\xi}\right) \boldsymbol{v}\, d\boldsymbol{v} + O\left(d\boldsymbol{v}^2\right) \tag{5.13}$$

In the limit of vanishingly small values of $d\boldsymbol{v}$, the overall velocity for *this specific set* of particles is simply given by the product of the particle number and the velocity $\boldsymbol{v}$. Our intent, however, is to evaluate the overall velocity of the *entire population* per unit volume of physical space. To obtain this vector, we have to integrate equation (5.13) over Ω_v. Doing so yields:

$$\int_{\Omega_v} \left(\int_{\Omega_\xi} f_n(\boldsymbol{\xi}, \boldsymbol{v}, \boldsymbol{x}, t)\, d\boldsymbol{\xi}\right) \boldsymbol{v}\, d\boldsymbol{v} = \int_{\Omega_\zeta} f_n(\boldsymbol{\zeta}, \boldsymbol{x}, t)\, \boldsymbol{v}\, d\boldsymbol{\zeta} \tag{5.14}$$

The overall velocity of the entire population can be also computed, by definition, by multiplying the average velocity $\langle \boldsymbol{v} \rangle_n (\boldsymbol{x}, t)$ by the number density $n(\boldsymbol{x}, t)$. Equating this product to equation (5.14) results in the definition previously reported, equation (5.11).

5.3 Generalized population balance equation

The generalized population balance equation is a continuity statement written in terms of the number, volume or mass density functions. It can be derived by writing a balance equation on the particles contained in some fixed subregion of the particle state space (Ramkrishna, 2000). Let us consider a finite control volume Λ_ψ in the particle state space. This is the union of three disjuncted control volumes: Λ_ξ in the internal state space, Λ_v in the velocity state space and Λ_x in the physical space. These domains must not be confused with the overall domains of variation of the variables involved, namely Ω_ψ, Ω_ξ, Ω_v and Ω_x. In fact, it is:

$$\Lambda_\psi \subseteq \Omega_\psi \quad ; \quad \Lambda_\xi \subseteq \Omega_\xi \quad ; \quad \Lambda_v \subseteq \Omega_v \quad ; \quad \Lambda_x \subseteq \Omega_x \tag{5.15}$$

Let the boundaries of each control volume be $\partial\Lambda_\psi$, $\partial\Lambda_\xi$, $\partial\Lambda_v$ and $\partial\Lambda_x$, respectively. The balance equation of the particle number can be written as:

$$Acc = In - Out + Gen$$

where Acc is the accumulation, $In - Out$ is the net convective input and Gen is the generation. These terms refer to the control volume Λ_ψ and are usually written per unit time; thus, Acc is the rate of accumulation (*i.e.*, rate of change of the number of particles present in Λ_ψ), Gen is the rate of generation (*i.e.*, number of particles generated within Λ_ψ per unit time) and so on. The number $N(t)$ of particles present at time t in Λ_ψ is:

$$N(t) = \int_{\Lambda_\psi} f_n(\boldsymbol{\psi}, t)\, d\boldsymbol{\psi} \tag{5.16}$$

Accordingly, the rate of change of the number of particles contained in Λ_ψ is given by:

$$Acc = \frac{dN}{dt} = \frac{d}{dt}\int_{\Lambda_\psi} f_n\, d\boldsymbol{\psi} = \int_{\Lambda_\psi} \frac{\partial f_n}{\partial t}\, d\boldsymbol{\psi} \tag{5.17}$$

where the order of derivation and integration has been reversed since Λ_ψ is not time-dependent. The net convective flow rate of particles entering Λ_x is:

$$(In - Out)_x = -\int_{\Lambda_\xi}\int_{\Lambda_v}\int_{\partial\Lambda_x} f_n \boldsymbol{v}\cdot d\boldsymbol{S}_x\, d\boldsymbol{\xi}\, d\boldsymbol{v} \tag{5.18}$$

where $d\boldsymbol{S}_x$ is a differential surface vector normal to $\partial\Lambda_x$ and pointing outwards. If we now use the Gauss theorem, we can turn this surface integral into a volume integral:

$$(In - Out)_x = -\int_{\Lambda_\psi} \boldsymbol{\nabla}_x \cdot \left(f_n \boldsymbol{v}\right) d\boldsymbol{\psi} \tag{5.19}$$

Here $\boldsymbol{\nabla}_x\cdot$ is the divergence operator in the three-dimensional physical space. Being an internal coordinate, $\boldsymbol{v}$ could be removed from the divergence sign, and the integrand in equation (5.19) could be rewritten as $\boldsymbol{v}\cdot\boldsymbol{\nabla}_x f_n$. To preserve generality, however, we leave equation (5.19) in the present form. In the velocity state and internal state spaces, the particles move with velocities $\dot{\boldsymbol{v}}$ (particle acceleration fulfilling Newton's second law of dynamics) and $\dot{\boldsymbol{\xi}}$ (internal state vector rate of change), respectively. Thus, the net convective flow rate of particles entering Λ_v is:

$$(In - Out)_v = -\int_{\Lambda_x}\int_{\Lambda_\xi}\int_{\partial\Lambda_v} f_n \dot{\boldsymbol{v}}\cdot d\boldsymbol{S}_v\, d\boldsymbol{\xi}\, d\boldsymbol{x} = -\int_{\Lambda_\psi} \boldsymbol{\nabla}_v \cdot \left(f_n \dot{\boldsymbol{v}}\right) d\boldsymbol{\psi} \tag{5.20}$$

Analogously, the net convective flow rate of particles entering Λ_ξ is given by:

$$(In - Out)_\xi = -\int_{\Lambda_x}\int_{\Lambda_v}\int_{\partial\Lambda_\xi} f_n \dot{\boldsymbol{\xi}}\cdot d\boldsymbol{S}_\xi\, d\boldsymbol{v}\, d\boldsymbol{x} = -\int_{\Lambda_\psi} \boldsymbol{\nabla}_\xi \cdot \left(f_n \dot{\boldsymbol{\xi}}\right) d\boldsymbol{\psi} \tag{5.21}$$

Here the vectors $d\boldsymbol{S}_\xi$ and $d\boldsymbol{S}_v$ are differential surface vectors respectively normal to $\partial\Lambda_\xi$ and $\partial\Lambda_v$ and pointing outwards. Moreover, $\boldsymbol{\nabla}_\xi\cdot$ and $\boldsymbol{\nabla}_v\cdot$ are divergence operators in the n-dimensional phase space of the internal coordinates and in the three-dimensional phase space of the velocity coordinates, respectively. Since $\boldsymbol{\nabla}_\xi\cdot$ operates always on n-dimensional vectors, it entails the sum of n partial derivatives (thus, it is a generalized divergence in the sense of vector calculus). The net convective contribution is therefore equal to:

$$In - Out = -\int_{\Lambda_\psi}\Big(\boldsymbol{\nabla}_x\cdot\big(f_n\boldsymbol{v}\big)+\boldsymbol{\nabla}_v\cdot\big(f_n\dot{\boldsymbol{v}}\big)+\boldsymbol{\nabla}_\xi\cdot\big(f_n\dot{\boldsymbol{\xi}}\big)\Big)d\boldsymbol{\psi} \tag{5.22}$$

Within Λ_ψ particles can generate due to discontinuous jumps (or events) such as collisions between particles (referred to also as encounters), aggregation or breakage of particles. For instance, if two particles located outside Λ_v collide, their velocities change abruptly; after the encounter, one or even both particles might be located inside Λ_v, having entered the volume without crossing its boundaries. We express the rate of generation as:

$$Gen = \int_{\Lambda_\psi} h_n(\boldsymbol{\psi},t)d\boldsymbol{\psi} \tag{5.23}$$

where h_n is the number of particles generated per unit volume of particle state space and unit time owing to discrete events (mainly collisions between particles, since aggregation, breakage and alike events are secondary processes resulting from particle encounters). Being an integral function, the term is referred to as *collision integral*. Statistical physics tells us that h_n is not closed, for it involves velocity correlations between *two* particles (Chapman & Cowling, 1970). Thus, a closure is required to relate it to the NDF. Putting all the foregoing results together, we obtain:

$$\int_{\Lambda_\psi}\Big(\frac{\partial f_n}{\partial t}+\boldsymbol{\nabla}_x\cdot\big(f_n\boldsymbol{v}\big)+\boldsymbol{\nabla}_v\cdot\big(f_n\dot{\boldsymbol{v}}\big)+\boldsymbol{\nabla}_\xi\cdot\big(f_n\dot{\boldsymbol{\xi}}\big)-h_n\Big)d\boldsymbol{\psi}=0 \tag{5.24}$$

This equation is fulfilled for *any* arbitrary control volume Λ_ψ only if the integrand is zero; thus, the following relation, referred to as generalized population balance equation, must hold:

$$\frac{\partial f_n}{\partial t}+\boldsymbol{\nabla}_x\cdot\big(f_n\boldsymbol{v}\big)+\boldsymbol{\nabla}_v\cdot\big(f_n\dot{\boldsymbol{v}}\big)+\boldsymbol{\nabla}_\xi\cdot\big(f_n\dot{\boldsymbol{\xi}}\big)=h_n \tag{5.25}$$

The GPBE can also be written in terms of volume and mass density functions. Multiplying the equation above by the particle volume yields:

$$\frac{\partial f_v}{\partial t}+\boldsymbol{\nabla}_x\cdot\big(f_v\boldsymbol{v}\big)+\boldsymbol{\nabla}_v\cdot\big(f_v\dot{\boldsymbol{v}}\big)+\boldsymbol{\nabla}_\xi\cdot\big(f_n\dot{\boldsymbol{\xi}}\big)v_p=h_v \tag{5.26}$$

where $h_v\equiv h_n v_p$. Note that v_p is not a function of $\boldsymbol{v}$, $\boldsymbol{x}$ and t; being either an internal coordinate or a known function of internal coordinates, with respect to these variables v_p is a constant and can be included under the sign of partial derivation. Using the identity:

$$\boldsymbol{\nabla}_\xi \cdot \left(f_n \dot{\boldsymbol{\xi}}\right) v_p = \boldsymbol{\nabla}_\xi \cdot \left(f_v \dot{\boldsymbol{\xi}}\right) - f_n \dot{\boldsymbol{\xi}} \cdot \boldsymbol{\nabla}_\xi v_p \tag{5.27}$$

we can rewrite equation (5.26) as:

$$\frac{\partial f_v}{\partial t} + \boldsymbol{\nabla}_x \cdot \left(f_v \boldsymbol{v}\right) + \boldsymbol{\nabla}_v \cdot \left(f_v \dot{\boldsymbol{v}}\right) + \boldsymbol{\nabla}_\xi \cdot \left(f_v \dot{\boldsymbol{\xi}}\right) = h_v + f_n \dot{\boldsymbol{\xi}} \cdot \boldsymbol{\nabla}_\xi v_p \tag{5.28}$$

Similarly, if we multiply equation (5.25) by the particle mass, and use the identity:

$$\boldsymbol{\nabla}_\xi \cdot \left(f_n \dot{\boldsymbol{\xi}}\right) m_p = \boldsymbol{\nabla}_\xi \cdot \left(f_m \dot{\boldsymbol{\xi}}\right) - f_n \dot{\boldsymbol{\xi}} \cdot \boldsymbol{\nabla}_\xi m_p \tag{5.29}$$

defining $h_m \equiv h_n m_p$, we obtain:

$$\frac{\partial f_m}{\partial t} + \boldsymbol{\nabla}_x \cdot \left(f_m \boldsymbol{v}\right) + \boldsymbol{\nabla}_v \cdot \left(f_m \dot{\boldsymbol{v}}\right) + \boldsymbol{\nabla}_\xi \cdot \left(f_m \dot{\boldsymbol{\xi}}\right) = h_m + f_n \dot{\boldsymbol{\xi}} \cdot \boldsymbol{\nabla}_\xi m_p \tag{5.30}$$

The generalized population balance equation governs the evolution of all the properties describing a population of particles. Its solution completely characterizes the system, telling us how the particles move in physical space and how their linear momenta and internal properties change. All the classical transport equations of continuum mechanics can be derived from the GPBE by computing appropriate moments of the equation (Chapman & Cowling, 1970). As an example, in Appendix B, we derive the averaged equations of conservation of the mass and linear momentum for a polydisperse suspension. Solving the GPBE, however, is extremely difficult, for the equation is integro-differential with a dimensionality higher than classical transport equations. An effective strategy of solving the problem is given by the *method of moments*, described in § 5.5, which turns the single GPBE into a set of three-dimensional transport equations. This procedure entails loss of information, for only an infinite set of equations could be equivalent to the original equation, but renders the problem tractable with the required accuracy in many application of industrial interest.

5.4 Solving the generalized population balance equation

The generalized population balance equation, if properly recast, takes the form of a Fredholm or Volterra integral equation of the second kind (Ramkrishna, 2000). The existence and uniqueness of the solution of this equation is a standard subject in many mathematical textbooks (Petrovsky, 1957); therefore, we can be sure that the GPBE can be, at least in principle, solved. There are, nonetheless, very few analytical solution strategies, and those that do exist are almost invariably for such simplified and idealized problems that cannot be used for real systems.

A first analytical method is that of *successive approximations*. The generalized population balance equation is rearranged as an integral equation in the number density function. This equation features on the left-hand side the number density function and on the right-hand side an NDF functional with respect to the particle state. The method substitutes into the functional the approximation for the

number density function of order n to calculate its next, and more accurate, approximation of order $n+1$. For more details, we refer to Ramkrishna (2000). Another analytical method is that of *Laplace transforms*. These are particularly suitable for obtaining analytical solutions of generalized population balance equations featuring convolution integrals in the collision integral. This usually happens in monovariate aggregating systems where the internal coordinate coincides with the particle size. An example is also reported in Ramkrishna (2000). We finally cite the *method of characteristics*, which is efficient when the physics are simple. This analytical technique solves the GPBE by reducing it to an ordinary differential equation (ODE), and is usually powerful for linear growth processes. The main disadvantage of all these methods is that they do not generalize to systems with complex physics.

Generalized population balance equations can be solved numerically by the *methods of weighted residuals*. Here the strategy is to approximate the number density function by a linear combination of basis functions, whose coefficients are determined so that the combination satisfies the GPBE. The set of basis functions is generally obtained from an orthonormal family, whereas the coefficients of expansion are obtained by orthogonalizing the residuals with either the same set of functions used to expand the distribution or other suitable sets of weighing functions.

An alternative numerical technique is the *discretized population balance approach*, also referred to as *class method*. This integrates the generalized population balance equation over subintervals in a partition of the generalized internal state space; then, using the mean value theorem, transforms the continuous GPBE into a set of ordinary differential equations expressing macroscopic balances for the number of particles in each interval. This set has as many equations as the number of intervals, or granular classes, making up the partition. The major drawback of the method is that the number of particles is conserved only in the limit of an infinite number of classes. Also, the solution of the generalized population balance equation strongly depends on the adopted computational grid, and since the number of discretized equations increases with the number of classes, high computational time is necessary for solving the GPBE on a sufficiently fine grid.

Often, engineers are only interested in some integral properties of the number density function known as *moments*. These properties may be more significant than others either because they control the product quality or because they are easier to measure and monitor. The idea behind the *method of moments* is to derive transport equations for the moments of interest by integrating out all the internal coordinates from the generalized population balance equation. The main advantage of the method is that the number of scalars required is very small, which makes the implementation in CFD feasible. However, the moment transport equations are unclosed, since for any given set of moments that the modeler wishes to track the equations usually involve also moments external to the set. For this reason, the method has been scarcely applied. To overcome this problem, we can resort to quadrature methods that approximate the number density function using finite-mode representations. These methods are described and investigated in the present chapter.

An entirely different class of methods that we can adopt to model populations of particles are the *Monte Carlo methods*. These are based on *artificial realizations*, also referred to as *sample paths*, of

the system behaviour. Initially, a population of particles in a prescribed spatial domain finds itself in a state known in a statistical sense. As it evolves, the population undergoes deterministic (continuous) changes in particle state, described by ordinary differential equations, and random (discontinuous) changes in particle state, due to processes such as aggregation, breakage and nucleation, with specified probabilities. To create a realization of the system behaviour, we artificially generate random variables that satisfy the specified probability laws of change. By generating numerous realizations, we can determine the expected behaviour of the system by averaging all the sample paths. This technique is extremely powerful, but requires a lot of computing power; with the computational resources usually available today, it is still not practical for real applications.

5.5 The method of moments

The *method of moments* (MOM) of Hulburt & Katz (1964) is based on the idea of reducing the GPBE dimensionality to that of classical transport equations by integrating the internal coordinates out. To explain the method, we consider a population characterized by a one-dimensional particle state space, and assume that the collision integral is zero. Equation (5.25) then becomes:

$$\frac{\partial f_n}{\partial t} + \frac{\partial}{\partial \xi}\left(f_n \dot{\xi}\right) = 0 \tag{5.31}$$

where ξ is the single coordinate. Given a generic function $\varphi(\xi, \boldsymbol{x}, t)$, the integral transform:

$$\varphi(\xi, \boldsymbol{x}, t) \rightarrow \mathscr{M}_k(\varphi)(\boldsymbol{x}, t) \equiv \int_{\Omega_\xi} \varphi(\xi, \boldsymbol{x}, t)\xi^k d\xi \tag{5.32}$$

defines the moment of order k with respect to the coordinate ξ of the function $\varphi(\xi, \boldsymbol{x}, t)$. If we apply this transform to equation (5.31), we obtain:

$$\frac{d}{dt}\int_{\Omega_\xi} f_n \xi^k d\xi + \int_{\Omega_\xi} \frac{\partial}{\partial \xi}\left(f_n \dot{\xi}\right)\xi^k d\xi = 0 \tag{5.33}$$

Whereas equation (5.31) is two-dimensional, equation (5.33) is one-dimensional. By integrating out the internal coordinate, we have left behind only the time dependence. The information that equation (5.33) provides, however, is less detailed than that contained in the GPBE. The method of moments represents therefore a tradeoff in which the dimensionality of the analytical problem is reduced at the price of obtaining averaged, rather than distributed, information about the repartition of the particle properties. From the GPBE we can derive an infinite number of one-dimensional transport equations. The same method can be applied to equation (5.25); integrating out all the internal coordinates, we can obtain as many three-dimensional transport equations as we wish to consider (two of such equations are derived in Appendix B). In many applications of engineering interest, nevertheless, a set of few equations often describes well enough the particulate process (Randolph & Larson, 1971).

Let us examine in more detail equation (5.33). To work on a concrete example, we take ξ to be the particle size; accordingly, $\Omega_\xi \equiv [0, +\infty]$. Since it is:

$$\frac{\partial}{\partial \xi}\left(f_n \dot{\xi}\right)\xi^k = \frac{\partial}{\partial \xi}\left(f_n \dot{\xi} \xi^k\right) - k f_n \dot{\xi} \xi^{k-1} \tag{5.34}$$

equation (5.33) yields:

$$\frac{d}{dt}\int_0^{+\infty} f_n \xi^k d\xi = \left(f_n \dot{\xi} \xi^k\right)\Big|_0 - \left(f_n \dot{\xi} \xi^k\right)\Big|_{+\infty} + k\int_0^{+\infty} f_n \dot{\xi} \xi^{k-1} d\xi \tag{5.35}$$

When any internal coordinate diverges, f_n goes to zero faster than any other function; this property is referred to as *regularity condition* (Chapman & Cowling, 1970); in this instance, it means that the expected number of particles having infinite size is zero. The second term on the right-hand side of equation (5.35) is therefore zero. The flux at the origin, conversely, might not be null (Ramkrishna, 2000; Marchisio & Fox, 2007); in most applications, though, also this term vanishes. Assuming that this is the case, we can rewrite equation (5.35) as:

$$\frac{d}{dt}\int_0^{+\infty} f_n \xi^k d\xi = k\int_0^{+\infty} f_n \dot{\xi} \xi^{k-1} d\xi \tag{5.36}$$

This is the transport equation that governs the evolution of the moment of order k of the NDF. We can consider a set of as many equations as we like. Suppose that we wish to track only the first ν integer moments; we then have to write equation (5.36) ν times, letting k vary from 0 to $\nu - 1$. The resulting set is said to be closed only if the right-hand side of equation (5.36) is a function of *lower-order moments*, that is, moments of order less than or equal to k. If this happens, the set is self-sufficient and no other equations are required. On the other hand, if *higher-order moments* appear, no matter how many equations we choose to consider, the set will always be unclosed. For instance, if the rate of change of the internal coordinate is constant, equation (5.36) yields:

$$\frac{d}{dt}\int_0^{+\infty} f_n \xi^k d\xi = k\dot{\xi}\int_0^{+\infty} f_n \xi^{k-1} d\xi \tag{5.37}$$

The problem is then closed, for the transport equation of the k-th moment of the NDF features only the moment of order $k-1$. However, if $\dot{\xi}$ is given by the power law $\xi_0 \xi^\alpha$, where ξ_0 and α are positive constants, than it is:

$$\frac{d}{dt}\int_0^{+\infty} f_n \xi^k d\xi = k\xi_0\int_0^{+\infty} f_n \xi^{k-1+\alpha} d\xi \tag{5.38}$$

The integral on the right-hand side is the moment of the NDF of order $k - 1 + \alpha$; thus, if α is greater than one, the equation is unclosed, for it involves a higher-order moment.

Often the method of moments results in an unclosed set of equations; when this happens, closure is needed. This entails finding an approximate expression of high accuracy that allows relating the unclosed terms to the available set of moments. In the next sections, we present two efficient methods

that succeed in this task; they are referred to as *direct quadrature method of moments* (DQMOM) and *quadrature method of moments* (QMOM).

5.6 Closures based on quadrature approximations

To simplify the mathematics and describe the methods clearly, we restrict the analysis to monovariate systems. These are characterized by one-dimensional generalized internal state spaces; accordingly, $\boldsymbol{\zeta}$ reduces to a scalar. Being a vector, the particle velocity cannot be an internal coordinate, otherwise the distribution would be multivariate. Three alternative scenarios are possible. The simplest involves a population of motionless elements whose internal state is fully described by a single scalar coordinate; the system is then purely monovariate, for no other internal coordinate is present. Alternatively, the particles move in physical space, but share the same velocity, which is a *known function of time and external coordinates*. In fluid-particle systems characterized by vanishingly small Stokes numbers, for example, the velocity of each element of the population coincides with the velocity of the fluid, which either is known or can be found by integrating the transport equations of the environmental phase. Finally, the particles can move with different velocities, but these must be *known functions of the internal coordinate* ξ. When this occurs, a *conditional relationship* is present between particle velocity and internal coordinate. This often happens in multiphase flows when ξ coincides with the particle diameter. The particle velocity is controlled by the fluid-particle interactions, which in turn depend on the particle size; thus, if elements within a certain (differential) size range move with a certain velocity, all the others external to that range must move with different velocities. In the last two scenarios, even if the system is not purely monovariate, its volume density function can be reduced to a monovariate distribution. When all the particles of the population share the same velocity, denoted here by $\boldsymbol{u}\,(\boldsymbol{x},t)$, the VDF takes the form:

$$f_v(\xi,\boldsymbol{v},\boldsymbol{x},t)=\hat{f}_v(\xi,\boldsymbol{x},t)\boldsymbol{\delta}\Big[\boldsymbol{v}-\boldsymbol{u}(\boldsymbol{x},t)\Big] \tag{5.39}$$

The multidimensional Dirac delta function is defined as:

$$\boldsymbol{\delta}\Big[\boldsymbol{v}-\boldsymbol{u}(\boldsymbol{x},t)\Big]\equiv\prod_{k=1}^{3}\delta\Big[v_k-u_k(\boldsymbol{x},t)\Big] \tag{5.40}$$

where v_k and $u_k(\boldsymbol{x},t)$ are the k-th components of the vectors $\boldsymbol{v}$ and $\boldsymbol{u}(\boldsymbol{x},t)$, respectively. The function $f_v(\xi,\boldsymbol{v},\boldsymbol{x},t)$ describes the distribution of the population over the internal coordinate ξ and the particle velocity $\boldsymbol{v}$. In particular, it tells us that all the elements share the same velocity $\boldsymbol{u}(\boldsymbol{x},t)$. This piece of information, however, is unnecessary because already known. We can reduce the dimensionality of the distribution by integrating the velocity coordinates out. Doing so leads to the monovariate density function $\hat{f}_v(\xi,\boldsymbol{x},t)$. In fact, we have:

$$\hat{f}_v(\xi,\boldsymbol{x},t)=\int_{\Omega_v}f_v(\xi,\boldsymbol{v},\boldsymbol{x},t)d\boldsymbol{v} \tag{5.41}$$

Similarly, when a conditional relationship exists between internal coordinate and particle velocity, the VDF needs not describe the distribution over the latter, for if the volume fraction of elements with internal coordinate in the range $d\xi$ around ξ is $f_v(\xi, \boldsymbol{x}, t)d\xi$, the same is the fraction with velocity in the range $d\boldsymbol{v}$ around $\boldsymbol{v}(\xi, \boldsymbol{x}, t)$. Moreover, the number of elements with internal coordinate in the range specified and velocity external to the range $d\boldsymbol{v}$ around $\boldsymbol{v}(\xi, \boldsymbol{x}, t)$ is clearly zero.

To overcome the problem of closure described in § 5.5, the methods approximate the VDF as a summation of multidimensional Dirac delta functions:

$$f_v(\boldsymbol{\xi}, \boldsymbol{v}, \boldsymbol{x}, t) \approx \sum_{i=1}^{\nu} \phi_i(\boldsymbol{x}, t) \boldsymbol{\delta}\Big[\boldsymbol{\xi} - \boldsymbol{\xi}_i(\boldsymbol{x}, t)\Big] \boldsymbol{\delta}\Big[\boldsymbol{v} - \boldsymbol{v}_i(\boldsymbol{x}, t)\Big] \tag{5.42}$$

This formula, which refers to multivariate distributions, represents the disperse phase by ν different classes, each having a volume fraction $\phi_i(\boldsymbol{x}, t)$, a particle velocity $\boldsymbol{v}_i(\boldsymbol{x}, t)$ and an n-dimensional internal state vector $\boldsymbol{\xi}_i(\boldsymbol{x}, t)$. The scalar functions $\phi_i(\boldsymbol{x}, t)$ are the *weights* of the quadrature, whereas the vector functions $\boldsymbol{v}_i(\boldsymbol{x}, t)$ and $\boldsymbol{\xi}_i(\boldsymbol{x}, t)$ are the *nodes*. Moreover, it is:

$$\boldsymbol{\delta}\Big[\boldsymbol{\xi} - \boldsymbol{\xi}_i(\boldsymbol{x}, t)\Big] \equiv \prod_{k=1}^{n} \delta\Big[\xi_k - \xi_{i,k}(\boldsymbol{x}, t)\Big] \quad ; \quad \boldsymbol{\delta}\Big[\boldsymbol{v} - \boldsymbol{v}_i(\boldsymbol{x}, t)\Big] \equiv \prod_{k=1}^{3} \delta\Big[v_k - v_{i,k}(\boldsymbol{x}, t)\Big] \tag{5.43}$$

where ξ_k, $\xi_{i,k}(\boldsymbol{x}, t)$ and $v_{i,k}(\boldsymbol{x}, t)$ are the k-th components of the coordinate $\boldsymbol{\xi}$ and of the quadrature nodes $\boldsymbol{\xi}_i(\boldsymbol{x}, t)$ and $\boldsymbol{v}_i(\boldsymbol{x}, t)$, respectively. To simplify the notation, the dependence of any function on some or all of its arguments will be from now on left out. For a monovariate distribution, the quadrature approximation reduces to:

$$f_v(\xi, \boldsymbol{x}, t) \approx \sum_{i=1}^{\nu} \phi_i(\boldsymbol{x}, t) \delta\Big[\xi - \xi_i(\boldsymbol{x}, t)\Big] \tag{5.44}$$

Turning integrals of the VDF into summations, this formula eliminates the closure problem. This is the common element between QMOM and DQMOM; the difference lies in the computation of nodes and weights. QMOM forces them to agree with a set of independent lower-order moments (McGraw, 1997). These are tracked by transport equations, while nodes and weights are back-calculated. While for multivariate distributions to do so we must solve a nonlinear algebraic system, for monovariate distributions we can build a sequence of monic orthogonal polynomials based on an inner product that adopts the VDF as weighting function (see § C.3 of Appendix C). The nodes coincide with the roots of the polynomial of order ν, whereas the weights come as a consequence (Dette & Studden, 1997). The functional form of equation (5.44) is then equivalent to a Gaussian integration. Finding the roots of polynomials is notoriously an ill-conditioned problem (Press et al., 2002). For monovariate VDFs, the *product-difference* (PD) *algorithm* of Gordon (1968) determines nodes and weights by finding the eigenvalues of a real symmetric tridiagonal matrix (refer to § 5.7.2). Being based on the theory of canonical moments of monovariate functions (Dette & Studden, 1997), the algorithm cannot be

applied when a higher number of internal coordinates are present. The quadrature approximation must then be determined by solving a nonlinear algebraic system at each grid point of the computational domain and at each time step. This renders QMOM less attractive, since the method loses much of its simplicity and efficiency. Deriving transport equations that govern directly the evolution of the nodes and weights, DQMOM is more immediate and computationally cheaper. Back-calculation is only required to initialize the problem, since at first the VDF moments, and not the quadrature nodes and weights, are usually known (refer to § 5.7.2).

We first present the direct quadrature method of moments, considering the most general scenario where a conditional relationship exists between particle velocity and internal coordinate. To guide the reader through the theoretical analysis, we anticipate its main steps:

1) We write the GPBE for monovariate distributions, and adopt the quadrature formula (5.44) to represent the VDF by means of ν particle classes, each having a volume fraction $\phi_i(\boldsymbol{x}, t)$ and an internal coordinate $\xi_i(\boldsymbol{x}, t)$.
2) In the GPBE, we replace the VDF with its finite-mode representation, obtaining 2ν transport equations that govern the evolution of the quadrature weights and weighted nodes.
3) To determine the source terms of these equations, we take moment transforms of the discretized GPBE. The unknowns being 2ν, an equivalent number of moments must be considered. Any set of independent moments is acceptable, but the source terms depend on the moments selected, for different moments preserve different properties of the VDF.
4) To define the physical problem, we must assign boundary and initial conditions. To set the latter, that is, to initialize the quadrature weights and weighted nodes, we must know the initial values of at least 2ν moments of the VDF. Equating them to the discretized moment expressions, we derive a nonlinear algebraic system whose solution yields $\phi_i(\boldsymbol{x}, t_0)$ and $\xi_i(\boldsymbol{x}, t_0)$.
5) For monovariate systems, a better technique is available. This is based on the product-difference algorithm proposed by Gordon (1968), which uses the 2ν VDF moments to build a real symmetric tridiagonal matrix whose eigenvalues yield the quadrature nodes, and whose eigenvectors allow determining the quadrature weights.

5.7 Direct quadrature method of moments

For a monovariate distribution, equation (5.28) takes the form:

$$\frac{\partial f_v}{\partial t} + \boldsymbol{\nabla}_x \cdot \left(f_v \boldsymbol{v}\right) + \frac{\partial}{\partial \xi}\left(f_v \dot{\xi}\right) = h_v + \frac{\dot{\xi}}{v_p}\frac{dv_p}{d\xi} f_v \tag{5.45}$$

As already done in § 5.6, we favor the volume density function, even if this complicates the GPBE mathematical form. This choice is convenient because we are usually interested in volume fractions

and not number fractions. Using equation (5.44), we can write:

$$\frac{\partial f_v}{\partial t} = \frac{\partial}{\partial t}\sum_{i=1}^{\nu}\phi_i\delta(\xi-\xi_i) = \sum_{i=1}^{\nu}\left(\frac{\partial\phi_i}{\partial t}\delta(\xi-\xi_i) - \frac{\partial\xi_i}{\partial t}\phi_i\delta'(\xi-\xi_i)\right) \tag{5.46}$$

where the derivation chain rule has been applied. The function $\delta'(\xi-\xi_i)$ denotes the derivative of $\delta(\xi-\xi_i)$ with respect to $\xi-\xi_i$ and is defined by the integral property (Arfken, 1985):

$$\int_{\xi_a}^{\xi_c} f(\xi)\delta'(\xi-\xi_b)d\xi = -\frac{df}{d\xi}(\xi_b) \quad ; \quad \xi_a<\xi_b<\xi_c \tag{5.47}$$

This property is crucial, since to derive transport equations from the GPBE we must integrate the latter and compute its moments. The identity:

$$\frac{\partial\xi_i}{\partial t}\phi_i = \frac{\partial}{\partial t}\big(\phi_i\xi_i\big) - \frac{\partial\phi_i}{\partial t}\xi_i \tag{5.48}$$

allows rearranging equation (5.46) as:

$$\frac{\partial f_v}{\partial t} = \sum_{i=1}^{\nu}\left(\frac{\partial\phi_i}{\partial t}\delta - \frac{\partial}{\partial t}\big(\phi_i\xi_i\big)\delta' + \frac{\partial\phi_i}{\partial t}\xi_i\delta'\right) \tag{5.49}$$

The second term on the left-hand side of equation (5.45) is manipulated similarly. If a conditional relationship is present between the particle velocity and the internal coordinate, $\boldsymbol{v}$ is a known function of the variables ξ, $\boldsymbol{x}$ and t; accordingly, we can write:

$$f_v\boldsymbol{v} = \left(\sum_{i=1}^{\nu}\phi_i(\boldsymbol{x},t)\delta\Big[\xi-\xi_i(\boldsymbol{x},t)\Big]\right)\boldsymbol{v}(\xi,\boldsymbol{x},t) =$$

$$\sum_{i=1}^{\nu}\phi_i(\boldsymbol{x},t)\boldsymbol{v}\Big[\xi_i(\boldsymbol{x},t),\boldsymbol{x},t\Big]\delta\Big[\xi-\xi_i(\boldsymbol{x},t)\Big] = \sum_{i=1}^{\nu}\phi_i(\boldsymbol{x},t)\boldsymbol{v}_i(\boldsymbol{x},t)\delta\Big[\xi-\xi_i(\boldsymbol{x},t)\Big] \tag{5.50}$$

where $\boldsymbol{v}_i(\boldsymbol{x},t)$ is the velocity of the elements of the quadrature class i. Thus, it is:

$$\boldsymbol{\nabla}_x\cdot\big(f_v\boldsymbol{v}\big) = \boldsymbol{\nabla}_x\cdot\sum_{i=1}^{\nu}\phi_i\boldsymbol{v}_i\delta = \sum_{i=1}^{\nu}\Big(\boldsymbol{\nabla}_x\cdot\big(\phi_i\boldsymbol{v}_i\big)\delta - \phi_i\boldsymbol{v}_i\cdot\boldsymbol{\nabla}_x\xi_i\delta'\Big) \tag{5.51}$$

Then, using the identity:

$$\phi_i\boldsymbol{v}_i\cdot\boldsymbol{\nabla}_x\xi_i = \boldsymbol{\nabla}_x\cdot\big(\phi_i\xi_i\boldsymbol{v}_i\big) - \xi_i\boldsymbol{\nabla}_x\cdot\big(\phi_i\boldsymbol{v}_i\big) \tag{5.52}$$

we obtain:

$$\boldsymbol{\nabla}_x\cdot\big(f_v\boldsymbol{v}\big) = \sum_{i=1}^{\nu}\Big(\boldsymbol{\nabla}_x\cdot\big(\phi_i\boldsymbol{v}_i\big)\delta - \boldsymbol{\nabla}_x\cdot\big(\phi_i\xi_i\boldsymbol{v}_i\big)\delta' + \boldsymbol{\nabla}_x\cdot\big(\phi_i\boldsymbol{v}_i\big)\xi_i\delta'\Big) \tag{5.53}$$

The convective term in internal state space is rewritten as:

$$\frac{\partial}{\partial \xi}\big(f_v \dot{\xi}\big) = \frac{\partial}{\partial \xi}\left(\dot{\xi}(\xi)\sum_{i=1}^{\nu}\phi_i\delta\right) = \frac{\partial}{\partial \xi}\sum_{i=1}^{\nu}\phi_i\dot{\xi}(\xi_i)\delta = \sum_{i=1}^{\nu}\phi_i\dot{\xi}(\xi_i)\delta' \tag{5.54}$$

whereas the last term on the right-hand side of equation (5.45) yields:

$$\frac{\dot{\xi}(\xi)}{v_p}\frac{dv_p}{d\xi}f_v = \frac{\dot{\xi}(\xi)}{v_p}\frac{dv_p}{d\xi}\sum_{i=1}^{\nu}\phi_i\delta = \frac{1}{v_p}\frac{dv_p}{d\xi}\sum_{i=1}^{\nu}\phi_i\dot{\xi}(\xi_i)\delta \tag{5.55}$$

If we put together all the previous results, the GPBE becomes:

$$\sum_{i=1}^{\nu}\left(c_i^{\phi}\delta - \big(c_i^{\xi} - \xi_i c_i^{\phi}\big)\delta' + \phi_i\dot{\xi}(\xi_i)\delta'\right) = h_v + \frac{1}{v_p}\frac{dv_p}{d\xi}\sum_{i=1}^{\nu}\phi_i\dot{\xi}(\xi_i)\delta \tag{5.56}$$

where, by definition, it is:

$$\frac{\partial \phi_i}{\partial t} + \boldsymbol{\nabla}_x\cdot\big(\phi_i\boldsymbol{v}_i\big) \equiv c_i^{\phi}(\boldsymbol{x},t) \quad ; \quad \frac{\partial}{\partial t}\big(\phi_i\xi_i\big) + \boldsymbol{\nabla}_x\cdot\big(\phi_i\xi_i\boldsymbol{v}_i\big) \equiv c_i^{\xi}(\boldsymbol{x},t) \tag{5.57}$$

Equation (5.56) expresses the generalized population balance equation for a monovariate population of particles whose velocities are conditioned on the scalar property ξ and whose VDF fulfills equation (5.44). The unknowns are the functions $\phi_i(\boldsymbol{x},t)$ and $\xi_i(\boldsymbol{x},t)$, which denote the weights and nodes of the quadrature approximation, respectively. Their evolution in time and physical space is governed by equations (5.57); these define the functions $c_i^{\phi}(\boldsymbol{x},t)$ and $c_i^{\xi}(\boldsymbol{x},t)$, but can be regarded as transport equations for the quadrature weights and weighted nodes. The source terms $c_i^{\phi}(\boldsymbol{x},t)$ and $c_i^{\xi}(\boldsymbol{x},t)$ are unknown, but can be determined by computing moment transforms of the GPBE.

Note that the method cannot yield any additional transport equations. If the VDF is monovariate, the particle velocity distribution is known, and no equations for the functions $\boldsymbol{v}_i(\boldsymbol{x},t)$ are needed (neither can be derived). To obtain dynamical equations for each particle class, the VDF must include the particle velocity as an independent variable and can no longer be monovariate.

5.7.1 Source terms of the transport equations

In monovariate particle populations, the internal coordinate often coincides with the particle diameter (or volume). With this choice, equation (5.56) reduces to:

$$\sum_{i=1}^{\nu}\left(c_i^{\phi}\delta - \big(c_i^{\xi} - \xi_i c_i^{\phi}\big)\delta' + \phi_i\dot{\xi}(\xi_i)\delta'\right) = h_v + 3\sum_{i=1}^{\nu}\frac{\phi_i\dot{\xi}(\xi_i)}{\xi_i}\delta \tag{5.58}$$

Henceforth, we shall focus on the equation above; generalizing the results, however, is immediate. To determine the source terms $c_i^{\phi}(\boldsymbol{x},t)$ and $c_i^{\xi}(\boldsymbol{x},t)$, we apply the moment transform (5.32) to equation

(5.58). To simplify the notation, we denote the moment transform of the volume density function by $\mathscr{M}_k(\boldsymbol{x},t)$. For the first term of the equation, we have:

$$\mathscr{M}_k\left(\sum_{i=1}^{\nu} c_i^{\phi}\,\delta\right) = \sum_{i=1}^{\nu} c_i^{\phi} \int_{\Omega_\xi} \xi^k\,\delta\,d\xi = \sum_{i=1}^{\nu} c_i^{\phi}\,\xi_i^k \tag{5.59}$$

Using the integral property (5.47), we transform the second term as:

$$\mathscr{M}_k\left(\sum_{i=1}^{\nu} \left(c_i^{\xi} - \xi_i c_i^{\phi}\right)\delta'\right) = \sum_{i=1}^{\nu} \left(c_i^{\xi} - \xi_i c_i^{\phi}\right) \int_{\Omega_\xi} \xi^k\,\delta'\,d\xi = -k \sum_{i=1}^{\nu} \left(c_i^{\xi} - \xi_i c_i^{\phi}\right)\xi_i^{k-1} \tag{5.60}$$

Similarly for the third term:

$$\mathscr{M}_k\left(\sum_{i=1}^{\nu} \phi_i \dot{\xi}(\xi_i)\,\delta'\right) = \sum_{i=1}^{\nu} \phi_i \dot{\xi}(\xi_i) \int_{\Omega_\xi} \xi^k\,\delta'\,d\xi = -k \sum_{i=1}^{\nu} \phi_i \xi_i^{k-1} \dot{\xi}(\xi_i) \tag{5.61}$$

The moment transform of the second term on the right-hand side of equation (5.58) gives:

$$\mathscr{M}_k\left(3\sum_{i=1}^{\nu} \frac{\phi_i \dot{\xi}(\xi_i)}{\xi_i}\,\delta\right) = 3\sum_{i=1}^{\nu} \frac{\phi_i \dot{\xi}(\xi_i)}{\xi_i} \int_{\Omega_\xi} \xi^k\,\delta\,d\xi = 3\sum_{i=1}^{\nu} \phi_i \xi_i^{k-1} \dot{\xi}(\xi_i) \tag{5.62}$$

Putting together all these results, we obtain the algebraic equation:

$$(1-k)\sum_{i=1}^{\nu} c_i^{\phi}\,\xi_i^k + k\sum_{i=1}^{\nu} c_i^{\xi}\,\xi_i^{k-1} = \mathscr{M}_k(h_v) + (3+k)\sum_{i=1}^{\nu} \phi_i \xi_i^{k-1} \dot{\xi}(\xi_i) \tag{5.63}$$

This is an algebraic equation in the 2ν unknowns $c_i^{\phi}(\boldsymbol{x},t)$ and $c_i^{\xi}(\boldsymbol{x},t)$. To find these functions, we need 2ν independent equations. These can be obtained by writing equation (5.63) for 2ν different values of the parameter k; since the equations are in general coupled, a *linear algebraic system* of order 2ν must be solved. *Any independent set of moments* can be considered. Nevertheless, being related to the mean and the coefficient of variation of the distribution (Randolph & Larson, 1971), the zeroth and first-order moments have special physical meaning and should always be part of the set. The best choice of additional moments is usually problem-dependent. Here we use *integer moments* ($k \in \mathbb{N}$), but if fractional-order moments ($k \in \mathbb{R}$) have particular physical meaning (*e.g.*, they appear in measurable quantities), they can certainly be adopted.

The independence of the moments can be verified by checking if the coefficient matrix $\boldsymbol{X}$ of the linear system obtained from equation (5.63) is singular (a square matrix is singular if and only if its determinant is zero). For instance, if we use the first 2ν integer moments, we can express the system in matrix notation as $\boldsymbol{X}\,\boldsymbol{c} = \boldsymbol{s}$, where the elements $x_{p,q}$ of $\boldsymbol{X}$ are:

$$\begin{aligned} x_{p,q} &= (2-p)\,\xi_q^{p-1} \quad ; \quad 1 \leqslant p \leqslant 2\,\nu \quad ; \quad 1 \leqslant q \leqslant \nu \\ x_{p,q} &= (p-1)\,\xi_q^{p-2} \quad ; \quad 1 \leqslant p \leqslant 2\,\nu \quad ; \quad \nu+1 \leqslant q \leqslant 2\,\nu \end{aligned} \tag{5.64}$$

the elements c_p of the vector $\boldsymbol{c}$ are:

$$c_p = c_p^{\phi} \quad ; \quad 1 \leqslant p \leqslant \nu \quad \text{and} \quad c_p = c_p^{\xi} \quad ; \quad \nu + 1 \leqslant p \leqslant 2\nu \tag{5.65}$$

and the elements s_p of the vector $\boldsymbol{s}$ are:

$$s_p = \mathscr{M}_{p-1}(h_v) + (p+2) \sum_{i=1}^{\nu} \phi_i \xi_i^{p-2} \dot{\xi}(\xi_i) \quad ; \quad 1 \leqslant p \leqslant 2\nu \tag{5.66}$$

If $\boldsymbol{X}$ is non-singular, we obtain $c_i^{\phi}(\boldsymbol{x}, t)$ and $c_i^{\xi}(\boldsymbol{x}, t)$ by simply inverting $\boldsymbol{X}$. Sometimes, however, the matrix is not full rank because some nodes coincide. This occurs when a subset of the ν delta functions used to represent the VDF is unnecessary. To overcome the problem, we add small perturbations to the non-distinct $\xi_i(\boldsymbol{x}, t)$ so that $\boldsymbol{X}$ becomes full rank. The perturbations, required only in the definition of $\boldsymbol{X}$, leave the weights $\phi_i(\boldsymbol{x}, t)$ unchanged (Marchisio & Fox, 2005).

The 2ν transport equations (5.57) that govern the evolution of the functions $\phi_i(\boldsymbol{x}, t)$ and $\xi_i(\boldsymbol{x}, t)$ are now closed, as long as the internal state velocity $\dot{\xi}$ and the collision integral h_v are known. The theory of transport phenomena provides constitutive expressions for $\dot{\xi}$. If the particles shrink owing to surface chemical reactions, for instance, the shrinking-core model (Levenspiel, 1999) gives the particle size rate of change. The discontinuous event term is harder to model and a vast literature is available on this subject; for a comprehensive discussion, we refer to Ramkrishna (2000).

We conclude this section by reporting the Lagrangian formulation of the transport equations; obtained by combining equations (5.57), these take the form:

$$\frac{D_i \phi_i}{Dt} = c_i^{\phi}(\boldsymbol{x}, t) - \phi_i(\boldsymbol{x}, t) \boldsymbol{\nabla}_x \cdot \boldsymbol{v}_i(\boldsymbol{x}, t) \quad ; \quad \frac{D_i \xi_i}{Dt} = \frac{c_i^{\xi}(\boldsymbol{x}, t) - \xi_i(\boldsymbol{x}, t) c_i^{\phi}(\boldsymbol{x}, t)}{\phi_i(\boldsymbol{x}, t)} \tag{5.67}$$

where the material derivative that refers to the i-th quadrature class is based on its velocity $\boldsymbol{v}_i(\boldsymbol{x}, t)$; in other words, by definition it is:

$$\frac{D_i(\cdot)}{Dt} \equiv \frac{\partial(\cdot)}{\partial t} + \boldsymbol{v}_i \cdot \boldsymbol{\nabla}(\cdot) \tag{5.68}$$

5.7.2 Boundary and initial conditions

To solve the differential problem (5.57), we need boundary and initial conditions. On the boundaries of the system, we can prescribe either the quadrature weights and weighted nodes or their fluxes. The initial conditions, on the other hand, can be assigned if at the initial time t_0 at least 2ν independent moments of the VDF are known everywhere within the computational domain. Assuming to know the function $f_v(\xi, \boldsymbol{x}, t_0)$, we can calculate its moments as:

$$\mathscr{M}_k(\boldsymbol{x}, t_0) = \int_{\Omega_\xi} f_v(\xi, \boldsymbol{x}, t_0) \xi^k d\xi \tag{5.69}$$

Using equation (5.44), we can then write:

$$\mathscr{M}_k(\boldsymbol{x}, t_0) = \sum_{i=1}^{\nu} \phi_i(\boldsymbol{x}, t_0) \xi_i^k(\boldsymbol{x}, t_0) \tag{5.70}$$

This is a nonlinear equation in the unknowns $\phi_i(\boldsymbol{x}, t_0)$ and $\xi_i(\boldsymbol{x}, t_0)$. We can find these functions by writing the equation for 2ν different values of k and solving the resulting *nonlinear algebraic system*. Whereas for multivariate distributions no alternatives exist, for monovariate distributions we can use the product-difference algorithm of Gordon (1968).

In equations (5.69) and (5.70), we can choose any value of k; that is, we can use any moment of the VDF to evaluate $\phi_i(\boldsymbol{x}, t_0)$ and $\xi_i(\boldsymbol{x}, t_0)$. Different choices, of course, result in different algebraic systems and, in turn, in different initial conditions. This must not surprise, for initial conditions based on different moments preserve different properties of the VDF. Among the many possible choices, however, one is particularly accurate. If we choose to preserve *the first 2ν integer moments* of the volume density function, $\phi_i(\boldsymbol{x}, t_0)$ and $\xi_i(\boldsymbol{x}, t_0)$ fulfill the condition:

$$\int_{\Omega_\xi} f_v(\xi, \boldsymbol{x}, t_0) \xi^k d\xi = \sum_{i=1}^{\nu} \phi_i(\boldsymbol{x}, t_0) \xi_i^k(\boldsymbol{x}, t_0) \tag{5.71}$$

for any integer k from 0 up to $2\nu - 1$. Hence, it must also be:

$$\int_{\Omega_\xi} f_v(\xi, \boldsymbol{x}, t_0) p_k(\xi) d\xi = \sum_{i=1}^{\nu} \phi_i(\boldsymbol{x}, t_0) p_k(\xi_i(\boldsymbol{x}, t_0)) \tag{5.72}$$

for any polynomial $p_k(\xi)$ of degree k with $0 \leqslant k \leqslant 2\nu - 1$. This is true insomuch as integration is distributive and $p_k(\xi)$ is a linear combination of polynomials ξ^k with $0 \leqslant k \leqslant 2\nu - 1$. Thus, this particular choice of nodes and weights renders equation (5.44) a *Gaussian quadrature*: with only ν nodes, the approximation reaches an accuracy of order $2\nu - 1$, instead of $\nu - 1$ which is the order of accuracy yielded by a normal quadrature formula (refer to §C.5 of Appendix C). Other choices of moments in equation (5.70) would lead to different nodes and weights, and equation (5.44) would be no longer a Gaussian quadrature. Therefore, preserving the first 2ν integer moments of the VDF is the most convenient option from the standpoint of mathematical accuracy.

This important property suggests an alternative, and much more efficient, method of calculating the quadrature coefficients $\xi_i(\boldsymbol{x}, t_0)$. These, in fact, are the roots of the monic orthogonal polynomial $\pi_\nu(\xi, \boldsymbol{x}, t_0)$ of degree ν based on the inner product definition:

$$\langle p_i, p_j \rangle \equiv \int_{\Omega_\xi} f_v(\xi, \boldsymbol{x}, t) p_i(\xi) p_j(\xi) d\xi \quad ; \quad \forall\, p_i, p_j \in \mathbb{P}_n(\xi) \tag{5.73}$$

that adopts as weighting function the VDF itself. Note that $f_v(\xi, \boldsymbol{x}, t)$ is positive-defined as required by any inner product definition. Here $p_i(\xi)$ and $p_j(\xi)$ are polynomials of the vector space $\mathbb{P}_n(\xi)$ of

the real polynomials $p(\xi)$ of degree at most n.

We can find the nodes by building a sequence of monic orthogonal polynomials using the recursive relation (refer to §C.4 of Appendix C):

$$\pi_{k+1}(\xi) = (\xi - \alpha_k)\pi_k(\xi) - \beta_k \pi_{k-1}(\xi) \tag{5.74}$$

where by definition:

$$\pi_{-1}(\xi) \equiv 0 \quad ; \quad \pi_0(\xi) \equiv 1 \quad ; \quad \alpha_k \equiv \frac{\langle \pi_k, \xi\pi_k \rangle}{\langle \pi_k, \pi_k \rangle} \quad ; \quad \beta_k \equiv \frac{\langle \pi_k, \pi_k \rangle}{\langle \pi_{k-1}, \pi_{k-1} \rangle} > 0 \tag{5.75}$$

Once $\pi_\nu(\xi, \boldsymbol{x}, t_0)$ is determined, its roots provide the abscissas $\xi_i(\boldsymbol{x}, t_0)$. Finding these roots, though, is anything but trivial; very often the problem is ill-conditioned (Press et al., 2002) and the numerical algorithms that perform the calculation do not converge easily. The product-difference algorithm of Gordon (1968), conversely, computes the roots of $\pi_\nu(\xi, \boldsymbol{x}, t_0)$, and simultaneously the quadrature weights and nodes, by solving an eigenproblem involving a real symmetric tridiagonal matrix. This is far easier to do numerically (Press et al., 2002). The method is based on the recursive formula (5.74); this can be rearranged in the more convenient form:

$$\xi\pi_k(\xi) = \beta_k \pi_{k-1}(\xi) + \alpha_k \pi_k(\xi) + \pi_{k+1}(\xi) \tag{5.76}$$

This equation generates the linear system:

$$\xi \boldsymbol{\pi}_{\nu-1}(\xi) = \boldsymbol{A}\boldsymbol{\pi}_{\nu-1}(\xi) + \boldsymbol{r}_\nu(\xi) \tag{5.77}$$

Here the matrix $\boldsymbol{A}$ of the polynomial coefficients is given by:

$$\boldsymbol{A} = \begin{pmatrix} \alpha_0 & 1 & 0 & \cdots & 0 & 0 & 0 & \cdots & 0 & 0 & 0 \\ \beta_1 & \alpha_1 & 1 & \cdots & 0 & 0 & 0 & \cdots & 0 & 0 & 0 \\ \vdots & \vdots & \vdots & \cdots & \vdots & \vdots & \vdots & \cdots & \vdots & \vdots & \vdots \\ 0 & 0 & 0 & \cdots & \beta_k & \alpha_k & 1 & \cdots & 0 & 0 & 0 \\ \vdots & \vdots & \vdots & \cdots & \vdots & \vdots & \vdots & \cdots & \vdots & \vdots & \vdots \\ 0 & 0 & 0 & \cdots & 0 & 0 & 0 & \cdots & \beta_{\nu-2} & \alpha_{\nu-2} & 1 \\ 0 & 0 & 0 & \cdots & 0 & 0 & 0 & \cdots & 0 & \beta_{\nu-1} & \alpha_{\nu-1} \end{pmatrix} \tag{5.78}$$

The vector $\boldsymbol{\pi}_{\nu-1}(\xi)$ of the polynomials $\pi_k(\xi)$ of degree k smaller than ν is:

$$\boldsymbol{\pi}_{\nu-1}(\xi) = \begin{pmatrix} \pi_0 & \pi_1 & \pi_2 & \cdots & \pi_k & \cdots & \pi_{\nu-2} & \pi_{\nu-1} \end{pmatrix}^T \tag{5.79}$$

Finally, the residual vector $\boldsymbol{r}_\nu(\xi)$ is:

$$\boldsymbol{r}_\nu(\xi) = \begin{pmatrix} 0 & 0 & 0 & \cdots & 0 & \cdots & 0 & \pi_\nu \end{pmatrix}^T \tag{5.80}$$

Since the quadrature nodes are the roots of the polynomial $\pi_\nu(\xi)$, for any $\xi_i(\boldsymbol{x}, t_0)$ the vector $\boldsymbol{r}_\nu(\xi_i)$ vanishes and equation (5.77) reduces to:

$$\boldsymbol{A}\boldsymbol{\pi}_{\nu-1}(\xi_i) = \xi_i \boldsymbol{\pi}_{\nu-1}(\xi_i) \tag{5.81}$$

Thus, *the quadrature nodes $\xi_i(\boldsymbol{x}, t_0)$ coincide with the eigenvalues of the matrix $\boldsymbol{A}$* (Lang, 2004). Many efficient algorithms solve eigenproblems for *real symmetrical matrices*; thus, when a problem involving a real unsymmetrical matrix comes along (as in our case, since $\boldsymbol{A}$ is real and tridiagonal, but not symmetrical), it is convenient, if possible, to transform the matrix into a symmetrical one having the same eigenvalues. This can be done by looking for an invertible matrix $\boldsymbol{D}$ that satisfies the following similarity condition (Bronson, 1989; Lipschutz & Lipson, 2001):

$$\boldsymbol{B} = \boldsymbol{D}\boldsymbol{A}\boldsymbol{D}^{-1} \tag{5.82}$$

where $\boldsymbol{B}$ is symmetrical. If $\boldsymbol{D}$ exists, $\boldsymbol{A}$ and $\boldsymbol{B}$ are similar and have the same eigenvalues, for similar matrices have the same characteristic equation. Note, however, that the eigenvectors are different and related by the following expression:

$$\boldsymbol{\omega}(\xi_i) = \boldsymbol{D}^{-1}\boldsymbol{\pi}_{\nu-1}(\xi_i) \tag{5.83}$$

where $\boldsymbol{\omega}(\xi_i)$ is the eigenvector of $\boldsymbol{B}$ corresponding to the eigenvalue $\xi_i(\boldsymbol{x}, t_0)$. It can be proved that for tridiagonal matrices the transformation (5.82) is always possible and $\boldsymbol{D}$ is diagonal. In our case, its diagonal elements d_k are given by:

$$d_1 = 1 \quad ; \quad d_k = \left(\prod_{i=1}^{k-1} \sqrt{\beta_i} \right)^{-1} \quad ; \quad 2 \leqslant k \leqslant \nu \tag{5.84}$$

As previously pointed out, the coefficients β_i are positive-defined and never vanish. If we perform the transformation just described, we obtain:

$$\boldsymbol{B} = \begin{pmatrix} \alpha_0 & \sqrt{\beta_1} & \cdots & 0 & 0 & 0 & \cdots & 0 & 0 \\ \sqrt{\beta_1} & \alpha_1 & \cdots & 0 & 0 & 0 & \cdots & 0 & 0 \\ \vdots & \vdots & \cdots & \vdots & \vdots & \vdots & \cdots & \vdots & \vdots \\ 0 & 0 & \cdots & \sqrt{\beta_k} & \alpha_k & \sqrt{\beta_{k+1}} & \cdots & 0 & 0 \\ \vdots & \vdots & \cdots & \vdots & \vdots & \vdots & \cdots & \vdots & \vdots \\ 0 & 0 & \cdots & 0 & 0 & 0 & \cdots & \alpha_{\nu-2} & \sqrt{\beta_{\nu-1}} \\ 0 & 0 & \cdots & 0 & 0 & 0 & \cdots & \sqrt{\beta_{\nu-1}} & \alpha_{\nu-1} \end{pmatrix} \tag{5.85}$$

To find the quadrature nodes, we then have to solve the eigenproblem:

$$\boldsymbol{B}\boldsymbol{\omega}(\xi_i) = \xi_i \boldsymbol{\omega}(\xi_i) \tag{5.86}$$

To find the eigenvalues of $\boldsymbol{B}$, we must first calculate the elements of the matrix itself. To evaluate the coefficients α_k and β_k, we could use equation (5.75), but this would entail finding the ν polynomials $\boldsymbol{\pi}_k(\xi)$ of the sequence. The product-difference algorithm of Gordon (1968) performs the calculation much more effectively. The algorithm consists of the following steps. First, the elements $g_{p,q}$ of the so-called *Gordon matrix* $\boldsymbol{G}$, which is a square matrix of dimension $2\nu + 1$, must be calculated. The elements of the first column of the matrix are:

$$g_{1,1} = 1 \quad ; \quad g_{p,1} = 0 \quad ; \quad 2 \leqslant p \leqslant 2\nu + 1 \tag{5.87}$$

The elements of the second column are:

$$g_{p,2} = \mathscr{M}_{p-1}(\boldsymbol{x}, t_o)(-1)^{\,p-1} \quad ; \quad 1 \leqslant p \leqslant 2\nu \quad ; \quad g_{p,2\nu+1} = 0 \tag{5.88}$$

The remaining elements are given by a product-difference scheme:

$$\begin{aligned} g_{p,q} = g_{1,q-1}\, g_{p+1,q-2} - g_{1,q-2}\, g_{p+1,q-1} \quad ; \quad & \begin{cases} 1 \leqslant p \leqslant 2(\nu+1) - q \\ 3 \leqslant q \leqslant 2\nu + 1 \end{cases} \\ g_{p,q} = 0 \quad ; \quad & \begin{cases} 2(\nu+1) - (q-1) \leqslant p \leqslant 2\nu + 1 \\ 3 \leqslant q \leqslant 2\nu + 1 \end{cases} \end{aligned} \tag{5.89}$$

The coefficients α_k and β_k are then given by:

$$\alpha_k = \varsigma_{2k} + \varsigma_{2k+1} \quad ; \quad 0 \leqslant k \leqslant \nu - 1 \quad \text{and} \quad \beta_k = \varsigma_{2k}\varsigma_{2k-1} \quad ; \quad 1 \leqslant k \leqslant \nu - 1 \tag{5.90}$$

where the elements ς_k are defined as:

$$\varsigma_0 = 0 \quad ; \quad \varsigma_k = \frac{g_{1,k+2}}{g_{1,k+1}\, g_{1,k}} \quad ; \quad 1 \leqslant k \leqslant 2\nu - 1 \tag{5.91}$$

Once the elements of $\boldsymbol{B}$ are known, we can calculate its eigenvalues and eigenvectors (the latter are needed to compute the quadrature weights). The quadrature nodes are necessarily real, and not complex, because the eigenvalues of any real symmetric matrix are real (Lang, 2004).

To determine the quadrature weights, we could use equation (5.70). Since the nodes are known, it suffices to write the equation for the chosen ν values of k and solve the resulting linear algebraic system. This, however, is unnecessary, for the PD algorithm tells us that:

$$\phi_i(\boldsymbol{x}, t_o) = \mathscr{M}_0(\boldsymbol{x}, t_o) w_1^2(\xi_i, \boldsymbol{x}, t_o) \tag{5.92}$$

where $w_1(\xi_i, \boldsymbol{x}, t_o)$ denotes the first component of the eigenvector $\boldsymbol{w}(\xi_i, \boldsymbol{x}, t_o)$ of the matrix $\boldsymbol{B}$. Note that in general the eigenvectors are defined up to a proportionality constant, and therefore only the ratios between their components, and not the components themselves, are meaningful. In equation (5.92), however, the eigenvectors are assumed of unit magnitude.

5.7.3 Summary

We can summarize the main steps of the method as follows:

1) We write the GPBE for monovariate distributions.
2) Using a quadrature formula, we represent the VDF by ν particle classes, each having a volume fraction $\phi_i(\boldsymbol{x}, t)$ and an internal coordinate $\xi_i(\boldsymbol{x}, t)$.
3) We introduce the approximated VDF in the monovariate GPBE, obtaining 2ν transport equations that govern the evolution of the quadrature weights and weighted nodes.
4) We calculate moment transforms of the GPBE to determine the source terms $c_i^{\phi}(\boldsymbol{x}, t)$ and $c_i^{\xi}(\boldsymbol{x}, t)$ of the transport equations. Since the unknowns are 2ν, an equivalent number of independent moments must be considered. We have to solve, therefore, a linear algebraic system of order 2ν. The solution of the system, and in turn the functional form of the source terms, depends on the moments considered. Different moments preserve different properties of the VDF.
5) To fully define the physical problem in hand, we must assign boundary and initial conditions. To set the former, we specify on the system boundaries either the quadrature weights and weighted nodes or their fluxes. To set the latter, we must know at least 2ν moments of the VDF at the initial time t_0. Equating these values to the moment expressions based on the quadrature approximation, we derive a nonlinear algebraic system whose solution yields $\phi_i(\boldsymbol{x}, t_0)$ and $\xi_i(\boldsymbol{x}, t_0)$.
6) For monovariate systems, we can adopt a better technique to solve the system, since the quadrature nodes are the roots of the monic orthogonal polynomial $\pi_\nu(\xi, \boldsymbol{x}, t_0)$ of degree ν based on the inner product definition that adopts as weighting function the VDF. This technique, proposed by Gordon (1968), uses the 2ν VDF moments to build a real symmetric tridiagonal matrix whose eigenvalues yield the quadrature nodes $\xi_i(\boldsymbol{x}, t_0)$ and whose eigenvectors allow determining the quadrature weights $\phi_i(\boldsymbol{x}, t_0)$.

5.8 Quadrature method of moments

This method tracks the moments of the VDF and back-calculates the quadrature nodes and weights by solving the nonlinear algebraic system (5.70). For monovariate distributions, the PD algorithm described in §5.7.2 provides the solution more easily. However, whereas DQMOM runs the algorithm just once to initialize the quadrature variables, QMOM runs it at each time step of the numerical simulation and at each grid point of the computational domain.

To derive the transport equations of the VDF moments, we use equation (5.45), which represents the generalized population balance equation for a monovariate distribution. If the internal coordinate coincides with the particle diameter and a conditional relationship exists between the latter and the particle velocity, equation (5.45) reduces to:

$$\frac{\partial f_v}{\partial t} + \boldsymbol{\nabla}_x \cdot \left(f_v \boldsymbol{v}\right) + \frac{\partial}{\partial \xi}\left(f_v \dot{\xi}\right) = h_v + \frac{3 f_v \dot{\xi}}{\xi} \tag{5.93}$$

Let us apply the moment transform (5.32) to each term of this equation. For the first, we have:

$$\mathscr{M}_k\left(\frac{\partial f_v}{\partial t}\right) = \int_{\Omega_\xi} \frac{\partial f_v}{\partial t}\xi^k d\xi = \int_{\Omega_\xi} \frac{\partial}{\partial t}\big(f_v \xi^k\big)\, d\xi = \frac{\partial}{\partial t}\int_{\Omega_\xi} f_v \xi^k d\xi = \frac{\partial \mathscr{M}_k}{\partial t} \tag{5.94}$$

For the second term, we write:

$$\mathscr{M}_k\Big(\boldsymbol{\nabla}_x \cdot \big(f_v \boldsymbol{v}\big)\Big) = \int_{\Omega_\xi} \boldsymbol{\nabla}_x \cdot \big(f_v \boldsymbol{v}\big)\xi^k d\xi = \int_{\Omega_\xi} \boldsymbol{\nabla}_x \cdot \big(f_v \xi^k \boldsymbol{v}\big)\, d\xi \tag{5.95}$$

$$= \boldsymbol{\nabla}_x \cdot \int_{\Omega_\xi} f_v \xi^k \boldsymbol{v}\, d\xi = \boldsymbol{\nabla}_x \cdot \big(\mathscr{M}_k \boldsymbol{v}_k\big) \tag{5.96}$$

where the velocity $\boldsymbol{v}_k(\boldsymbol{x}, t)$ with which the k-th moment is convected is defined to be:

$$\boldsymbol{v}_k(\boldsymbol{x}, t) \equiv \frac{1}{\mathscr{M}_k(\boldsymbol{x}, t)} \int_{\Omega_\xi} f_v(\xi, \boldsymbol{x}, t)\xi^k \boldsymbol{v}(\xi, \boldsymbol{x}, t) d\xi \tag{5.97}$$

Here $\boldsymbol{v}(\xi, \boldsymbol{x}, t)$ is the conditional relationship between particle velocity and particle diameter. Using the quadrature approximation, equation (5.44), we notice that:

$$f_v(\xi, \boldsymbol{x}, t)\xi^k \boldsymbol{v}(\xi, \boldsymbol{x}, t) = \sum_{i=1}^{\nu} \phi_i(\boldsymbol{x}, t)\xi_i^k(\boldsymbol{x}, t)\boldsymbol{v}_i(\boldsymbol{x}, t)\delta\Big[\xi - \xi_i(\boldsymbol{x}, t)\Big] \tag{5.98}$$

whence, equation (5.97) becomes:

$$\boldsymbol{v}_k(\boldsymbol{x}, t) = \frac{1}{\mathscr{M}_k(\boldsymbol{x}, t)} \sum_{i=1}^{\nu} \phi_i(\boldsymbol{x}, t)\xi_i^k(\boldsymbol{x}, t)\boldsymbol{v}_i(\boldsymbol{x}, t) \tag{5.99}$$

The moment transforms of the remaining terms of equation (5.93) have been evaluated previously; refer to equations (5.54), (5.55), (5.61) and (5.62). The final result therefore is:

$$\frac{\partial \mathscr{M}_k}{\partial t} + \boldsymbol{\nabla}_x \cdot \big(\mathscr{M}_k \boldsymbol{v}_k\big) = \mathscr{S}_k(\boldsymbol{x}, t) \tag{5.100}$$

where the source term on the right-hand side is:

$$\mathscr{S}_k(\boldsymbol{x}, t) \equiv \mathscr{M}_k(h_v) + (3 + k)\sum_{i=1}^{\nu} \phi_i \xi_i^{k-1} \dot{\xi}(\xi_i) \tag{5.101}$$

Equation (5.100) governs the evolution of $\mathscr{M}_k(\boldsymbol{x}, t)$. The functions of real interest, however, are the quadrature nodes and weights, which we can back-calculate using the PD algorithm. As before, since the unknowns are 2ν, we need 2ν equations in the functions $\phi_i(\boldsymbol{x}, t)$ and $\xi_i(\boldsymbol{x}, t)$. These are given by equation (5.70), which relates the nodes and weights to the moments; accordingly, 2ν moments must be tracked. At each time step of the simulation and at each grid point of the computational domain,

once the moments have been determined, we can generate the Gordon matrix using equations (5.87), (5.88) and (5.89). Successively, we can build the tridiagonal symmetric matrix $\boldsymbol{B}$ and compute its eigenvalues and eigenvectors. These yield the functions $\phi_i(\boldsymbol{x}, t)$ and $\xi_i(\boldsymbol{x}, t)$.

QMOM and DQMOM are equivalent from a theoretical point of view; numerically, however, DQMOM offers many advantages, especially when the problem involves multivariate distributions. Since QMOM tracks the moments of the VDF, back-calculation of the quadrature nodes and weights is necessary. In general, this means solving a nonlinear algebraic system at each time step and each point of the computational grid; for monovariate distributions, it means running the PD algorithm an equal number of times. The method is therefore considerably more expensive than DQMOM, which instead tracks directly the functions of interest. Moreover, the moment transport equations appear to be less stable numerically than those involving nodes and weights. Consequently, DQMOM is often preferred. The equivalence of the two methods, however, should be proved numerically.

5.9 Conclusions

The classical Eulerian-Eulerian equations of motion for fluidized suspensions of equal particles do not allow for variations in particle size. In reality, however, particles can shrink, aggregate, break or nucleate; their size distribution therefore continuously changes in time and space. These changes are closely related to the physical process examined and reflect the presence of chemical reactions, attrition and several other effects. Modelling these aspects is essential for an accurate description of the physics. To do so, we must employ a more powerful approach that hinges on the generalized population balance equation, which completely describes the distribution of the population members over the properties of interest. The GPBE captures all the physics of the problem; hence, no other equations, at least in principle, are needed. Nonetheless, since its dimensionality is higher than that of classical transport equations, integrating the GPBE is extremely difficult. The method of moments is a tradeoff between complexity and accuracy: it replaces the single multidimensional GPBE with a set of three-dimensional averaged transport equations that govern the distribution moments. The set is often unclosed and closure is needed to render it self-sufficient. A solution is representing the population by a finite number of classes, each with a volume fraction and a specific set of internal properties; the VDF is thus approximated by a quadrature formula that turns integrals into summations; the closure problem is therefore solved. QMOM tracks the moments of the distribution and back-calculates the quadrature nodes and weights; DQMOM directly tracks the latter. Being based on the same idea, the two methods are equivalent from a theoretical standpoint; numerically, however, DQMOM offers several advantages and is therefore often preferred.

Chapter 6

Application of the direct quadrature method of moments to polydisperse gas-fluidized suspensions

In this chapter, we study the dynamics of a gas-fluidized powder initially made up of two superposed layers of polydisperse particles with equal density and different size distribution.

1) We describe the properties of the powders, reporting their experimental fluidization curves and particle size distributions.
2) We present the experimental apparatus and illustrate the experiments that we conducted.
3) We simulate the dynamics of the fluidized suspension, using a two-node direct quadrature method of moments, and we compare numerical and experimental results.

6.1 Introduction

We intend to simulate the fluidization dynamics of a polydisperse suspension, using the modelling approach presented in Chapter 5. Being the first time that we apply this approach, we consider a simple application to validate the model. Moreover, since the direct quadrature method of moment

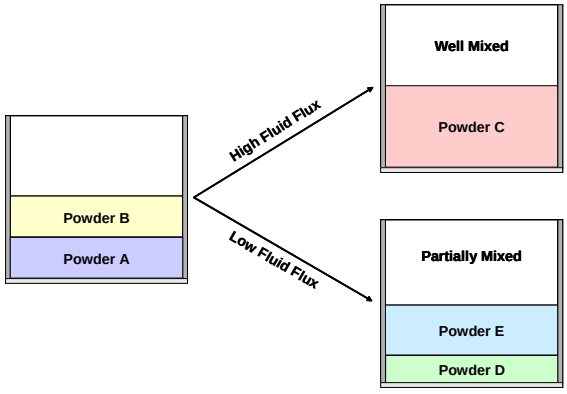

Figure 6.1: Different fluidization dynamics depending on the superficial fluid flux.

(DQMOM) is numerically more stable than the quadrature method of moments (QMOM), we use only the former and postpone the comparison between the two models to a future work.

Let us consider a fixed bed made up of two superposed layers of polydisperse particles of equal density (see Figure 6.1). Referred to as *powder A* and *powder B*, respectively, the lower and upper layers differ only in particle size distribution (PSD), the one on top having a greater mean particle size. If the PSDs are reasonably narrow, the materials have well-defined minimum fluidization velocities; we denote them by u_A and u_B, where u_B is greater than u_A. The dynamics of the fluidized system depends on the ratio u_s/u_B, where u_s is the superficial velocity of the fluid. If the ratio is greater than one, the two powders thoroughly mix; at lower ratios, powder B partially mixes with powder A and partially segregates towards the bottom of the bed (Yang, 2003). The two conditions are depicted in Figure 6.1. At high fluid fluxes, the system reaches a configuration where only one powder, perfectly homogeneous, is present. At low fluid fluxes, conversely, two layers coexist: the lower contains the segregated biggest particles of powder B, whereas the upper is a mix of powder A and the remaining particles of powder B. At very low fluid fluxes, if the two powders considerably differ in mean particle size, complete inversion can take place, with powder A lying on top of powder B.

Here we investigate the simplest case: perfect mixing. Choosing a superficial fluid velocity greater than u_B, we thoroughly mix powders A and B. The resulting powder, referred to in Figure 6.1 as *powder C*, is described by a particle size distribution that combines the two original ones. Using the direct quadrature method of moments, we propose to predict the new distribution and check that it reasonably agrees with the experimental one.

6.2 Experimental materials

The powders are ballotini with particle density 2500 $\mathrm{kg/m^3}$. To obtain representative samples of the materials, avoid stratification and assure good homogeneity, we riffled large batches of powder. We then determined the particle size distributions by sieve analysis, performing three measurements for each material. Figures 6.2 - 6.5 report the normal and cumulative particle size distributions for powders A and B. Using these data, we can compute the mean particle sizes of the distributions and their coefficients of variation (Randolph & Larson, 1971). There are several definitions for the former; here, we use the surface-volume diameter (Geldart, 1973) defined as:

$$d_{sv} \equiv \left(\sum_{i=1}^{n} \frac{\omega(\xi_{i-1}, \xi_i)}{d(\xi_{i-1}, \xi_i)} \right)^{-1} \tag{6.1}$$

where n is the number of sieves, ξ_i is the aperture of the i-th sieve, $\omega(\xi_{i-1}, \xi_i)$ is the mass fraction of powder in the size range (ξ_{i-1}, ξ_i) and $d(\xi_{i-1}, \xi_i)$ is the arithmetic average of ξ_{i-1} and ξ_i. Following Geldart (1973), we estimate the coefficient of variation using the expression:

$$c.v. \approx \frac{\xi(0.84) - \xi(0.16)}{2\xi(0.50)} \tag{6.2}$$

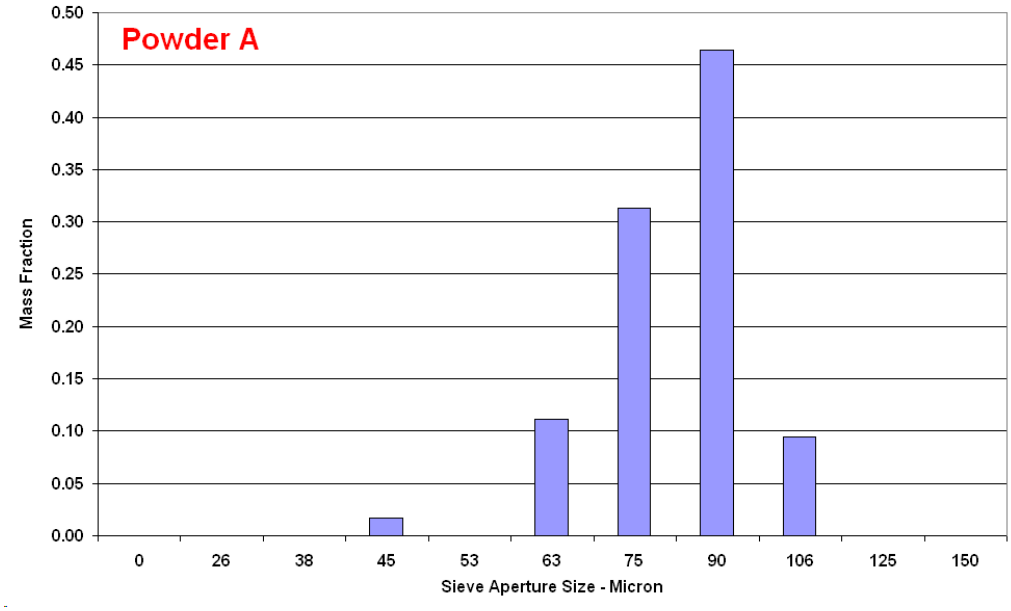

Figure 6.2: Normal particle size distribution for powder A.

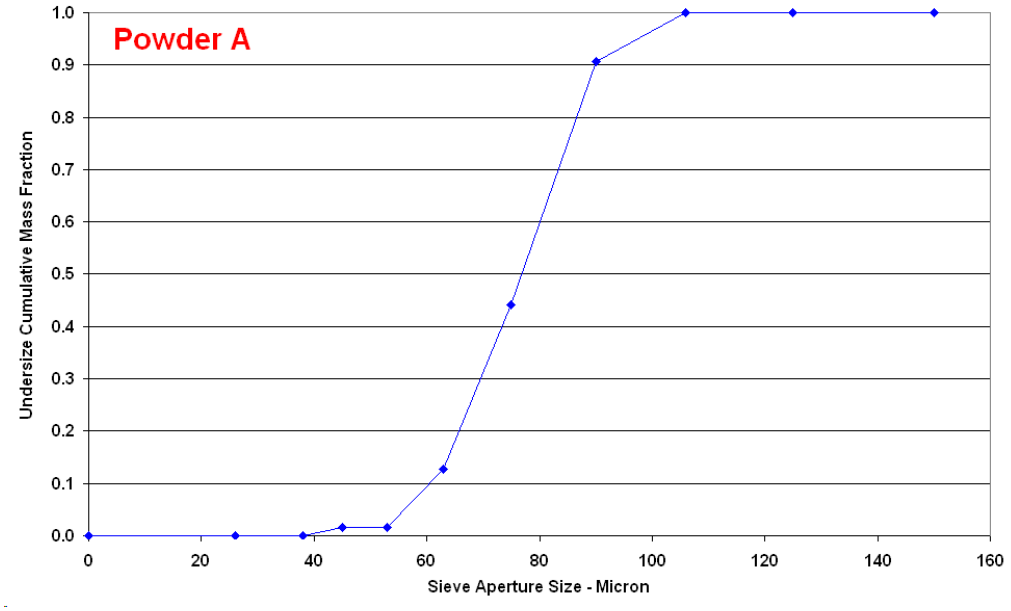

Figure 6.3: Cumulative particle size distribution for powder A.

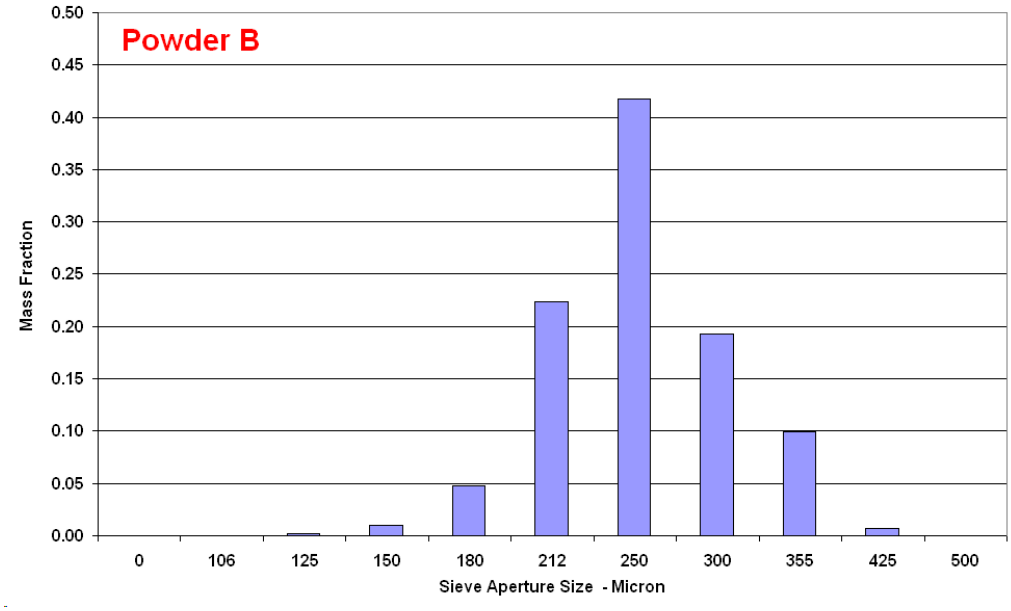

Figure 6.4: Normal particle size distribution for powder B.

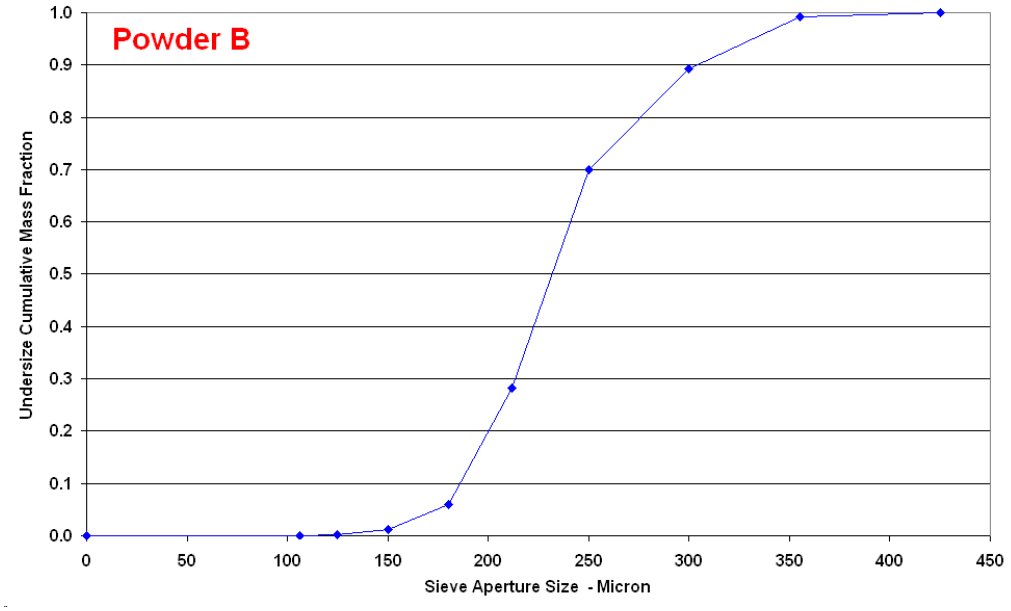

Figure 6.5: Cumulative particle size distribution for powder B.

where $\xi(0.16)$, $\xi(0.50)$ and $\xi(0.84)$ are obtained from the cumulative particle size distribution and represent the sizes corresponding to the undersize cumulative mass fractions of 0.16, 0.50 and 0.84, respectively; this means, for instance, that 16% of the powder mass is made up of particles of size less than $\xi(0.16)$. Equation (6.2) is correct only for *normal distributions*, but usually provides a good estimate of $c.v.$ for distributions of granular materials (Randolph & Larson, 1971). For powders A and B, the surface-volume mean particle diameters and coefficients of variation are equal to 88 μm, 273 μm, 0.16 and 0.20, respectively. The classification of Geldart (1973) reported in Table 6.1 gives an idea of the relative spread judged from the number of sieves on which the middle 70% of the powder mass lies; according to it, both powders have fairly narrow distributions.

Using diagrams of the unrecoverable pressure drop through the bed against the superficial fluid velocity, we measured the minimum fluidization velocities u_A and u_B of both powders. By definition, these are the velocities at which the horizontal fluidized bed lines intersect the sloping packed bed lines obtained by gradually decreasing the fluid flow rate. Figures 6.6 and 6.7 report the ratio between the measured unrecoverable pressure drop through the bed and the theoretical effective weight of the bed for powders A and B; u_A and u_B are roughly equal to 1.00 cm/s and 6.40 cm/s, respectively.

From the particle size distributions reported in Figures 6.2 and 6.4, we can also calculate the moments of the monovariate volume density functions (VDFs) that characterize the two powders. It can be shown (refer to Appendix E) that it is:

$$\mathscr{M}_k \approx (1-\varepsilon) \sum_{i=1}^{n} \frac{\omega(\xi_{i-1},\xi_i)}{\xi_i - \xi_{i-1}} \cdot \frac{\xi_i^{k+1} - \xi_{i-1}^{k+1}}{k+1} \tag{6.3}$$

where $\mathscr{M}_k$ is the VDF moment of order k and ε is the powder voidage. Equation (6.3) tells us that $\mathscr{M}_k$ is a function of ε; this is because, whereas the PSD refers to solid mass fractions on a *void-free basis*, the VDF accounts for the presence of voids and provides volume densities – that is, volumes

Number of sieves	$c.v.$	Type of distribution
1	0.00	very narrow
2	0.03	narrow
3	0.17	fairly narrow
4	0.25	fairly wide
5	0.33	wide
6	0.41	wide
7	0.48	wide
9	0.60	very wide
11	0.70	very wide
> 13	> 0.80	extremely wide

Table 6.1: Width of size distributions based on the coefficient of variation (Geldart, 1973). The first column reports the number of sieves on which the middle 70% of the powder mass lies.

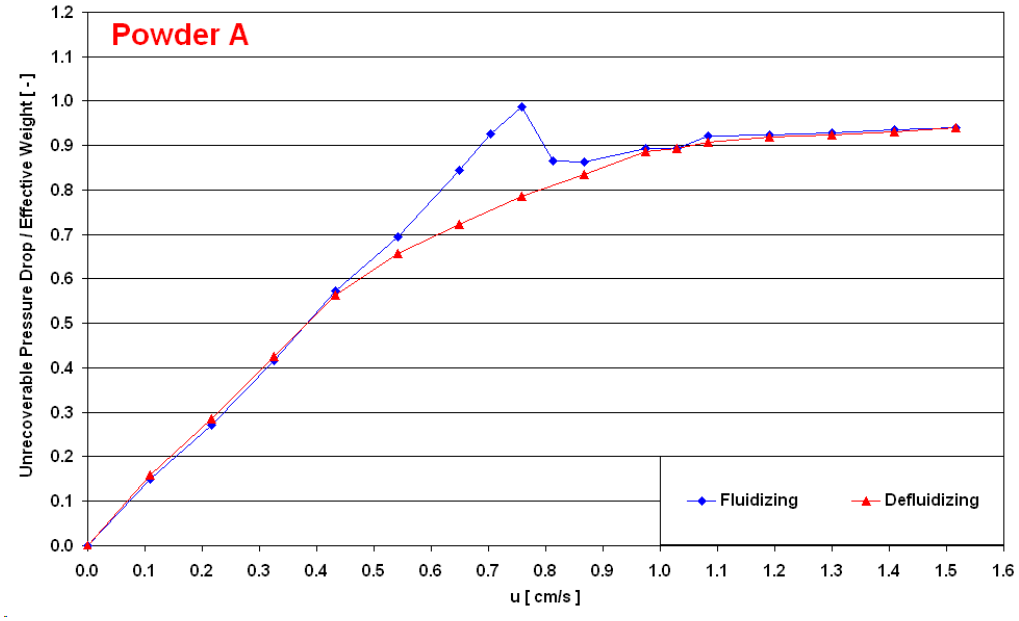

Figure 6.6: Pressure drop profile for powder A.

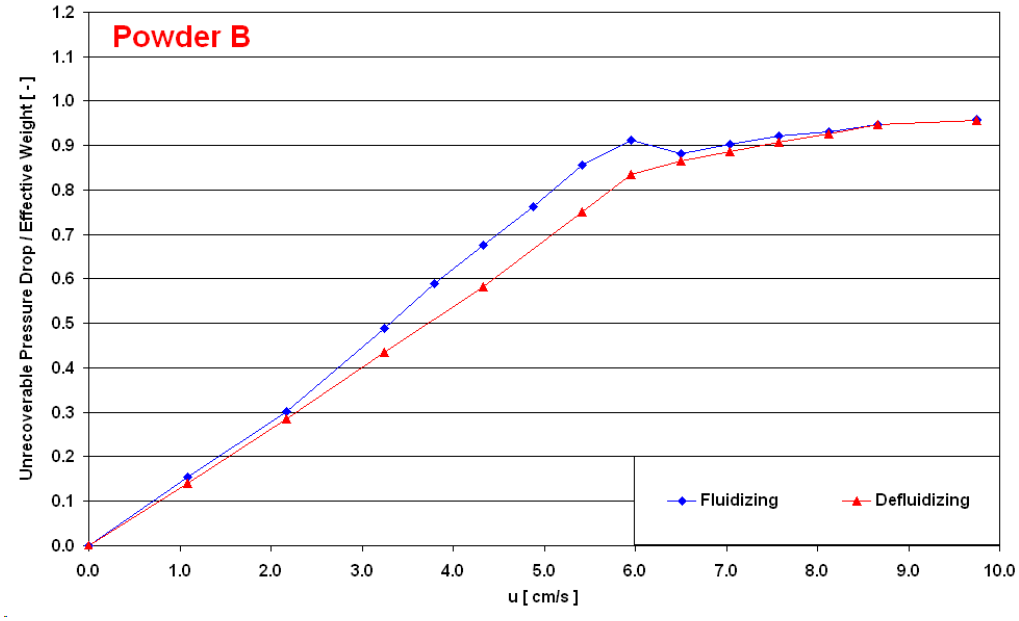

Figure 6.7: Pressure drop profile for powder B.

Moments of the volume density function				
Powder	$\mathscr{M}_0\ [-]$	$\mathscr{M}_1\ [\mu\mathrm{m}]$	$\mathscr{M}_2\ [\mu\mathrm{m}^2]$	$\mathscr{M}_3\ [\mu\mathrm{m}^3]$
A	0.600	$5.45 \cdot 10^1$	$5.06 \cdot 10^3$	$4.82 \cdot 10^5$
B	0.600	$1.70 \cdot 10^2$	$4.98 \cdot 10^4$	$1.52 \cdot 10^7$
Quadrature nodes and weights				
Powder	$\xi_1\ [\mu\mathrm{m}]$	$\phi_1\ [-]$	$\xi_2\ [\mu\mathrm{m}]$	$\phi_2\ [-]$
A	75	0.262	103	0.338
B	240	0.380	355	0.220

Table 6.2: Values of the VDF moments and of the quadrature nodes and weights obtained from the experimental PSDs reported in Figures 6.2 and 6.4 assuming a void fraction of 0.400.

of solid per unit volume of physical space. Once the moments are known, we can compute the nodes and weights of the VDF quadrature approximation:

$$f_v(\xi, \boldsymbol{x}, t_0) \approx \sum_{i=1}^{\nu} \phi_i(\boldsymbol{x}, t_0) \delta\Big[\xi - \xi_i(\boldsymbol{x}, t_0)\Big] \tag{6.4}$$

If the powders are homogeneous – and this is true if they are properly mixed before being loaded in the vessel – the quadrature nodes and weights do not depend on the spatial coordinate $\boldsymbol{x}$. Here, as previously said, we employ a two-node quadrature formula; accordingly, we have two nodes and two weights. To determine their values, we need four moments. If we use the first four integer moments of the distribution, equation (6.4) is a Gaussian quadrature, and we can use the product-difference (PD) algorithm of Gordon (1968) to compute the unknowns. The results are shown in Table 6.2. With a two-node representation, powders A and B become bidisperse suspensions: the first with particles of sizes 75 μm and 103 μm and volume fractions 0.262 and 0.338, respectively, whereas the second with particles of sizes 240 μm and 355 μm and volume fractions 0.380 and 0.220, respectively. As we shall see in § 6.5.2, we will use these values to initialize the quadrature weights and weighted nodes in the numerical simulation.

6.3 Experimental apparatus, methodology and results

The experimental set-up consists of a two-dimensional plexiglass rectangular column, 600 mm high, 350 mm wide and 10 mm deep, with a 3.5 mm thick uniform permeable sintered bronze rectangular plate as distributor. Nitrogen is supplied via flow meters. Pressure taps are installed 100 mm apart along the height of the bed from which pressure readings as a function of the superficial gas velocity are collected via a digitron electronic manometer. A system of two interlocked on/off valves operated simultaneously is installed on the rig to evacuate instantaneously the fluidizing gas during the bed

freeze tests that we performed to analyze the mixing and segregation in the bed. Figure 6.8 shows a photograph of the set-up and a schematic representation of the rig.

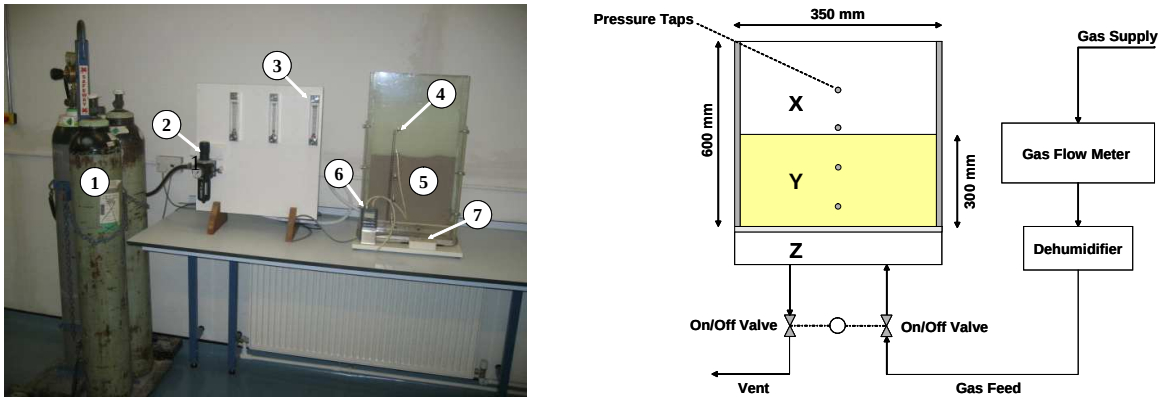

Figure 6.8: Photograph and schematic representation of the experimental apparatus. 1) nitrogen tanks, 2) oil filter, 3) flow meters, 4) pressure taps, 5) fluidized bed, 6) electronic manometer, 7) on/off valves control switch, X) freeboard, Y) fluidized bed, Z) windbox.

As shown in Figure 6.1, in the experiment we filled half of the column with powder, forming two layers of equal height (15 cm): the lower of powder A and the upper of powder B. We placed the coarser powder on top, to enhance the fluidization dynamics and verify if segregation occurs. At the high fluid fluxes used in this study, the two powders should mix almost perfectly, turning into a uniform suspension; however, if any segregation should take place, this is because the coarser powder naturally tends to sink towards the bottom of the bed. Thus, if we had placed powder B below powder A, we would have hindered this motion. After loading the powders, we fed nitrogen for ten minutes, a time sufficient to reach pseudo stationary conditions (as we checked by observing the bed). To ensure vigorous mixing, we set the superficial velocity of the gas to 15 cm/s, which results in a ratio u_s/u_B equal to 2.35. Successively, we performed a so-called *bed freeze test*: by operating the interlocked on/off valves shown in Figure 6.8, we abruptly cut off the gas supply to the bed, and vented the gas in the windbox of the vessel to the atmosphere. With this configuration, most of the interstitial gas in the powder initially escapes through the vent, finding there a lower fluid dynamic resistance. Then, as the particles accumulate on the distributor plate and the pressure drop across the settled bed becomes greater than that in the upper bed, the gas escapes from the top of the bed. This process is very quick, so the powder retains its instantaneous distribution, as if it were frozen. We then split the resting bed into five layers of equal height (6 cm), collected each layer by means of a sampling probe and sieved it to obtain its particle size distribution. The probe was designed by Dr. Olumuyiwa Owoyemi, a former UCL student of the fluidization modelling research group, and is shown in Figure 6.9; to operate it, we embedded it vertically into the fixed bed and collected the granular material into a sampling container; a vacuum pump provided the suction required to suck the material.

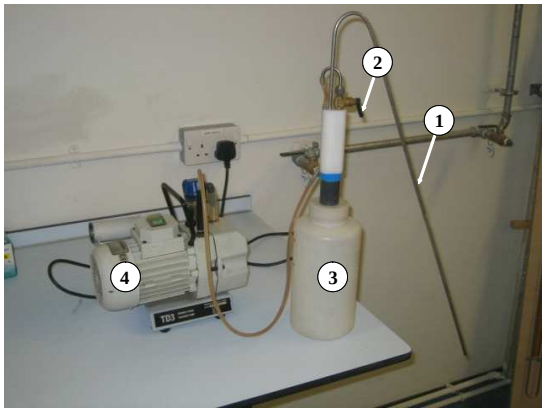

Figure 6.9: Sampling probe used to extract the granular material from the fixed bed. 1) steel probe, 2) vacuum actuator, 3) sample collector, 4) vacuum pump.

As expected, the two powders mixed almost perfectly, the particle size distributions of the five layers being nearly identical. Figures 6.10 and 6.11 report the PSDs of the most significant layers: the lowest, which directly lies on the distributor, and the highest, which separates the bed from the freeboard. The new PSDs seem to be obtained by juxtaposing the two original distributions reported in Figures 6.2 and 6.4; this clearly indicates very good mixing.

From the PSDs, we can compute the first four integer moments of the distributions and, applying the PD algorithm of Gordon (1968), the corresponding quadrature nodes and weights. Table 6.3 shows the results, which refer to the PSD of the bottom layer. The two-node representation again models the powder as a bidisperse suspension; the two sets of particles have diameters 105 μm and 304 μm and volume fractions 0.331 and 0.269, respectively. Note that, since the particles are inert and do not break, agglomerate or nucleate, and since perfect mixing is attained, the nodes take on values that are intermediate between their original ones; from 75 μm and 240 μm the first node tends to 105 μm, whereas from 103 μm and 355 μm the second node tends to 304 μm.

Moments of the volume density function			
$\mathscr{M}_0\ [-]$	$\mathscr{M}_1\ [\mu\text{m}]$	$\mathscr{M}_2\ [\mu\text{m}^2]$	$\mathscr{M}_3\ [\mu\text{m}^3]$
0.600	$1.16 \cdot 10^2$	$2.85 \cdot 10^4$	$7.95 \cdot 10^6$
Quadrature nodes and weights			
$\xi_1\ [\mu\text{m}]$	$\phi_1\ [-]$	$\xi_2\ [\mu\text{m}]$	$\phi_2\ [-]$
105	0.331	304	0.269

Table 6.3: Values of the VDF moments and of the quadrature nodes and weights obtained from the experimental PSD of the bottom layer assuming a void fraction of 0.400.

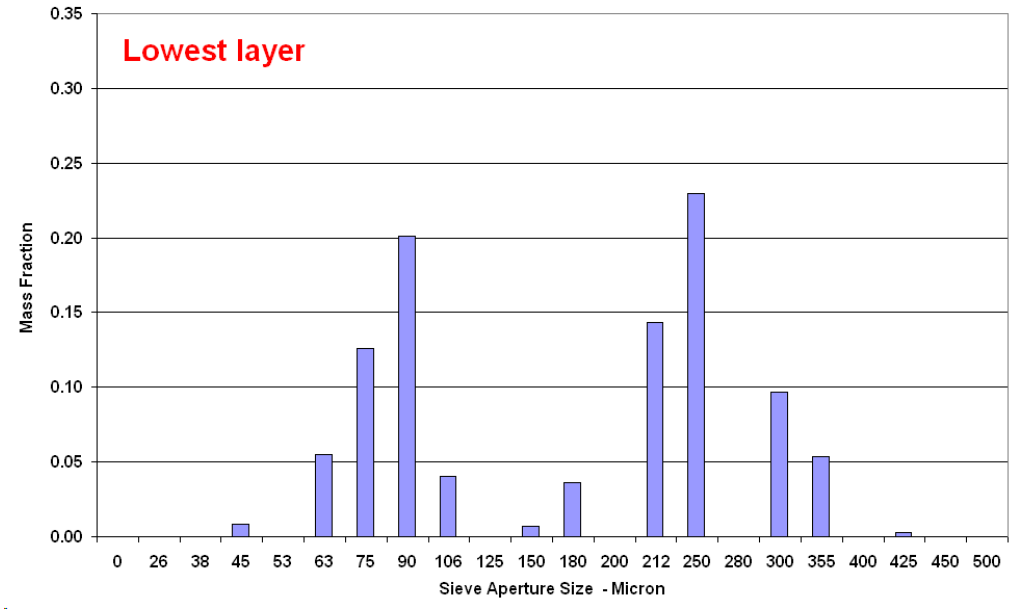

Figure 6.10: Particle size distribution of the lowest layer, which directly lies on the distributor.

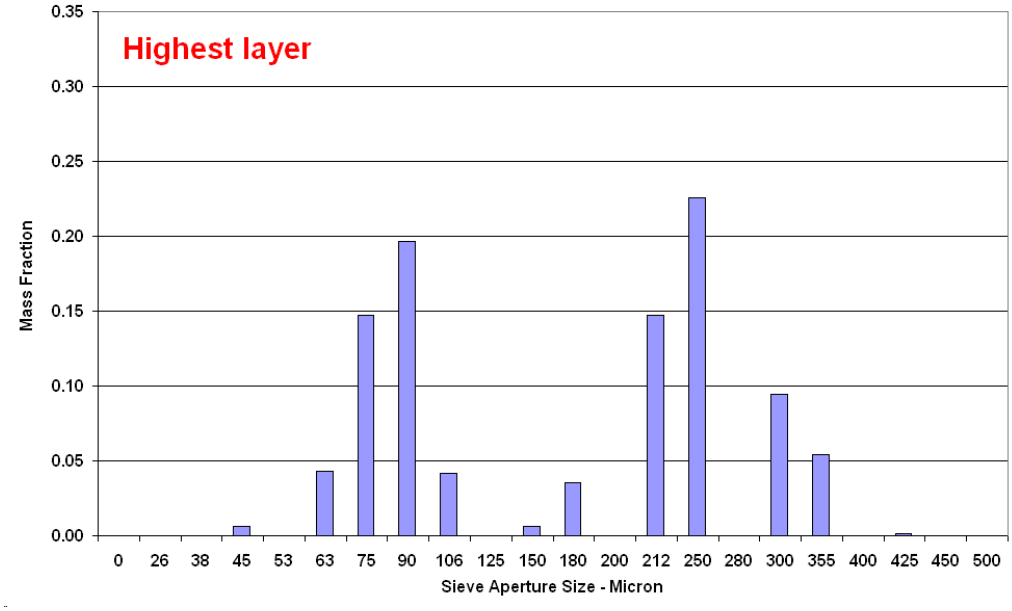

Figure 6.11: Particle size distribution of the highest layer, which separates the bed from the freeboard.

6.4 Theoretical calculations

This study aims to predict the PSDs shown in Figures 6.10 and 6.11 by solving the DQMOM transport equations described in Chapter 5. As already explained, the direct quadrature method of moments solves the generalized population balance equation (GPBE) and tracks the evolution in time and physical space of the volume density function; from this, we can easily reconstruct the particle size distribution. Not solving the n-dimensional GPBE, we cannot obtain a continuous distribution: the quadrature approximation consents to find only a finite set of nodes with relative weights; these must then be compared with those found experimentally. Therefore, we cannot validate the results using the block diagrams of Figures 6.10 and 6.11, but we must instead use Table 6.3.

Before discussing the simulation, we make some preliminary calculations to understand which computational results we should expect. If we assume perfect mixing, a simple mass balance provides the PSD of the resulting powder. Since we intend to anticipate the results that the numerical code should give, to perform the calculation we must employ the same data that the code knows. Hence, we must not consider the real powders A and B, whose PSDs are reported in Figures 6.2 and 6.4, but we have to use their quadrature approximations reported in Table 6.2. Thus, we model powder A as a binary suspension of particles with diameters 75 μm and 103 μm and volume fractions 0.262 and 0.338, respectively, and powder B as a binary suspension of particles with diameters 240 μm and 355 μm and volume fractions 0.380 and 0.220, respectively. Since the void fraction for both powders is equal to 0.400, the void-free mass fractions for powder A are 0.437 and 0.563, whereas those for powder B are 0.633 and 0.367 (these are obtained by simply dividing the volume fractions by 0.600). If we now mix these two idealized powders, which have the same overall mass, we obtain a suspension that consists of four particle sets with diameters 75 μm, 103 μm, 240 μm and 355 μm and void-free mass fractions 0.218, 0.282, 0.317 and 0.183, respectively. From this PSD, assuming once again a void fraction of 0.400, we can compute the first four integer moments and the corresponding quadrature nodes and weights. The results are reported in Table 6.4, and are quite similar to those obtained from the experiments, which are reported in Table 6.2.

Moments of the volume density function			
$\mathscr{M}_0\ [-]$	$\mathscr{M}_1\ [\mu\text{m}]$	$\mathscr{M}_2\ [\mu\text{m}^2]$	$\mathscr{M}_3\ [\mu\text{m}^3]$
0.600	$1.12 \cdot 10^2$	$2.73 \cdot 10^4$	$7.78 \cdot 10^6$
Quadrature nodes and weights			
$\xi_1\ [\mu\text{m}]$	$\phi_1\ [-]$	$\xi_2\ [\mu\text{m}]$	$\phi_2\ [-]$
102	0.360	314	0.240

Table 6.4: Values of the VDF moments and of the quadrature nodes and weights obtained from the theoretical four-node PSD of powders A and B mix assuming a void fraction of 0.400.

6.5 Numerical simulation

To simulate the dynamics of the bed, we use the direct quadrature method of moments presented in Chapter 5 coupled with the volume averaged dynamical equations derived in Chapter 2. The internal coordinate of interest in this study is the particle size; since the particles move in physical space, however, to fully identify their states we need to assign also their velocities. The generalized internal state space is therefore four-dimensional, and the VDF multivariate. Thus, we should write:

$$f_v(\xi, \boldsymbol{v}, \boldsymbol{x}, t) \approx \sum_{i=1}^{\nu} \phi_i(\boldsymbol{x}, t)\, \delta\Big[\xi - \xi_i(\boldsymbol{x}, t)\Big]\, \boldsymbol{\delta}\Big[\boldsymbol{v} - \boldsymbol{v}_i(\boldsymbol{x}, t)\Big] \tag{6.5}$$

where $\xi_i(\boldsymbol{x}, t)$ and $\boldsymbol{v}_i(\boldsymbol{x}, t)$ denote the diameter and velocity of the i-th particle class. If we applied the same approach discussed in § 5.7, we could derive three-dimensional transport equations for all the quadrature nodes and weights, *including the particle velocities*. The equations for the $\phi_i(\boldsymbol{x}, t)$ would resemble continuity equations, those for the $\boldsymbol{v}_i(\boldsymbol{x}, t)$, dynamical equations. Here, nevertheless, we adopt an alternative technique: we assume that the volume averaged dynamical equations derived in Chapter 2 hold; these equations relate the velocities $\boldsymbol{v}_i(\boldsymbol{x}, t)$ to the diameters $\xi_i(\boldsymbol{x}, t)$, creating a conditional relationship between the two:

$$\boldsymbol{v}_i(\boldsymbol{x}, t) = \boldsymbol{v}\Big[\xi_i(\boldsymbol{x}, t), \boldsymbol{x}, t\Big] \tag{6.6}$$

The particle size is the only independent internal coordinate that remains, and the VDF becomes monovariate; the transport equations of § 5.7 therefore suffice to describe its evolution.

6.5.1 Multiphase fluid dynamic model

Since the particles are inert and do not break, aggregate or nucleate, the source terms $c_i^{\phi}(\boldsymbol{x}, t)$ and $c_i^{\xi}(\boldsymbol{x}, t)$ in equation (5.57) are null. Hence, it is:

$$\frac{\partial \phi_i}{\partial t} + \boldsymbol{\nabla} \cdot \big(\phi_i \boldsymbol{v}_i\big) = 0 \quad ; \quad \frac{\partial}{\partial t}\big(\phi_i \xi_i\big) + \boldsymbol{\nabla} \cdot \big(\phi_i \xi_i \boldsymbol{v}_i\big) = 0 \tag{6.7}$$

where $\boldsymbol{\nabla}\cdot$ operates in physical space. These equations govern the evolution of the quadrature weights and weighted nodes; they are equations of conservation, since no generation is present. The transport equations for the fluid and the dynamical equations for the two quadrature classes are derived by volume averaging. These equations are reported in Table 2.1 of Chapter 2 for systems of n particle phases; for bidisperse systems, the dynamical equation for the i-th particle phase is:

$$\rho_i \left[\frac{\partial}{\partial t}(\phi_i \boldsymbol{v}_i) + \boldsymbol{\nabla} \cdot (\phi_i \boldsymbol{v}_i \boldsymbol{v}_i)\right] = \boldsymbol{\nabla} \cdot \langle \boldsymbol{S} \rangle_p^i + n_i \langle \boldsymbol{f} \rangle_p^i + n_i \langle \boldsymbol{f} \rangle_p^{ik} + \phi_i \rho_i \boldsymbol{g} \tag{6.8}$$

where ρ_i is the particle density, $n_i(\boldsymbol{x}, t)$ is the number density, $\langle \boldsymbol{S} \rangle_p^i(\boldsymbol{x}, t)$ is the effective solid stress tensor, and $\langle \boldsymbol{f} \rangle_p^i(\boldsymbol{x}, t)$ and $\langle \boldsymbol{f} \rangle_p^{ik}(\boldsymbol{x}, t)$ are the interaction forces per unit particle exerted respectively

by the fluid and by the particle class k on the particle class i. The fluid continuity equation is:

$$\frac{\partial \varepsilon}{\partial t} + \boldsymbol{\nabla} \cdot \Big(\varepsilon \langle \boldsymbol{u} \rangle_f \Big) = 0 \tag{6.9}$$

where $\varepsilon(\boldsymbol{x}, t)$ is the fluid volume fraction and $\langle \boldsymbol{u} \rangle_f(\boldsymbol{x}, t)$ is the volume averaged fluid velocity. Finally, the linear momentum equation of conservation for the fluid is:

$$\rho_f \left[\frac{\partial}{\partial t} \Big(\varepsilon \langle \boldsymbol{u} \rangle_f \Big) + \boldsymbol{\nabla} \cdot \Big(\varepsilon \langle \boldsymbol{u} \rangle_f \langle \boldsymbol{u} \rangle_f \Big) \right] = \boldsymbol{\nabla} \cdot \langle \boldsymbol{S} \rangle_f - \sum_{i=1}^{2} \Big(n_i \langle \boldsymbol{f} \rangle_p^i \Big) + \varepsilon \rho_f \boldsymbol{g} \tag{6.10}$$

where ρ_f is the fluid density, assumed constant, and $\langle \boldsymbol{S} \rangle_f(\boldsymbol{x}, t)$ is the effective fluid stress tensor.

The Newtonian constitutive equations (3.1) and (3.2) close the effective stress tensors. The fluid has constant shear viscosity and negligible dilatational viscosity; the kinetic theory of granular gases (Gidaspow, 1994) models the flow properties of the solids. The fluid-particle interaction comprises buoyancy and drag forces; we define the first as:

$$n_i \langle \boldsymbol{f}_s \rangle_p^i = -\, \phi_i \, \boldsymbol{\nabla} \langle p \rangle_f \tag{6.11}$$

and close the second using the new constitutive equation derived in Chapter 3. Notice that we have to modify this equation, since the original one is based on the classical definition of buoyancy force, equation (3.4). Using equation (3.19), we obtain:

$$n_i \langle \boldsymbol{f}_d \rangle_p^i = \beta_i \Big(\langle \boldsymbol{u} \rangle_f - \boldsymbol{v}_i \Big) \quad ; \quad \beta_i = \frac{3}{4} C_D(Re_i) \frac{\rho_f \| \langle \boldsymbol{u} \rangle_f - \boldsymbol{v}_i \| \varepsilon \phi_i}{\xi_i} \varepsilon^{-\psi_e(\varepsilon, Re_i)} \tag{6.12}$$

where, adopting the empirical correlation of Dallavalle (1948), we express the drag force coefficient $C_D(Re_i)$ and the particle Reynolds number Re_i as follows:

$$C_D(Re_i) = \Big(0.63 + 4.8 Re_i^{-1/2} \Big)^2 \quad ; \quad Re_i \equiv \frac{\rho_f}{\mu_f} \varepsilon \| \langle \boldsymbol{u} \rangle_f - \boldsymbol{v}_i \| \xi_i \tag{6.13}$$

The closure of Syamlal (1987) models the solid-solid interaction force as:

$$n_i \langle \boldsymbol{f} \rangle_p^{ik} = \zeta_{ik} (\boldsymbol{v}_k - \boldsymbol{v}_i) \tag{6.14}$$

where the drag coefficient ζ_{ik} is:

$$\zeta_{ik} = \frac{3\pi}{4} (1 + e_{ik}) \left(1 + F_{ik} \frac{\pi}{4} \right) \frac{\phi_i \rho_i \phi_k \rho_k g_{ik} (\xi_i + \xi_k)^2}{\rho_i \xi_i^3 + \rho_k \xi_k^3} \| \boldsymbol{v}_k - \boldsymbol{v}_i \| \tag{6.15}$$

Here e_{ik} is a coefficient of restitution equal to 0.97 and F_{ik} is a coefficient of friction equal to 0.15. Following Lebowitz (1964), we express the radial distribution function g_{ik} as:

$$g_{ik} = \frac{1}{\varepsilon} \left[1 + \frac{3 \xi_i \xi_k}{\varepsilon (\xi_i + \xi_k)} \left(\frac{\phi_i}{\xi_i} + \frac{\phi_k}{\xi_k} \right) \right] \tag{6.16}$$

This fluid dynamic model, presented here for two particle classes, can be easily extended to any number of classes: the more we consider, the better the quadrature approximation becomes.

6.5.2 Boundary and initial conditions

The computational grid (uniform, with square cells of 5 mm side) is two-dimensional; hence, front and back wall effects are neglected. On the left and right walls, no-slip boundary conditions apply. At the bottom of the bed, a uniform inlet gas velocity of 15 cm$/$s is specified. At the upper boundary, the pressure is set to $1.015 \cdot 10^5$ Pa. On all the boundaries, the fluxes of the quadrature weights and weighted nodes are set to zero.

In its initial state, the bed is fixed and made up of two superposed layers; these are 15 mm high, and together occupy half of the vessel. In the lower layer, which contains powder A, the quadrature nodes are 75 μm and 103 μm, while the quadrature weights are 0.262 and 0.338, respectively. In the upper layer, which contains powder B, the quadrature nodes are 240 μm and 355 μm, while the quadrature weights are 0.380 and 0.220, respectively. The void fraction, consequently, is everywhere 0.400. These data derive from the experimental PSDs described in §6.2.

6.5.3 Numerical schemes and techniques

To run the simulation, we used the commercial CFD code *Fluent 6.3*. The governing and constitutive equations were implemented in the *Multi Fluid Model* of the package, which is based on a Eulerian description of the flow.

We used the pressure-based solver, which is recommended for low-speed incompressible flows. To convert scalar transport equations into algebraic equations that can be solved numerically, the code adopts a finite-volume discretization scheme. To ensure convergence, we discretized in space through a first-order upwind scheme, where cell-face quantities are determined by assuming that the cell-center values of any field variable represent cell-averages that hold throughout the entire cells; thus, face quantities are identical to cell quantities, and are set equal to the cell-center values in the upstream cells (relative to the direction of the normal velocity). Temporal discretization is first order accurate and implicit. To couple pressure and velocity, we adopted the SIMPLE (Simultaneous Solution of Non-linearly Coupled Equations) algorithm of Lo (1989); no other coupling algorithms are allowed by the code for Eulerian multiphase calculations.

At each time step, we used a maximum of 100 iterations to compute the flow variables. Setting the tolerance to 10^{-5}, we usually attained convergence within the iteration limit. The time step was set to 10^{-4} s. Under-relaxation factors of 0.20 were adopted for all the variables.

6.5.4 Results and discussion

The simulation includes two stages: a first where the system is fluidized by feeding gas at a superficial velocity of 15 cm/s, and a second where the gas supply is cut off and the system settles again into a packed bed. To reach pseudo stationary conditions, we simulated the fluidized bed for ten seconds, before cutting off the gas supply; the settling phase took instead about two seconds to complete. Figure 6.12 reports the profiles of the quadrature nodes and weights at the start of the simulation, at pseudo steady-state and at the end of the simulation. Phases 2 and 3 represent the first and second particle classes, respectively.

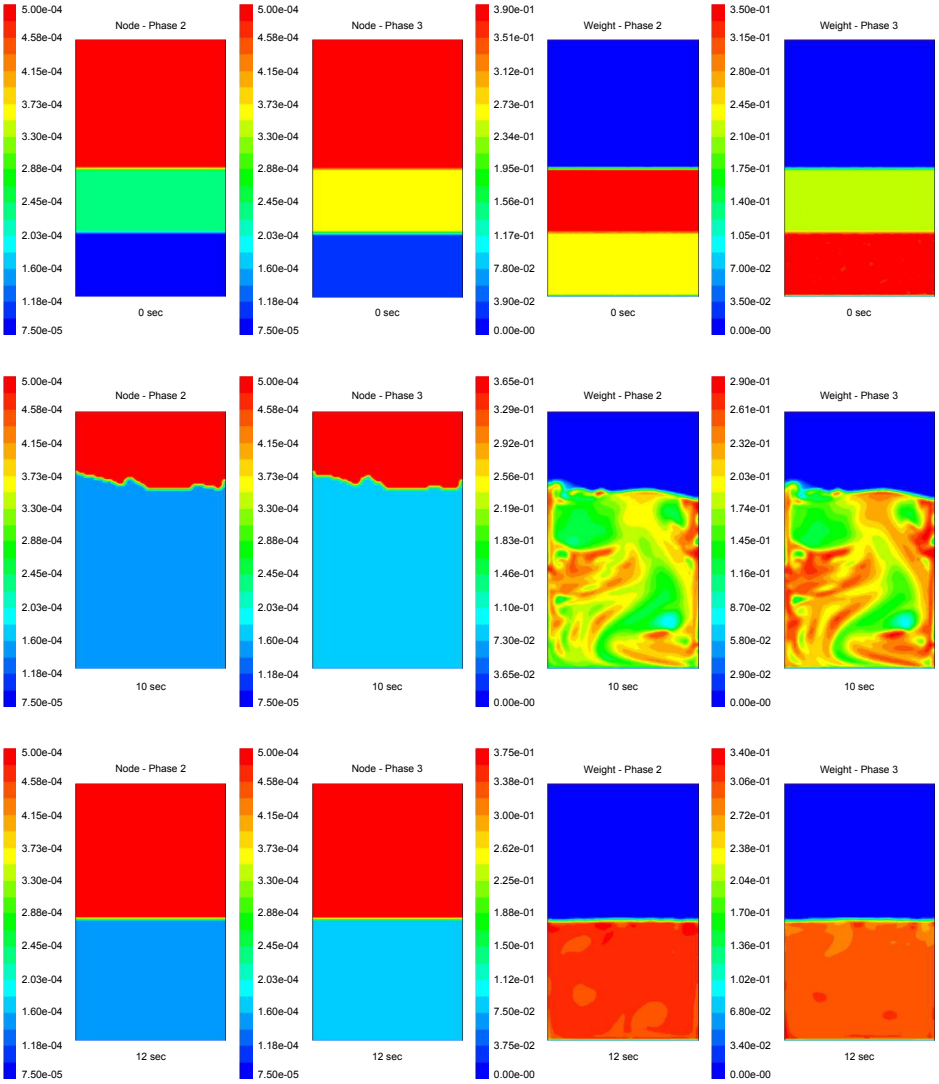

Figure 6.12: Profiles of the quadrature nodes and weights at the start of the simulation, at pseudo steady-state and at the end of the simulation. Phases 2 and 3 represent the first and second particle classes, respectively.

	$\varepsilon\,[-]$	$\phi_1\,[-]$	$\phi_2\,[-]$	$\omega_1\,[-]$	$\omega_2\,[-]$
Highest layer	0.440	0.302	0.258	0.539	0.461
Lowest layer	0.360	0.340	0.300	0.531	0.469
Entire bed	0.400	0.320	0.280	0.534	0.466

Table 6.5: Quadrature weights and void-free mass fractions in the lowest and highest layers of the bed and averaged over the entire bed two seconds after the feed cut off.

At the high fluid velocity used, the dynamics of the fluidized bed is very fast. The volume fraction profiles are not homogeneous, for the system operates in the bubbling regime, but vigorous mixing occurs continuously. This was observed both in the experiment and in the simulation. Nevertheless, whereas in the real bed big bubbles were clearly visible, in the simulated bed they can hardly be seen. This is a well-known problem of the Eulerian averaged equations of motion that is most probably related to numerical diffusion (which smooths out the void fraction gradients) and the constitutive modelling of the solid stress.

As done in the experiment, we divide the settled bed into five layers. Table 6.5 reports the values of the quadrature weights in the highest and lowest layers, showing also the averaged values for the entire bed. The lowest layer is more densely packed, having a voidage of 0.360; this is the maximum packing limit used in the simulation. The highest layer has instead a voidage of 0.440. To check if segregation has taken place, we must therefore use void-free mass fractions; these are also reported in Table 6.5, and are almost identical in both layers. The highest layer is slightly richer in the smaller particle class; this difference, however, is entirely negligible, and might be related to the settling phase, for whereas in the experiment the bed settling is instantaneous, in the simulation it takes two seconds, a time during which segregation might start. Note that in the simulation, after the gas supply is cut off, the interstitial gas in the powder leaves entirely through the bed surface, since no vent is present. This slows down the bed collapse.

The quadrature nodes have homogeneous profiles throughout the entire domain, being equal to 165 μm and 190 μm everywhere in the bed. These values do not change during the settling phase. Table 6.6 reports the experimental, theoretical and computational values of the quadrature nodes and weights. The numerical and experimental weights are similar (error within $\pm 5\%$), but the nodes are quite different (error within $\pm 60\%$). Qualitatively, their values are acceptable, since ξ_1 is between 75 μm and 240 μm, and ξ_2 is between 103 μm and 355 μm; quantitatively, they are unsatisfactory. To

	$\varepsilon\,[-]$	$\phi_1\,[-]$	$\phi_2\,[-]$	$\xi_1\,[\mu\mathrm{m}]$	$\xi_2\,[\mu\mathrm{m}]$
Experimental	0.400	0.331	0.269	105	304
Theoretical	0.400	0.360	0.240	102	314
Computational	0.400	0.320	0.280	165	190

Table 6.6: Experimental, theoretical and computational values of the quadrature nodes and weights.

explain this discrepancy, we need to examine more critically the transport equations that govern the evolution of the quadrature weights and weighted nodes. In Eulerian form, these are expressed by equations (6.7); in Lagrangian form, they become:

$$\frac{D_i\phi_i}{Dt} = -\phi_i \boldsymbol{\nabla}\cdot\boldsymbol{v}_i \quad ; \quad \frac{D_i\xi_i}{Dt} = 0 \quad \text{where} \quad \frac{D_i(\cdot)}{Dt} \equiv \frac{\partial(\cdot)}{\partial t} + \boldsymbol{v}_i\cdot\boldsymbol{\nabla}(\cdot) \tag{6.17}$$

The first equation tells us that in each differential material element the quadrature weights vary only if the divergences of their velocity fields are not zero. If the elements expand or contract, the quadrature weights change accordingly to preserve the phase volumes. The second equation tells us that along the stream lines the quadrature nodes remain constant to their initial values. The motion rearranges the elements within the domain, causing what we usually call *macromixing*; each element, however, evolves independently, without interacting with the other elements; therefore, no *micromixing* takes place. This is what we would observe if we were able to solve *exactly* the equations reported above. The numerical solution is quite different, as Figure 6.12 clearly shows: here micromixing does occur, since the quadrature nodes change and tend towards a common value. This is caused by numerical diffusion. Only diffusion allows for micromixing, and since no diffusive terms appear in the transport equations, its origin must be numerical.

The results are therefore wrong, because we are not solving the real equations of the model. This unexpected outcome, however, has made us realize something important that before we had not fully appreciated: the quadrature nodes will never mix microscopically if we do not account for diffusion. We lost this contribution when we assumed that the particle velocity was conditioned on the particle size (refer to § 6.5). As we previously pointed out, the particle velocity is an internal coordinate that we should consider; doing so, however, would render the distribution multivariate and complicate the problem significantly. To simplify the analysis, we assumed that the velocity was conditioned on the particle size, reducing the number of internal coordinates to one. Evidence now shows that this approximation is too restrictive. To overcome the problem we have two alternatives: either we include the velocity in the distribution, or we continue to use a monovariate distribution, but we introduce a *smearing effect* that results from the unaccounted-for internal coordinate. In this instance, this means that particles of identical size ξ_i can have different velocities, and $\boldsymbol{v}_i$ must be interpreted as their *average velocity*. This introduces in the generalized population balance equation an additional term related to the convection fluxes due to the velocity fluctuations; thus, if $\boldsymbol{v}(\xi,\boldsymbol{x},t)$ is the mean velocity conditioned on ξ and $\hat{\boldsymbol{v}}(\boldsymbol{x},t)$ is the velocity fluctuation, we can write:

$$\frac{\partial f_v}{\partial t} + \boldsymbol{\nabla}_x\cdot\big(f_v\boldsymbol{v}\big) + \boldsymbol{\nabla}_x\cdot\big(f_v\hat{\boldsymbol{v}}\big) + \frac{\partial}{\partial\xi}\big(f_v\dot{\xi}\big) = h_v + \frac{\dot{\xi}}{v_p}\frac{dv_p}{d\xi}f_v \tag{6.18}$$

If to close the advection term due to the velocity field $\hat{\boldsymbol{v}}(\boldsymbol{x},t)$ we resort to the Fick's law of diffusion (Bird et al., 2007), we can rewrite equation (6.18) as:

$$\frac{\partial f_v}{\partial t} + \boldsymbol{\nabla}_x\cdot\big(f_v\boldsymbol{v}\big) - \boldsymbol{\nabla}_x\cdot\big(\mathscr{D}_x\boldsymbol{\nabla}_x f_v\big) + \frac{\partial}{\partial\xi}\big(f_v\dot{\xi}\big) = h_v + \frac{\dot{\xi}}{v_p}\frac{dv_p}{d\xi}f_v \tag{6.19}$$

where $\mathscr{D}_x$ is a diffusion coefficient. With similar passages to those presented in § 5.7, we can derive new DQMOM transport equations. If we assume that aggregation, breakage, shrinkage and similar continuous and discontinuous effects are all absent, *i.e.*, the particles are inert and do nothing beside moving and colliding in physical space, the resulting equations are (Marchisio & Fox, 2005):

$$\frac{\partial \phi_i}{\partial t} + \boldsymbol{\nabla}_x \cdot \left(\phi_i \boldsymbol{v}_i\right) - \boldsymbol{\nabla}_x \cdot \left(\mathscr{D}_x \boldsymbol{\nabla}_x \phi_i\right) = c_i^{\phi} \tag{6.20}$$

$$\frac{\partial}{\partial t}\left(\phi_i \xi_i\right) + \boldsymbol{\nabla}_x \cdot \left(\phi_i \xi_i \boldsymbol{v}_i\right) - \boldsymbol{\nabla}_x \cdot \left(\mathscr{D}_x \boldsymbol{\nabla}_x (\phi_i \xi_i)\right) = c_i^{\xi} \tag{6.21}$$

where the source terms on the right-hand side are equal to:

$$c_i^{\phi} = \frac{6(\mathscr{C}_j - \mathscr{C}_i)}{(\xi_i - \xi_j)^2} \quad ; \quad c_i^{\xi} = \frac{2\mathscr{C}_j(\xi_j + 2\xi_i) - 2\mathscr{C}_i(\xi_i + 2\xi_j)}{(\xi_i - \xi_j)^2} \tag{6.22}$$

Here i and j denote the two quadrature classes and the terms $\mathscr{C}_i$ and $\mathscr{C}_j$ are defined to be:

$$\mathscr{C}_i \equiv \mathscr{D}_x \phi_i (\boldsymbol{\nabla}_x \xi_i \cdot \boldsymbol{\nabla}_x \xi_i) \quad ; \quad \mathscr{C}_j \equiv \mathscr{D}_x \phi_j (\boldsymbol{\nabla}_x \xi_j \cdot \boldsymbol{\nabla}_x \xi_j) \tag{6.23}$$

One thing is crucial: the diffusive flux $\boldsymbol{\nabla}_x \cdot \left(\mathscr{D}_x \boldsymbol{\nabla}_x f_v\right)$ in the GPBE does not only generate diffusion in the transport equations of the quadrature weights and weighted nodes, *but also generates source terms*. In this application, since neither continuous nor discontinuous processes change the particle sizes, we expected c_i^{ϕ} and c_i^{ξ} to be zero, as they were in equations (6.7). However, as equations (6.22) and (6.23) tell us, the source terms do not vanish, but are related to the diffusion coefficient $\mathscr{D}_x$ and the quadrature node gradients $\boldsymbol{\nabla}_x \xi_i$ and $\boldsymbol{\nabla}_x \xi_j$. When we solved numerically equations (6.7), even if we had not accounted for the diffusive fluxes, these had been generated by numerical diffusion, and therefore, albeit indirectly, they had been taken into consideration. This, as pointed out, ensured that the nodes could mix microscopically. The source terms, though, were missing, and this explains why the final values of the quadrature nodes were wrong. If we solve numerically equations (6.20) and (6.21), we should obtain better results. To estimate the diffusion coefficient $\mathscr{D}_x$, we use the relation reported by Gidaspow (1994) for monodisperse fluidized suspensions:

$$\mathscr{D}_x = \frac{1}{3\sqrt{\pi}} \frac{\sqrt{\Theta} d_p}{\phi} \tag{6.24}$$

where Θ is the granular temperature, ϕ is the overall volume fraction of solid and d_p is the diameter of the particles (assumed to be all identical). In our simulations, the granular temperature has an order of magnitude of 10^{-4} $\mathrm{m}^2/\mathrm{s}^2$. Therefore, taking ϕ equal to 0.50 and d_p equal to 200 μm, we obtain a diffusion coefficient of about 10^{-6} m^2/s. To estimate the coefficient $\mathscr{D}_n$ of numerical diffusion, we can use the simple relation reported by Ferziger & Peric (2002):

$$\mathscr{D}_n = \frac{u L_c}{2} \tag{6.25}$$

	$\varepsilon\,[-]$	$\phi_1\,[-]$	$\phi_2\,[-]$	$\xi_1\,[\mu\mathrm{m}]$	$\xi_2\,[\mu\mathrm{m}]$
Experimental	0.400	0.331	0.269	105	304
Theoretical	0.400	0.360	0.240	102	314
Computational	0.400	0.328	0.272	103	312

Table 6.7: Experimental, theoretical and computational values of the quadrature nodes and weights.

where u is the velocity at which the property is convected and L_c is the length of the computational cell. This relation is valid only for the first order upwind discretization scheme, which we adopt in the simulation; higher order schemes are less diffusive but also less stable. Taking as characteristic velocity $0.10\ \mathrm{m/s}$, a value that has the same order of magnitude as the superficial velocity of the fluid, and L_c equal to 5 mm, we obtain a diffusion coefficient of about $10^{-4}\ \mathrm{m^2/s}$. Numerical diffusion, therefore, outweighs physical diffusion.

If we solve the revised DQMOM transport equations using the value for $\mathscr{D}_x$ just computed, the fluidized suspension behaves qualitatively as shown in Figure 6.12; for this reason, we do not report once again the snapshots of the computational profiles. The quantitative results, conversely, are quite different and agree almost perfectly with the experimental data. Table 6.7 reports the new numerical predictions, along with the experimental and theoretical values of the quadrature nodes and weights. As we can see, the match is now more than satisfactory. This confirms the importance of accounting for diffusion in the generalized population balance equation and the crucial role played by the source terms featuring in the revised DQMOM transport equations.

6.5.5 A numerical experiment using four particle classes

As equation (6.23) shows, the source terms c_i^{ϕ} and c_i^{ξ} vanish only when the quadrature node gradients are null. This means that if we forgot to account for the source terms in a system where the quadrature node profiles are initially uniform (that is, at the start of the simulation the nodes have the same values everywhere) and the particle sizes remain constant, the numerical results would be nevertheless accurate. This is the only instance in which this can happen. To prove this point, we make a numerical experiment. We consider two idealized bidisperse powders: the first, which occupies the lower half of the bed, with particles of $75\ \mu$m and $103\ \mu$m and volume fractions of 0.262 and 0.338, respectively; the second, which occupies the upper half of the bed, with particles of $240\ \mu$m and $355\ \mu$m and volume fractions of 0.380 and 0.220, respectively. If we mix them, we obtain a new powder formed by four particle classes with the same sizes and, going from the smallest to the biggest, void-free mass fractions of 0.218, 0.282, 0.317 and 0.183, and volume fractions of 0.131, 0.169, 0.190 and 0.110, respectively. Let us now simulate this system using the old DQMOM transport equations (6.7), where no physical diffusion and source terms are implemented, and four particle classes. Initially, two classes are present only in the lower half of the bed, whereas the other two only in the upper half of the bed. The first two have nodes equal to $75\ \mu$m and $103\ \mu$m and weights equal to 0.262 and 0.338,

	$\phi_1\,[-]$	$\phi_2\,[-]$	$\phi_3\,[-]$	$\phi_4\,[-]$
Upper half of packed bed	0.000	0.000	0.380	0.220
Lower half of packed bed	0.262	0.338	0.000	0.000
	$\xi_1\,[\mu\mathrm{m}]$	$\xi_2\,[\mu\mathrm{m}]$	$\xi_3\,[\mu\mathrm{m}]$	$\xi_4\,[\mu\mathrm{m}]$
Upper half of packed bed	75	103	240	355
Lower half of packed bed	75	103	240	355

Table 6.8: Initial conditions used in the simulation with four particle classes.

respectively; the other two have nodes equal to 240 μm and 355 μm and weights equal to 0.380 and 0.220, respectively. These initial conditions are reported in Table 6.8. As we can see *the node profiles are uniform everywhere within the system*; the only thing that changes between the lower and upper halves of the bed are the quadrature weights. If we fluidize the system using a superficial fluid flux of 15 cm/s, the four classes should perfectly mix to give a homogeneous suspension. We expect the nodes to remain the same and the weights to tend towards 0.131, 0.169, 0.190 and 0.110.

Table 6.9 reports the quadrature nodes and weights and the void-free mass fractions in the lowest and highest layers of the bed and averaged over the entire bed four seconds after the feed cut off. The nodes, as expected, have retained their initial values. The weights, conversely, have evolved towards the theoretical values of perfect mixing. The highest layer of the bed, however, is slightly richer in the smaller particle classes, whereas the lowest layer of the bed, in the bigger ones. This segregation occurs during the settling of the bed and, as previously pointed out, cannot be avoided.

	$\varepsilon\,[-]$	$\phi_1\,[-]$	$\phi_2\,[-]$	$\phi_3\,[-]$	$\phi_4\,[-]$
Highest layer	0.388	0.150	0.182	0.187	0.093
Lowest layer	0.374	0.122	0.166	0.202	0.136
Entire bed	0.380	0.136	0.174	0.195	0.115
		$\omega_1\,[-]$	$\omega_2\,[-]$	$\omega_3\,[-]$	$\omega_4\,[-]$
Highest layer	–	0.245	0.297	0.306	0.152
Lowest layer	–	0.195	0.265	0.323	0.217
Entire bed	–	0.219	0.280	0.315	0.185
		$\xi_1\,[\mu\mathrm{m}]$	$\xi_2\,[\mu\mathrm{m}]$	$\xi_3\,[\mu\mathrm{m}]$	$\xi_4\,[\mu\mathrm{m}]$
Highest layer	–	75	103	240	355
Lowest layer	–	75	103	240	355
Entire bed	–	75	103	240	355

Table 6.9: Quadrature nodes and weights and void-free mass fractions in the lowest and highest layers of the bed and averaged over the entire bed four seconds after the feed cut off.

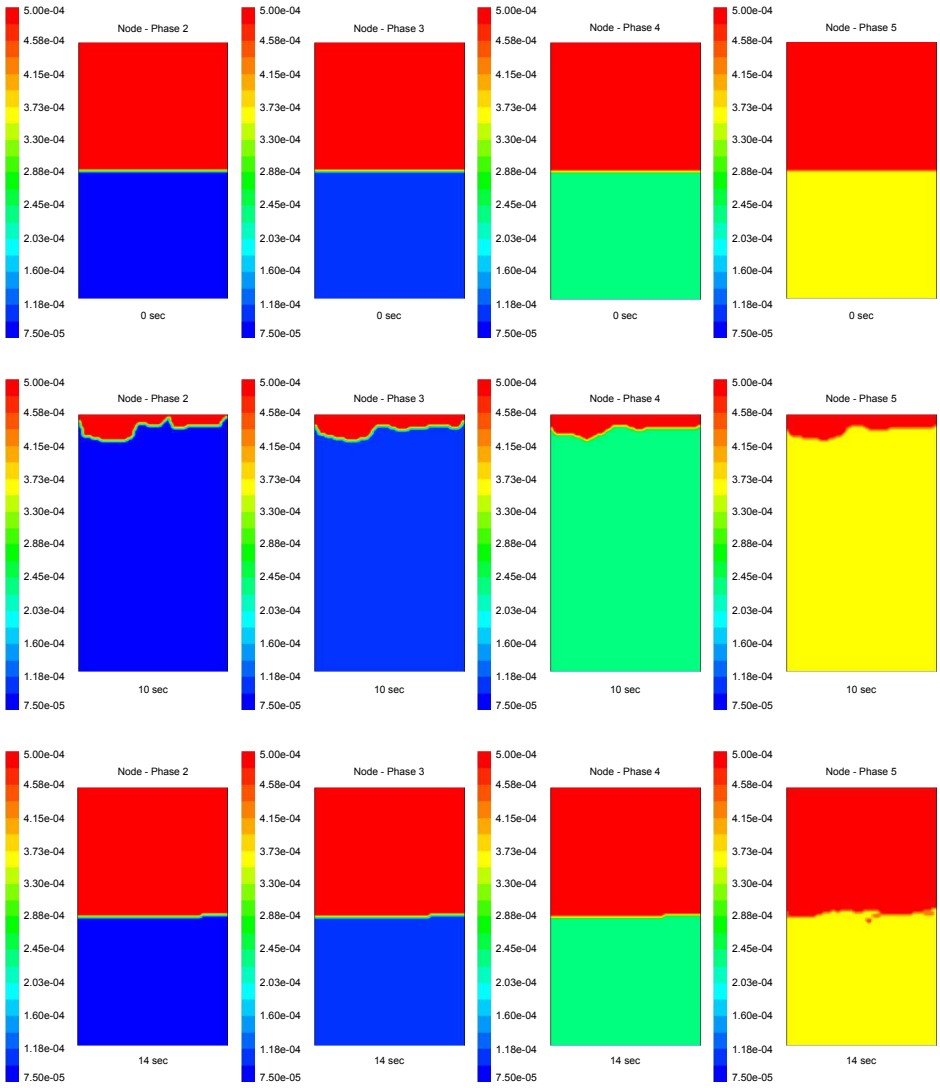

Figure 6.13: Profiles of the quadrature nodes at the start of the simulation, at pseudo steady-state and at the end of the simulation. Phases 2, 3, 4 and 5 represent the first, second, third and fourth particle classes, respectively.

In the real experiment, the bed settles on the distributor almost instantaneously, retaining therefore its particle distribution; in the simulation, conversely, it settles more slowly and segregation can start taking place. Its effect is now more pronounced because the settling phase takes about four seconds to complete – twice as much as in the two-node simulation.

The numerical results are therefore correct, even if the source terms have not been implemented. This does not surprise, because in this very special problem the nodes profiles were flat and the source terms were zero. In any other case, however, as found out in §6.5.4, neglecting the source terms leads to grossly inaccurate predictions.

Figure 6.13 reports the profiles of the quadrature nodes at the start of the simulation, at pseudo steady-state and at the end of the simulation. Phases 2, 3, 4 and 5 represent the first, second, third

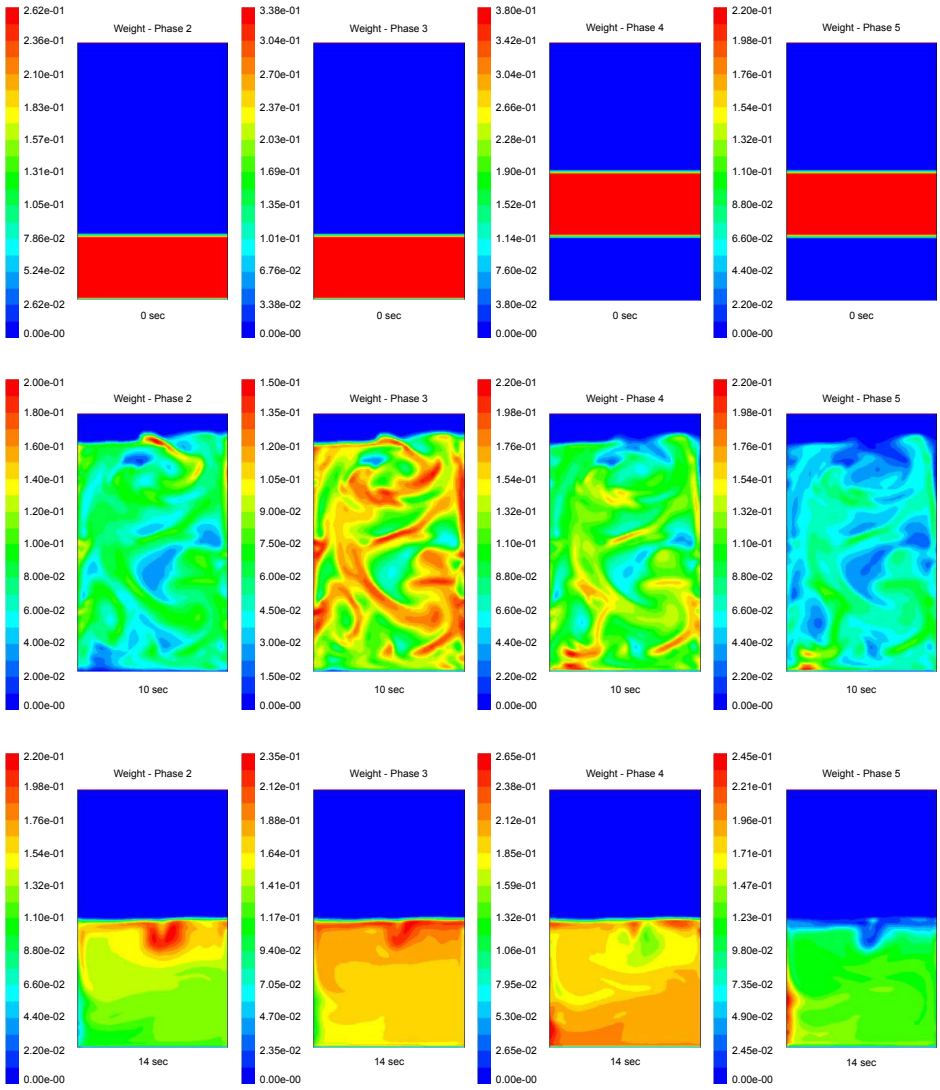

Figure 6.14: Profiles of the quadrature weights at the start of the simulation, at pseudo steady-state and at the end of the simulation. Phases 2, 3, 4 and 5 represent the first, second, third and fourth particle classes, respectively.

and fourth particle classes, respectively. The nodes remain constant throughout the entire process; the dynamics of the suspension is therefore reflected only by the evolution of the quadrature weights, which coincide with the volume fractions of the four particle classes. Their profiles are shown in Figure 6.14. Initially, the four powders are segregated: two in the lower half of the bed and two in the upper half of the bed. Successively, when the bed is fluidized, vigorous mixing takes place, and the four classes spread over the entire bed. Two things are worth noting. When we use four particle classes instead of just two, the fluidized bed expands much more; this is apparent is we compare Figure 6.14 with Figure 6.12. This is because the particle classes of smaller size are blown towards the top of the vessel, and in their upward motion drag along the other particle classes; the overall result is a greater expansion of the bed. Also, the time the bed takes to settle after the gas is cut off

is about four seconds, twice as much as before. Again, this is because of the smaller particle classes, which take more time to sink down.

6.6 Conclusions

The direct quadrature method of moments captures the changes in the particle size distribution of a particulate system initially made up of two polydisperse segregated powders that eventually mix. To obtain accurate results, however, we cannot assume that particles of identical size have also identical velocity, but we have to include a smearing effect over the mean particle velocity of each quadrature class. This generates diffusion in the transport equations of the GPBE and of the quadrature weights and weighted nodes. In the latter two equations also source terms arise, and neglecting them leads to erroneous predictions. We have also noticed that contrary to the experimental bed collapse, the simulated bed collapse is quite slow, and the longer it takes to complete, the more the bed tends to segregate and alter its steady-state configuration. Unfortunately, the more particle classes we use, the more this problem becomes serious. This is because the smaller particle classes take longer to settle and slow down the bed collapse.

Chapter 7

Conclusions and future work

Fluidization is used nowadays in several industrial processes, for energy conversion, waste disposal, food processing and many other applications. Designing fluidized beds, however, is complex, because their performance is strongly affected by the suspension fluid dynamics, which can vary significantly when the properties of the fluid, those of the particles, the process variables and the geometry of the equipment change. For many years, and in part still today, process engineers have used pilot plants and scaling-up relationships to design fluidized beds. This practice is risky, for the fluid dynamics in the industrial units can radically differ from that observed in small-scale prototypes. Computational fluid dynamics (CFD) offers a valuable alternative, because it consents to simulate the full-scale units directly and to study how these respond to changes in geometry and process conditions. With the recent advances in computational softwares and processors, CFD has become an almost indispensable tool for both researchers and process engineers. One thing, however, must be clear: the results of the numerical simulations are as good as the mathematical models that the codes solve. These models, therefore, must be accurate enough to provide reliable information.

To model multiphase flows, we can use various approaches; in this work, we have opted for the Eulerian-Eulerian, where the fluid and the particles are treated as interacting continua. This modelling is the cheapest computationally, and directly provides the information that we need to design and investigate real systems. The Eulerian equations of change, nevertheless, are not closed, because they contain some terms related to microscopic, and not averaged, flow variables. These terms, which we need to express constitutively, represent the fluid dynamic stress internal to each phase and the interaction forces between the phases. They play therefore a dominant role, and the numerical results are strongly affected by the closures that we use to express them.

To begin our study, in Chapter 2 we derived the Eulerian-Eulerian locally averaged equations of change for fluidized suspensions of n particle classes, by extending the work of Anderson & Jackson (1967) and Jackson (1997, 1998), which catered for monodisperse suspensions. We first considered only two sets of particles, and after generalized the results to any number of sets. We conducted this analysis primarily to elucidate how the fluid dynamic stress and the interaction forces between the phases origin. As previously said, these terms have unclosed analytical expressions, which cannot be

implemented in numerical codes; however, only these expressions can makes us understand clearly their physical meaning. They show us, for instance, how the fluid-particle interaction force relates to the local velocity gradients that develop on the particle surfaces, and they allow us to differentiate between the collisional stress, which arises from particle collisions, and the kinetic stress, which arises from velocity fluctuations about their means. They also let us fully appreciate the problem of closure, and why its solution is so complex to tackle theoretically.

In Chapter 3, we addressed the problem of closure regarding the interaction force between the fluid and the particles. This comprises various contributions, but two are dominant: the buoyancy and the drag forces. Three definitions exist for the former; we endorsed the classical definition based on the Archimedes's principle, since this ensures that the force is constant and unrelated to the fluid dynamic field. Many constitutive expressions for the drag are available, but they all present a shortcoming: they are not consistent with the empirical equation of Richardson & Zaki (1954), which is the most reliable correlation that we have to predict the expansion profiles of homogeneous, non-cohesive systems. In this chapter, we derived a new constitutive equation for the drag force that agrees with this correlation for any fluid dynamic regimes and void fractions. To test this closure, we calculated analytically the expansion profiles of liquid-fluidized uniform beds, and compared the results with those obtained from other well-known constitutive equations and with experimental data reported in the literature. We obtained good results, more accurate than those yielded by the other closures tested.

The Ergun (1952) closure agrees quite well with the Richardson & Zaki correlation for a value of the void fraction equal to 0.40 and in the limits of viscous and inertial regimes. In the intermediate region, conversely, it overestimates the force (error in bed expansion up to $+15\%$). At lower powder compactions, the closure always overestimates the force, particularly in the inertial regime (error in bed expansion up to $+40\%$); it should therefore be used only for packed beds or very dense fluidized suspensions. The constitutive expressions of Lewis et al. (1949), Wen & Yu (1966) and Kmiec (1982) are accurate in the creeping and turbulent limits, but in the intermediate region they overestimate the force (error in bed expansion up to $+20\%$). Because the error is greater at low void fractions, these closures should be used, as suggested by Gidaspow (1994), only at void fractions higher than 0.80. The constitutive equation of Di Felice (1994) also yields good predictions in the viscous and inertial regimes, overestimating the force in the intermediate region (error in bed expansion up to $+12\%$); again, the error increases as the void fraction decreases. The new closure relationship agrees with the Richardson & Zaki correlation for any fluid dynamic regimes and void fractions and is always more accurate than the other closures. Whereas its error is usually within $\pm 5\%$, and never exceeds $\pm 10\%$, the error of the other expressions is often greater and can even exceed $\pm 20\%$.

In Chapter 3, we also advanced a new equation of closure for the elastic force, which represents the component of the drag related to void fraction gradients that arise when the homogeneity of the suspension is lost. In uniform systems the elastic force is zero, but it plays an important role in the study of the stability of the particulate fluidization regime. If we do not include the elastic force in the fluid-particle interaction force, the averaged equations of motion tell us that homogeneous

beds are never formally stable. Conversely, its inclusion results into a simple analytical criterion that discriminates between stable and unstable fluidization. The elastic force was originally introduced by Foscolo & Gibilaro (1987); their closure, however, lacks general validity and can only be used to study analytically the behavior of one-dimensional suspensions near equilibrium. Our new closure is instead always valid and reduces to the original closure only in the viscous and inertial fluid dynamic limits when equilibrium is approached.

In Chapter 4, we investigated the dynamics and stability of uniform fluidized beds, and we tested the new closures for the drag and elastic forces by validating their predictions against experimental data. We simulated the expansion profiles of liquid-fluidized uniform beds by integrating numerically the averaged equations of change. For each system and fluid flow rate, we ran three simulations, using our drag force closure and those of Ergun (1952) and Wen & Yu (1966). We chose these equations because they are adopted by the majority of the commercial CFD codes. Our closure predicted more accurately the bed expansion over a broad range of operating conditions, always agreeing with the Richardson & Zaki correlation. Its error never exceeded $\pm 5\%$, often being less than $\pm 2\%$, whereas that of the Ergun (1952) and Wen & Yu (1966) equations was within $\pm 25\%$ and $\pm 10\%$, respectively. Furthermore, whereas the accuracy of these last two equations was strongly dependent on the voidage, that of our new equation was not.

Then, we studied the stability of gas-fluidized uniform beds, first analytically by linear stability analysis, using our new closure and those of Foscolo & Gibilaro (1987) and Jean & Fan (1992), and then computationally. The analytical results showed us that for powders with mean particle diameter greater than about 90 μm, our equation was more accurate than that of Foscolo & Gibilaro (1987). The former yielded an error within $\pm 5\%$, whereas the latter within $\pm 20\%$. Between 90 μm and 40 μm exactly the opposite occurred, the closure of Foscolo & Gibilaro (1987) giving better results. For powders of very small particles both models failed. This is most probably caused by the interparticle forces, which for very fine powders cannot be neglected (these models are hydrodynamical and do not account for them). We always found good agreement between our closure and that of Jean & Fan (1992), something that we expected since both models use the same buoyancy force definition, and the systems analyzed were operated in the viscous regime and near equilibrium.

Finally, we simulated the transition of a gas-fluidized bed from the particulate to the aggregative regime. We ran two simulations: in one we used our model, while in the other we used the model of Gidaspow (1994), where the elastic force is not implemented. In both cases, the numerical results did not match the experimental evidence. Whereas the real system started bubbling quite abruptly when a well-defined fluid flow rate was reached, the simulated system moved gradually towards the bubbling regime and reached it much later. The transition was not sudden, but very slow. Therefore, the equations of motion, or more correctly the closures on which they are based, were not able to describe correctly this physical problem. Moreover, the inclusion of the elastic force did not change the quality of the numerical predictions. This force seems to play a key role only in the linear stability analysis of the equilibrium solutions of the one-dimensional equations of change.

The averaged equations of motion for fluidized suspensions that we derived in Chapter 2 do not allow the particle size to vary. However, particles can nucleate, shrink, aggregate and break; their size distribution therefore continuously changes in time and space. To describe the physics correctly, we must model these changes. In Chapter 5, we presented a powerful modelling approach that makes this possible. This is based on the generalized population balance equation (GPBE), which governs the distribution of a population of particles over any property of interest. The GPBE captures all the physics of the problem, so that no additional equations of conservation are needed. Nevertheless, since its dimensionality is higher than that of classical transport equations, integrating the GPBE is extremely hard. The method of moments replaces the GPBE with a set of three-dimensional averaged transport equations that govern the moments of the distribution. The set is often unclosed and must be made self-sufficient. We presented two methods to overcome the problem: the direct quadrature method of moments (DQMOM) and the quadrature method of moments (QMOM). Both represent the population by a finite number of classes, each with a volume fraction and a specific set of internal properties; the distribution is thus approximated by a quadrature formula that turns integrals into summations; the closure problem is therefore solved. QMOM tracks the moments of the distribution and back-calculates the quadrature nodes and weights; DQMOM directly tracks the latter. Being based on the same idea, the two methods are equivalent from a theoretical standpoint; numerically, however, DQMOM offers several advantages and is therefore often preferred.

In Chapter 6, we used DQMOM to simulate the mixing of two superposed layers of polydisperse particles with different size distributions. We also investigated the system experimentally, comparing numerical and experimental results. The particles were inert and we assumed that neither continuous nor discontinuous processes could change their sizes. Thus, chemical reaction, aggregation, breakage and nucleation were all absent, and only the mixing of the two particle layers could change the local size distribution of the powder. In the experiment, we fluidized the system for ten minutes, to be sure that pseudo stationary conditions could be reached, and we then cut off the fluid feed abruptly, venting the excess gas in the windbox of the vessel to the atmosphere. This ensures that the pseudo stationary particle size distribution (PSD) does not change during the bed collapse. In the simulation we tried to do the same. We fluidized the bed for ten seconds, which is enough to reach the pseudo steady-state, and we then cut off the gas supply. Now, however, the collapse was not almost instantaneous, as it was in the experiment, but took about two seconds to complete. The particle size distribution, though, did not change significantly during this time. To analyze mixing and segregation, we then divided the fixed bed into five layers. In the experiment, we determined the particle size distribution of each layer by sieve analysis, and we then computed the moments of the distributions and the quadrature nodes and weights. Afterwards, we compared the latter with the numerical nodes and weights averaged in each layer. Both the experiment and the simulation told us that the bed had perfectly mixed, the five layers having almost identical quadrature nodes and weights. Moreover, the numerical nodes in the final configuration lied between the initial nodes that represented the two superposed particle layers in the initial configuration. The numerical results were

therefore qualitatively correct. Quantitatively, however, we initially found a difference between the experimental and the numerical nodes: whereas the error for the weights was within $\pm 5\%$, that for the nodes was within $\pm 60\%$. This was consequence of the too restrictive assumption that particles of equal size have identical velocities. To obtain accurate results, we allowed for a smearing effects over the particle velocity that introduced in the GPBE a diffusive term and in the transport equations for the weights and weighted nodes diffusive and source terms. The modified transport equations finally yielded correct results (error within $\pm 3\%$) in full agreement with the experimental data.

7.1 Future work

In Chapter 2, we derived the mathematical expressions of the effective stress tensors of the fluid and particle phases, showing that they are unclosed. Finding constitutive equations for these quantities is extremely difficult, and to simplify the problem, researchers always assume that the Eulerian phases are Newtonian, so that the stress is proportional to their averaged rates of deformation. This view is oversimplistic. For monodisperse suspensions and in the limit of low particle concentrations and small Reynolds and Stokes numbers, Jackson (1997) solved the closure problem analytically, showing that, even for these simple systems, the stress tensors take on much more complex expressions. Moreover, even if we do accept to model the stress with Newtonian closures, there are clear indications that the results of the granular kinetic theory alone are insufficient (Jackson, 2000). Since the fluid dynamic stresses affect the suspension dynamics, its fluidity, the shape of the bubbles and many other important properties, this problem clearly deserves to be studied thoroughly. Only when new and more accurate closures are found, we will be able to describe fluidization dynamics more realistically.

The fluid dynamic models used in multiphase flows and implemented in commercial CFD codes do not account for interparticle forces. Whereas these do not affect the dynamics of coarse powders (that is, those belonging to the Groups B and D of the Geldart (1973) classification), they certainly affect, and sometimes dominate, the dynamics of fine powders. To properly simulate the behavior of Group A powders, we have to include these forces in the linear momentum balance equations. This would also allow us to predict more correctly the transition from the particulate to the aggregative fluidization regimes. The problem is that their modelling is anything but trivial; notwithstanding, this issue must not be overlooked with the pretence that these forces are unimportant, and researchers should endeavor to find appropriate constitutive expressions.

In Chapter 5, we presented a theory that permits to model polydisperse fluidized suspensions, and more generally populations of discrete elements. This hinges on the generalized population balance equation, which we solve using either the direct quadrature method of moments or the quadrature method of moments. These methods are theoretically equivalent, but numerically QMOM is more expensive. In Chapter 6, we applied DQMOM to predict the mixing of two polydisperse powders of different mean particle diameter, showing that the method was correctly implemented, and that the

results were accurate. This is an ongoing work that actually just started: QMOM and DQMOM have never been implemented to model dense fluidized suspensions, and we still have to test the methods, see how they work, validate the results, show their equivalence numerically and verify whether or not the results improve as we increase the accuracy of the quadrature approximation. Moreover, we still have to develop constitutive equations and implement and validate specific models able to account for chemical reactions and particle nucleation, aggregation and breakage.

Finally, it would be interesting to link continuum and discrete modelling. Continuum modelling has been performed with success in the last decades, but there is still a long way to go before we can regard it as a reliable predictive tool. This is because information at the particle level is needed in the continuum models, and researchers have not yet been able to formulate constitutive equations that can represent the complex behavior of particles in flow. There is still much to understand and quantify. Even if we accept that a collection of particles can be modelled as a continuum, we cannot neglect that its macroscopic behavior is dictated by the microscopic constituents. What we need is information on the microstructure and micromechanics of particle assemblies. To obtain it, we could, at least in principle, run experiments; nevertheless, some types of measurements are costly, time-consuming and often cannot be made with the required precision, whereas others are almost impossible to make at the present time. As a result, numerical methods have an important role to play. Discrete modelling is a tool that can furnish information on the microstructure of multiphase polydisperse systems in flow. So it is essential that researchers in both fields join their efforts towards a common goal instead of pursuing their interests independently as it often happens.

Appendix A

Mathematical proofs

A.1 Relationship between volume fraction and number density

We intend to find a relationship between the solid volume fraction $\phi_i(\boldsymbol{x}, t)$ and the particle number density $n_i(\boldsymbol{x}, t)$. To this end, we expand the function in a Taylor series about the center of mass $\boldsymbol{x}^p$ of a generic particle of phase $\mathscr{F}_i$. Doing so yields:

$$\psi(\|\boldsymbol{x}-\boldsymbol{y}\|) = \psi(\|\boldsymbol{x}-\boldsymbol{x}^p\|) + \frac{\partial\psi}{\partial y_k}(\|\boldsymbol{x}-\boldsymbol{x}^p\|)(y_k - x_k^p) + \frac{1}{2}\frac{\partial^2\psi}{\partial y_k \partial y_l}(\|\boldsymbol{x}-\boldsymbol{x}^p\|)(y_k - x_k^p)(y_l - x_l^p) + \cdots \tag{A.1}$$

Equation (A.1) can be equivalently written as:

$$\psi(\|\boldsymbol{x}-\boldsymbol{y}\|) = \psi(\|\boldsymbol{x}-\boldsymbol{x}^p\|) - \frac{\partial\psi}{\partial x_k}(\|\boldsymbol{x}-\boldsymbol{x}^p\|)(y_k - x_k^p) + \frac{1}{2}\frac{\partial^2\psi}{\partial x_k \partial x_l}(\|\boldsymbol{x}-\boldsymbol{x}^p\|)(y_k - x_k^p)(y_l - x_l^p) - \cdots \tag{A.2}$$

To prove this, we first note that:

$$\frac{\partial\psi}{\partial y_k}(\|\boldsymbol{x}-\boldsymbol{y}\|) = -\frac{\partial\psi}{\partial x_k}(\|\boldsymbol{x}-\boldsymbol{y}\|) \tag{A.3}$$

whence, it is:

$$\frac{\partial^2\psi}{\partial y_k \partial y_l}(\|\boldsymbol{x}-\boldsymbol{y}\|) = +\frac{\partial^2\psi}{\partial x_k \partial x_l}(\|\boldsymbol{x}-\boldsymbol{y}\|) \tag{A.4}$$

$$\frac{\partial^3\psi}{\partial y_k \partial y_l \partial y_m}(\|\boldsymbol{x}-\boldsymbol{y}\|) = -\frac{\partial^3\psi}{\partial x_k \partial x_l \partial x_m}(\|\boldsymbol{x}-\boldsymbol{y}\|) \tag{A.5}$$

$$\frac{\partial^4\psi}{\partial y_k \partial y_l \partial y_m \partial y_n}(\|\boldsymbol{x}-\boldsymbol{y}\|) = +\frac{\partial^4\psi}{\partial x_k \partial x_l \partial x_m \partial x_n}(\|\boldsymbol{x}-\boldsymbol{y}\|) \tag{A.6}$$

and so on. Replacing in equation (2.14) the weighting function with its Taylor series yields:

$$\phi_i(\boldsymbol{x},t) = \phi_i^0(\boldsymbol{x},t) - \phi_i^1(\boldsymbol{x},t) + \frac{1}{2}\,\phi_i^2(\boldsymbol{x},t) - \cdots \tag{A.7}$$

where each term of the series is defined as:

$$\phi_i^0(\boldsymbol{x},t) \equiv \sum_{\mathscr{F}_i} \int_{\Omega_p} \psi(\|\boldsymbol{x}-\boldsymbol{x}^p\|)\, dV_y \tag{A.8}$$

$$\phi_i^1(\boldsymbol{x},t) \equiv \sum_{\mathscr{F}_i} \int_{\Omega_p} \frac{\partial \psi}{\partial x_k}(\|\boldsymbol{x}-\boldsymbol{x}^p\|)(y_k - x_k^p)\, dV_y \tag{A.9}$$

$$\phi_i^2(\boldsymbol{x},t) \equiv \sum_{\mathscr{F}_i} \int_{\Omega_p} \frac{\partial^2 \psi}{\partial x_k \partial x_l}(\|\boldsymbol{x}-\boldsymbol{x}^p\|)(y_k - x_k^p)(y_l - x_l^p)\, dV_y \tag{A.10}$$

and so on. In equation (A.8), the term $\psi(\|\boldsymbol{x}-\boldsymbol{x}^p\|)$ is not a function of $\boldsymbol{y}$; thus, it is:

$$\phi_i^0(\boldsymbol{x},t) = \sum_{\mathscr{F}_i} \left[\psi(\|\boldsymbol{x}-\boldsymbol{x}^p\|) \int_{\Omega_p} dV_y \right] = v_i \sum_{\mathscr{F}_i} \psi(\|\boldsymbol{x}-\boldsymbol{x}^p\|) = n_i(\boldsymbol{x},t) v_i \tag{A.11}$$

Note that all the particles of phase $\mathscr{F}_i$ are identical and therefore have the same volume. As regards $\phi_i^1(\boldsymbol{x},t)$, since the term $(y_k - x_k^p)$ is not a function of $\boldsymbol{x}$, we can write:

$$\phi_i^1(\boldsymbol{x},t) = \sum_{\mathscr{F}_i} \int_{\Omega_p} \frac{\partial}{\partial x_k} \Big[\psi(\|\boldsymbol{x}-\boldsymbol{x}^p\|)(y_k - x_k^p) \Big] dV_y \tag{A.12}$$

As the integral is taken over a volume independent of $\boldsymbol{x}$, the order of derivation and integration can be inverted. Then, reminding that $\psi(\|\boldsymbol{x}-\boldsymbol{x}^p\|)$ is not a function of $\boldsymbol{y}$ and that partial derivatives are distributive, we can write:

$$\phi_i^1(\boldsymbol{x},t) = \frac{\partial}{\partial x_k} \sum_{\mathscr{F}_i} \left[\psi(\|\boldsymbol{x}-\boldsymbol{x}^p\|) \int_{\Omega_p} y_k - x_k^p \; dV_y \right] = \frac{\partial \langle \phi_k \rangle_p^i}{\partial x_k} \tag{A.13}$$

where:

$$\langle \phi_k \rangle_p^i(\boldsymbol{x},t) \equiv \sum_{\mathscr{F}_i} \left[\psi(\|\boldsymbol{x}-\boldsymbol{x}^p\|) \int_{\Omega_p} y_k - x_k^p \; dV_y \right] \tag{A.14}$$

The term $\phi_i^2(\boldsymbol{x},t)$ can be manipulated similarly; the final result is:

$$\phi_i^2(\boldsymbol{x},t) = \frac{\partial^2}{\partial x_k \partial x_l} \sum_{\mathscr{F}_i} \left[\psi(\|\boldsymbol{x}-\boldsymbol{x}^p\|) \int_{\Omega_p} (y_k - x_k^p)(y_l - x_l^p) dV_y \right] = \frac{\partial^2 \langle \phi_{kl} \rangle_p^i}{\partial x_k} \tag{A.15}$$

where:

$$\langle \phi_{kl} \rangle_p^i(\boldsymbol{x}, t) \equiv \sum_{\mathscr{F}_i} \left[\psi(\|\boldsymbol{x} - \boldsymbol{x}^p\|) \int_{\Omega_p} (y_k - x_k^p)(y_l - x_l^p) dV_y \right] \tag{A.16}$$

Thus, equation (A.7) can be expressed as:

$$\phi_i(\boldsymbol{x}, t) = n_i(\boldsymbol{x}, t) v_i - \frac{\partial \langle \phi_k \rangle_p^i}{\partial x_k}(\boldsymbol{x}, t) + \frac{1}{2} \frac{\partial^2 \langle \phi_{kl} \rangle_p^i}{\partial x_k \partial x_l}(\boldsymbol{x}, t) - \cdots \tag{A.17}$$

The volume fraction $\phi_i(\boldsymbol{x}, t)$ can therefore be replaced by an infinite series of successively higher spatial derivatives, the first term of such series being equal to the density $n_i(\boldsymbol{x}, t)$ times the particle volume v_i. It can be easily shown that this term is the dominant one in the series. To do so, one has to compare the orders of magnitude of the terms featuring on the right-hand side of equation (A.17); this can be done by introducing dimensionless spatial variables which replace the coordinates x_k with their dimensionless counterparts x_k / r_m, where r_m is the smallest macroscopic length scale of interest. Then successive terms in the series contain successively increasing powers of r_i / r_m as factors, where r_i is the particle radius. Hence, all but the first two terms on the right-hand side of equation (A.17) can be neglected with an error of $O(r_p^2 / r_m^2)$ relative to the two terms retained. In the present case, since we have assumed the solid particles to be identical and spherical, all these concepts can be shown very clearly. We start by expressing equation (A.17) in an equivalent but much more convenient way; to this end, we resort to two useful mathematical relations:

$$\int_{\Omega_p} y_k - x_k^p \, dV_y = 0 \quad ; \quad \int_{\Omega_p} (y_k - x_k^p)(y_l - x_l^p) dV_y = \frac{\delta_{kl}}{5} r_i^2 \, v_i \tag{A.18}$$

where δ_{kl} denotes the Kronecker delta – these results, of course, are valid as long as the integrals are taken over a spherical volume. Accordingly, it is:

$$\langle \phi_k \rangle_p^i(\boldsymbol{x}, t) = 0 \quad ; \quad \langle \phi_{kl} \rangle_p^i(\boldsymbol{x}, t) = \frac{\delta_{kl}}{5} r_i^2 \, v_i \, n_i(\boldsymbol{x}, t) \tag{A.19}$$

whence:

$$\phi_i(\boldsymbol{x}, t) = n_i(\boldsymbol{x}, t) v_i + \frac{\delta_{kl}}{10} r_i^2 \, v_i \frac{\partial^2 n_i}{\partial x_k \partial x_l}(\boldsymbol{x}, t) - \cdots \tag{A.20}$$

We then introduce dimensionless spacial variables, so that:

$$\bar{x}_k = \frac{x_k}{r_m} \quad ; \quad \frac{\partial}{\partial x_k} = \frac{1}{r_m} \frac{\partial}{\partial \bar{x}_k} \tag{A.21}$$

The choice of r_m as characteristic length is motivated by its representing the length scale of the smallest point-to-point macroscopic variation of any variable; accordingly, r_m denotes as well the characteristic length over which the gradients of the averaged variables are calculated. Using these

last relations, we can rewrite equation (A.20) as:

$$\bar{\phi}_i(\bar{\boldsymbol{x}},t) = \bar{n}_i(\bar{\boldsymbol{x}},t)v_i + \frac{\delta_{kl}}{10}\left(\frac{r_i^2}{r_m^2}\right)v_i\,\frac{\partial^2\bar{n}_i}{\partial\bar{x}_k\partial\bar{x}_l}(\bar{\boldsymbol{x}},t) - \cdots \tag{A.22}$$

Since r_i (microscopic length scale) is far smaller that r_m (macroscopic length scale), all the powers of r_i/r_m are vanishingly small; we can therefore truncate the series at the first term, committing an error of $O(r_i^2/r_m^2)$ relative to the term retained. Switching back to the original variables, it is:

$$\phi_i(\boldsymbol{x},t) = n_i(\boldsymbol{x},t)v_i + O\left(\frac{r_i^2}{r_m^2}\right) \tag{A.23}$$

A.2 Fluid phase local averages of point variable spatial derivatives

In the present section, we intend to find an expression for fluid phase local averages of point variable spatial derivatives. To this end, we start by considering the derivative:

$$\frac{\partial}{\partial x_k}\Big[\varepsilon(\boldsymbol{x},t)\langle\xi\rangle_f(\boldsymbol{x},t)\Big] \tag{A.24}$$

Then, using the definition of fluid phase local average given in equation (2.11) and applying the derivation chain rule, we rewrite the quantity above as:

$$\begin{aligned}\frac{\partial}{\partial x_k}\int_{\Omega_f}\xi(\boldsymbol{y},t)\psi(\|\boldsymbol{x}-\boldsymbol{y}\|)dV_y &= \int_{\Omega_f}\xi(\boldsymbol{y},t)\frac{\partial\psi}{\partial x_k}(\|\boldsymbol{x}-\boldsymbol{y}\|)dV_y\\ &= -\int_{\Omega_f}\xi(\boldsymbol{y},t)\frac{\partial\psi}{\partial y_k}(\|\boldsymbol{x}-\boldsymbol{y}\|)dV_y\\ = \int_{\Omega_f}\frac{\partial\xi}{\partial y_k}(\boldsymbol{y},t)\psi(\|\boldsymbol{x}-\boldsymbol{y}\|)dV_y &- \int_{\Omega_f}\frac{\partial}{\partial y_k}\Big[\xi(\boldsymbol{y},t)\psi(\|\boldsymbol{x}-\boldsymbol{y}\|)\Big]dV_y\end{aligned} \tag{A.25}$$

For the first term, it is:

$$\int_{\Omega_f}\frac{\partial\xi}{\partial y_k}(\boldsymbol{y},t)\psi(\|\boldsymbol{x}-\boldsymbol{y}\|)dV_y = \varepsilon(\boldsymbol{x},t)\left\langle\frac{\partial\xi}{\partial x_k}\right\rangle_f(\boldsymbol{x},t) \tag{A.26}$$

For the second, the Gauss's theorem allows writing:

$$\begin{aligned}\int_{\Omega_f}\frac{\partial}{\partial y_k}\Big[\xi(\boldsymbol{y},t)\psi(\|\boldsymbol{x}-\boldsymbol{y}\|)\Big]dV_y &= \int_{\partial\Omega_f}\xi(\boldsymbol{y},t)m_k(\boldsymbol{y},t)\psi(\|\boldsymbol{x}-\boldsymbol{y}\|)dS_y\\ &- \sum_{i=1}^{2}\sum_{\mathscr{F}_i}\int_{\partial\Omega_p}\xi(\boldsymbol{y},t)n_k(\boldsymbol{y},t)\psi(\|\boldsymbol{x}-\boldsymbol{y}\|)dS_y\end{aligned} \tag{A.27}$$

where $\partial\Omega_f$ is the surface bounding the whole system of interest, $\partial\Omega_p$ is the surface bounding the generic particle of phase $\mathscr{F}_i$ at time t, $m_k(\boldsymbol{x},t)$ is the k-th component of the versor normal to the surface $\partial\Omega_f$ pointing outwards and $n_k(\boldsymbol{x},t)$ is the k-th component of the versor normal to the surface $\partial\Omega_p$ pointing from the solid towards the fluid.

Provided that the shortest distance from the generic point $\boldsymbol{x}$ to the surface $\partial\Omega_f$ is considerably larger than the weighting function averaging radius, the first term of the right-hand side of equation (A.27) is much smaller than the second one and can be safely neglected; hence, it is:

$$\varepsilon(\boldsymbol{x},t)\left\langle\frac{\partial\xi}{\partial x_k}\right\rangle_f(\boldsymbol{x},t)$$

$$=\frac{\partial}{\partial x_k}\Big[\varepsilon(\boldsymbol{x},t)\langle\xi\rangle_f(\boldsymbol{x},t)\Big]-\sum_{i=1}^{2}\sum_{\mathscr{F}_i}\int_{\partial\Omega_p}\xi(\boldsymbol{y},t)n_k(\boldsymbol{y},t)\psi(\|\boldsymbol{x}-\boldsymbol{y}\|)dS_y \tag{A.28}$$

A.3 Fluid phase local averages of point variable time derivatives

We propose to derive an expression for fluid phase local averages of point variable time derivatives. Similarly to what has been done in § A.2, we start by considering the derivative:

$$\frac{\partial}{\partial t}\Big[\varepsilon(\boldsymbol{x},t)\langle\xi\rangle_f(\boldsymbol{x},t)\Big] \tag{A.29}$$

Using the definition of fluid phase local average given in equation (2.11) and applying the Leibnitz's theorem allows writing the quantity above as:

$$\frac{\partial}{\partial t}\int_{\Omega_f}\xi(\boldsymbol{y},t)\psi(\|\boldsymbol{x}-\boldsymbol{y}\|)dV_y=\int_{\Omega_f}\frac{\partial}{\partial t}\Big[\xi(\boldsymbol{y},t)\psi(\|\boldsymbol{x}-\boldsymbol{y}\|)\Big]dV_y$$

$$-\sum_{i=1}^{2}\sum_{\mathscr{F}_i}\int_{\partial\Omega_p}\xi(\boldsymbol{y},t)\boldsymbol{v}_s(\boldsymbol{y},t)\cdot\boldsymbol{n}(\boldsymbol{y},t)\psi(\|\boldsymbol{x}-\boldsymbol{y}\|)dS_y$$

$$+\int_{\partial\Omega_f}\xi(\boldsymbol{y},t)\boldsymbol{u}_\infty(\boldsymbol{y},t)\cdot\boldsymbol{m}(\boldsymbol{y},t)\psi(\|\boldsymbol{x}-\boldsymbol{y}\|)dS_y \tag{A.30}$$

where $\boldsymbol{v}_s(\boldsymbol{y},t)$ and $\boldsymbol{u}_\infty(\boldsymbol{y},t)$ are the point velocities of the surfaces $\partial\Omega_p$ and Ω_f, respectively. Note that, since on the surface of each particle no-slip boundary conditions hold, it is:

$$\forall\,\boldsymbol{y}\in\partial\Omega_p:\boldsymbol{v}_s(\boldsymbol{y},t)=\boldsymbol{u}(\boldsymbol{y},t) \tag{A.31}$$

The integral computed on $\partial\Omega_f$ can be neglected for the same reasons given in § A.2. Moreover, since $\psi(\|\boldsymbol{x}-\boldsymbol{y}\|)$ is not time dependent, the first term on the right-hand side of equation (A.30) can be

equivalently expressed as:

$$\int_{\Omega_f} \frac{\partial \xi}{\partial t}(\boldsymbol{y},t)\psi(\|\boldsymbol{x}-\boldsymbol{y}\|)dV_y = \varepsilon(\boldsymbol{x},t)\left\langle \frac{\partial \xi}{\partial t}\right\rangle_f(\boldsymbol{x},t) \tag{A.32}$$

The final result is:

$$\varepsilon(\boldsymbol{x},t)\left\langle \frac{\partial \xi}{\partial t}\right\rangle_f(\boldsymbol{x},t)$$

$$= \frac{\partial}{\partial t}\Big[\varepsilon(\boldsymbol{x},t)\langle\xi\rangle_f(\boldsymbol{x},t)\Big] + \sum_{i=1}^{2}\sum_{\mathscr{F}_i}\int_{\partial\Omega_p}\xi(\boldsymbol{y},t)\boldsymbol{u}(\boldsymbol{y},t)\cdot\boldsymbol{n}(\boldsymbol{y},t)\psi(\|\boldsymbol{x}-\boldsymbol{y}\|)dS_y \tag{A.33}$$

A.4 Particle phase local averages of point variable time derivatives

We seek to derive an expression for particle phase local averages of point variable time derivatives. In this case, the starting point is the derivative:

$$\frac{\partial}{\partial t}\Big[n_i(\boldsymbol{x},t)\langle\xi\rangle_p^i(\boldsymbol{x},t)\Big] \tag{A.34}$$

We use the definition of particle phase local average given in equation (2.18) and apply the partial derivatives distributive property to express the quantity above as:

$$\sum_{\mathscr{F}_i}\frac{\partial}{\partial t}\Big[\xi^p(t)\psi(\|\boldsymbol{x}-\boldsymbol{x}^p\|)\Big]$$

$$= \sum_{\mathscr{F}_i}\left[\frac{d\xi^p}{dt}(t)\psi(\|\boldsymbol{x}-\boldsymbol{x}^p\|)\right] + \sum_{\mathscr{F}_i}\left[\xi^p(t)\frac{\partial\psi}{\partial t}(\|\boldsymbol{x}-\boldsymbol{x}^p\|)\right] \tag{A.35}$$

From the definition of particle phase local average, it is:

$$\sum_{\mathscr{F}_i}\left[\frac{d\xi^p}{dt}(t)\psi(\|\boldsymbol{x}-\boldsymbol{x}^p\|)\right] = n_i(\boldsymbol{x},t)\left\langle\frac{d\xi}{dt}\right\rangle_p^i(\boldsymbol{x},t) \tag{A.36}$$

Applying the derivation chain rule yields:

$$\sum_{\mathscr{F}_i}\left[\xi^p(t)\frac{\partial\psi}{\partial t}(\|\boldsymbol{x}-\boldsymbol{x}^p\|)\right] = \sum_{\mathscr{F}_i}\left[\xi^p(t)\frac{dx_k^p}{dt}(t)\frac{\partial\psi}{\partial x_k^p}(\|\boldsymbol{x}-\boldsymbol{x}^p\|)\right]$$

$$= -\sum_{\mathscr{F}_i}\left[\xi^p(t)v_k^p(t)\frac{\partial\psi}{\partial x_k}(\|\boldsymbol{x}-\boldsymbol{x}^p\|)\right] \tag{A.37}$$

$$= -\frac{\partial}{\partial x_k}\sum_{\mathscr{F}_i}\Big[\xi^p(t)v_k^p(t)\psi(\|\boldsymbol{x}-\boldsymbol{x}^p\|)\Big] = -\frac{\partial}{\partial x_k}\sum_{\mathscr{F}_i}\Big[n_i(\boldsymbol{x},t)\langle\xi v_k\rangle_p^i(\boldsymbol{x},t)\Big] \tag{A.38}$$

where the partial derivatives commutative property and the definition of particle phase local average have been once more invoked. Thus, the final result is:

$$n_i(\boldsymbol{x},t)\left\langle\frac{d\xi}{dt}\right\rangle_p^i(\boldsymbol{x},t)=\frac{\partial}{\partial t}\Big[n_i(\boldsymbol{x},t)\langle\xi\rangle_p^i(\boldsymbol{x},t)\Big]+\frac{\partial}{\partial x_k}\sum_{\mathscr{F}_i}\Big[n_i(\boldsymbol{x},t)\langle\xi v_k\rangle_p^i(\boldsymbol{x},t)\Big] \tag{A.39}$$

Appendix B

Averaged transport equations as moment transforms of the generalized population balance equation

B.1 Introduction

The generalized population balance equation describes the distribution of discrete elements over the properties that characterize their physical state. Its solution tells us how the elements move in physical space and how their momenta and internal properties evolve. To model a discrete system, we require no additional equations. Nevertheless, being integro-differential and with higher dimensionality than classical equations of change, the GPBE is extremely difficult to solve. The method of moments offers a tradeoff between complexity and accuracy: deriving from the GPBE as many three-dimensional transport equations as we like by integrating all the internal coordinates out, including the velocity, it leaves behind only the dependence on time and spatial coordinates. Hence, the dimensionality of the analytical problem is reduced at the price of obtaining averaged, rather than distributed, information about the repartition of the element properties. Different moment transforms of the GPBE preserve different properties of the VDF; the more moments we consider, the more information we retain. Two particularly important transport equations obtained by this method are the continuity and dynamical equations of classical continuum mechanics.

B.2 Continuity equation

Let us apply the integral transform:

$$\varphi(\boldsymbol{\zeta}, \boldsymbol{x}, t) \rightarrow \mathscr{T}_c(\varphi)(\boldsymbol{x}, t) \equiv \int_{\Omega_\zeta} \varphi(\boldsymbol{\zeta}, \boldsymbol{x}, t) m_p d\boldsymbol{\zeta} \tag{B.1}$$

to the generalized population balance equation (5.25). The particle mass m_p is either a component of the generalized internal state vector $\boldsymbol{\zeta}$ or a known function of it. The equation above is the moment

transform of the function $\varphi(\boldsymbol{\zeta}, \boldsymbol{x}, t)$ of the first order with respect to m_p and of the zeroth order with respect to all the other internal coordinates. If in equation (B.1) we formally replace $\varphi(\boldsymbol{\zeta}, \boldsymbol{x}, t)$ with equation (5.25), we obtain:

$$\int_{\Omega_\zeta} \left(\frac{\partial f_n}{\partial t} + \boldsymbol{\nabla}_x \cdot \left(f_n \boldsymbol{v} \right) + \boldsymbol{\nabla}_v \cdot \left(f_n \dot{\boldsymbol{v}} \right) + \boldsymbol{\nabla}_\xi \cdot \left(f_n \dot{\boldsymbol{\xi}} \right) - h_n \right) m_p d\boldsymbol{\zeta} = 0 \tag{B.2}$$

The left-hand side is a sum of five separate integrals. The first gives:

$$\int_{\Omega_\zeta} \frac{\partial f_n}{\partial t} m_p d\boldsymbol{\zeta} = \int_{\Omega_\zeta} \frac{\partial f_m}{\partial t} d\boldsymbol{\zeta} = \frac{\partial}{\partial t} \int_{\Omega_\zeta} f_m d\boldsymbol{\zeta} = \frac{\partial \rho_d}{\partial t} \tag{B.3}$$

The second integral is also easy to compute:

$$\int_{\Omega_\zeta} \boldsymbol{\nabla}_x \cdot \left(f_n \boldsymbol{v} \right) m_p d\boldsymbol{\zeta} = \int_{\Omega_\zeta} \boldsymbol{\nabla}_x \cdot \left(f_m \boldsymbol{v} \right) d\boldsymbol{\zeta} = \boldsymbol{\nabla}_x \cdot \int_{\Omega_\zeta} f_m \boldsymbol{v} d\boldsymbol{\zeta} = \boldsymbol{\nabla}_x \cdot \left(\rho_d \langle \boldsymbol{v} \rangle_m \right) \tag{B.4}$$

For the third integral, it is:

$$\int_{\Omega_\zeta} \boldsymbol{\nabla}_v \cdot \left(f_n \dot{\boldsymbol{v}} \right) m_p d\boldsymbol{\zeta} = \int_{\Omega_\zeta} \boldsymbol{\nabla}_v \cdot \left(f_m \dot{\boldsymbol{v}} \right) d\boldsymbol{\zeta}$$

$$= \int_{\Omega_\xi} \left(\int_{\Omega_v} \boldsymbol{\nabla}_v \cdot \left(f_m \dot{\boldsymbol{v}} \right) d\boldsymbol{v} \right) d\boldsymbol{\xi} = \int_{\Omega_\xi} \left(\int_{-\infty}^{+\infty} \int_{-\infty}^{+\infty} \int_{-\infty}^{+\infty} \frac{\partial}{\partial v_i} \left(f_m \dot{v}_i \right) dv_1 dv_2 dv_3 \right) d\boldsymbol{\xi} \tag{B.5}$$

Here v_i and $\dot{v}_i$ denote the i-th components of the vectors $\boldsymbol{v}$ and $\dot{\boldsymbol{v}}$, respectively, with respect to a Cartesian vector basis $\{\boldsymbol{e}_1, \boldsymbol{e}_2, \boldsymbol{e}_3\}$. The limits of integration over v_1, v_2 and v_3 extend to infinity since the Cartesian components of the particle velocity can in principle assume any real value between $-\infty$ and $+\infty$. The integral within brackets is the sum of three triple integrals that can be evaluated separately. In the coordinate direction $\boldsymbol{e}_1$, we have:

$$\int_{-\infty}^{+\infty} \int_{-\infty}^{+\infty} \int_{-\infty}^{+\infty} \frac{\partial}{\partial v_1} \left(f_m \dot{v}_1 \right) dv_1 dv_2 dv_3 = \int_{-\infty}^{+\infty} \int_{-\infty}^{+\infty} \Big[f_m \dot{v}_1 \Big]_{-\infty}^{+\infty} dv_2 dv_3 \tag{B.6}$$

The regularity condition (refer to §5.5) tells us that when v_1 diverges f_m goes to zero faster than any other function; accordingly, it is:

$$\Big[f_m \dot{v}_1 \Big]_{-\infty}^{+\infty} = 0 \tag{B.7}$$

The same holds in the other two coordinate directions; hence, the integral in equation (B.5) is null. We reach the same result using the Gauss theorem in the velocity state space:

$$\int_{\Omega_\xi} \left(\int_{\Omega_v} \boldsymbol{\nabla}_v \cdot \left(f_m \dot{\boldsymbol{v}} \right) d\boldsymbol{v} \right) d\boldsymbol{\xi} = \int_{\Omega_\xi} \left(\int_{\partial\Omega_v} f_m \dot{\boldsymbol{v}} \cdot d\boldsymbol{S}_v \right) d\boldsymbol{\xi} = 0 \tag{B.8}$$

where we have applied the regularity condition on the boundary $\partial\Omega_v$ (as previously said, Ω_v stretches out to infinity). The forth integral in equation (B.2) is solved by parts:

$$\int_{\Omega_\zeta} \boldsymbol{\nabla}_\xi \cdot \left(f_n \dot{\boldsymbol{\xi}}\right) m_p d\boldsymbol{\zeta} = \int_{\Omega_\zeta} \boldsymbol{\nabla}_\xi \cdot \left(f_m \dot{\boldsymbol{\xi}}\right) d\boldsymbol{\zeta} - \int_{\Omega_\zeta} f_n \dot{\boldsymbol{\xi}} \cdot \boldsymbol{\nabla}_\xi m_p d\boldsymbol{\zeta} \tag{B.9}$$

where we have used equation (5.29). The first term on the right-hand side gives:

$$\int_{\Omega_\zeta} \boldsymbol{\nabla}_\xi \cdot \left(f_m \dot{\boldsymbol{\xi}}\right) d\boldsymbol{\zeta} = \int_{\Omega_v} \left(\int_{\partial\Omega_\xi} f_m \dot{\boldsymbol{\xi}} \cdot d\boldsymbol{S}_\xi \right) d\boldsymbol{v} \tag{B.10}$$

The internal state space is not usually unbounded; consequently, the surface integral above does not always vanish; so one must pay attention to how this term is handled in the derivation of the continuity equation (Ramkrishna, 2000; Marchisio & Fox, 2007). The second integral on the right-hand side of equation (B.9) and the fifth integral on the left-hand side of equation (B.2) are left as they are. Putting all the results together, we obtain:

$$\frac{\partial \rho_d}{\partial t} + \boldsymbol{\nabla}_x \cdot \left(\rho_d \langle \boldsymbol{v} \rangle_m \right) = \int_{\Omega_\zeta} S_m d\boldsymbol{\zeta} \tag{B.11}$$

where the source term S_m is defined to be:

$$S_m \equiv -\boldsymbol{\nabla}_\xi \cdot \left(f_m \dot{\boldsymbol{\xi}}\right) + h_m + f_n \dot{\boldsymbol{\xi}} \cdot \boldsymbol{\nabla}_\xi m_p \tag{B.12}$$

We can also derive the continuity equation in terms of number density and volume fraction; similar passages to those shown in the derivation of equation (B.11) yield:

$$\frac{\partial n}{\partial t} + \boldsymbol{\nabla}_x \cdot \left(n \langle \boldsymbol{v} \rangle_n \right) = \int_{\Omega_\zeta} S_n d\boldsymbol{\zeta} \quad ; \quad \frac{\partial \phi}{\partial t} + \boldsymbol{\nabla}_x \cdot \left(\phi \langle \boldsymbol{v} \rangle_v \right) = \int_{\Omega_\zeta} S_v d\boldsymbol{\zeta} \tag{B.13}$$

where the source terms are given by:

$$S_n \equiv -\boldsymbol{\nabla}_\xi \cdot \left(f_n \dot{\boldsymbol{\xi}}\right) + h_n \quad ; \quad S_v \equiv -\boldsymbol{\nabla}_\xi \cdot \left(f_v \dot{\boldsymbol{\xi}}\right) + h_v + f_n \dot{\boldsymbol{\xi}} \cdot \boldsymbol{\nabla}_\xi v_p \tag{B.14}$$

B.3 Dynamical equation

Let us apply the integral transform:

$$\varphi(\boldsymbol{\zeta}, \boldsymbol{x}, t) \rightarrow \mathscr{T}_v(\varphi)(\boldsymbol{x}, t) \equiv \int_{\Omega_\zeta} \varphi(\boldsymbol{\zeta}, \boldsymbol{x}, t) m_p \boldsymbol{v} d\boldsymbol{\zeta} \tag{B.15}$$

to the generalized population balance equation (5.25). This is the moment transform of the function $\varphi(\boldsymbol{\zeta}, \boldsymbol{x}, t)$ of the first order with respect to $m_p \boldsymbol{v}$ and of the zeroth order with respect to all the other

internal coordinates. The transformation yields:

$$\int_{\Omega_\zeta} \left(\frac{\partial f_n}{\partial t} + \boldsymbol{\nabla}_x \cdot \left(f_n \boldsymbol{v} \right) + \boldsymbol{\nabla}_v \cdot \left(f_n \dot{\boldsymbol{v}} \right) + \boldsymbol{\nabla}_\xi \cdot \left(f_n \dot{\boldsymbol{\xi}} \right) - h_n \right) m_p \boldsymbol{v} d\boldsymbol{\zeta} = \boldsymbol{0} \tag{B.16}$$

This equation is the sum of five integrals. The first gives:

$$\int_{\Omega_\zeta} \frac{\partial f_n}{\partial t} m_p \boldsymbol{v} d\boldsymbol{\zeta} = \int_{\Omega_\zeta} \frac{\partial}{\partial t} (f_m \boldsymbol{v}) d\boldsymbol{\zeta} = \frac{\partial}{\partial t} \int_{\Omega_\zeta} f_m \boldsymbol{v} d\boldsymbol{\zeta} = \frac{\partial}{\partial t} \left(\rho_d \langle \boldsymbol{v} \rangle_m \right) \tag{B.17}$$

We treat the second integral similarly:

$$\int_{\Omega_\zeta} \boldsymbol{\nabla}_x \cdot \left(f_n \boldsymbol{v} \right) m_p \boldsymbol{v} d\boldsymbol{\zeta} = \int_{\Omega_\zeta} \boldsymbol{\nabla}_x \cdot \left(f_m \boldsymbol{v} \boldsymbol{v} \right) d\boldsymbol{\zeta} = \boldsymbol{\nabla}_x \cdot \int_{\Omega_\zeta} f_m \boldsymbol{v} \boldsymbol{v} d\boldsymbol{\zeta} = \boldsymbol{\nabla}_x \cdot \left(\rho_d \langle \boldsymbol{v} \boldsymbol{v} \rangle_m \right) \tag{B.18}$$

where we have used the tensorial identity (Tai, 1997):

$$\boldsymbol{\nabla}_x \cdot (\boldsymbol{a} \boldsymbol{b}) = (\boldsymbol{\nabla}_x \cdot \boldsymbol{a}) \boldsymbol{b} + \boldsymbol{a} \cdot \boldsymbol{\nabla}_x \boldsymbol{b} \tag{B.19}$$

choosing $\boldsymbol{a}$ and $\boldsymbol{b}$ equal to $f_n \boldsymbol{v}$ and $m_p \boldsymbol{v}$, respectively. Since $\boldsymbol{b}$ is not a function of $\boldsymbol{x}$, $\boldsymbol{\nabla}_x \boldsymbol{b}$ vanishes. To evaluate the third integral in equation (B.16), we use the identity (B.19), replacing $\boldsymbol{\nabla}_x$ with $\boldsymbol{\nabla}_v$ and choosing $\boldsymbol{a}$ and $\boldsymbol{b}$ equal to $f_n \dot{\boldsymbol{v}}$ and $m_p \boldsymbol{v}$, respectively. Doing so yields:

$$\int_{\Omega_\zeta} \boldsymbol{\nabla}_v \cdot \left(f_n \dot{\boldsymbol{v}} \right) m_p \boldsymbol{v} d\boldsymbol{\zeta} = \int_{\Omega_\zeta} \boldsymbol{\nabla}_v \cdot \left(f_m \dot{\boldsymbol{v}} \boldsymbol{v} \right) d\boldsymbol{\zeta} - \int_{\Omega_\zeta} f_n \dot{\boldsymbol{v}} \cdot \boldsymbol{\nabla}_v \left(m_p \boldsymbol{v} \right) d\boldsymbol{\zeta} \tag{B.20}$$

The Gauss theorem allows writing:

$$\int_{\Omega_\zeta} \boldsymbol{\nabla}_v \cdot \left(f_m \dot{\boldsymbol{v}} \boldsymbol{v} \right) d\boldsymbol{\zeta} = \int_{\Omega_\xi} \left(\int_{\partial \Omega_v} f_m \dot{\boldsymbol{v}} \boldsymbol{v} \cdot d\boldsymbol{S}_v \right) d\boldsymbol{\xi} = \boldsymbol{0} \tag{B.21}$$

The surface integral vanishes since the velocity state space is unbounded. The second integral on the right-hand side of equation (B.20) gives:

$$\int_{\Omega_\zeta} f_n \dot{\boldsymbol{v}} \cdot \boldsymbol{\nabla}_v \left(m_p \boldsymbol{v} \right) d\boldsymbol{\zeta} = \int_{\Omega_\zeta} f_m \dot{\boldsymbol{v}} \cdot \boldsymbol{\nabla}_v \boldsymbol{v} \, d\boldsymbol{\zeta} = \int_{\Omega_\zeta} f_m \dot{\boldsymbol{v}} d\boldsymbol{\zeta} = \rho_d \langle \dot{\boldsymbol{v}} \rangle_m \tag{B.22}$$

Note that m_p is not a function of $\boldsymbol{v}$ and can be removed from the gradient; furthermore, $\boldsymbol{\nabla}_v \boldsymbol{v}$ is computed in the velocity state space and coincides with the unit tensor. The term $\rho_d \langle \dot{\boldsymbol{v}} \rangle_m$ is a mean acceleration; we can express it, in compliance with Newton's second law of dynamics, as the product of the number density $n(\boldsymbol{x}, t)$ and a number-averaged force per unit particle:

$$\rho_d \langle \dot{\boldsymbol{v}} \rangle_m = \int_{\Omega_\zeta} f_m \dot{\boldsymbol{v}} d\boldsymbol{\zeta} = \int_{\Omega_\zeta} f_n m_p \dot{\boldsymbol{v}} d\boldsymbol{\zeta} = \int_{\Omega_\zeta} f_n \boldsymbol{f}_o d\boldsymbol{\zeta} = n \langle \boldsymbol{f}_o \rangle_n \tag{B.23}$$

where $\boldsymbol{f}_o = m_p \dot{\boldsymbol{v}}$ is the force acting on a single particle of mass m_p. The term $\langle \boldsymbol{f}_o \rangle_n (\boldsymbol{x}, t)$ is the mean overall force per unit particle acting on the disperse phase; accordingly, it encompasses contact

forces (for instance the force exerted on the particles by a surrounding medium, if present) and field forces (due for instance to gravitational or magnetic fields). We denote the first by $\langle \boldsymbol{f} \rangle_n(\boldsymbol{x}, t)$ and the second by $\langle \boldsymbol{b} \rangle_n(\boldsymbol{x}, t)$. If the only body force is gravitational, it is:

$$n\langle \boldsymbol{b} \rangle_n = \int_{\Omega_\zeta} f_n m_p \boldsymbol{g} d\boldsymbol{\zeta} = \boldsymbol{g} \int_{\Omega_\zeta} f_m d\boldsymbol{\zeta} = \rho_d \boldsymbol{g} \tag{B.24}$$

The traction force due the fluid-particle interaction consists of buoyancy force and dynamic force (related to the fluid motion, it encompasses drag force, virtual mass force, local fluid acceleration force, lift force and alike contributions). If we express the buoyancy force, denoted by $n\langle \boldsymbol{f}_s \rangle_n(\boldsymbol{x}, t)$, using the Archimedes's closure (see §3.3.1), we have:

$$n\langle \boldsymbol{f}_s \rangle_n = -\int_{\Omega_\zeta} f_n \rho_f v_p \boldsymbol{g} d\boldsymbol{\zeta} = -\rho_f \boldsymbol{g} \int_{\Omega_\zeta} f_v d\boldsymbol{\zeta} = -\phi \rho_f \boldsymbol{g} \tag{B.25}$$

where ρ_f is the fluid density. Thus, we can write:

$$\rho_d \langle \dot{\boldsymbol{v}} \rangle_m = n\langle \boldsymbol{f}_o \rangle_n = n\langle \boldsymbol{f}_k \rangle_n + (\rho_d - \phi \rho_f)\boldsymbol{g} \tag{B.26}$$

Here $n\langle \boldsymbol{f}_k \rangle_n(\boldsymbol{x}, t)$ denotes the dynamic force. If ρ_p is constant (*i.e.*, all the particles have the same density), equation (5.9) allows rewriting the relation above in the more familiar form:

$$\rho_d \langle \dot{\boldsymbol{v}} \rangle_m = n\langle \boldsymbol{f}_o \rangle_n = n\langle \boldsymbol{f}_k \rangle_n + \phi(\rho_p - \rho_f)\boldsymbol{g} \tag{B.27}$$

The forth integral in equation (B.16) is solved by parts using the identity (5.29):

$$\int_{\Omega_\zeta} \boldsymbol{\nabla}_\xi \cdot \left(f_n \dot{\boldsymbol{\xi}}\right) m_p \boldsymbol{v} d\boldsymbol{\zeta} = \int_{\Omega_\zeta} \boldsymbol{\nabla}_\xi \cdot \left(f_m \dot{\boldsymbol{\xi}}\right) \boldsymbol{v} d\boldsymbol{\zeta} - \int_{\Omega_\zeta} \left(f_n \dot{\boldsymbol{\xi}} \cdot \boldsymbol{\nabla}_\xi m_p\right) \boldsymbol{v} d\boldsymbol{\zeta} \tag{B.28}$$

We integrate the first term on the right-hand side as follows:

$$\int_{\Omega_\zeta} \boldsymbol{\nabla}_\xi \cdot \left(f_m \dot{\boldsymbol{\xi}}\right) \boldsymbol{v} d\boldsymbol{\zeta} = \int_{\Omega_v} \left(\int_{\partial\Omega_\xi} f_m \dot{\boldsymbol{\xi}} \cdot d\boldsymbol{S}_\xi \right) \boldsymbol{v} d\boldsymbol{v} \tag{B.29}$$

Since Ω_ξ does not usually extend to infinity, the integral may not vanish. The second integral on the right-hand side of equation (B.28) and the fifth integral in equation (B.16) are left as they are. Putting all the results together, we obtain:

$$\frac{\partial}{\partial t}\left(\rho_d \langle \boldsymbol{v} \rangle_m\right) + \boldsymbol{\nabla}_x \cdot \left(\rho_d \langle \boldsymbol{v}\boldsymbol{v} \rangle_m\right) = \int_{\Omega_\zeta} S_m \boldsymbol{v} d\boldsymbol{\zeta} + n\langle \boldsymbol{f} \rangle_n + \rho_d \boldsymbol{g} \tag{B.30}$$

The velocity of each particle differs from the local mean velocity of the population; the difference between the two, named *peculiar velocity*, is denoted by $\hat{\boldsymbol{v}}$. Since $\langle \boldsymbol{v} \rangle_m(\boldsymbol{x}, t)$ is not a function of the generalized internal state coordinate, it is:

$$\rho_d \langle \boldsymbol{v}\boldsymbol{v} \rangle_m = \langle \boldsymbol{v} \rangle_m \langle \boldsymbol{v} \rangle_m \int_{\Omega_\zeta} f_m d\boldsymbol{\zeta} + 2\langle \boldsymbol{v} \rangle_m \int_{\Omega_\zeta} f_m \hat{\boldsymbol{v}} d\boldsymbol{\zeta} + \int_{\Omega_\zeta} f_m \hat{\boldsymbol{v}}\hat{\boldsymbol{v}} d\boldsymbol{\zeta} \tag{B.31}$$

The second term on the right-hand side vanishes:

$$\int_{\Omega_\zeta} f_m \hat{\boldsymbol{v}} d\boldsymbol{\zeta} = \int_{\Omega_\zeta} f_m \boldsymbol{v} d\boldsymbol{\zeta} - \langle \boldsymbol{v} \rangle_m \int_{\Omega_\zeta} f_m d\boldsymbol{\zeta} = \rho_d \langle \boldsymbol{v} \rangle_m - \rho_d \langle \boldsymbol{v} \rangle_m = \mathbf{0} \tag{B.32}$$

Thus, equation (B.31) reduces to:

$$\rho_d \langle \boldsymbol{v}\boldsymbol{v} \rangle_m = \rho_d \langle \boldsymbol{v} \rangle_m \langle \boldsymbol{v} \rangle_m + \rho_d \langle \hat{\boldsymbol{v}}\hat{\boldsymbol{v}} \rangle_m \tag{B.33}$$

The tensor $-\rho_d \langle \hat{\boldsymbol{v}}\hat{\boldsymbol{v}} \rangle_m$ is the *kinetic stress tensor*, and is related to the flow of linear momentum through surfaces moving at the particle mean velocity $\langle \boldsymbol{v} \rangle_m$. As equation (B.33) clearly indicates, the overall linear momentum flow rate through a fixed surface is given by two contributions. The first is equal to the flow rate calculated by assuming that all the particles move with the mean velocity $\langle \boldsymbol{v} \rangle_m$ relative to the surface, carrying the average linear momentum $m_p \langle \boldsymbol{v} \rangle_m$. This contribution is governed by the convection tensor $\rho_d \langle \boldsymbol{v} \rangle_m \langle \boldsymbol{v} \rangle_m$. The second is equal to the flow rate through the surface, assuming that the latter moves with the mean particle velocity $\langle \boldsymbol{v} \rangle_m$. In this case, the particles move relative to the surface with a velocity equal to their peculiar velocity and the flow rate is governed by the kinetic stress tensor. This is defined to be:

$$\langle \boldsymbol{S}_k \rangle_m \equiv -\rho_d \langle \hat{\boldsymbol{v}}\hat{\boldsymbol{v}} \rangle_m = -\int_{\Omega_\zeta} f_m \hat{\boldsymbol{v}}\hat{\boldsymbol{v}} d\boldsymbol{\zeta} \tag{B.34}$$

In terms of number and volume density functions, the definitions of kinetic stress tensor are:

$$\langle \boldsymbol{S}_k \rangle_n \equiv -n \langle \hat{\boldsymbol{v}}\hat{\boldsymbol{v}} \rangle_n = -\int_{\Omega_\zeta} f_n \hat{\boldsymbol{v}}\hat{\boldsymbol{v}} d\boldsymbol{\zeta} \quad ; \quad \langle \boldsymbol{S}_k \rangle_v \equiv -\phi \langle \hat{\boldsymbol{v}}\hat{\boldsymbol{v}} \rangle_v = -\int_{\Omega_\zeta} f_v \hat{\boldsymbol{v}}\hat{\boldsymbol{v}} d\boldsymbol{\zeta} \tag{B.35}$$

where it is understood that in each case the velocity fluctuation $\hat{\boldsymbol{v}}$ is evaluated with respect to the mean velocity of the particle mixture consistent with the average used. The integral on the right-hand side of equation (B.30) is related to the *collisional stress tensor*, defined so that:

$$\boldsymbol{\nabla}_x \cdot \langle \boldsymbol{S}_c \rangle_n \equiv \int_{\Omega_\zeta} S_n \boldsymbol{v} d\boldsymbol{\zeta} \;\; ; \;\; \boldsymbol{\nabla}_x \cdot \langle \boldsymbol{S}_c \rangle_v \equiv \int_{\Omega_\zeta} S_v \boldsymbol{v} d\boldsymbol{\zeta} \;\; ; \;\; \boldsymbol{\nabla}_x \cdot \langle \boldsymbol{S}_c \rangle_m \equiv \int_{\Omega_\zeta} S_m \boldsymbol{v} d\boldsymbol{\zeta} \tag{B.36}$$

The stress internal to the disperse phase arises from the transport of linear momentum by two distinct mechanisms. Momentum is transmitted by collision-free motion, when particles move together with their momenta $m_p \boldsymbol{v}$ from one position to another; the velocities of the particles do not change, but the particles change their positions. This kind of momentum transfer is described by the *kinetic component* of the stress tensor. The second mechanism of momentum transfer is due to particle collisions. Here the velocities of the particles are modified, but not their positions. This mechanism is described by the *collisional component* of the stress tensor (Brilliantov & Poschel, 2004). The sum of kinetic and collisional stress tensors constitute the stress tensor of the dispersion:

$$\langle \boldsymbol{S} \rangle_n \equiv \langle \boldsymbol{S}_k \rangle_n + \langle \boldsymbol{S}_c \rangle_n \quad ; \quad \langle \boldsymbol{S} \rangle_v \equiv \langle \boldsymbol{S}_k \rangle_v + \langle \boldsymbol{S}_c \rangle_v \quad ; \quad \langle \boldsymbol{S} \rangle_m \equiv \langle \boldsymbol{S}_k \rangle_m + \langle \boldsymbol{S}_c \rangle_m \tag{B.37}$$

We can now rewrite the dynamical equation (B.30) in the form:

$$\frac{\partial}{\partial t}\Big(\rho_d \langle \boldsymbol{v} \rangle_m\Big) + \boldsymbol{\nabla}_x \cdot \Big(\rho_d \langle \boldsymbol{v} \rangle_m \langle \boldsymbol{v} \rangle_m\Big) = \boldsymbol{\nabla}_x \cdot \langle \boldsymbol{S} \rangle_m + n \langle \boldsymbol{f} \rangle_n + \rho_d \boldsymbol{g} \tag{B.38}$$

Analogous expressions hold in terms of number and volume densities. For monodisperse populations of solid particles, the particle volume, density and mass are constant, all number, volume and mass averages coincide and equation (B.38) becomes:

$$\rho_p \left[\frac{\partial}{\partial t}\Big(\phi \langle \boldsymbol{v} \rangle_v\Big) + \boldsymbol{\nabla}_x \cdot \Big(\phi \langle \boldsymbol{v} \rangle_v \langle \boldsymbol{v} \rangle_v\Big)\right] = \boldsymbol{\nabla}_x \cdot \langle \boldsymbol{S} \rangle_v + n \langle \boldsymbol{f} \rangle_v + \phi \rho_p \boldsymbol{g} \tag{B.39}$$

This equation is equal to the dynamical equation for the solid phase reported in Table 4.1, which was obtained using the volume averaging scheme described in Chapter 2.

B.4 Conclusions

In the previous two sections, we have derived the averaged equations of conservation of the mass and linear momentum of a population of particles by computing moment transforms of the GPBE. By integrating the internal coordinates out, we have lowered the dimensionality of the problem, retaining only the dependence on time and spatial coordinates. We can use the same technique to obtain other transport equations, like for instance the energy equation. The more equations we consider, the more information we preserve. In the mathematical theory of non-uniform gases, where the particle velocity is the only internal coordinate, the general form of the GPBE moment transform is referred to as *Enskog equation* (Chapman & Cowling, 1970).

Appendix C

Polynomial Interpolation and Gaussian Quadrature

C.1 Interpolant polynomials – definition, existence, uniqueness

Given $n+1$ distinct real points $x_0, x_1, \ldots, x_n$ and real numbers $f_0, f_1, \ldots, f_n$, we seek a function $p : \mathbb{R} \to \mathbb{R}$ so that $p(x_i) = f_i$ for $i = 0, 1, \ldots, n$. This function is called an *interpolant*. Let us denote by $\mathbb{P}_n(x)$ the set of all real polynomials $p(x)$ of degree at most n:

$$p(x) = c_0 + c_1 x + c_2 x^2 + \cdots + c_n x^n \tag{C.1}$$

We observe that each $p \in \mathbb{P}_n(x)$ is uniquely defined by its $n+1$ coefficients. In other words, we have $n+1$ degrees of freedom, while interpolation at $x_0, x_1, \ldots, x_n$ provides $n+1$ conditions:

$$p(x_0) = c_0 + c_1 x_0 + c_2 x_0^2 + \cdots + c_n x_0^n = f_0$$

$$p(x_1) = c_0 + c_1 x_1 + c_2 x_1^2 + \cdots + c_n x_1^n = f_1$$

$$p\,(x_2) = c_0 + c_1\, x_2 + c_2\, x_2^2 + \ldots + c_n\, x_2^n = f_2$$

$$\ldots\ldots\ldots\ldots\ldots\ldots\ldots\ldots\ldots\ldots\ldots\ldots\ldots\ldots$$

$$p(x_n) = c_0 + c_1 x_n + c_2 x_n^2 + \cdots + c_n x_n^n = f_n$$

This, intuitively, justifies seeking an interpolant from $\mathbb{P}_n(x)$. Although to determine the polynomial interpolant we could solve the linear system above, this can be accomplished much more easily by using the explicit *Lagrange formula*. The interpolant $p(x)$ takes the expression:

$$p(x) = \sum_{k=0}^{n} f_k \prod_{\substack{l=0 \\ l \neq k}}^{n} \frac{x - x_l}{x_k - x_l} \quad ; \quad x \in \mathbb{R} \tag{C.2}$$

Note that $p \in \mathbb{P}_n(x)$, as required. We wish to show that $p(x)$ interpolates the data. To this end, we define the following functions referred to as *Lagrange cardinal polynomials*:

$$L_k(x) \equiv \prod_{\substack{l=0 \\ l \neq k}}^{n} \frac{x - x_l}{x_k - x_l} \quad ; \quad k = 0, 1, \ldots, n \tag{C.3}$$

Clearly, it is $L_k(x_j) = \delta_{kj}$ where δ_{kj} is the Kronecker delta. Hence:

$$p(x_j) = \sum_{k=0}^{n} f_k L_k(x_j) = \sum_{k=0}^{n} f_k \delta_{kj} = f_j \quad ; \quad j = 0, 1, \ldots, n$$

This proves that $p(x)$ is an interpolant.

We have therefore proved that there exists a polynomial interpolant, and we have shown how to find its functional expression. We now propose to show that the interpolant is unique. To this end, suppose that both $p \in \mathbb{P}_n(x)$ and $q \in \mathbb{P}_n(x)$ interpolate to the same $n + 1$ data. Then the nth degree polynomial $p - q$ vanishes at $n + 1$ distinct points. But the only nth degree polynomial with $n + 1$ zeros is the zero polynomial. Therefore $p - q \equiv 0$ and the interpolant polynomial is unique.

C.2 Orthogonality in vector spaces

In general, a *scalar* (or *inner*) *product* is any function $\mathbb{V} \times \mathbb{V} \to \mathbb{R}$, where $\mathbb{V}$ is a vector space over the reals, subject to the following three axioms:

Axiom 1 $\langle \boldsymbol{x}, \boldsymbol{y} \rangle = \langle \boldsymbol{y}, \boldsymbol{x} \rangle \; \forall \, \boldsymbol{x}, \boldsymbol{y} \in \mathbb{V}$.

Axiom 2 $\langle \boldsymbol{x}, \boldsymbol{x} \rangle \geqslant 0 \; \forall \, \boldsymbol{x} \in \mathbb{V}$ and $\langle \boldsymbol{x}, \boldsymbol{x} \rangle = 0$ if and only if $\boldsymbol{x} = \boldsymbol{0}$.

Axiom 3 $\langle a\boldsymbol{x} + b\boldsymbol{y}, \boldsymbol{z} \rangle = a \langle \boldsymbol{x}, \boldsymbol{z} \rangle + b \langle \boldsymbol{y}, \boldsymbol{z} \rangle \; \forall \, \boldsymbol{x}, \boldsymbol{y}, \boldsymbol{z} \in \mathbb{V}$ and $\forall \, a, b \in \mathbb{R}$.

Given a scalar product, $\boldsymbol{x}, \boldsymbol{y} \in \mathbb{V}$ are orthogonal if and only if $\langle \boldsymbol{x}, \boldsymbol{y} \rangle = 0$.

Let $\mathbb{V} = C[a, b]$, where $[a, b]$ is a closed interval of $\mathbb{R}$ and $C[a, b]$ is the space of all continuous functions from $[a, b]$ to $\mathbb{R}$. $w \in \mathbb{V}$ be a fixed *positive* function. We define the inner product between the continuous functions f and g as:

$$\langle f, g \rangle \equiv \int_a^b w(x) f(x) g(x) dx \quad ; \quad \forall \, f, g \in \mathbb{V} \tag{C.4}$$

It is easy to verify all three axioms of the scalar product. Note that different inner products lead to different orthogonal functions.

C.3 Orthogonal polynomials – definition, existence, uniqueness

Given a scalar (or inner) product in $\mathbb{V} = \mathbb{P}_n(x)$, we say that $\pi_n \in \mathbb{P}_n(x)$ is *the* nth *monic orthogonal polynomial* if π_n is monic, and if $\langle \pi_n, p \rangle = 0$ for *all* $p \in \mathbb{P}_{n-1}(x)$. We remind that, by definition, a polynomial in $\mathbb{P}_n(x)$ is *monic* if the coefficient of x^n therein equals one.

Theorem For every $n \geqslant 0$ there exists one and only one monic orthogonal polynomial of degree n. Moreover, any $p \in \mathbb{P}_n(x)$ can be expanded as a linear combination of $\pi_0, \pi_1, \ldots, \pi_n$.

Proof We let $\pi_0(x) \equiv 1$ and prove the theorem by induction on n. Thus, suppose that $\pi_0, \pi_1, \ldots, \pi_n$ have been already derived consistently with both assertions of the theorem and let $q(x) = x^{n+1}$. Note that $q(x)$ is a monic polynomial in $\mathbb{P}_{n+1}(x)$. Let us consider the following polynomial:

$$\pi_{n+1}(x) = q(x) - \sum_{k=0}^{n} \frac{\langle q, \pi_k \rangle}{\langle \pi_k, \pi_k \rangle} \, \pi_k(x) \quad ; \quad x \in \mathbb{R} \tag{C.5}$$

Clearly, $\pi_{n+1}(x)$ is a monic polynomial in $\mathbb{P}_{n+1}(x)$, since all the terms in the sum are of degree $\leqslant n$. Let $m \in \{0, 1, \ldots, n\}$. It follows from equation (C.5) and the induction hypothesis that:

$$\langle \pi_{n+1}, \pi_m \rangle = \langle q, \pi_m \rangle - \left\langle \sum_{k=0}^{n} \frac{\langle q, \pi_k \rangle}{\langle \pi_k, \pi_k \rangle} \, \pi_k(x), \pi_m \right\rangle = \langle q, \pi_m \rangle - \sum_{k=0}^{n} \frac{\langle q, \pi_k \rangle}{\langle \pi_k, \pi_k \rangle} \langle \pi_k, \pi_m \rangle$$

Since π_k and π_m are orthogonal, their scalar product is zero for any $k \neq m$. Hence:

$$\langle \pi_{n+1}, \pi_m \rangle = \langle q, \pi_m \rangle - \frac{\langle q, \pi_m \rangle}{\langle \pi_m, \pi_m \rangle} \langle \pi_m, \pi_m \rangle = 0$$

Therefore, π_{n+1} is orthogonal to $\pi_0, \pi_1, \ldots, \pi_n$. Consequently, according to the second inductive assertion, it is orthogonal to all $p \in \mathbb{P}_n(x)$.

In order to prove uniqueness, we suppose the existence of two monic orthogonal polynomials $\pi_{n+1} \in \mathbb{P}_{n+1}(x)$ and $\hat{\pi}_{n+1} \in \mathbb{P}_{n+1}(x)$. Let $p = \pi_{n+1} - \hat{\pi}_{n+1}$. Since both π_{n+1} and $\hat{\pi}_{n+1}$ are monic, $p \in \mathbb{P}_n(x)$. Hence, $\langle \pi_{n+1}, p \rangle = \langle \hat{\pi}_{n+1}, p \rangle = 0$. This implies:

$$\langle \pi_{n+1}, p \rangle - \langle \hat{\pi}_{n+1}, p \rangle = \langle \pi_{n+1} - \hat{\pi}_{n+1}, p \rangle = \langle p, p \rangle = 0$$

Thus, we deduce $p \equiv 0$.

Finally, to prove that each $p \in \mathbb{P}_{n+1}(x)$ is a linear combination of $\pi_0, \pi_1, \ldots, \pi_{n+1}$, we note that we can always write it in the form $p(x) = c\pi_{n+1}(x) + q(x)$, where c is the coefficient of x^{n+1} in $p(x)$ and where $q \in \mathbb{P}_n(x)$. According to the induction hypothesis, $q(x)$ can be expanded as a linear combination of $\pi_0, \pi_1, \ldots, \pi_n$, hence our assertion is true.

C.4 The three-term recurrence relation

How can we construct monic orthogonal polynomials? Equation (C.5) might help, but a considerably better procedure follows from the next theorem.

Theorem Monic orthogonal polynomials are given by the recursive formula:

$$\pi_{n+1}(x) = (x - \alpha_n)\pi_n(x) - \beta_n \pi_{n-1}(x) \quad ; \quad n \in \mathbb{N} \tag{C.6}$$

where by definition:

$$\pi_{-1}(x) \equiv 0 \quad ; \quad \pi_0(x) \equiv 1 \tag{C.7}$$

and where the coefficients α_n and β_n are given by:

$$\alpha_n \equiv \frac{\langle \pi_n, x\pi_n \rangle}{\langle \pi_n, \pi_n \rangle} \quad ; \quad \beta_n \equiv \frac{\langle \pi_n, \pi_n \rangle}{\langle \pi_{n-1}, \pi_{n-1} \rangle} > 0 \tag{C.8}$$

Proof Pick $n \geqslant 0$ and let:

$$\psi(x) = \pi_{n+1}(x) - (x - \alpha_n)\pi_n(x) + \beta_n \pi_{n-1}(x)$$

We propose to prove that $\psi(x) = 0$. Since π_n and π_{n+1} are monic, it follows that $\psi \in \mathbb{P}_n(x)$. Note, that $x\pi_n \in \mathbb{P}_{n+1}(x)$ and is monic; however, $x\pi_n(x) \neq \pi_{n+1}(x)$ and therefore $\langle \pi_n, x\pi_n \rangle \neq 0$.

The definition of $\psi(x)$ and the properties of the scalar product yield:

$$\langle \psi, \pi_l \rangle = \langle \pi_{n+1}, \pi_l \rangle - \langle x\pi_n, \pi_l \rangle + \alpha_n \langle \pi_n, \pi_l \rangle + \beta_n \langle \pi_{n-1}, \pi_l \rangle \quad ; \quad l, n \in \mathbb{N}$$

Because of orthogonality of π_{n-1}, π_n and π_{n+1}:

$$\langle \psi, \pi_l \rangle = 0 \quad ; \quad 0 \leqslant l \leqslant n - 2$$

Because of monicity $\pi_n(x) = x\pi_{n-1}(x) + q(x)$ where $q \in \mathbb{P}_{n-1}(x)$. Consequently:

$$\langle \psi, \pi_{n-1} \rangle = -\langle x\pi_n, \pi_{n-1} \rangle + \beta_n \langle \pi_{n-1}, \pi_{n-1} \rangle = -\langle \pi_n, x\pi_{n-1} \rangle + \beta_n \langle \pi_{n-1}, \pi_{n-1} \rangle$$

$$= -\langle \pi_n, \pi_n \rangle + \langle \pi_n, q \rangle + \beta_n \langle \pi_{n-1}, \pi_{n-1} \rangle = -\langle \pi_n, \pi_n \rangle + \langle \pi_n, \pi_n \rangle = 0$$

where the definition of β_n has been used. Similarly, from the definition of α_n:

$$\langle \psi, \pi_n \rangle = -\langle x\pi_n, \pi_n \rangle + \alpha_n \langle \pi_n, \pi_n \rangle = -\langle x\pi_n, \pi_n \rangle + \langle x\pi_n, \pi_n \rangle = 0$$

Thus, $\psi \in \mathbb{P}_n(x)$ obeys $\langle \psi, \pi_l \rangle = 0$ for $l = 0, 1, \ldots, n$; as a consequence, $\psi(x)$ must necessarily be

the zero polynomial. This can be proved easily. We can always express $\psi(x)$ as a linear combination of monic orthogonal polynomials:

$$\psi(x) = \psi_0 + \psi_1 \pi_1(x) + \psi_2 \pi_2(x) + \ldots + \psi_n \pi_n(x)$$

Since $\langle \psi, \pi_l \rangle = 0$ for $l = 0, 1, \ldots, n$, the following relation follows:

$$\langle \psi, \pi_l \rangle = \psi_l \langle \pi_l, \pi_l \rangle = 0 \quad ; \quad l = 0, 1, \ldots, n$$

But since $\langle \pi_l, \pi_l \rangle \neq 0$, it must be $\psi_l = 0$ for $l = 0, 1, \ldots, n$. Thus, $\psi(x) = 0$ and the theorem is finally proved.

C.5 Gaussian quadrature

Let us consider again the space $C[a, b]$ and a scalar product defined as per equation (C.4). We intend to approximate integrals by finite sums:

$$\int_a^b w(x) f(x) dx \approx \sum_{k=1}^{\nu} \phi_k f(\xi_k) \quad ; \quad f \in C[a, b] \tag{C.9}$$

The above is known as a *quadrature formula*. Here ν (number of nodes) is given; moreover, the points $\phi_1, \ldots, \phi_\nu$ (the *weights*) and $\xi_1, \ldots, \xi_\nu$ (the *nodes*) are *independent* of the choice of $f(x)$.

A reasonable approach to achieving high accuracy is to require that the approximant is exact for all $f \in \mathbb{P}_m(x)$, where m is as large as possible. This results in a *Gaussian quadrature* and we will demonstrate that $m = 2\nu - 1$ can be attained. Firstly, we claim that $m = 2\nu$ is impossible (*i.e*, if we choose to work with ν nodes, we can never attain an accuracy equal to 2ν). To prove this, we choose arbitrary nodes $\xi_1, \ldots, \xi_\nu$ and note that:

$$p(x) = \prod_{k=1}^{\nu} (x - \xi_k)^2 \in \mathbb{P}_{2\nu}(x)$$

Since both $w(x)$ and $p(x)$ are positively defined, it must necessarily be:

$$\int_a^b w(x) p(x) dx > 0$$

However, since the point $\xi_1, \ldots, \xi_\nu$ are zeros for $p(x)$, the following equality holds:

$$\sum_{k=1}^{\nu} \phi_k p(\xi_k) = 0$$

Thus, for the polynomial $p \in P_{2\nu}(x)$ the quadrature formula (C.9) cannot be exact.

Theorem Given $n \geqslant 1$, all the zeros of the nth monic orthogonal polynomial $\pi_n(x)$ are real, distinct and lie in the interval $[a, b]$.

Proof Recall that $\pi_0(x) \equiv 1$. Thus, by orthogonality:

$$\int_a^b w(x)\pi_n(x)dx = \int_a^b w(x)\pi_0(x)\pi_n(x)dx = \langle \pi_0, \pi_n \rangle = 0$$

Since both $w(x)$ and $\pi_0(x)$ are positively defined, we deduce that $\pi_n(x)$ must change sign *at least* once in $[a, b]$. Denote by $m \geqslant 1$ the number of the sign changes of $\pi_n(x)$ in $[a, b]$ and assume that $m \leqslant n - 1$. We want to prove that this assumption is impossible and that m cannot be less than n. Let us denote the points where a sign change occurs by $\zeta_1, \ldots, \zeta_m$ and define the function:

$$q(x) = \prod_{j=1}^{m} (x - \zeta_j) \in \mathbb{P}_m(x)$$

Also this function changes sign in $\zeta_1, \ldots, \zeta_m$. Thus, $\pi_n(x)q(x)$ never changes sign in $[a, b]$. Since, $q \in \mathbb{P}_m(x)$ and $m \leqslant n - 1$, it follows that $\langle q, \pi_n \rangle = 0$. But, from our construction, $\pi_n(x)q(x)$ does not change sign in $[a, b]$ and vanishes at a finite number of points; hence:

$$|\langle q, \pi_n \rangle| = \left| \int_a^b w(x)q(x)\pi_n(x)dx \right| = \int_a^b w(x) \left| q(x)\pi_n(x) \right| dx > 0$$

This is clearly a contradiction. So $m = n$ and the proof is complete.

We begin our construction of the *Gaussian quadrature* by choosing *arbitrarily* pairwise-distinct nodes $\xi_1, \ldots, \xi_\nu \in [a, b]$ and define the *interpolatory weights*:

$$\phi_k \equiv \int_a^b w(x) \prod_{\substack{j=1 \\ j \neq k}}^{\nu} \frac{x - \xi_j}{\xi_k - \xi_j} \, dx \quad ; \quad k = 1, 2, \ldots, \nu \tag{C.10}$$

Theorem The quadrature formula with the above choice is exact for all $f \in \mathbb{P}_{\nu-1}(x)$. Moreover, if $\xi_1, \ldots, \xi_\nu$ are the zeros of π_ν then it is exact for all $f \in \mathbb{P}_{2\nu-1}(x)$.

Proof Every $f \in \mathbb{P}_{\nu-1}(x)$ is its own interpolating polynomial, hence by Lagrange's formula:

$$f(x) = \sum_{k=1}^{\nu} f(\xi_k) \prod_{\substack{j=1 \\ j \neq k}}^{\nu} \frac{x - \xi_j}{\xi_k - \xi_j} \quad ; \quad k = 1, 2, \ldots, \nu \tag{C.11}$$

The quadrature is exact for all $f \in \mathbb{P}_{\nu-1}(x)$ if:

$$\int_a^b w(x)f(x)dx = \sum_{k=1}^{\nu} \phi_k f(\xi_k)$$

This, in conjunction with the interpolating-polynomial representation, yields the stipulated form of

the weights $\phi_1, \ldots, \phi_\nu$. Indeed, we have:

$$\int_a^b w(x) f(x) dx = \int_a^b w(x) \sum_{k=1}^{\nu} f(\xi_k) \prod_{\substack{j=1 \\ j \neq k}}^{\nu} \frac{x - \xi_j}{\xi_k - \xi_j} dx = \int_a^b \sum_{k=1}^{\nu} w(x) f(\xi_k) \prod_{\substack{j=1 \\ j \neq k}}^{\nu} \frac{x - \xi_j}{\xi_k - \xi_j} dx$$

$$= \sum_{k=1}^{\nu} \int_a^b w(x) f(\xi_k) \prod_{\substack{j=1 \\ j \neq k}}^{\nu} \frac{x - \xi_j}{\xi_k - \xi_j} dx = \sum_{k=1}^{\nu} f(\xi_k) \int_a^b w(x) \prod_{\substack{j=1 \\ j \neq k}}^{\nu} \frac{x - \xi_j}{\xi_k - \xi_j} dx = \sum_{k=1}^{\nu} \phi_k f(\xi_k)$$

Thus, we have proved that the quadrature formula (C.9), with an *arbitrary* choice of ν nodes and with the weights calculated as per equation (C.10) is exact for all $f \in \mathbb{P}_{\nu-1}(x)$. Note that the weights depend only on the selected nodes $\xi_1, \ldots, \xi_\nu$ and on the weighting function $w(x)$. They do *not* depend on the function $f(x)$.

Let $\xi_1, \ldots, \xi_\nu$ be the zeros of $\pi_\nu(x)$. Thus, the nodes are no longer selected arbitrarily, they are *calculated* by finding the roots of $\pi_\nu(x)$. We want to prove that with this choice of nodes, and by calculating the weights as per equation (C.10), the quadrature formula (C.9) (based on ν nodes only) is exact for all $f \in \mathbb{P}_{2\nu-1}(x)$. To this end, we start by showing that given any $f \in \mathbb{P}_{2\nu-1}(x)$, we can represent it uniquely as $f(x) = q(x)\pi_\nu(x) + r(x)$ where $q \in \mathbb{P}_{\nu-1}$ and $r \in \mathbb{P}_{\nu-1}$. Reminding that any polynomial can be represented as a linear combination of monic orthogonal polynomials:

$$f(x) = \left(f_0 + f_1 \pi_1(x) + \cdots + f_{\nu-1} \pi_{\nu-1}(x) \right) + \pi_\nu(x) \left(f_\nu + \cdots + f_{2\nu-1} \frac{\pi_{2\nu-1}(x)}{\pi_\nu(x)} \right)$$

This proves our point, showing also that the representation is unique. Now, by orthogonality:

$$\int_a^b w(x) f(x) dx = \int_a^b w(x) q(x) \pi_\nu(x) dx + \int_a^b w(x) r(x) dx$$

$$= \langle q, \pi_\nu \rangle + \int_a^b w(x) r(x) dx = \int_a^b w(x) r(x) dx$$

On the other hand, the particular choice of quadrature knots gives:

$$\sum_{k=1}^{\nu} \phi_k f(\xi_k) = \sum_{k=1}^{\nu} \phi_k q(\xi_k) \pi_\nu(\xi_k) + \sum_{k=1}^{\nu} \phi_k r(\xi_k) = \sum_{k=1}^{\nu} \phi_k r(\xi_k)$$

Note that the nodes $\xi_1, \ldots, \xi_\nu$ are the zeros of $\pi_\nu(x)$, thus $\pi_\nu(\xi_k) = 0$ for $k = 1, \ldots, \nu$. Hence, the integral and the approximant coincide, because $r \in \mathbb{P}_{\nu-1}$ and the quadrature is exact for all polynomial in $\mathbb{P}_{\nu-1}$.

C.6 Gauss quadrature algorithm

To summarize, the aim is to evaluate numerically the definite integral in equation (C.9). To do so, we approximate it with the finite sum shown on the right-hand side of the equation. If we use the Gaussian quadrature formula, both the weights $\phi_1, \ldots, \phi_\nu$ and the nodes $\xi_1, \ldots, \xi_\nu$ must be computed. To calculate the latter, we proceed as follows:

1) Use the three-term recurrence relation (C.6) to evaluate $\pi_\nu(x)$.
2) Calculate the ν roots $\xi_1, \ldots, \xi_\nu$ of $\pi_\nu(x)$. These, as previously proved, are real, distinct and lie in the interval $[a, b]$ of interest.
3) Calculate the interpolatory weights $\phi_1, \ldots, \phi_\nu$ using equation (C.10).
4) Evaluate the definite integral using the quadrature formula in equation (C.9).

Note that the polynomial $\pi_\nu(x)$, the nodes $\xi_1, \ldots, \xi_\nu$ and the weights $\phi_1, \ldots, \phi_\nu$ depend only on the interval $[a, b]$ and on the weighting function $w(x)$; they are independent of the functional form of $f(x)$. For any weighting function $w(x)$, the calculation of nodes and weights must be performed just once and is valid for any function $f(x)$.

Appendix D

Two applications of the direct quadrature method of moments

D.1 Introduction

For monovariate distributions, the DQMOM transport equations are:

$$\frac{\partial \phi_i}{\partial t} + \boldsymbol{\nabla}_x \cdot \left(\phi_i \boldsymbol{v}_i\right) = c_i^{\phi}(\boldsymbol{x}, t) \quad ; \quad \frac{\partial}{\partial t}\left(\phi_i \xi_i\right) + \boldsymbol{\nabla}_x \cdot \left(\phi_i \xi_i \boldsymbol{v}_i\right) = c_i^{\xi}(\boldsymbol{x}, t) \tag{D.1}$$

They track in time and physical space the quadrature weights and weighted nodes. To solve them, we need to determine the source terms $c_i^{\phi}(\boldsymbol{x}, t)$ and $c_i^{\xi}(\boldsymbol{x}, t)$. These are given by the equation:

$$(1-k)\sum_{i=1}^{\nu} c_i^{\phi} \xi_i^k + k \sum_{i=1}^{\nu} c_i^{\xi} \xi_i^{k-1} = \mathscr{M}_k(h_v) + (3+k)\sum_{i=1}^{\nu} \phi_i \xi_i^{k-1} \dot{\xi}(\xi_i) \tag{D.2}$$

which is obtained by applying the moment transform (5.32) to equation (5.58). If to approximate the VDF we use a quadrature formula based on ν classes, we need to determine 2ν source terms. Thus, we have to write equation (D.2) for 2ν different values of the parameter k. We then obtain a linear algebraic system whose solution yields the functions $c_i^{\phi}(\boldsymbol{x}, t)$ and $c_i^{\xi}(\boldsymbol{x}, t)$. In general, to solve this system we have to use numerical algorithms; nevertheless, in very simple applications finding the analytical solution is possible. We now show how this can be done when to approximate the VDF we use a quadrature formula with one or two classes.

D.2 DQMOM with a one-node quadrature approximation

Let us consider a quadrature approximation with only one node, and let us denote the weight by $\phi_1(\boldsymbol{x}, t)$ and the node by $\xi_1(\boldsymbol{x}, t)$. From equation (D.2) we can easily derive $c_1^{\phi}(\boldsymbol{x}, t)$ and $c_1^{\xi}(\boldsymbol{x}, t)$.

If we choose $k = 0$ and $k = 1$, the equation yields:

$$c_1^{\phi} = \mathscr{M}_0(h_v) + \frac{3\phi_1\dot{\xi}(\xi_1)}{\xi_1} \quad ; \quad c_1^{\xi} = \mathscr{M}_1(h_v) + 4\phi_1\dot{\xi}(\xi_1) \tag{D.3}$$

By choosing $k = 0$ and $k = 1$, we have preserved the first two moments of the VDF. Any other choice is possible; k does not have to be integer either. We only require that the two algebraic equations be linearly independent. However, since the zeroth moment is related to the suspension volume fraction, and the first moment is related to the mean of the distribution, these moments should always be preserved. From equation (D.3), we then obtain:

$$\frac{\partial\phi_1}{\partial t} + \boldsymbol{\nabla}_x \cdot \left(\phi_1 \boldsymbol{v}\right) = \mathscr{M}_0(h_v) + \frac{3\phi_1\dot{\xi}(\xi_1)}{\xi_1} \tag{D.4}$$

This provides the evolution in time and physical space of the quadrature weight. Since we are using a one-node quadrature approximation, $\phi_1(\boldsymbol{x}, t)$ coincides with the overall volume fraction of the suspension $\phi(\boldsymbol{x}, t)$. For the quadrature weighted node we have:

$$\frac{\partial}{\partial t}\left(\phi_1\xi_1\right) + \boldsymbol{\nabla}_x \cdot \left(\phi_1\xi_1\boldsymbol{v}\right) = \mathscr{M}_1(h_v) + 4\phi_1\dot{\xi}(\xi_1) \tag{D.5}$$

Since we are using one particle class, it is:

$$\mathscr{M}_0 = \phi = \phi_1 \quad ; \quad \mathscr{M}_1 = \phi\langle\xi\rangle_v = \phi_1\xi_1 \tag{D.6}$$

where $\langle\xi\rangle_v(\boldsymbol{x}, t)$ is the VDF mean. These two equations, which in this case form a linear algebraic system, are enough to determine the initial values of the quadrature weights and nodes.

D.3 DQMOM with a two-node quadrature approximation

We now consider a two-node quadrature approximation, and denote by $\phi_i(\boldsymbol{x}, t)$, $\xi_i(\boldsymbol{x}, t)$, $c_i^{\phi}(\boldsymbol{x}, t)$ and $c_i^{\xi}(\boldsymbol{x}, t)$ the weight, node and source terms of the i-th quadrature class. If we use the first four moments of the GPBE, writing equation (5.63) for $k = 0$, 1, 2 and 3, and define:

$$\mathscr{S}_k \equiv \mathscr{M}_k(h_v) + (3 + k)\sum_{i=1}^{\nu}\phi_i\xi_i^{k-1}\dot{\xi}(\xi_i) \tag{D.7}$$

we obtain the following linear algebraic system:

$$\begin{pmatrix} 1 & 1 & 0 & 0 \\ 0 & 0 & 1 & 1 \\ -1\xi_1^2 & -1\xi_2^2 & 2\xi_1 & 2\xi_2 \\ -2\xi_1^2 & -2\xi_2^2 & 3\xi_1^2 & 3\xi_2^2 \end{pmatrix} \begin{pmatrix} c_1^{\phi} \\ c_2^{\phi} \\ c_1^{\xi} \\ c_2^{\xi} \end{pmatrix} = \begin{pmatrix} \mathscr{S}_0 \\ \mathscr{S}_1 \\ \mathscr{S}_2 \\ \mathscr{S}_3 \end{pmatrix} \tag{D.8}$$

The first two equations give:

$$c_2^{\phi} = \mathscr{S}_0 - c_1^{\phi} \quad ; \quad c_2^{\xi} = \mathscr{S}_1 - c_1^{\xi} \tag{D.9}$$

whereas the third equation yields:

$$-\Big(\xi_1^2 c_1^{\phi} + \xi_2^2 c_2^{\phi}\Big) + 2\Big(\xi_1 c_1^{\xi} + \xi_2 c_2^{\xi}\Big) = \mathscr{S}_2 \tag{D.10}$$

If we substitute equation (D.9) into equation (D.10), we obtain:

$$c_1^{\xi} = C_0 c_1^{\phi} + C_1 \quad ; \quad C_0 \equiv \frac{1}{2}(\xi_1 + \xi_2) \quad ; \quad C_1 \equiv \frac{\xi_2^2 \mathscr{S}_0 - 2\xi_2 \mathscr{S}_1 + \mathscr{S}_2}{2(\xi_1 - \xi_2)} \tag{D.11}$$

The forth and final equation of the set is:

$$-2\Big(\xi_1^3 c_1^{\phi} + \xi_2^3 c_2^{\phi}\Big) + 3\Big(\xi_1^2 c_1^{\xi} + \xi_2^2 c_2^{\xi}\Big) = \mathscr{S}_3 \tag{D.12}$$

Replacing equations (D.9) and (D.11) into equation (D.12) gives:

$$c_1^{\phi} = \frac{2\xi_2^3 \mathscr{S}_0 + \mathscr{S}_3 - 3\big(C_1 \xi_1^2 - C_2 \xi_2^2\big)}{3C_0\big(\xi_1^2 - \xi_2^2\big) - 2\big(\xi_1^3 - \xi_2^3\big)} \quad ; \quad C_2 \equiv \frac{\xi_2^2 \mathscr{S}_0 - 2\xi_1 \mathscr{S}_1 + \mathscr{S}_2}{2(\xi_1 - \xi_2)} \tag{D.13}$$

Equation (D.13) can be rearranged in the form:

$$c_1^{\phi} = \frac{\xi_2^2(3\xi_1 - \xi_2)\mathscr{S}_0 - 6\xi_1\xi_2\mathscr{S}_1 + 3(\xi_1 + \xi_2)\mathscr{S}_2 - 2\mathscr{S}_3}{(\xi_1 - \xi_2)^3} \tag{D.14}$$

Then, from equation (D.9), it is:

$$c_2^{\phi} = \frac{\xi_1^2(3\xi_2 - \xi_1)\mathscr{S}_0 - 6\xi_1\xi_2\mathscr{S}_1 + 3(\xi_1 + \xi_2)\mathscr{S}_2 - 2\mathscr{S}_3}{(\xi_2 - \xi_1)^3} \tag{D.15}$$

whereas from equation (D.11), we obtain:

$$c_1^{\xi} = \frac{2\xi_1^2\xi_2^2\mathscr{S}_0 - \xi_2(4\xi_1^2 + \xi_1\xi_2 + \xi_2^2)\mathscr{S}_1 + 2(\xi_1^2 + \xi_1\xi_2 + \xi_2^2)\mathscr{S}_2 - (\xi_1 + \xi_2)\mathscr{S}_3}{(\xi_1 - \xi_2)^3} \tag{D.16}$$

Finally, equation (D.9), gives:

$$c_2^{\xi} = \frac{2\xi_1^2\xi_2^2\mathscr{S}_0 - \xi_1(4\xi_2^2 + \xi_1\xi_2 + \xi_1^2)\mathscr{S}_1 + 2(\xi_1^2 + \xi_1\xi_2 + \xi_2^2)\mathscr{S}_2 - (\xi_1 + \xi_2)\mathscr{S}_3}{(\xi_2 - \xi_1)^3} \tag{D.17}$$

The transport equations for the two quadrature weights are:

$$\frac{\partial \phi_1}{\partial t} + \boldsymbol{\nabla}_x \cdot \big(\phi_1 \boldsymbol{v}_1\big) = c_1^{\phi}(\boldsymbol{x}, t) \quad ; \quad \frac{\partial \phi_2}{\partial t} + \boldsymbol{\nabla}_x \cdot \big(\phi_2 \boldsymbol{v}_2\big) = c_2^{\phi}(\boldsymbol{x}, t) \tag{D.18}$$

Those for the quadrature weighted nodes are:

$$\frac{\partial}{\partial t}\big(\phi_1\xi_1\big) + \boldsymbol{\nabla}_x \cdot \big(\phi_1\xi_1\boldsymbol{v}_1\big) = c_1^{\xi}(\boldsymbol{x},t) \quad ; \quad \frac{\partial}{\partial t}\big(\phi_2\xi_2\big) + \boldsymbol{\nabla}_x \cdot \big(\phi_2\xi_2\boldsymbol{v}_2\big) = c_2^{\xi}(\boldsymbol{x},t) \tag{D.19}$$

where now the source terms are known as functions of the quadrature weights and weighted nodes themselves. Since we are using two particle classes, it is:

$$\mathscr{M}_0 = \phi = \phi_1 + \phi_2 \quad ; \quad \mathscr{M}_1 = \phi\langle\xi\rangle_v = \phi_1\xi_1 + \phi_2\xi_2 \tag{D.20}$$

where $\phi\,(\boldsymbol{x},t)$ is the overall volume fraction of the suspension and $\langle\xi\rangle_v(\boldsymbol{x},t)$ is the VDF mean. Note that to calculate the initial values of the quadrature weights and nodes we need two additional equations; to obtain them, we consider the second and third VDF moments:

$$\mathscr{M}_2 = \phi\langle\xi^2\rangle_v = \phi_1\xi_1^2 + \phi_2\xi_2^2 \quad ; \quad \mathscr{M}_3 = \phi\langle\xi^3\rangle_v = \phi_1\xi_1^3 + \phi_2\xi_2^3 \tag{D.21}$$

The four relations in equations (D.20) and (D.21) constitute a non-linear algebraic system that we can solve using the PD algorithm of Gordon (1968).

Appendix E

Moments of monovariate volume density functions from experimental particle size distributions

E.1 Introduction

When using DQMOM or QMOM, we must initialize the variables in the transport equations. We must therefore determine either the quadrature nodes and weights or the moments of the volume density function (VDF). Since we can calculate the former from the moments themselves – either by solving a non-linear algebraic system, or by using the product-difference algorithm of Gordon (1968) – we must always compute the moments first. Here, we show how to calculate them from the experimental particle size distribution (PSD) of the powder. We assume that the system is monovariate and homogeneous. The internal coordinate is the particle diameter.

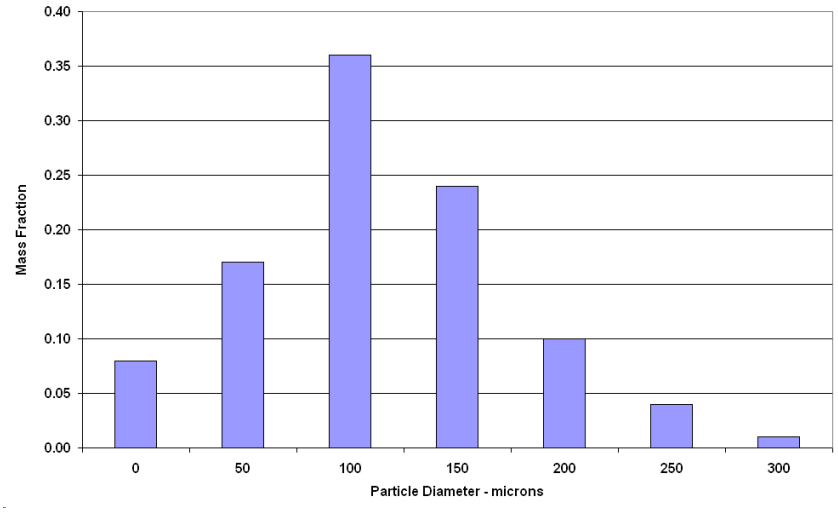

Figure E.1: Example of an experimental particle size distribution obtained by sieving.

E.2 Moment calculation from the experimental PSD

We usually determine the particle size distribution of a particulate system by sieving: we riffle the powder to make it homogeneous, and we then sieve a sample of it. A block diagram usually reports the results; Figure E.1 provides an example.

Let us consider two values ξ_{i-1} and ξ_i of the internal coordinate. The height of the column located between ξ_{i-1} and ξ_i is equal to the mass fraction of particles with diameter in the range (ξ_{i-1}, ξ_i). If we denote by M_s the total mass of solid and by $m_s(\xi_{i-1}, \xi_i)$ and $\omega(\xi_{i-1}, \xi_i)$ the mass and mass fraction of particles with diameter in the range (ξ_{i-1}, ξ_i), it is:

$$\omega(\xi_{i-1}, \xi_i) \equiv \frac{m_s(\xi_{i-1}, \xi_i)}{M_s} \tag{E.1}$$

The system is monovariate; therefore, the particles must have the same density. As a consequence, mass fractions and volume fractions coincide. We can thus write:

$$\omega(\xi_{i-1}, \xi_i) \equiv \frac{m_s(\xi_{i-1}, \xi_i)}{M_s} = \frac{v_s(\xi_{i-1}, \xi_i)}{V_s} \equiv \phi^*(\xi_{i-1}, \xi_i) \tag{E.2}$$

where V_s is the total volume of solid, whereas $v_s(\xi_{i-1}, \xi_i)$ and $\phi^*(\xi_{i-1}, \xi_i)$ are respectively the volume and volume fraction of particles with diameter in the range (ξ_{i-1}, ξ_i). To evaluate the moments of the volume density function, we first need to determine the function itself. To this end, we need to convert the volume fractions $\phi^*(\xi_{i-1}, \xi_i)$, which are calculated on a *void-free basis*, to new volume fractions $\phi(\xi_{i-1}, \xi_i)$, which *account for the presence of voids*. It is:

$$\phi(\xi_{i-1}, \xi_i) \equiv \frac{v_s(\xi_{i-1}, \xi_i)}{V_s + V_f} = \frac{\phi^*(\xi_{i-1}, \xi_i) V_s}{V_s + V_f} = \phi^*(\xi_{i-1}, \xi_i)(1 - \varepsilon) \tag{E.3}$$

where V_f is the total volume of fluid (or of void space), and ε is the fluid volume fraction. $\phi(\xi_{i-1}, \xi_i)$ is related to the VDF, since it is:

$$\phi(\xi_{i-1}, \xi_i) = \int_{\xi_{i-1}}^{\xi_i} f_v(\xi) d\xi = f_v(\xi_{i-1}, \xi_i)(\xi_i - \xi_{i-1}) \tag{E.4}$$

Here, we have used the mean value theorem of integral calculus; thus, $f_v(\xi_{i-1}, \xi_i)$ denotes the mean value of the VDF in the interval (ξ_{i-1}, ξ_i). In general, the function is not constant in (ξ_{i-1}, ξ_i), but since the sieve analysis is discrete, we know nothing about $f_v(\xi)$ in these intervals; we must therefore approximate it with its mean values $f_v(\xi_{i-1}, \xi_i)$. Using equation (E.4), we can easily determine the moments of the distribution; for the generic moment of order k, we first write:

$$\mathscr{M}_k \equiv \int_0^{+\infty} f_v(\xi) \xi^k d\xi = \sum_{i=1}^{+\infty} \int_{\xi_{i-1}}^{\xi_i} f_v(\xi) \xi^k d\xi \tag{E.5}$$

In each interval (ξ_{i-1}, ξ_i), we then approximate the VDF with its mean value:

$$\int_{\xi_{i-1}}^{\xi_i} f_v(\xi)\xi^k d\xi \approx \frac{\phi(\xi_{i-1},\xi_i)}{\xi_i - \xi_{i-1}} \int_{\xi_{i-1}}^{\xi_i} \xi^k d\xi = \frac{\phi(\xi_{i-1},\xi_i)}{\xi_i - \xi_{i-1}} \cdot \frac{\xi_i^{k+1} - \xi_{i-1}^{k+1}}{k+1} \tag{E.6}$$

Introducing this relation into equation (E.5) yields:

$$\mathscr{M}_k \approx \sum_{i=1}^{+\infty} \frac{\phi(\xi_{i-1},\xi_i)}{\xi_i - \xi_{i-1}} \cdot \frac{\xi_i^{k+1} - \xi_{i-1}^{k+1}}{k+1} = (1-\varepsilon) \sum_{i=1}^{+\infty} \frac{\omega(\xi_{i-1},\xi_i)}{\xi_i - \xi_{i-1}} \cdot \frac{\xi_i^{k+1} - \xi_{i-1}^{k+1}}{k+1} \tag{E.7}$$

where equations (E.2) and (E.3) have been used. If the PSD is based on n sieves, we must truncate the summation at the n-th term.

Notation

Dimensions are given in terms of mass (M), length (L), time (t) and dimensionless $(-)$. Some vectors have components with different dimensions; for these quantities dimensions are *not applicable* $(N.A.)$. For some other quantities, the dimensions *depend on the application* $(D.O.A.)$. Uppercase and lowercase boldface symbols are tensors and vectors, respectively. Some of the symbols used infrequently are not listed, but are defined where they first appear in the text.

Non-bracketed roman symbols

a	wave amplitude growth rate	$1/t$
C	constitutive function	$-$
C_D	particle drag force coefficient	$-$
C_f	faxen force coefficient	$-$
C_l	lift force coefficient	$-$
C_v	virtual mass force coefficient	$-$
C_D^t	terminal particle drag force coefficient	$-$
C_D^*	particle drag force coefficient	$-$
$\hat{C}_D^*$	alternative functional dependence for C_D^*	$-$
c_i^ξ	source term in the i-th quadrature weighted node transport equation	$D.O.A.$
c_i^ϕ	source term in the i-th quadrature weight transport equation	$D.O.A.$
$c.v.$	coefficient of variation	$-$
D	constitutive function	$-$
$\mathscr{D}_x$	coefficient of physical diffusion	L^2/T
$\mathscr{D}_n$	coefficient of numerical diffusion	L^2/T
d_p	diameter of particle p	L
d_{sv}	surface-volume mean particle diameter	L
E_f	elastic modulus	M/Lt^2
E_j	elastic modulus	M/Lt^2

E_r	elastic modulus	M/Lt^2
E_r^e	equilibrium elastic modulus	M/Lt^2
e_{ik}	coefficient of restitution for collisions between particles of phases $\mathscr{F}_i$ and $\mathscr{F}_k$	$-$
$\boldsymbol{f}_d$	drag force	ML/t^2
$\boldsymbol{f}^{pq}$	contact force exerted by particle q on particle p	ML/t^2
$\boldsymbol{f}^{qp}$	contact force exerted by particle p on particle q	ML/t^2
F	constitutive function	ML/t^2
$\hat{F}$	alternative functional dependence for F	ML/t^2
F_{ik}	coefficient of friction for phases $\mathscr{F}_i$ and $\mathscr{F}_k$	$-$
F_1	constitutive function	ML/t^2
F_2	constitutive function	ML/t^2
F_{45}	undersize cumulative mass fraction for a sieve aperture size equal to 45 μm	$-$
$\mathscr{F}_i$	particle phase i	$-$
f_m	mass density function	$D.O.A.$
f_v	volume density function	$D.O.A.$
f_n	number density function	$D.O.A.$
$\boldsymbol{g}$	gravitational field	L/t^2
G	constitutive function	ML/t^2
g_{ik}	radial distribution function for phases $\mathscr{F}_i$ and $\mathscr{F}_k$	$-$
H	constitutive function	$-$
h_m	collision integral	$D.O.A.$
h_n	collision integral	$D.O.A.$
h_v	collision integral	$D.O.A.$
$\boldsymbol{I}$	identity tensor	$-$
k	wave number	$1/L$
$\mathscr{M}_k$	moment of order k of the volume density function	$D.O.A.$
$\mathscr{M}_k(\varphi)$	moment of order k of the generic function φ	$D.O.A.$
m_p	mass of particle p	M
$\boldsymbol{n}$	unit vector normal to $\partial\Omega_p$	$-$
$\boldsymbol{n}^{pq}$	unit vector in the direction of $\boldsymbol{x}^{pq} - \boldsymbol{x}^p$	$-$
N	constitutive function	$-$
n	overall number of particles per unit volume of physical space	$1/L^3$
n_e	Richardson & Zaki exponent	$-$

n_i	number of particles of phase $\mathscr{F}_i$ per unit volume of physical space	$1/L^3$
p_k	real polynomial of degree k	$-$
r	distance between two generic points of physical space	L
r_a	weighting function radius	L
r_i	radius of the particles of phase $\mathscr{F}_i$	L
r_m	macroscopic length scale	L
r_p	radius of particle p	L
Re	particle Reynolds number	$-$
Re_i	particle Reynolds number for phase $\mathscr{F}_i$	$-$
Re_t	terminal particle Reynolds number	$-$
Re^*	particle Reynolds number	$-$
S_f	stability function	$-$
S_j	stability function	$-$
S_r	stability function	$-$
$\mathscr{S}_k$	source term in the k-th moment transport equation	$D.O.A.$
$\boldsymbol{T}$	point stress tensor of the fluid	M/Lt^2
t	time	t
t_e	characteristic response time	t
$\boldsymbol{u}$	point velocity of the fluid	L/t
$\hat{\boldsymbol{u}}$	deviation of the point velocity $\boldsymbol{u}$ from the averaged velocity $\langle \boldsymbol{u} \rangle_f$	L/t
$\boldsymbol{u}_s$	superficial velocity of the fluid	L/t
u_d	dynamic wave velocity	L/t
u_{de}	bed surface velocity during bed collapse or expansion	L/t
u_k	kinematic wave velocity	L/t
u_{ks}	discontinuity surface velocity during bed collapse or expansion	L/t
u_s	magnitude of the superficial velocity of the fluid	L/t
u_t	unhindered terminal settling velocity of the particles	L/t
$\boldsymbol{v}$	position vector in velocity state space	L/t
$\dot{\boldsymbol{v}}$	velocity vector in velocity state space	L/t^2
$\hat{\boldsymbol{v}}$	peculiar velocity of the particles (with respect to any averaged velocity)	L/t
$\boldsymbol{v}_i$	quadrature node in velocity state space	L/t
$\boldsymbol{v}^p$	velocity of the center of mass of particle p	L/t
$\dot{\boldsymbol{v}}^p$	acceleration of the center of mass of particle p	L/t^2

v_i	volume of a single particle of phase $\mathscr{F}_i$	L^3
v_p	volume of particle p	L^3
$\boldsymbol{x}$	position vector in physical space	L
$\boldsymbol{x}^p$	position vector of the center of mass of particle p	L
$\boldsymbol{x}^q$	position vector of the center of mass of particle q	L
$\boldsymbol{x}^{pq}$	position vector of the point of mutual contact between particles p and q	L
$\boldsymbol{y}$	position vector in physical space	L

Bracketed roman symbols

$\langle \cdot \rangle$	overall volume average (based on weighting function)	$N.A.$
$\langle \cdot \rangle_e$	ensemble average	$N.A.$
$\langle \cdot \rangle_f$	fluid phase volume average (based on weighting function)	$N.A.$
$\langle \cdot \rangle_m$	disperse phase mass average (based on mass density function)	$N.A.$
$\langle \cdot \rangle_n$	disperse phase number average (based on number density function)	$N.A.$
$\langle \cdot \rangle_p$	particle phase volume average (based on weighting function)	$N.A.$
$\langle \cdot \rangle_t$	time average	$N.A.$
$\langle \cdot \rangle_v$	disperse phase volume average (based on volume density function)	$N.A.$
$\langle \cdot \rangle_p^i$	particle phase volume average for phase $\mathscr{F}_i$ (based on weighting function)	$N.A.$
$\langle \cdot \rangle_s^i$	solid phase volume average for phase $\mathscr{F}_i$ (based on weighting function)	$N.A.$
$\langle \boldsymbol{A} \rangle_f$	second-order tensor, component of $\langle \boldsymbol{S} \rangle_f$	ML^2/t^2
$\langle \boldsymbol{B} \rangle_f$	third-order tensor, component of $\langle \boldsymbol{S} \rangle_f$	ML^3/t^2
$\langle \boldsymbol{D} \rangle_f$	averaged rate of deformation tensor of the fluid	$1/t$
$\langle \boldsymbol{D} \rangle_p$	averaged rate of deformation tensor of the particle phase	$1/t$
$\langle \boldsymbol{f} \rangle_p$	equivalent of $\langle \boldsymbol{f} \rangle_p^i$ for monodisperse suspensions	ML/t^2
$\langle \boldsymbol{f} \rangle_p^i$	averaged interaction force exerted by the fluid on phase $\mathscr{F}_i$	ML/t^2
$\langle \boldsymbol{f} \rangle_p^{ik}$	averaged interaction force exerted by phase $\mathscr{F}_k$ on phase $\mathscr{F}_i$	ML/t^2
$\langle \boldsymbol{f}_a \rangle_p$	averaged local fluid acceleration force	ML/t^2
$\langle \boldsymbol{f}_d \rangle_p$	averaged drag force	ML/t^2
$\langle \boldsymbol{f}_e \rangle_p$	averaged elastic force	ML/t^2
$\langle \boldsymbol{f}_f \rangle_p$	averaged faxen force	ML/t^2
$\langle \boldsymbol{f}_l \rangle_p$	averaged lift force	ML/t^2
$\langle \boldsymbol{f}_s \rangle_p$	averaged buoyancy force	ML/t^2
$\langle \boldsymbol{f}_v \rangle_p$	averaged virtual mass force	ML/t^2

$\langle \boldsymbol{f}_d \rangle_p^{\bullet}$	averaged drag force (based on an alternative buoyancy force definition)	ML/t^2
$\langle \boldsymbol{f}_s \rangle_p^{*}$	averaged buoyancy force (alternative definition)	ML/t^2
$\langle \boldsymbol{f}_s \rangle_p^{\circ}$	averaged buoyancy force (alternative definition)	ML/t^2
$\langle \boldsymbol{f}_s \rangle_p^{\bullet}$	averaged buoyancy force (alternative definition)	ML/t^2
$\langle f_d \rangle_p^{d}$	one-dimensional averaged dynamic drag force	ML/t^2
$\langle f_d \rangle_p^{e}$	one-dimensional averaged equilibrium drag force	ML/t^2
$\langle \boldsymbol{M} \rangle_p^{i}$	second-order tensor, component of $\langle \boldsymbol{S} \rangle_p^{i}$	ML^2/t^2
$\langle \boldsymbol{M} \rangle_p^{ik}$	second-order tensor, component of $\langle \boldsymbol{S} \rangle_p^{i}$	ML^2/t^2
$\langle \boldsymbol{N} \rangle_p^{i}$	third-order tensor, component of $\langle \boldsymbol{S} \rangle_p^{i}$	ML^3/t^2
$\langle \boldsymbol{N} \rangle_p^{ik}$	third-order tensor, component of $\langle \boldsymbol{S} \rangle_p^{i}$	ML^3/t^2
$\langle \mathscr{P} \rangle_f$	averaged modified pressure of the fluid	M/Lt^2
$\langle p \rangle_f$	averaged pressure of the fluid	M/Lt^2
$\langle p \rangle_p$	averaged pressure of the particle phase	M/Lt^2
$\langle \boldsymbol{S} \rangle_f$	effective stress tensor of the fluid	M/Lt^2
$\langle \boldsymbol{S} \rangle_p$	equivalent of $\langle \boldsymbol{S} \rangle_p^{i}$ for monodisperse suspensions	M/Lt^2
$\langle \boldsymbol{S} \rangle_p^{i}$	effective stress tensor of phase $\mathscr{F}_i$	M/Lt^2
$\langle \boldsymbol{T} \rangle_f$	averaged point stress tensor of the fluid	M/Lt^2
$\langle \boldsymbol{u} \rangle_f$	averaged velocity of the fluid	L/t
$\langle \boldsymbol{v} \rangle_m$	mass averaged velocity of the disperse phase	L/t
$\langle \boldsymbol{v} \rangle_n$	number averaged velocity of the disperse phase	L/t
$\langle \boldsymbol{v} \rangle_p$	equivalent of $\langle \boldsymbol{v} \rangle_p^{i}$ for monodisperse suspensions	L/t
$\langle \boldsymbol{v} \rangle_v$	volume averaged velocity of the disperse phase	L/t
$\langle \boldsymbol{v} \rangle_p^{i}$	averaged velocity of phase $\mathscr{F}_i$	L/t

Non-bracketed Greek symbols

α	exponent of the drag force corrective function	$-$
α_d	exponent of the drag force corrective function	$-$
$\hat{\alpha}_d$	exponent of the drag force corrective function	$-$
$\tilde{\alpha}_d$	exponent of the drag force corrective function	$-$
β	drag force coefficient	M/L^3t
$\hat{\beta}$	alternative functional dependence for β	M/L^3t
β_i	drag force coefficient for phase $\mathscr{F}_i$	M/L^3t
ε	volume of fluid per unit volume of physical space	$-$

$\hat{\varepsilon}$	deviation of the bed voidage ε from the equilibrium bed voidage $\bar{\varepsilon}$	$-$
$\bar{\varepsilon}$	equilibrium bed voidage	$-$
$\tilde{\varepsilon}$	effective bed voidage	$-$
ε_D	theoretical equilibrium bed voidage	$-$
ε_E	theoretical equilibrium bed voidage	$-$
$\varepsilon_{M\&L}$	theoretical equilibrium bed voidage	$-$
$\varepsilon_{R\&Z}$	theoretical equilibrium bed voidage	$-$
$\varepsilon_{W\&Y}$	theoretical equilibrium bed voidage	$-$
$\hat{\varepsilon}_a$	wave initial amplitude	$-$
ε_{exp}	experimental equilibrium bed voidage	$-$
$\varepsilon^{mb}_{F\&G}$	theoretical minimum bubbling voidage	$-$
$\varepsilon^{mb}_{J\&F}$	theoretical minimum bubbling voidage	$-$
$\varepsilon^{mb}_{M\&L}$	theoretical minimum bubbling voidage	$-$
ε^{mb}_{exp}	experimental minimum bubbling voidage	$-$
$\boldsymbol{\zeta}$	position vector in generalized internal state space	$N.A.$
ζ_{ik}	drag force coefficient for the force exerted by phase $\mathscr{F}_k$ on phase $\mathscr{F}_i$	M/L^3t
Θ	granular temperature	L^2/T^2
θ	penetration distance	L
κ_f	dilatational viscosity of the fluid	M/Lt
κ_p	dilatational viscosity of the particle phase	M/Lt
Λ_v	control volume in velocity state space	L^3/t^3
$\partial\Lambda_v$	boundary of the control volume Λ_v	L^2/t^2
Λ_x	control volume in physical space	L^3
$\partial\Lambda_x$	boundary of the control volume Λ_x	L^2
Λ_ξ	control volume in internal state space	$D.O.A.$
$\partial\Lambda_\xi$	boundary of the control volume Λ_ξ	$D.O.A.$
Λ_ψ	control volume in particle state space	$D.O.A.$
$\partial\Lambda_\psi$	boundary of the control volume Λ_ψ	$D.O.A.$
μ_f	shear viscosity of the fluid	M/Lt
μ_p	shear viscosity of the particle phase	M/Lt
ν	number of nodes in a quadrature formula	$-$
ν_w	wave velocity	L/t
$\boldsymbol{\xi}$	position vector in internal state space	$N.A.$

$\dot{\boldsymbol{\xi}}$	velocity vector in internal state space	$N.A.$
$\boldsymbol{\xi}_i$	quadrature node in internal state space	$N.A.$
π_k	real monic orthogonal polynomial of degree k	$-$
ρ_d	overall mass of particles per unit volume of physical space	M/L^3
ρ_f	density of the fluid	M/L^3
ρ_i	density of the particles of phase $\mathscr{F}_i$	M/L^3
ρ_p	density of particle p	M/L^3
τ_a	averaging time interval	t
τ_m	macroscopic time scale	t
τ_t	turbulent time scale	t
ϕ	overall volume of particles per unit volume of physical space	$-$
ϕ_i	volume of particles of phase $\mathscr{F}_i$ per unit volume of physical space	$-$
φ	drag force corrective function	$-$
$\boldsymbol{\psi}$	position vector in particle state space	$N.A.$
ψ	weighting function	$1/L^3$
ψ_e	exponent of the drag force corrective function	$-$
Ω	domain of integration bounding the suspension	L^3
Ω_a	averaging volume	L^3
Ω_f	domain of integration bounding the fluid	L^3
Ω_p	domain of integration bounding particle p	L^3
$\partial\Omega_p$	boundary of the domain Ω_p	L^2
Ω_v	domain of variation of the coordinate vector $\boldsymbol{v}$	L^3/t^3
Ω_x	domain of variation of the coordinate vector $\boldsymbol{x}$	L^3
Ω_ζ	domain of variation of the coordinate vector $\boldsymbol{\zeta}$	$D.O.A.$
Ω_ξ	domain of variation of the coordinate vector $\boldsymbol{\xi}$	$D.O.A.$
Ω_ψ	domain of variation of the coordinate vector $\boldsymbol{\psi}$	$D.O.A.$
ω_i	void-free mass fraction of phase $\mathscr{F}_i$	$-$

Bracketed Greek symbols

$\langle\Phi\rangle_p^d$	one-dimensional averaged dynamic net force	ML/t^2
$\langle\Phi\rangle_p^e$	one-dimensional averaged equilibrium net force	ML/t^2

Mathematical symbols

D_f/Dt	material derivative for the fluid phase	$1/t$
D_i/Dt	material derivative for the i-th quadrature class	$1/t$
D_p/Dt	material derivative for the particle phase	$1/t$
$d\boldsymbol{S}_v$	differential surface vector normal to $\partial\Lambda_v$	L^2/t^2
$d\boldsymbol{S}_x$	differential surface vector normal to $\partial\Lambda_x$	L^2
$d\boldsymbol{S}_\xi$	differential surface vector normal to $\partial\Lambda_\xi$	$N.A.$
dS_y	differential integration surface where $\boldsymbol{y}$ is the integration variable	L^2
dV_y	differential integration volume where $\boldsymbol{y}$ is the integration variable	L^3
$d\boldsymbol{v}$	differential integration volume in velocity state space	L^3/t^3
$d\boldsymbol{x}$	differential integration volume in physical state space	L^3
$d\boldsymbol{\zeta}$	differential integration volume in generalized internal state space	$D.O.A.$
$d\boldsymbol{\xi}$	differential integration volume in internal state space	$D.O.A.$
$d\boldsymbol{\psi}$	differential integration volume in particle state space	$D.O.A.$
$\boldsymbol{\delta}$	multidimensional Dirac delta function	$D.O.A.$
δ	Dirac delta function	$D.O.A.$
δ'	derivative of the Dirac delta function	$D.O.A.$
$\boldsymbol{\nabla}$	gradient operator in physical space	$1/L$
$\boldsymbol{\nabla}\cdot$	divergence operator in physical space	$1/L$
$\boldsymbol{\nabla}\times$	curl operator in physical space	$1/L$
$\boldsymbol{\nabla}_v$	gradient operator in velocity state space	t/L
$\boldsymbol{\nabla}_x$	gradient operator in physical state space	$1/L$
$\boldsymbol{\nabla}_\xi$	gradient operator in internal state space	$N.A.$
$\boldsymbol{\nabla}_v\cdot$	divergence operator in velocity state space	t/L
$\boldsymbol{\nabla}_x\cdot$	divergence operator in physical state space	$1/L$
$\boldsymbol{\nabla}_\xi\cdot$	divergence operator in internal state space	$N.A.$

Bibliography

Arfken, J. B. 1985. *Mathematical methods for physicists*. Academic Press.

Anderson, T. B. & Jackson, R. 1967. A fluid mechanical description of fluidized beds. Equations of motion. Ind. Eng. Chem. Fundam. **6**, 527.

Astarita, G. 1993. Forces acting on particles in a fluidized bed. Chem. Eng. Sci. **48**, 3438.

Astarita, G. & Marrucci, G. 1974. *Principles of Non-Newtonian Fluid Mechanics*. McGraw-Hill.

Auton, T. R., Hunt, J. C. R. & Prud'homme, M. 1988. The force exerted on a body in inviscid, unsteady, non-uniform, rotational flow. J. Fluid Mech. **197**, 241.

Barnea, E. & Mizrahi, J. 1973. A generalized approach to the fluid dynamics of particulate systems. Chem. Eng. Sci. **5**, 171.

Basset, A. B. 1888. *Treatise on Hydrodynamics*. Deighton Bell.

Batchelor, G. K. 1967. *An Introduction to Fluid Dynamics*. Cambridge University Press.

Batchelor, G. K. & Green, J. T. 1972. The determination of the bulk stress in a suspension of spherical particles to order c^2. J. Fluid Mech. **56**, 401.

Bird, R. B., Stewart, W. E. & Lightfoot, E. N. 1960. *Transport Phenomena*. Wiley.

Bird, R. B., Stewart, W. E. & Lightfoot, E. N. 2007. *Transport Phenomena*. Wiley.

Birkhoff, G. 1950. *Hydrodynamics*. Princeton University Press for University of Cincinnati.

Brenner, H. 1964. The Stokes resistence of an arbitrary particle - Part IV. Arbitrary fields of flow. Chem. Eng. Sci. **19**, 703.

Brilliantov, N. V. & Poschel T. 2004. *Kinetic Theory of Granular Gases*. Oxford University Press.

Brinkman, H. C. 1952. The viscosity of concentrated suspensions and solutions. J. Chem. Phys. **20**, 571.

Bronson, R. 1989. *Matrix Operations*. McGrow-Hill.

Buwa, V. V. & Ranade, V. V. 2002. Dynamics of gas-liquid flow in a rectangular bubble column: experiments and single/multi-group CFD simulation. Chem. Eng. Sci. **57**, 4715.

Buyevich, Y. A. 1971. Statistical hydrodynamics of disperse systems. Part 1. Physical background and general equations. J. Fluid Mech. **49**, 489.

Cammarata, L., Lettieri, P., Michale, G. & Colman, D. 2003. 2D and 3D CFD simulations of bubbling fluidized beds using Eulerian-Eulerian models. IJCRE. **1**, 48.

Chapman, S. & Cowling, T. G. 1970. *The Mathematical Theory of Non-Uniform Gases*. Cambridge University Press.

Clift, R., Seville, J. P. K., Moore, S. C. & Chavarie, C. 1987. Comments on buoyancy on fluidized beds. Chem. Eng. Sci. **42**, 191.

Cooper, S. & Coronella, C. J. 2005. CFD simulations of particle mixing in a binary fluidized bed. Powder Technol. **151**, 27.

Crowe, C. 2005. *Multiphase Flow Handbook*. CRC Press Inc.

Curtis, J. & van Wachem, B. G. M. 2004. Modeling particle-laden flows: A research outlook. AIChE J. **50**, 11.

Dallavalle, J. M. 1948. *Micromeritics*. Pitman.

Davidson, D. 2002. The role of computational fluid dynamics in process industries. The Bridge. **32**, 4.

Delhaye, J. M. & Achard, J. L. 1977. On the use of averaging operators in two phase flow modeling. Thermal and Hydraulic Aspects of Nuclear Reactor Safety. Part 1: Light Water Reactors. ASME Winter Meeting.

Delhaye, J. M. & Achard, J. L. 1978. On the averaging operators introduced in two-phase flow. In *Transient Two-phase Flow*. In Proc. of CSNI Specialists Meeting, Toronto, August 3-4.

Dette, H. & Studden, W. J. 1997. *The theory of canonical moments with applications in statistics, probability, and analysis*. Wiley.

Di Felice, R. 1994. The voidage function for fluid-particle interaction systems. Int. J. Multiphase Flow **20**, 153.

Drew, D. A. 1971. Averaged field equations for two-phase media. Stud. Appl. Math. **50**, 133.

Drew, D. A. 1983. Mathematical modelling of two-phase flow. Annu. Rev. Fluid Mech. **15**, 261.

Drew, D. A. & Lahey, R. T. 1993. Analytical modelling of multiphase flow. In *Particulate Two-Phase Flow*. Butterworth-Heinemann.

Drew, D. A. & Passman, S. L. 1998. *Theory of Multicomponent Fluids*. Applied Mathematical Sciences. Springer.

Drew, D. A. & Segel, L. A. 1971. Averaged equations for two-phase flows. Stud. Appl. Math. **50**, 205.

Einstein, A. 1906. Eine Neue Bestimmung der Molekuldimensionen. Ann. Phys. **19**, 289.

Einstein, A. 1911. Berichtigung zu meiner Arbeit: Eine Neue Bestimmung der Molekuldimensionen. Ann. Phys. **34**, 591.

Enwald, H., Peirano, E. & Almstedt, A. E. 1996. Eulerian two-phase flow theory applied to fluidization. Int. J. Multiphase Flow **22**, 21.

Epstein, N. 1984. Comments on a unified model for particulate expansion of fluidized beds and flow in fixed porous media. Chem. Eng. Sci. **39**, 1533.

Ergun, S. 1952. Fluid flow through packed columns. Chem. Eng. Progr. **48**, 89.

Fan, R., Marchisio, D. L. & Fox, R. O. 2004. Application of the direct quadrature method of moments to polydisperse gas-solid fluidized beds. Powder Technol. **139**, 7.

Ferziger, J. H. & Peric, M. 2002. *Computational methods for fluid dynamics*. Springer.

Foscolo, P. U. & Gibilaro, L. G. 1984. A fully predictive criterion for the transition between particulate and aggregate fluidization. Chem. Eng. Sci. **39**, 1667.

Foscolo, P. U. & Gibilaro, L. G. 1987. Fluid dynamic stability of fluidized suspensions: The particle bed model. Chem. Eng. Sci. **42**, 1489.

Foscolo, P. U., Gibilaro, L. G., Waldram, S. P. 1983. A unified model for particulate expansion of fluidized beds and flow in fixed porous media. Chem. Eng. Sci. **38**, 1251.

Francis, A. W. 1933. Wall effect in falling fall method for viscosity. Physics **4**, 403.

Frankel, N. A. & Acrivos, A. 1967. On the viscosity of a concentrated suspension of solid spheres. Chem. Eng. Sci. **22**, 847.

Geldart, D. 1973. *Gas Fluidization Technology*. Wiley.

Geldart, D. & Wong, A. C. Y. 1984. Fluidization of powders showing degrees of cohesiveness – I. Bed expansion. Chem. Eng. Sci. **39**, 1481.

Geldart, D. & Wong, A. C. Y. 1985. Fluidization of powders showing degrees of cohesiveness – II. Experiments on retes of de-aeration. Chem. Eng. Sci. **40**, 653.

Georgi, H. 1993. *The Physics of Waves*. Prentice Hall.

Gera D., Syamlal M. & O'Brien T. J. 2004. Hydrodynamics of particle segregation in fluidized beds. Int. J. Multiphase Flow. **30**, 419.

Gibb, J. 1991. Pressure and viscous forces in an equilibrium fluidized suspension. Chem. Eng. Sci. **46**, 379.

Gibilaro, L. G. 2001. *Fluidization-Dynamics*. Butterworth Heinemann.

Gibilaro, L. G., Waldram, S. P. & Foscolo, P. U. 1984. A simple mechanistic description of the unsteady-state expansion of liquid-fluidized beds. Chem. Eng. Sci. **39**, 607.

Gidaspow, D. 1994. *Multiphase Flow and Fluidization*. Academic Press.

Gidaspow, D. & Ettehadieh B. 1983. Fluidization in two-dimensional beds with a jet. Part II: hydrodynamic modeling. Ind. Eng. Chem. Fundam. **22**, 193.

Gidaspow, D., Syamlal, M. & Seo, Y. C. 1986. Hydrodynamics of fluidization: supercomputer generated vs. experimental bubbles. J. Powder & Bulk Solids Tech. **10**, 19.

Godard, K. M. S. & Richardson, J. F. 1968. The behaviour of bubble-free fluidized beds. I. Chem. E. Symposium Series. **30**, 126.

Goldshtein, A. & Shapiro, M. 1995. Mechanics of collisional motion of granular materials. Part I. General hydrodynamic equations. J. Fluid Mech. **282**, 75.

Gordon, R. G. 1968. Error bounds in equilibrium statistical mechanics. Journal of Mathematical Physics **9**, 655.

Grace, J. R. 1970. The viscosity of fluidized beds. CJChE **48**, 30.

Graham, A. L. 1981. On the viscosity of suspensions of solid spheres. Appl. Sci. Res. **37**, 275.

Gurtin, M. E. 2003. *An Introduction to Continuum Mechanics*. Academic Press.

Haff, P. K. 1983. Grain flow as a fluid mechanical phenomenon. J. Fluid Mech. **134**, 401.

Happel, J. & Epstein, N. 1954. Viscous flow in multiparticle systems: cubical assemblages of uniform spheres. Ind. Eng. Chem. **46**, 1187.

Hoomans, B. P. B., Kuipers, J. A. M., Briels, W. J. & van Swaaij, W. P. M. 1996. Discrete particle simulation of a two-dimensional gas-fluidized bed: a hard sphere approach. Chem. Eng. Sci. **51**, 99.

Hinch, E. J. 1977. An averaged equation approach to particle interactions in a fluid suspension. J. Fluid Mech. **83**, 695.

Hulburt, H. M. & Katz, S. 1964. Some problems in particle technology. Chem. Eng. Sci. **19**, 555.

Jackson, R. 1963. The mechanics of fluidized beds: Part I. The stability of the state of uniform fluidization. Trans. Instn. Chem. Eng. **41**, 13.

Jackson, R. 1997. Locally averaged equations of motion for a mixture of identical spherical particles and a Newtonian fluid. Chem. Eng. Sci. **52**, 2457.

Jackson, R. 1998. Erratum. Chem. Eng. Sci. **53**, 1955.

Jackson, R. 2000. *The Dynamics of Fluidized Particles*. Cambridge Monographs on Mechanics. Cambridge University Press.

Jean, R. H. & Fan, L. S. 1992. On the model equations of Gibilaro and Foscolo with corrected buoyancy force. Powder Technol. **72**, 201.

Jenkins, J. T. 1987. Rapid flows of granular materials. In *Non-Classical Continuum Mechanics*. Cambridge University Press.

Jenkins, J. T. & Savage, S. B. 1983. A theory for the rapid flow of identical, smooth, nearly elastic, spherical particles. J. Fluid Mech. **130**, 187.

Johnson, P. C. & Jackson, R. 1987. Frictional-collisional constitutive relations for granular materials with application to plane shearing. J. Fluid Mech. **176**, 67.

Kafui, K. D., Thornton, C. & Adams, M. J. 2002. Discrete particle-continuum fluid modelling of gas-solid fluidised beds. Chem. Eng. Sci. **57**, 2395.

Khan, A. R. & Richardson, J. F. 1989. Fluid-particle interactions and flow characteristics of fluidized beds and settling suspensions of spherical particles. Chem. Eng. Comm. **78**, 111.

King, D. F., Mitchell, F. R. G. & Harrison, D. 1981. Dense phase viscosities of fluidized beds at elevated pressures. Powder Technol. **28**, 55.

Kleinstreuer, C. 2003. *Two-phase Flow*. Routledge.

Kmiec, A. 1982. Equilibrium of forces in a fluidized bed - experimental verification. J. Chem. Eng. **23**, 133.

Kuipers, J., van Duin, K., van Beckum, F. & van Swaaij, W. 1993. Computer simulation of the hydrodynamics of a two-dimensional gas-fluidized bed. Computers Chem. Eng. **17**, 839.

Kunii, D. & Levenspiel, O. 1989. *Fluidization Engineering*. Butterworth Heinemann.

Lai, W. M., Rubin, D. & Krempl, E. 1993. *Introduction to Continuum Mechanics*. Butterworth Heinemann.

Lang, S. 2004. *Linear Algebra*. Springer.

Lebowitz, J. L. 1964. Exact solution of generalised Percus-Yevick equation for a mixture of hard spheres. Phys. Rev. **133**, 895.

Lehr, F. & Mewes, D. 2001. A transport equation for the interfacial area density applied to bubble columns. Chem. Eng. Sci. **56**, 1159.

Lettieri, P. 1999. A study of the influence of temperature on the flow behaviour of solid materials in a gas fluidized bed. Ph.D. Dissertation. Department of Chemical Engineering, University College London.

Lettieri, P. 2002. Fluidization. Course notes. Department of Chemical Engineering, University College London.

Lettieri, P., Brandani, S., Yates, J. G. & Newton, D. 2001. A generalization of the Foscolo and Gibilaro Particle Bed Model to predict the fluid bed stability of some fresh FCC catalysts at elevated temperatures. Chem. Eng. Sci. **56**, 5401.

Lettieri, P., Cammarata, L., Michale, G. & Yates, J. G. 2003. CFD simulations of gas-fluidized beds using alternative Eulerian-Eulerian modelling approaches. IJCRE. **1**, 5.

Lettieri, P., Saccone, G. & Cammarata, L. 2004. Predicting the transition from bubbling to slugging fluidization using computational fluid dynamics. Chem. Eng. Res. Des. **82**, 939.

Lettieri, P., Yates, J. G. & Newton, D. 2000. The influence of interparticle forces on the fluidization behaviour of some industrial materials at high temperature. Powder Technol. **110**, 117.

Lettieri, P., Newton, D. & Yates, J. G. 2002. Homogeneous bed expansion of FCC catalysts, influence of temperature on the parameters of the Richardson-Zaki equation. Powder Technol. **123**, 221.

Leva, M. 1959. *Fluidization*. McGraw-Hill.

Levenspiel, O. 1999. *Chemical Reaction Engineering*. Wiley.

Lewis, W. K., Gilliland, W. C. & Bauer, W. C. 1949. Characteristics of fluidized particles. Ind. Eng. Chem. **41**, 1104.

Lipschutz, S. & Lipson, M. L. 2001. *Linear Algebra*. McGrow-Hill.

Lo, S. M. 1989. Mathematical basis of a multiphase flow model. AERE R 13432.

Lu, H., Wang, S., Zhao, Y., Yang, L., Gidaspow, D. & Ding, J. 2005. Prediction of particle motion in a two-dimensional bubbling fluidized bed using hard-sphere model. Chem. Eng. Sci. **60**, 3217.

Lun, C. K. K. 1991. Kinetic theory for granular flow of dense, slightly inelastic, slightly rough spheres. J. Fluid Mech. **223**, 539.

Lun, C. K. K., Savage, S. B., Jeffrey, D. J. & Chepurniy, N. 1984. Kinetic theories for granular flow: Inelastic particles in Couette flow and slightly inelastic particles in a general flow field. J. Fluid Mech. **140**, 223.

Makkawi, Y. & Ocone, R. 2006. A model for gas-solid flow in a horizontal duct with a smooth merge of rapid-intermediate-dense flows. Chem. Eng. Sci. **61**, 4271.

Marchisio, D. L. & Fox, R. O. 2005. Solution of population balance equations using the direct quadrature method of moments. J. Aerosol Sci. **36**, 43.

Marchisio, D. L. & Fox, R. O. 2007. *Multiphase reacting flows: modelling and simulation*. CISM courses and lectures No. 492. International Centre for Mechanical Sciences. Springer.

Massaudi, M. 2002. On the importance of material frame-indifference and lift forces in multiphase flows. Chem. Eng. Sci. **57**, 3687.

Massimilla, L., Donsi', G. & Zucchini, C. 1972. The structure of bubble-free gas fluidized beds of fine fluid cracking catalyst particles. Chem. Eng. Sci. **27**, 2005.

Massoudi, M., Rajagopal, K. R., Ekmann, J. M. & Mathur, M. P. 1992. Remarks on the modelling of fluidized systems. AIChE J. **38**, 471.

Maxey, M. R. & Riley, J. J. 1983. Equation of motion for a small rigid sphere in a nonuniform flow. Phys. Fluids **26**, 883.

McGraw, R. 1997. Description of aerosol dynamics by the quadrature method of moments. Aerosol Sci. Technol. **27**, 255.

Metzner, A. B. 1985. Rheology of suspensions in polymeric liquids. J. Rheol. **29**, 739.

Mooney, J. 1951. The viscosity of a concentrated suspension of spherical particles. J. Colloid Interphase Sci. **91**, 160.

Murray, J. D. 1965. On the mathematics of fluidization. J. Fluid Mech. **21**, 465.

Mutsers, S. M. P. & Rietema, K. 1977. The effect of interparticle forces on the expansion of a homogeneous gas-fluidized bed. Powder Technol. **18**, 239.

Nadim, A. & Stone, H. A. 1991. The motion of small particles and droplets in quadratic flows. Stud. Appl. Math. **85**, 53.

Nigmatulin, R. I. 1979. Spatial averaging in the mechanics of heterogeneous and dispersed systems. Int. J. Multiphase Flow. **5**, 353.

Olmos, E., Gentric, C., Vial, C., Wild, G. & Midoux, N. 2001. Numerical simulation of multiphase flow in bubble column reactors. Influence of bubble coalescence and break-up. Chem. Eng. Sci. **56**, 6359.

Othmer, D. F. 1956. *Fluidization*. Reinhold Publishing Corporation.

Ouyang, J. & Li, J. 1999. Particle-motion-resolved discrete model for simulating gas-solid fluidization. Chem. Eng. Sci. **54**, 2077.

Owoyemi, O., Mazzei, L. & Lettieri, P. 2007. CFD modeling of binary-fluidized suspensions and investigation of role of particle-particle drag on mixing and segregation. AIChE J. **53**, 1924.

Pain, C. C., Mansoorzadeh, S. & de Oliveira, C. R. E. 2001. A study of bubbling and slugging fluidised beds using the two-fluid granular temperature model. Int. J. Multiphase Flow. **27**, 527.

Pan, T. W., Joseph, D. D., Bai, R., Glowinski, R. & Sarin, V. 2002. Fluidization of 1204 spheres: simulation and experiments. J. Fluid Mech. **451**, 169.

Petrovsky, I. 1957. *Lectures on the Theory of Integral Equations*. Graylock Press.

Pigford, R. & Baron, T. 1965. Hydrodynamic stability of a fluidized bed. Ind. Eng. Chem. Fundam. **4**, 81.

Poletto, M. & Joseph, D. D. 1995. Effective density and viscosity of a suspension. J. Rheol. **39**, 323.

Press, W. H., Teukolsky, S. A., Vetterling, W. T. & Flannery, B. P. 2002. *Numerical Recipes in C++: The Art of Scientific Computing*. Cambridge University Press.

Pritchett, J. W., Blake, T. R. & Garg, S. K. 1978. A numerical model of gas fluidized beds. AIChE Symp. Ser. **176**, 134.

Prudhoe, J. & Whitmore, R. L. 1964. Terminal velocity of spheres in fluidized beds. Br. Chem. Eng. **9**, 371.

Ramkrishna, D. 2000. *Population Balances*. Academic Press.

Randolph, A. D. & Larson, M. A. 2001. *Theory of particulate processes*. Academic Press.

Reiling, V. G. 1992. Effect of type C particles on cohesion and viscosity of Type A powders. In *Fluidization VII* (Potter, O.E. & Nicklin, D.J., Editors), Engineering Foundation, New York, USA.

Richardson, J. F. & Zaki, W. N. 1954. Sedimentation and fluidization: Part I. Trans. Inst. Chem. Eng. **32**, 35.

Rietema, K. & Piepers, H. W. 1990. Effect of interparticle forces on the stability of gas-fluidized beds – I. Experimental evidence. Chem. Eng. Sci. **45**, 1627.

Rowe, P. N. 1987. A convenient empirical equation for estimation of the Richardson & Zaki exponent. Chem. Eng. Sci. **42**, 2795.

Rumpf, H. & Gupte, A. R. 1971. Einflüsse der porosität und korngrößenverteilung im widerstandsgesetz der porenströmung. Chem. Ing. Tech. **43**, 367.

Rutgers, R. 1962. Relative viscosity of suspensions of rigid spheres in Newtonian liquids. Rheol. Acta **2**, 202.

Saffman, P. G. 1965. The lift on a small sphere in a slow shear flow. J. Fluid Mech. **22**, 385.

Sandler, S. I. 1989. *Chemical and Engineering Thermodynamics*. Wiley.

Savage, S. B. 1982. Granular flows down rough inclines – review and extension. In Proc. of U.S. – Japan Seminar on New Models and Constitutive Relations in the Mechanics of Granular Materials. Jenkins J. T. & Satake M. Eds. Elsevier.

Schiller, L. & Naumann, Z. 1935. A drag coefficient correlation. Z. Ver. Deutsch. Ing. **77**, 318.

Syamlal, M. 1987. The particle-particle drag term in a multiparticle model of fluidization. National Technical Information Service. DOE/MC/21353-2373, NTIS/DE87006500.

Spalding, D. B. 1976. The calculation of free-convection phenomena in gas-liquid mixtures. ICHMT Seminar. Dubrovnik, Croatia.

Tai, C. 1997. *Generalized Vector and Dyadic Analysis*. Wiley-IEEE Press.

Thomas, D. G. 1965. Transport characteristics of suspension: VIII. A note on the viscosity of Newtonian suspensions of uniform spherical particles. J. Colloid Sci. **20**, 267.

Truesdell, C. 1977. *A First Course in Rational Continuum Mechanics*. Academic Press.

Tsuji, Y., Kawaguchi, T. & Tanaka, T. 1993. Discrete particle simulation of two-dimensional fluidized bed. Powder Technol. **77**, 79.

Vand, V. 1948. Viscosity of solutions and suspensions. I–lII. J. Phy. Colloid Chem. **52**, 277.

Venneker, B. C. H., Derksen, J. J. & van den Akker, H. E. A. 2002. Population balance modeling of aerated stirred vessels based on CFD. AIChE J. **48**, 673.

Ver, L. M. B. & Wang, J. K. 1995. Design criteria of a fluidized bed oyster nursery. Aquacultural Eng. **14**, 229.

Verloop, J. & Heertjes, P. M. 1970. Shock waves as a criterion for the transition from homogeneous to heterogeneous fluidization. Chem. Eng. Sci. **25**, 825.

van Wachem, B. G. M., Schouten, J. C., van den Bleek, C. M., Krishna, R. & Sinclair, J. L. 2001. CFD modeling of gas-fluidized beds with a bimodal particle mixture. AIChE J. **47**, 1292.

Wen, C. Y. & Yu, Y. H. 1966. Mechanics of Fluidization. Chem. Eng. Prog. Symp. Series **62**, 100.

Whitaker, S. 1969. Advances in the theory of fluid motion in porous media. Ind. Eng. Chem. **61**, 14.

Wilhelm, R. H. & Kwauk, M. 1948. Fluidization of solid particles. Chem. Eng. Progr. **44**, 201.

Xie, H. Y. & Geldart, D. 1995. Fluidization of FCC powders in the bubble-free regime: Effect of types of gases and temperature. Powder Technol. **82**, 269.

Yang, W. 2003. *Handbook of Fluidization and Fluid-Particle Systems*. Marcel Dekker.

Yang, J. & Renken, A. 2003. A generalized correlation for equilibrium of forces in liquid-solid fluidized beds. Chem. Eng. J. **92**, 7.

Yates, J. G., Cheesman, D. & Sergeev, Y. A. 1994. Experimental observations of voidage distribution around bubbles in a fluidized bed. Chem. Eng. Sci. **49**, 1885.

Zenz, F. A. & Othmer, D. F. 1960. *Fluidization and Fluid-Particle Systems*. Reinhold Publishing Corporation.

Zhang, D. Z. & Prosperetti, A. 1994. Averaged equations for inviscid disperse two-phase flow. J. Fluid. Mech. **267**, 185.

Zhang, D. Z. & Prosperetti, A. 1997. Momentum and energy equations for disperse two-phase flows and their closure for dilute suspensions. Int. J. Multiphase Flow. **23**, 425.

Publications

Refereed journals publications

1) Mazzei, L., Lettieri, P., Elson, T. & Colman, D. 2006. A revised monodimensional particle bed model for fluidized beds. Chem. Eng. Sci. **61**, 1958.
2) Mazzei, L. & Lettieri, P. 2006. A numerical algorithm for the analysis of the bubble dynamics in two-dimensional fluidized beds simulated by means of CFD multiphase flow codes. IJCRE **4**, 1.
3) Mazzei, L. & Lettieri, P. 2007. A drag force closure for uniformly dispersed fluidized suspensions. Chem. Eng. Sci. **62**, 6129.
4) Owoyemi, O., Mazzei, L. & Lettieri, P. 2007. CFD modeling of binary-fluidized suspensions and investigation of role of particle-particle drag on mixing and segregation. AIChE J. **53**, 1924.
5) Lettieri, P. & Mazzei, L. 2007. Analysis of the fluid-bed stability of some FCC catalysts at high temperature through considerations on the bed elasticity. China Particuology **6**, 30.
6) Mazzei, L. & Lettieri, P. 2008. CFD simulations of expanding/contracting homogeneous fluidized beds and their transition to bubbling. Chem. Eng. Sci. **63**, 5831.
7) Colafigli, A., Mazzei, L. Lettieri, P. & Gibilaro, L. G. 2008. Apparent viscosity measurements in a homogeneous gas-fluidized bed. Chem. Eng. Sci. In press.

Refereed conference publications

1) Mazzei, L., Lettieri, P., Elson, T. & Colman, D. 2005. A study of the stability and dynamics of gas-fluidized beds using a revised particle bed model. In Proc. of the 9th International Conference on Particulate Systems Analysis. Stratford-upon-Avon, UK, September 21.
2) Mazzei, L., Lettieri, P., Elson, T. & Colman, D. 2006. A study of the dynamics of homogeneous and bubbling fluidized beds by means of computational fluid dynamics. In Proc. of the 5th World Congress on Particle Technology. Orlando, USA, April 22.
3) Mazzei, L. & Lettieri, P. 2006. A study of fluidization dynamics by means of CFD. In Proc. of the 10th International Conference on Multiphase Flow in Industrial Plants. Tropea, Italy, September 19.

4) Mazzei, L. & Lettieri, P. 2007. A new fluid dynamic model for the CFD simulations of fluidized beds. In Proc. of the 12th International Conference on Fluidization. Harrison Hot Springs, Canada, May 13.
5) Mazzei, L., Lettieri, P. & Marchisio, D. L. 2008. Investigation into the dynamics of polydisperse fluidized beds by using the direct quadrature method of moments. In Proc. of the 11th International Conference on Multiphase Flow in Industrial Plants. Palermo, Italy, September 7.
6) Mazzei, L., Lettieri, P., & Marchisio, D. L. 2008. A study of the stability and dynamics of gas-fluidized beds using a revised particle bed model. In Proc. of the 10th International Conference on Particulate Systems Analysis. Stratford-upon-Avon, UK, September 7.

Other conference publications

1) Mazzei, L., Lettieri, P., Elson, T. & Colman, D. 2005. A modification of the Foscolo-Gibilaro particle bed model. In Book of Abstracts of the 4th conference on Computational Fluid Dynamics in Chemical Reaction Engineering. Barga, Italy, June 19.
2) Mazzei, L., Lettieri, P., Elson, T. & Colman, D. 2005. CFD simulations of gas-fluidized beds using a revised formulation of the multi-dimensional particle bed model. In Proc. of the AIChE Annual Meeting. Cincinnati, USA, November 30.
3) Mazzei, L., Lettieri, P. & Colman, D. 2007. A study of fluidization dynamics by means of CFD. In Proc. of the conference ParTec 2007. Nuremberg, Germany, March 27.
4) Mazzei, L., Lettieri, P. & Marchisio, D. L. 2008. Experimental validation of CFD models for polydisperse fluidized powders based on the quadrature methods of moments. In Proc. of the 5th conference on Computational Fluid Dynamics in Chemical Reaction Engineering. Whistler, Canada, June 15.